Development and Application of an Advanced Fuel Model for the Safety Analysis of the Generation IV Gas-cooled Fast Reactor

PAR

Petr PETKEVICH

Ingenieur-Physiker, Moskauer Ingenieur und Physikinstitut (Staatliche Universität), Russie
et de nationalité russe

EPFL

ÉCOLE POLYTECHNIQUE
FÉDÉRALE DE LAUSANNE

Suisse
2008

Abstract

Until about the year 2030, current-day nuclear power plants (NPPs) will be replaced by so-called Gen-III or Gen-III+ units, which are mainly based on light water reactor technology. The principal new features are increased safety and improved economical effectiveness. However, these systems use the same fuel forms and are based on the same fuel cycle. Beyond 2030, the interest is likely to shift towards fourth generation NPPs, which offer the possibility of complete fuel cycle closure. Generation-IV reactor concepts include both thermal and fast systems, and involve a wide range of fuel forms and compositions.

The present research has been focused on the development of a thermo-mechanical model for the innovative fuel design of the Generation-IV Gas-cooled Fast Reactor (GFR). The principal distinctive feature of the fuel is that the fuel pellets are arranged within plates which enclose an inner honeycomb structure. Apart from the geometry, the usage of new materials is foreseen. Thus, the fuel pellets are of mixed uranium-plutonium carbide, and the cladding is bulk or fiber-reinforced SiC. The setting up of an appropriate materials database was thus the very first task which had to be carried out in the current work.

The main purpose of the currently developed model is to provide reliable data, in the context of transient analysis, for the calculation of the principal neutronic feedbacks in the GFR core, viz. the fuel temperature for the Doppler effect and the fuel plate deformation for the axial core expansion effect. None of the available fuel modeling codes is suitable for a realistic simulation of the GFR fuel, as the inner honeycomb structure cannot be explicitly taken into account.

The development work has been carried out largely in the context of PSI's generic code system for fast reactor safety analysis, FAST. Thereby, it has mainly involved extension of the thermo-mechanical code FRED, developed originally for the modeling of traditional rodded fuel. Within the FAST system, FRED is coupled to the TRACE code for the thermal-hydraulic modeling, so that the present work has comprised not only the development of a 2D FRED model for the plate-type GFR fuel, but also the implementation of corresponding changes in TRACE for ensuring appropriate information exchange between the two codes.

The 2D thermo-mechanical model has been developed with certain assumptions. Since no experimental data exist for this fuel type, benchmarking of the new simulation tool was carried out by building up a detailed 3D model using the finite-elements code ANSYS. The 3D model has, moreover, been employed for conducting certain supplementary studies to obtain an in-depth understanding of the thermal and mechanical behavior of the fuel. It was found how the complex, multi-dimensional, heat transfer in the plate-type fuel accounts for the discrepancies between results of

2D and 1D simulations. Furthermore, it was shown that, under certain conditions, the temperature field can be well predicted by the 1D model with slight modifications of the solution algorithm. Other insights have been obtained from the detailed mechanical analysis. Thus, it has been shown that, during operation, cusping occurs at the pellet periphery which results in an unfavorable concentration of stresses both in pellet and cladding. Several alternative ways to optimize the fuel design and to avoid, or at least minimize, this effect have been proposed.

As mentioned, the new fuel model is intended for usage in GFR transient analysis. In order to quantify the impact of the current model developments, a range of hypothetical accident events have been analyzed using the FAST code system, with and without usage of the new fuel model. It has been shown that the pure geometry effects on the temperatures are quite significant. However, for the specific honeycomb structure geometry considered, these are somewhat mitigated by the fuel and cladding expansion and the corresponding decrease of the axial fuel-cladding gas gaps. Accounting for the deformations thus, in this case, brings the 2D model results closer to those of a 1D treatment.

The evolution of reactivity feedbacks and the reactor power were evaluated using a point-kinetics approximation and hence were driven by the average temperature change rate (dT/dt) rather than by the absolute temperature values. Correspondingly, the results from the two models are not drastically different. The more significant discrepancies have been obtained for the transients with similar magnitudes of the Doppler and axial core expansion effects (core overcooling, loss of heat sink). For the transient-overpower transient, which is mainly determined by the fuel temperature, very similar results are obtained for total reactivity and reactor power.

In brief, the present research has resulted in a flexible and easy-to-use simulation tool for carrying out reliable transient analysis for the Generation IV GFR with its innovative plate-type fuel, the implemented methodology combining an explicit accounting of the fuel inner structure with acceptable computing time.

Keywords: nuclear power plants, Generation-IV, gas-cooled fast reactor, GFR, plate-type fuel, thermo-mechanics, thermal-hydraulics, FAST code system, transient analysis, TRACE, fuel modeling.

Version Abrégée

Les centrales nucléaires actuelles vont être remplacées jusque dans les années 2030, par de nouvelles centrales de la troisième Génération (Gen-III ou Gen-III+). Ces nouvelles centrales seront essentiellement basées sur la technologie des réacteurs à eau légère, avec comme principales caractéristiques, une augmentation de la sûreté and une compétitivité économique encore accrue. Cependant, ces centrales utilisent le même combustible nucléaire et fonctionnent sur le même cycle de combustible. Au delà des années 2030, l'intérêt est de se tourner vers la quatrième génération de centrales nucléaires, qui va offrir la possibilité de fermer complètement le cycle du combustible. Les concepts de réacteurs de quatrième Génération (« Generation-IV ») se composent tant de systèmes thermiques que rapides et impliqueront d'un large éventail de combustibles nucléaire, tant en composition que en forme.

La présente recherche a été ciblée sur le développement d'un modèle thermo-méchanique du combustible, au design innovant, du Réacteur à Neutrons Rapides refroidi au Gaz (RNR-G) de la quatrième Génération. La principale caractéristique du combustible est que, les pastilles de combustible sont positionnées à l'intérieur de plaques formant, à l'intérieur, une structure en nid d'abeille. A part la géométrie, l'utilisation de nouveaux matériaux est envisagée. Ainsi, les pastilles de combustibles sont constituées de carbure mixte d'uranium et de plutonium et la gaine est formée de SiC massif ou renforcé de fibres. La constitution d'une base de données de matériaux appropriée fût ainsi la première tâche entreprise dans le présent travail.

Le but principal du modèle nouvellement développé est de fournir des données fiables, dans le contexte des analyses de transitoires, pour le calcul des principales contre-réactions (« feedbacks ») à l'intérieur du cœur du RNR-G, i.e. la température du combustible intervenant dans l'effet Doppler et la déformation de la plaque de combustible intervenant dans l'effet d'expansion axiale du cœur. Aucuns des codes de modélisation du combustible actuellement disponible n'est adapté à la simulation, en conditions réalistes, du combustible du RNR-G, la structure interne en nid d'abeille ne pouvant pas être prise en compte explicitement.

Le travail de développement a été largement réalisé dans le contexte du système générique de codes au PSI pour l'analyse de sûreté de réacteurs à neutrons rapides: FAST. Cela a impliqué, tout particulièrement, l'extension du code de thermo-méchanique FRED, originalement développé pour la modélisation de combustible traditionnel sous forme de barres. Dans le contexte du système FAST, FRED est couplé au code TRACE pour la modélisation de la thermo-hydraulique. De cette manière, le présent travail a comporté, non seulement le développement d'un modèle 2D de la plaque de combustible du RNR-G pour FRED, mais aussi

l'implémentation des modifications nécessaires dans TRACE, permettant un échange approprié d'information entre les deux codes.

Le modèle 2D thermo-mécanique a été développé sous certaines hypothèses. Comme il n'existe pas de données expérimentales pour ce type de combustible, les comparaisons de référence du nouvel outil de simulations ont été effectués en réalisant un modèle détaillé 3D basé sur le code aux éléments finies ANSYS. Le modèle 3D a été, qui plus est, utilisé pour la réalisation de certaines études supplémentaires, afin d'obtenir une compréhension en détail du comportement thermique et mécanique du combustible. Il a été trouvé comment le transfert de chaleur dans la plaque de combustible, de nature complexe et multidimensionnelle, explique les différences entre les résultats des simulations 2D et 1D. En outre, il a été montré, que sous certaines conditions, le champ de température peut être bien prédit, par le modèle 1D, avec de légères modifications de l'algorithme de solutions. D'autres compréhensions ont été obtenues avec l'analyse mécanique détaillée. Ainsi, il a été montré que, pendant le fonctionnement, une courbure (« cusping ») apparaît à la périphérie de la pastille, ce qui engendre une concentration défavorable de tensions tant dans la pastille que dans la gaine. Plusieurs solutions alternatives pour optimiser le design du combustible et, ainsi, éviter, ou du moins minimiser cet effet, ont été proposées.

Comme mentionné, le nouveau modèle de combustible est destiné à être utilisé pour l'analyse de transitoires du RNR-G. Pour pouvoir quantifier l'impact du modèle développé, une sélection d'événements accidentels hypothétiques a été analysée avec le système de codes FAST et ce, avec et sans le nouveau modèle du combustible. Il a été montré que l'effet de géométrie seule sur les températures est assez significatif. Par contre, pour la géométrie spécifique considerée de la structure en nid d'abeille, elles sont quelque peu atténuées par l'expansion du combustible et de la gaine, et la diminution correspondante du jeu axial entre la gaine et le combustible. En tenant compte des déformations, dans ce cas, le modèle 2D donne des résultats plus proches que ceux obtenus avec un traitement 1D.

L'évolution des contre-réactions de réactivité et la puissance du réacteur ont été évaluées en utilisant l'approximation de la cinétique point et donc, sont liées par le taux de changement (dT/dt) de la température moyenne, plutôt que par les valeurs absolues de température. En conséquence, les résultats obtenus par les deux modèles ne sont pas radicalement différents. Les différences les plus significatives ont été obtenues pour les transitoires combinant les amplitudes similaires pour les effets de Doppler et d'expansion axiale du cœur (sur-refroidissement, perte de source froide). Pour le transitoire de sur-puissance, qui est essentiellement gouverné par la température du combustible, des résultats très similaires sont obtenus pour la réactivité totale et la puissance du réacteur.

6

En bref, la présente recherche a résulté en un flexible outil de simulation, facile d'utilisation, pour effectuer, de manière fiable, l'analyse des transitoires du RNR-G de quatrième Génération, comportant un combustible à plaques innovant. La méthodologie implémentée combine une prise en compte explicite de la structure interne du combustible et un temps de simulation acceptable.

Mots clés: centrales nucléaires, Génération IV, réacteur à neutrons rapides refroidi au gaz, RNR-G, combustible à plaques, thermo-mécanique, thermo-hydraulique, système de codes FAST, analyse des transitoires, TRACE, modélisation du combustible.

Contents

10

1 INTRODUCTION

1.1 CURRENT STATUS OF NUCLEAR POWER

There are currently 436 nuclear power plants in operation around the world (see Fig. 1.1), producing 16% of the world's electricity [1] – the largest share provided by any non-greenhouse-gas-emitting source [2]. This yields a significant reduction in the environmental impact of today's electric generation. To continue to benefit from nuclear power in this way, new systems will be needed to replace plants as they retire. 31 reactor units are currently under construction [1] (see Fig. 1.2).
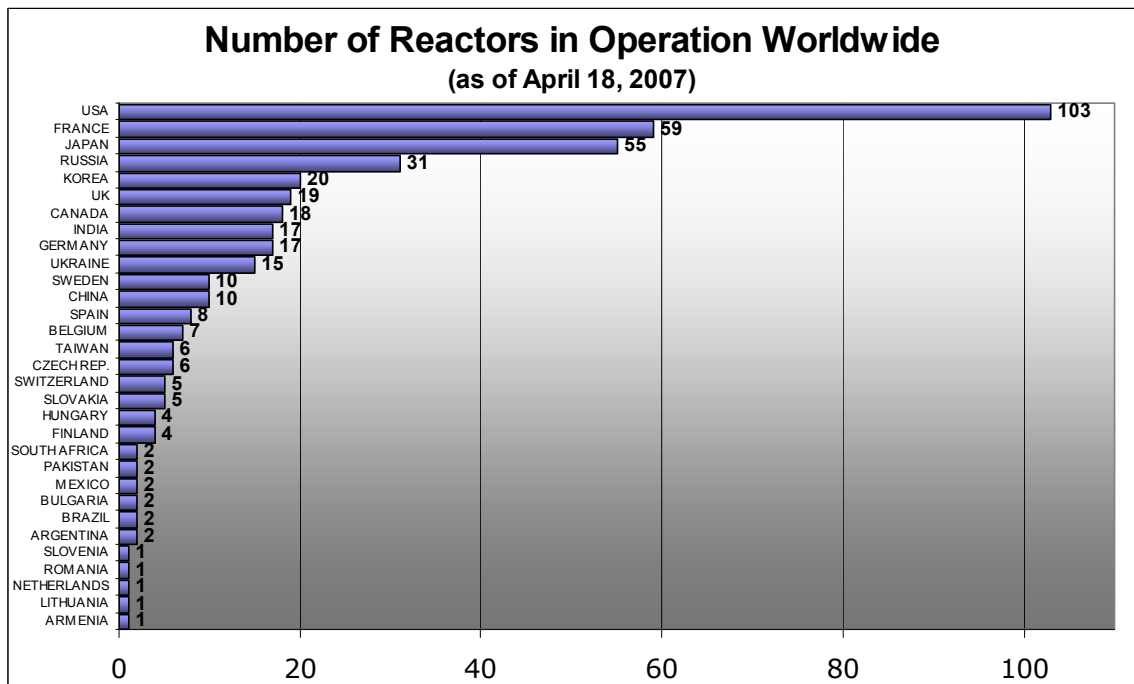
Fig. 1.1 Reactor units in operation

Viewed historically, the rapid development of commercial nuclear power in the 1950's to 1970's has been followed by a relatively long stagnation period. This has largely been a consequence of the reaction of both the public and of governments to the nuclear accidents of Three Mile Island (TMI) in 1979 and Chernobyl in 1986. Most of the reactors being operated nowadays are of the 1st or 2nd generation (75% of them being older than 20 years [1]; see Fig. 1.3) and will soon require replacement or life-time extension.

13

The growing world's population (which is expected to expand from currently about 6 billion to 10 billion people by the year 2050), improved standards of living in the developing countries and the corresponding rapid industrial growth – especially in India and China – as also the environmental effects and increasing costs of fossil fuels, are important factors which speak in favor of a nuclear renaissance. In the latter part of this century, the environmental benefits of nuclear energy can expand and even extend to other energy products besides electricity. For example, nuclear energy can be used to generate hydrogen for use in petroleum refinement and as a transportation fuel to reduce the dependence upon oil, as also to desalinate water in areas where fresh water is in short supply. To provide such extended applications, new systems will be needed, requiring significant research and development (R&D) on next-generation systems.
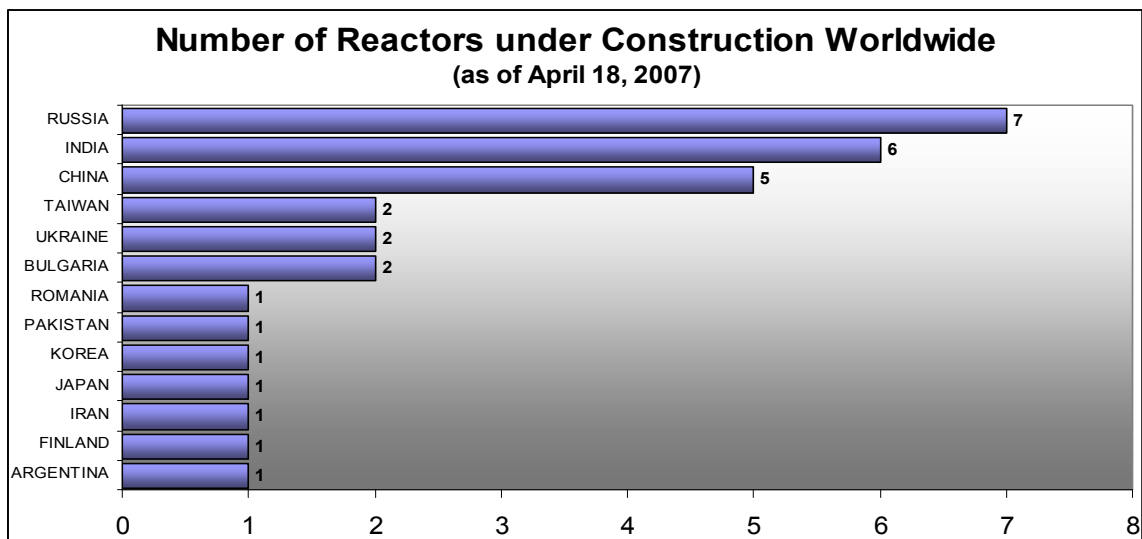
Fig. 1.2. Reactor units under construction

Generation III power plants were developed in the 1990s and correspond to a number of evolutionary designs, based on the proven and widely used pressurized and boiling water (PWR, BWR) technologies. These systems offer significant advances in safety and economics, and a number have been built, primarily in East Asia. Advances in Generation III are under way, resulting in several (so-called Generation III+) near-term deployable plants that are being considered by several countries. New plants built between now and 2030 will most probably be chosen from these designs.

14
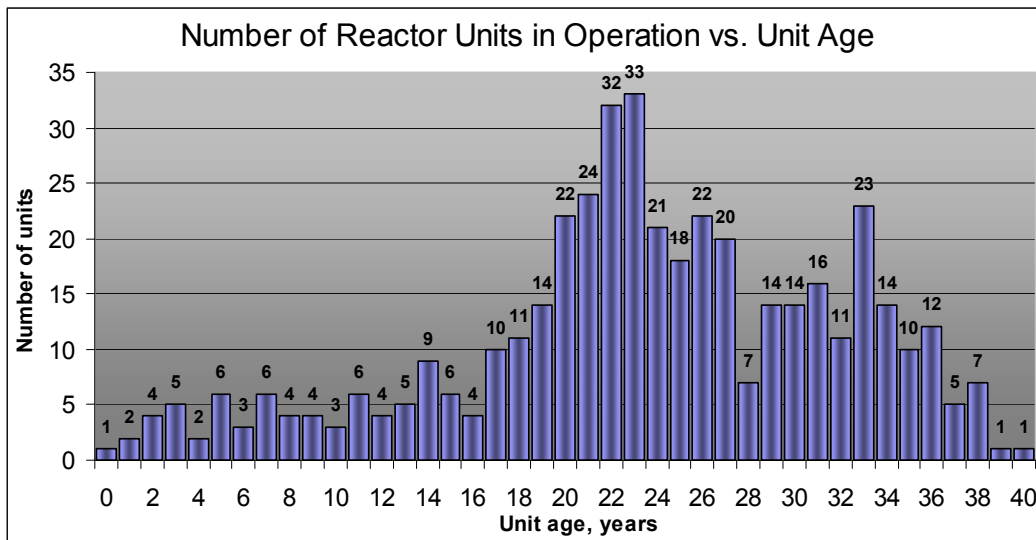
Fig. 1.3. Number of reactor units in operation vs. unit age

Beyond 2030, the prospects for innovative advances through renewed R&D have stimulated interest worldwide in a fourth generation of nuclear energy systems [3]. Ten countries, plus EURATOM, have joined together to form the Generation IV International Forum (GIF) to develop future nuclear energy systems that can be licensed, constructed, and operated in a manner that will provide competitively priced and reliable energy products while satisfactorily addressing nuclear safety, waste, proliferation, and public perception concerns. The objective for Generation IV systems is to have them available for international deployment about the year 2030, when many of the world's currently operating nuclear power plants will be at or near the end of their operating licenses. Fig. 1.4 shows, schematically, the different generations of nuclear power plants [3].
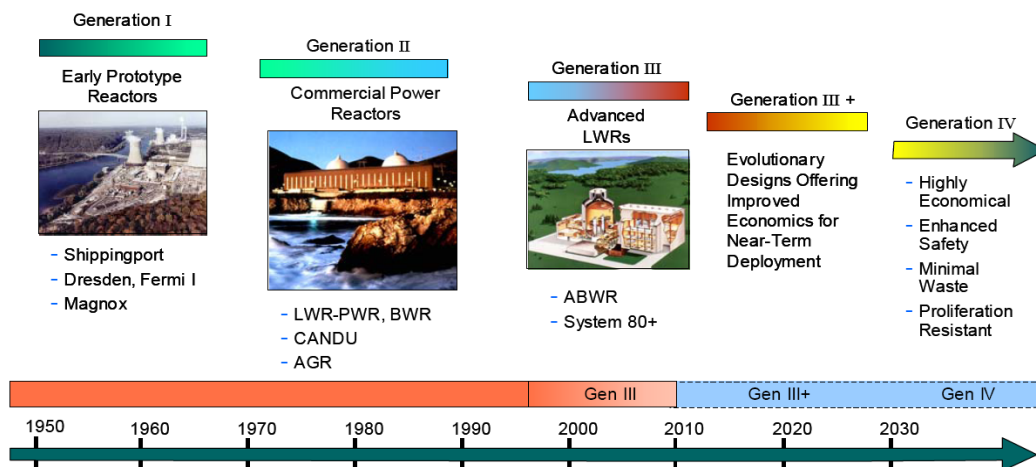
Fig. 1.4. Development of nuclear power plants

1.2 GOALS FOR GENERATION IV

As preparations for the Generation IV Technology Roadmap began, it was necessary to establish goals for these future nuclear energy systems. The goals have three purposes. First, they serve as the basis for developing criteria to assess and compare the systems in the technology roadmap. Second, they are challenging and stimulate the search for innovative nuclear energy systems – both fuel cycles and reactor technologies. Third, they will serve to motivate and guide the R&D on Generation IV systems as collaborative efforts get under way.

Eight goals for Generation IV (see Table 1.1) are defined in the four broad areas of sustainability, economics, safety and reliability, as well as proliferation resistance and physical protection. Sustainability goals focus on fuel utilization and waste management. Economics goals focus on competitive life cycle and energy production costs and financial risk. Safety and reliability goals focus on safe and reliable operation, improved accident management and minimization of consequences, investment protection, and essentially eliminating the technical need for off-site emergency response. The proliferation resistance and physical protection goal focuses on controlling and securing nuclear material and nuclear facilities.

Table 1.1. Goals for Generation IV nuclear energy systems

Sustainability –1 Generation IV nuclear energy systems will provide sustainable energy generation that meets clean air objectives and promotes long-term availability of systems and effective fuel utilization for worldwide energy production.   *Sustainability – 2* Generation IV nuclear energy systems will minimize and manage their nuclear waste and notably reduce the long-term stewardship burden, thereby improving protection for the public health and the environment.   *Economics – 1* Generation IV nuclear energy systems will have a clear life-cycle cost advantage over other energy sources.   *Economics – 2* Generation IV nuclear energy systems will have a level of financial risk comparable to other energy projects.   *Safety and Reliability – 1* Generation IV nuclear energy systems operations will excel in safety and reliability.   *Safety and Reliability – 2* Generation IV nuclear energy systems will have a very low likelihood and degree of reactor core damage.

Safety and Reliability – 3 Generation IV nuclear energy systems will eliminate the need for offsite emergency response.

Proliferation Resistance and Physical Protection Generation IV nuclear energy systems will increase the assurance that they are a very unattractive and the least desirable route for diversion or theft of weapons-usable materials, and provide increased physical protection against acts of terrorism.

Six types of advanced reactors, namely the gas-cooled fast reactor (GFR), the lead-cooled fast reactor (LFR), the molten-salt thermal reactor (MSR), the sodium-cooled fast reactor (SFR), the supercritical water-cooled reactor (both thermal and fast options) (SCWR) and the very high temperature thermal reactor (VHTR), have been selected for collaborative R&D, with the aim of improving economic competitiveness, safety, uranium resource economy, and reducing long-lived radioactive wastes. The reactor types together with the best-case deployment dates are listed in Table 1.2.

Table 1.2. The six Generation-IV systems

Abbreviation	Full name	Best-case deployment date
GFR	Gas-Cooled Fast Reactor	2025
LFR	Lead-Cooled Fast Reactor	2025
MSR	Molten Salt Reactor	2025
SCWR	Supercritical-Water-Cooled Reactor	2025
SFR	Sodium-Cooled Fast Reactor	2015
VHTR	Very-High-Temperature Reactor	2020

1.3 CURRENT INTEREST IN GAS-COOLED FAST REACTORS

The gas-cooled fast reactor (GFR) is one of the most promising candidate reactor types to meet the goals declared within the Gen-IV roadmap [3-12]. A fast spectrum would enable effective closure of the fuel cycle which implies, among other things, minor actinide recycling. Moreover, the high outlet coolant temperature would allow for both highly effective electricity generation (45-50% energy conversion efficiency)

and hydrogen production. Particularly, interest in the GFR has been expressed by France and Switzerland. R&D efforts are now underway with the final aim of realizing, in about 10-15 years, the Experimental and Technology Demonstration Reactor (ETDR), i.e. a GFR demonstrator.

The choice of helium coolant has a number of advantages over the competing liquid metal systems. It provides better seismic stability due to low coolant weight, as also chemical neutrality during air or water contact. The topic requiring special attention for any gas-cooled reactor is the circuit tightness and the core coolability during loss-of-flow and loss-of-coolant accidents.

The goal of a high coolant outlet temperature poses important materials-related questions, as the usage of oxide fuel with low thermal conductivity would lead to unacceptably high fuel temperatures. Accordingly, a number of alternative fuel options are being considered for the GFR core [5, 6]. The reference fuel design is quite different from conventional rodded designs. The fuel is arranged within "plates", with a honeycomb structure inside. Each cell of the honeycomb encloses a fuel pellet, and the structure is covered by thin walls from both sides. The principal distinctive feature of such a fuel layout is the total separation of the fuel pellets from each other, which would decrease the radioactivity release from the fuel element in case of its failure. A more detailed description of the fuel layout and the dimensions will be given in Chapters 2 and 3. Investigations related to the GFR core and fuel design can be found also in [13].

In addition to the Generation-IV International Forum selection process, the European Union, through the EU 5th Framework Programme, sponsored in 2002 an independent review of past developments related to the gas-cooled fast reactor (GFR, in the European context) and the relationship to currently operating gas-cooled thermal reactors, as well as to relevant aspects of current and past sodium cooled fast reactor technology. One conclusion from the study was: "A remarkable degree of flexibility (for the GFR) is possible for breeding and burning plutonium (with a broad range of fuel compositions) without the need for a change in the basic design". In future studies foreseen in the GFR project of the EU Programmes, a strong interest has been expressed in exploring the irradiation of minor actinides and long-lived fission products. As such, the GFR is currently viewed not only as a flexible tool for breeding or burning Pu, depending upon the fissile material requirements at a given point in time, but also for meeting the aim of reducing the overall mass of long-lived nuclear wastes.

1.4 THE "FAST" PROJECT AT PSI

The FAST (<u>F</u>ast-spectrum <u>A</u>dvanced <u>S</u>ystems for power production and resource managemen<u>T</u>) project at the Paul Scherrer Institute (PSI) is an activity in the area of fast spectrum core neutronics and safety analysis, with emphasis on generic developments and Generation IV systems. One of the objectives is to develop a general tool for analyzing the core statics and dynamic behavior of the complete reactor system, in the context of advanced fast spectrum concepts with different coolants. A code system of this complexity is particularly attractive in the context of safety related studies aimed at establishing the basic feasibility of the advanced fast reactors being proposed by GIF.

Using the FAST code system [14], it is possible to analyze, in a systematic manner, a wide variety of transients, including those which may lead to asymmetric core power conditions. This could be, for example, via control rod withdrawal or the insertion of moderating material leading to a reactivity increase (e.g. water/steam in a gas cooled core or gas bubbles in a liquid metal cooled core). In addition, through the modeling of the whole reactor system, it is possible to assess those phenomena, which depend on the direct interaction between the primary and secondary systems and the core behavior.

The extension of the FAST code system, in terms of the material properties database, as well as, in particular, the development and integration of a new fuel model to enable application to advanced gas-cooled fast reactors, represents the principal purpose of the present research.

1.5 GOALS OF THE PRESENT WORK

Thermo-mechanical fuel behavior analysis is particularly important for advanced reactor systems due to raised safety requirements. As indicated for the case of the GFR, the fuel types considered for advanced reactors often differ significantly from traditional designs and, in most cases, available codes cannot deal with such fuels without significant modification. The adaptation and appropriate qualification of existing fuel codes thus become important requirements for the transient analysis of such reactor systems.

It is in the above context that the present doctoral research sets out to develop, benchmark and apply a detailed transient thermo-mechanical model for predicting the behavior of the advanced fuel type currently being proposed for the Generation IV GFR. There has previously not been any numerical tool, which could permit adequate modeling of the described carbide fuel dispersed in a plate-type silicon-carbide honeycomb structure. The currently developed modeling methodology has

thus aimed at enabling, within the frame of the FAST code system, the assessment of the GFR fuel and reactor behavior taking account of such effects as fuel and matrix thermal expansion, swelling, fission gas release, pellet-clad mechanical interaction, etc. The basic goal is to combine a reasonable accuracy for the calculations with low CPU times.

No reference solutions or experiments are available for the proposed fuel type. Therefore, a proper benchmarking procedure has had to be established to verify the developed algorithms. The basic approach applied in this context has been to use a detailed finite-element solution as a reference. This is due to the reliability of this method, as demonstrated in a variety of research and industrial applications.

1.6   LAYOUT OF THE THESIS

The thesis is organized in 6 chapters.

The present introduction is followed by Chapter 2 which gives an overview of the available numerical tools within the FAST code system. Major attention is paid, in this context, to the fuel thermo-mechanical module (FRED), as this has formed the starting point for the present GFR fuel model development.

Chapter 3 describes the adaptation of the FRED rod-geometry, thermo-mechanical analysis methodology to the modeling of the heterogeneous plate-geometry GFR fuel. The original algorithms and coupling scheme for the thermo-mechanical and thermal-hydraulic modules, of the FAST code system, have also had to be adapted suitably in order to represent the stress-strain conditions in an adequate manner.

The benchmarking of the developed algorithms against detailed finite-elements analysis is presented in Chapter 4. In addition, certain important phenomena which are intrinsic to the GFR fuel geometry are analyzed using the detailed model, for better understanding of the fuel behavior under specific conditions.

Chapter 5 presents the application of the developed fuel model to a predefined set of hypothetical, unprotected transients for the GFR, viz.

- transient overpower

- core overcooling

- loss of heat sink

- loss of flow

The results are compared to the predictions of simplified models, in order to demonstrate the higher accuracies achieved via implementation of the new model.

Finally, the conclusions and certain recommendations for future work are presented in Chapter 6.

REFERENCES

1. Website of the IAEA Power reactor information system http://www.iaea.or.at/programmes/a2/

2. IEA Key world energy statistics 2007.

3. A Technology Roadmap for Generation IV Nuclear Energy Systems: Technical Roadmap Report, December, 2002.

4. J.C. Garnier, "The Gas Fast Reactor Project", CEA, CAPRA-CADRA Seminar, 5-7 April 2004.

5. J.C. Garnier, C. Poette, B. Mathieu, A. Conti, JP. Gaillard, "Preliminary design of an advanced Gas Cooled Fast Reactor core, fuel forms and primary system concept", Proc. of Int. Congress on Advances in Nuclear Power Plants, ICAPP'03, Córdoba, Spain, May 4-7, 2003.

6. N. Chauvin, J.C. Garnier, J.L. Seran, Ph. Brossard. "Requirements for Fuel and Structural Materials for Gas Cooled Fast Reactor (GFR), preliminary design", Proc. of Int. Congress on Advances in Nuclear Power Plants, ICAPP'03, Córdoba, Spain, May 4-7, 2003.

7. C. Bassi. "Core transient behavior of the Gas Cooled Fast Reactor", Proc. of Int. Congress on Advances in Nuclear Power Plants, ICAPP'03, Córdoba, Spain, May 4-7, 2003.

8. J.P. Gaillard, G. Mignot, A. Conti, "Thermal-hydraulic design of a Gas Cooled Fast Reactor", Proc. of Int. Congress on Advances in Nuclear Power Plants, ICAPP'03, Córdoba, Spain, May 4-7, 2003.

9. N. Tauveron, M. Saez, et. al. "Steady-state and transient simulations of Gas Cooled Reactor with the computer code CATHARE", Proc. of the 10th International Topical Meeting on Nuclear Reactor Thermal Hydraulics, NURETH-10, Seoul, Korea, October 5-9, 2003.

10. E. Studer, N. Coulon, et. al. "Gas Cooled Reactor Thermal-Hydraulics Using CAST3M and CRONOS2 codes", DEN/DM2S, April 24, 2003.

11. E.A. Hoffman and T.A. Taiwo, "Physics Studies of Preliminary Gas-Cooled Fast Reactor Designs", Proc. of Global 2003, New Orleans, LA November 16-20, 2003.

12. J.C. Garnier et. al., "Feasibility Study of an Advanced GFR Design Trends and Safety Options Status of France & US Studies", Global 2003, New Orleans, LA November 16-20, 2003.

13. N. Chauvin, J.Y. Malo et al., "GFR Fuel And Core Pre-Conceptual Design Studies", Proc. of Global 2007, Boise, Idaho, September 9-13, 2007.

14. K. Mikityuk, S. Pelloni, P. Coddington, E. Bubelis, R. Chawla. "FAST: An advanced code system for fast reactor transient analysis", Annals of Nuclear Energy. 32, 15, 1613-1631, 2005.

2   THESIS BACKGROUND

Following a brief description of the Generation IV Gas-cooled Fast Reactor (GFR) in Section 2.1, most of the present chapter describes the computational tools employed during the course of the present research. Thus, Section 2.2 gives a short overview of the FAST code system under development at PSI. This is followed by Sections 2.3, 2.4 and 2.5 describing three specific components of the code system, viz. ERANOS for the static neutronics, TRACE for the thermal-hydraulics, and PARCS for the neutron kinetics, respectively.

Section 2.6 gives a more detailed description of the FRED module, which provides the thermo-mechanical modeling in FAST and, as such, represents the main basis for the development work currently carried out. Finally, Section 2.7 introduces the general-purpose finite element analysis code ANSYS, used in the present research both as a benchmarking tool for the developed GFR fuel model and for certain supplementary investigations.

2.1   GFR CONCEPT DESCRIPTION

As mentioned in Chapter 1, the helium-cooled GFR (Fig. 2.1) [1-6] is one of the most promising candidates to meet the goals declared within the Generation-IV roadmap, since, as a fast spectrum system, it would enable effective closure of the fuel cycle which implies, among other things, minor actinide (MA) recycling. Furthermore, the high outlet temperature of the coolant would allow not only the generation of electricity with a high efficiency (45-50%), but also the simultaneous production of hydrogen and/or process heat. Such systems would also make it possible to use available fissile and fertile materials, including depleted uranium, much more efficiently than with thermal spectrum reactors based on the conventional once-through fuel cycle.
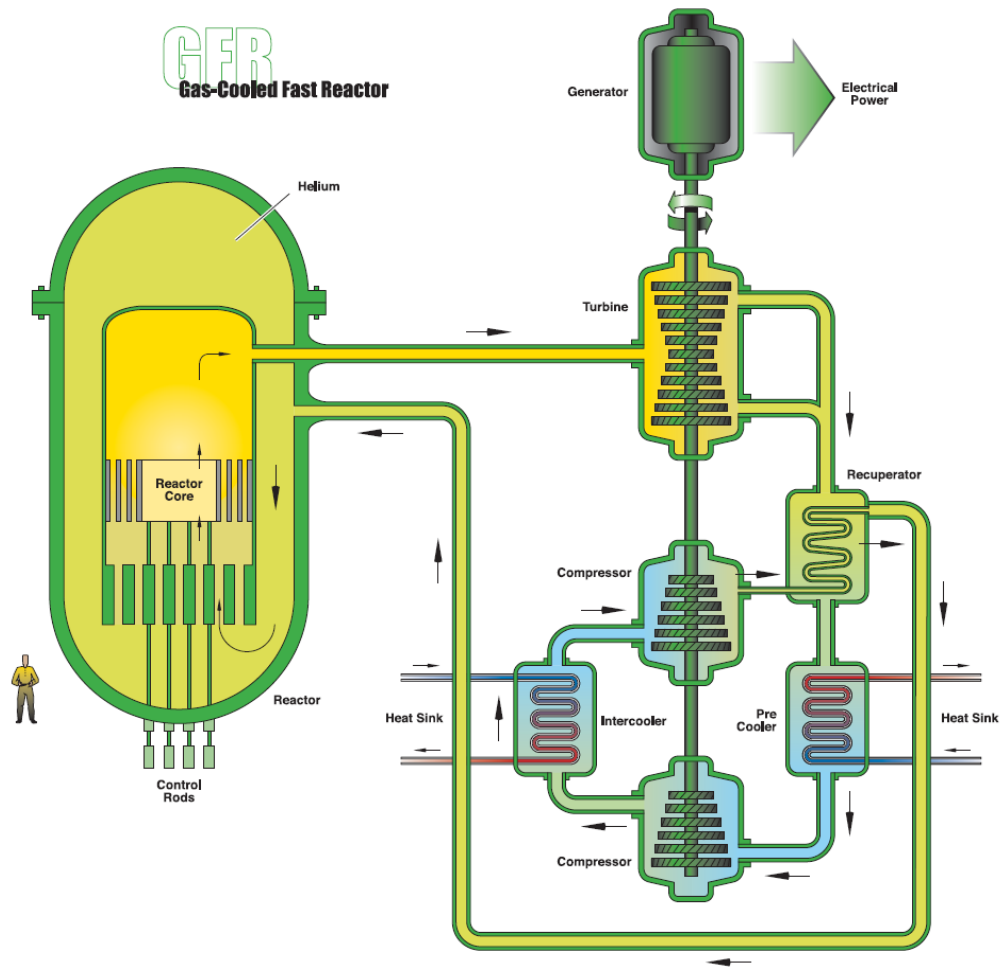
Fig. 2.1. Generation-IV Helium Gas-Cooled Fast Reactor

Among the Generation-IV International Forum (GIF) partners, there are several, notably France, which consider this particular advanced reactor type to be one of the most promising for the long term. Considerable R&D efforts are now underway with the final aim of realizing, in about 10-15 years, the ETDR (Experimental and Technology Demonstration Reactor), i.e. a GFR demonstrator.

GFR core design should be flexible enough to allow for operation with different plutonium and MA management characteristics, including burner, equilibrium and breeder options. Compared to lead-bismuth systems, the GFR has no problems with corrosion and coolant weight (seismic stability). Compared to sodium-cooled systems, the GFR operates with inert coolant (no dangerous interaction of coolant with air and water). The weak points of all gas-cooled reactor concepts relate to the difficulty of preventing small coolant leaks in normal operation due to their high operating pressure and, particularly for fast systems, to potential problems with removing the decay heat from the core in loss-of-coolant or loss-of-flow accidents.

In order to operate the reactor with high coolant temperatures, a number of alternative fuel options are being considered for the GFR core. The possible variations are in terms of different fuel forms, fuel types and fuel geometries [2, 3, 4]. The fuel design currently considered as a reference is shown in Fig. 2.2. Detailed specifications in terms of core size, as well as fuel plate dimensions, are a matter of continuing investigation and optimization [2-6].

a)   b)
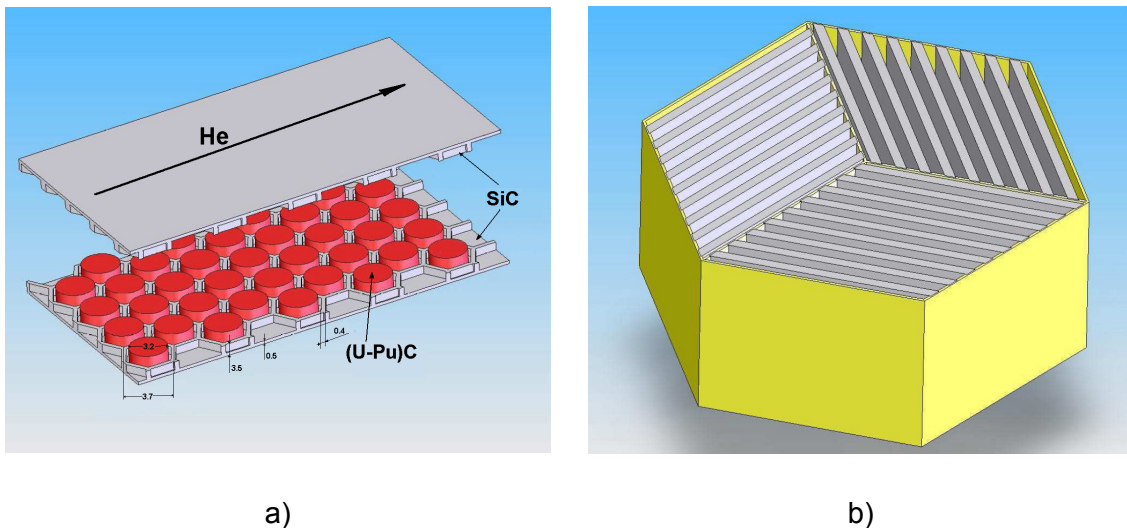
Fig. 2.2. a) Fuel element (plate), b) fuel assembly, view from above

In the reference GFR fuel design, mixed-carbide (PuC/UC) fuel pellets, of several millimeters length (the exact dimensions can vary and currently represent alternative design options) are arranged within a honeycomb structure. The latter is covered on both sides by thin (about 1 mm) ceramic walls (Fig. 2.2). The pellets are thus separated from each other by thin inner walls and, as a result, there is no common gas plenum as in traditional fuel rods. The design goal for this fuel type is that all the released fission products, including the gases, remain contained within the individual cells. In this way, there is a "local" confinement of the fission products, which will limit the activity release in the event of local plate failure. The resulting "plates" are enclosed within a hexcan (Fig. 2.2b).

There have been no numerical tools readily available for the detailed analysis of such a fuel type. The heterogeneous inner structure and corresponding deformation of the fuel can clearly be expected to affect the temperature field, and hence the reactivity feedbacks. From the viewpoint of operational safety, the mutual influence of the temperature field and the reactivity is one of the most important issues to be assessed during GFR modeling.

2.2 THE "FAST" CODE SYSTEM

The FAST code system [7] (Fig. 2.3) is a general computational tool for simulation of the static and dynamic behavior of fast-spectrum reactors (core, coupled to the energy conversion system). Its development and use at PSI aim at the analysis of advanced fast-spectrum concepts in multi-domains, including different coolants and different fuel types. The fast reactor modeling includes an integrated representation of the core neutronics and thermal-hydraulics and fuel behavior, coupled to models of the reactor primary and secondary systems. Well-established individual neutronic, thermal-hydraulic and fuel behavior modules are used. Such a general code system is particularly attractive in the context of safety-related studies aimed at establishing the basic feasibility of the various advanced fast reactors being proposed by the Generation-IV International Forum.
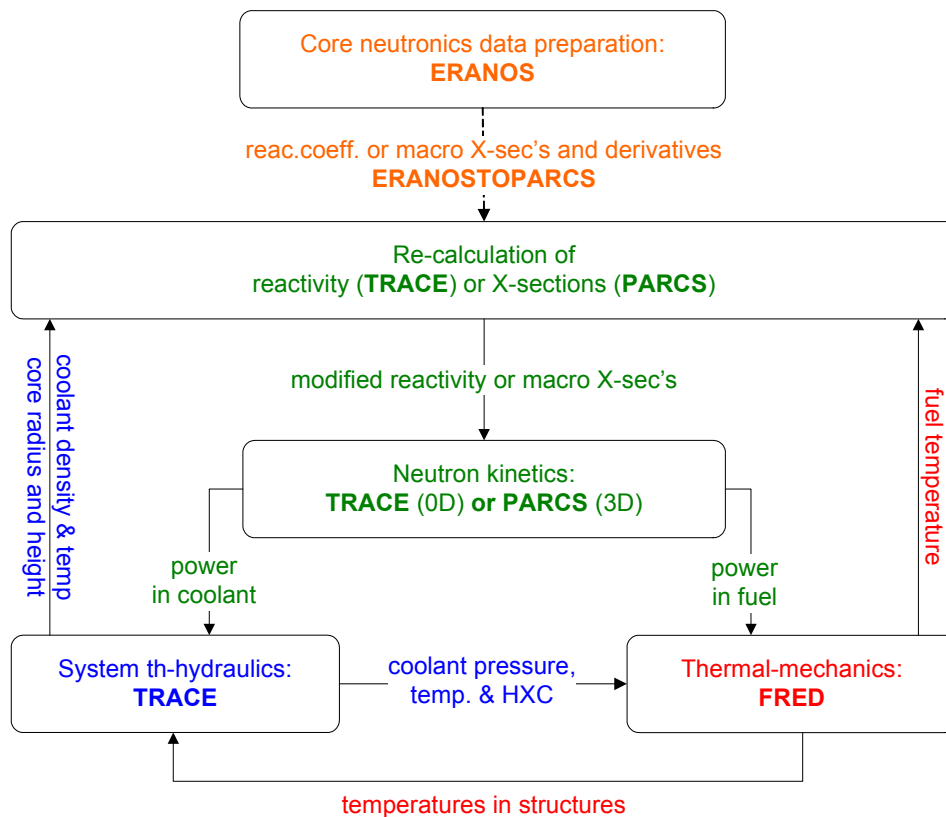
Fig. 2.3. FAST code system structure

As seen from Fig. 2.3, the neutronics code that is used to provide the basic nuclear cross-sections and their functionality in terms of fuel temperature, fuel density, coolant density, etc. is ERANOS [8-11]. This thus provides consistency with the analytical tools widely used in fast reactor static analysis.

28

TRACE is a best-estimate system code which can be used for transient and steady-state thermal-hydraulic calculations of different reactor systems. The database of the code includes physical properties of several coolants, including He which is essential for GFR analysis. The evolution of the core power is calculated in point-kinetics approximation. If the point-kinetics model is not sufficient, i.e. if spatial effects need to be adequately accounted for, it can be coupled with PARCS [12] which models the spatial kinetics of the core. The reactivity coefficients (for point-kinetics) or cross-section derivatives (for 3D kinetics) have to be precalculated by ERANOS.

PARCS is a three-dimensional (3D) reactor core simulator which solves the steady-state and time-dependent, multi-group neutron diffusion and SP3 transport equations. PARCS is coupled directly with TRACE, which provides the temperature and flow field information to PARCS during the transient calculations for recalculating of the group cross sections.

The transient fuel-rod thermal-mechanics code FRED [13, 14, 15] has been included in the FAST code system to calculate, in r-z geometry, the transient coupled changes in the temperature field, heat exchange coefficient, heat flux, stress, strain and failure probability for structural elements such as fuel rods, heat exchanger tubes, reactor vessel, etc. The FRED code uses the fields of temperature and pressure in the surrounding fluid calculated in TRACE [14, 16], as well as the power distribution calculated in PARCS [12] (see Fig. 2.3). The structural temperatures calculated by FRED are passed over to TRACE. In the case of a spatial-kinetics calculation, PARCS uses the core height and radius as well as fuel and coolant temperatures, computed by FRED and TRACE, to re-calculate the macroscopic cross sections of the corresponding materials.

As indicated earlier, the principal objective of the FAST project is generic in nature, viz. to be able to use the code system being developed for the in-depth analysis of advanced fast-spectrum systems, independent of the coolant and fuel type employed. The extension of the material properties database, and the development, integration and application of the new GFR fuel model, are the principal contributions of the present doctoral research. The extension of the FRED fuel model for this purpose, as also the corresponding adaption of the TRACE/FRED coupling scheme for GFR analysis, are described in Chapter 3.

2.3   ERANOS CODE: CALCULATION OF REACTIVITY COEFFICIENTS

The European Reactor ANalysis Optimized calculation System (ERANOS) has been developed and validated with the aim of providing a suitable basis for reliable neutronic calculations of current, as well as advanced fast reactor cores [9]. The deterministic ERANOS neutronic system consists of data libraries, codes and

calculation procedures which have been developed within the European Collaboration on Fast Reactors over the past 15 years or so [11].

The latest version of the ERANOS code and data system, ERANOS 2.0, contains all of the functions required for reference and design calculations of Liquid Metal Fast Reactor (LMFR) cores (as well as blankets, reflectors and shields), with extended capabilities for treating advanced reactor fuel subassemblies and cores, Accelerator Driven Systems (ADS) and Gas-cooled Fast Reactors (GFRs).

The ERANOS 2.0 reference calculation scheme is based on the ECCO cell and lattice code [17], which relies on the collision probability method in many groups using the sub-group method). The ERANOS 2.0 code package contains several neutron cross section libraries, all derived from the JEF-2.2 nuclear data evaluated files [18]. These include:

- a 1968-group library for the 37 main (resonant) nuclides,

- a 33-group library for fast-spectrum applications,

- a 175-group library for shielding calculations,

- a 172-group library for thermal-spectrum applications.

These libraries were obtained by processing the JEF-2.2 files with the NJOY and CALENDF codes [19]. Probability tables are included for the main 37 resonant nuclides.

In the present research, ERANOS is used to provide power distributions, as well as the necessary reactivity feedbacks, to be used in TRACE point-kinetics modeling. The calculation of the core neutronic parameters by ERANOS is a two-step approach.

First, a certain number of cells are defined and specified for ECCO analysis. There must be as many cells as the number of core regions with different isotopic compositions. These zones can be with different fuel compositions, control assemblies, places reserved for the monitoring equipment, etc. The results include k_{inf} values, as well as the micro- and macroscopic cross-sections condensed into a chosen number of energy groups.

Step two is the core geometry specification. The core must be comprised of the cells analyzed by ECCO. Fig. 2.4 gives a simple example of a core consisting of three different cell types (marked by different colors).

STEP 1

Hexcan
Fuel plate
Plate support structure

Homogenization

In: ρ_i

Out: σ_i,
$\Sigma_i = \rho_i \cdot \sigma_i$

ρ – nuclear density

σ – microscopic cross-section

Σ – macroscopic cross-section
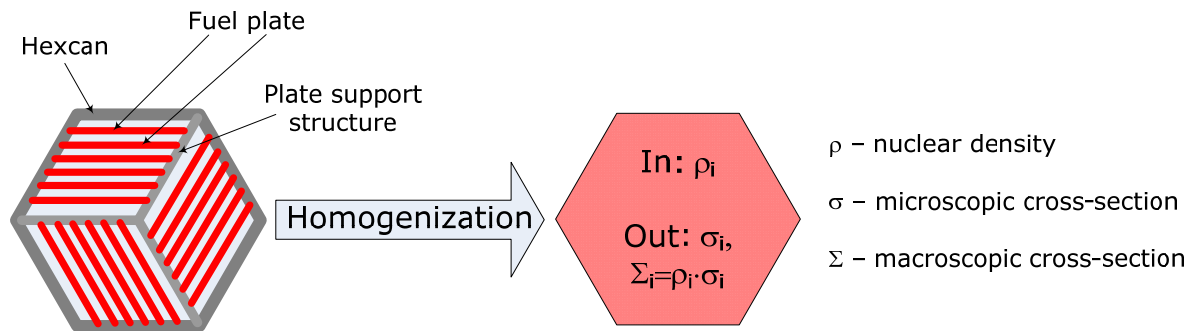
Number of cells to define equals to the number of core regions
with different isotopic compositions, such as
- fuel zones with different enrichments
- control assemblies
- places reserved for monitoring devices
The results include micro- and macroscopic cross-sections for
each cell type

STEP 2
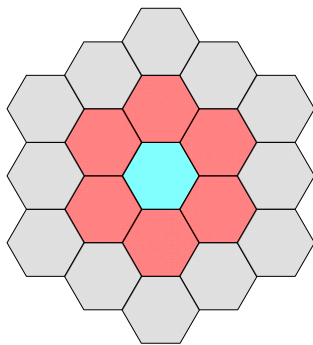
The core is composed of the predefined
cells to calculate flux, k_{eff} and other
parameters

Fig. 2.4. Schematics of the ERANOS calculating procedure

The important parameters to be derived by the ERANOS analysis are:

- power distribution,

- Doppler constant,

- axial core expansion reactivity coefficient,

- radial core expansion reactivity coefficient,

- coolant density reactivity coefficient,

- effective delayed neutron fraction,

- prompt neutron lifetime,

- delayed neutron parameters:

  o effective delayed neutron fraction per each group,

  o delayed neutron decay constants for each group.

The power distribution in the core, derived by ERANOS, is used for the TRACE analysis.

The Doppler constant is defined as:

$$K_D = \frac{\partial \rho}{\partial(\ln T_{fuel})}$$
<div align="right">Eq. 2.1</div>

To calculate this quantity, the fuel temperature is arbitrarily changed, and the two reactivity values corresponding to different fuel temperatures are calculated. The Doppler constant is approximated as ratio of reactivity change to difference of temperature logarithm.

The axial core expansion reactivity coefficient is defined as follows:

$$K_{axial} = \frac{\partial \rho}{\partial T} = \frac{\partial \rho}{\partial H_{core}} \cdot \frac{\partial H_{core}}{\partial T} = \frac{\partial \rho}{\partial H_{core}} \cdot \alpha \cdot H_{core},$$
<div align="right">Eq. 2.2</div>

where

T: average temperature of the core material which determines the axial core expansion,

α: core linear thermal expansion coefficient,

H_{core}:   average core height under nominal operating conditions.

Reactivity values are calculated by ECCO for nominal conditions and for the core with increased height (using the same temperatures, in order to separate axial core expansion and Doppler effects). The core height alteration is modeled by the decrease in the materials nuclear densities and the corresponding buckling change. $\frac{\partial \rho}{\partial H_{core}}$ is thus obtained and then multiplied by $\alpha \cdot H_{core}$ to get the temperature derivative as indicated in Eq. 2.2.

The axial expansion of a core constituted by traditional fuel elements (i.e. consisting of fuel rods) is driven either by fuel swelling and thermal expansion (in open-gap regime) or by joint expansion of the fuel and cladding (when the gap is closed). The GFR axial core expansion has a different nature. The fuel deformation is

accommodated by the free space within a honeycomb cell, and the axial expansion of the fuel plate is mainly determined by the thermal deformation of the SiC matrix. Thus, it is the thermal expansion coefficient for the cladding material which needs to be used.

The radial core expansion reactivity coefficient is calculated in a similar manner. The expansion is driven by the core support structure, and the thermal expansion coefficient corresponding to the diagrid material has to be employed:

$$K_{radial} = \frac{\partial \rho}{\partial T} = \frac{\partial \rho}{\partial R_{core}} \cdot \frac{\partial R_{core}}{\partial T} = \frac{\partial \rho}{\partial R_{core}} \cdot \alpha_{diagrid} \cdot R_{core} \qquad \textbf{Eq. 2.3}$$

where

T: average diagrid temperature,

$\alpha_{diagrid}$:   diagrid linear thermal expansion coefficient,

R_{core}:   average core radius under nominal operating conditions.

The radial core expansion coefficient is calculated as follows. The core dilatation is modeled by the corresponding decrease in the materials nuclear densities and the radial cell dimensions. The derivative $\frac{\partial \rho}{\partial R_{core}}$ can thus be calculated, the desired temperature derivative then being obtained from Eq. 2.3.

The coolant density reactivity coefficient is defined as follows:

$$K_{dens} = \frac{\partial \rho}{\partial \gamma}, \qquad \textbf{Eq. 2.4}$$

where γ is the gas density.

Calculations are done for nominal conditions (gas density corresponding to the nominal gas pressure in the core) and for the voided core (gas at atmospheric pressure) using the same gas temperature. The relevant density change can be expressed as follows:

$$\frac{\Delta \gamma}{\gamma_{nominal}} = \frac{\Delta P}{P_{nominal}}, \qquad \textbf{Eq. 2.5}$$

where

ΔP: change of the pressure from nominal to atmospheric,

$\Delta\gamma$:　　　　corresponding change of the gas density,

$P_{nominal}$:　　　　nominal pressure,

$\gamma_{nominal}$:　　　　average gas density under nominal operating conditions.

All the described effects are assumed to be additive, and they can thus be calculated independently from each other.

The resulting reactivity change during the transient analysis is calculated for each time step as

$$\Delta\rho = K_D \cdot \ln\left(\frac{T_f}{T_{f0}}\right) + K_{axial} \cdot \left(T_{clad} - T_{clad0}\right) + K_{radial} \cdot \left(T_{dia} - T_{dia0}\right) + K_{dens} \cdot \left(\gamma_{He} - \gamma_{He0}\right),$$ **Eq.**

2.6

where

T_{f0}:　　　　average fuel temperature at the beginning of a time step,

T_f:　　　　average fuel temperature at the end of a time step,

$T_{clad\,0}$:　　　　average cladding temperature at the beginning of a time step,

T_{clad}:　　　　average cladding temperature at the end of a time step,

$T_{dia\,0}$:　　　　average diagrid temperature at the beginning of a time step,

T_{dia}:　　　　average diagrid temperature at the end of a time step,

$\gamma_{He\,0}$:　　　　average helium density at the beginning of a time step,

γ_{He}:　　　　average helium density at the end of a time step,

2.4　　TRACE CODE: MAIN COMPONENTS USED TO OBTAIN THERMAL-HYDRAULIC BOUNDARY CONDITIONS

The TRACE code [16] was developed for best-estimate analyses of loss-of-coolant (LOCA) and other accidents, as also operational transients, in both pressurized light-water reactors (PWR) and boiling water reactors (BWR). The special models and databases were developed for analysis of fast-spectrum systems. Models used include non-homogeneous, non-equilibrium two-phase flow, generalized heat transfer, reflood, level tracking, reactor kinetics, etc. The partial differential equations that describe the two-phase flow and heat transfer are solved using finite difference

numerical methods. The heat-transfer equations are evaluated using a semi-implicit time differencing technique.

The TRACE code is used at PSI for the transient analysis of various reactor types, including Generation-IV reactor types such as liquid metal and gas cooled fast reactors. Its currently built-in physical properties database includes correlations for the following coolants:

- light water,

- heavy water,

- helium,

- sodium,

- air,

- lead-bismuth,

- CO_2.

The equations solved for each phase include:

- energy conservation equation,

- momentum conservation equation,

- continuity equation.

The number of reactor components in the problem and the manner in which they are coupled are arbitrary. Reactor hydraulic components in TRACE include pipes, plenums, pressurizers, pumps, jet pumps, separators, T-junctions, turbines, feedwater heaters, containment, valves and vessels with associated internals. Heat structure components representing fuel elements or other structures in the reactor system are available to compute 2D conduction and surface-convection heat transfer in Cartesian or cylindrical geometries. Power components are available as a means for delivering energy to the fluid via the heat structure or hydraulic component walls. Radiation enclosures components may be used to simulate radiation heat transfer between multiple arbitrary surfaces. FILL and BREAK components are used to apply the desired coolant-flow and pressure boundary conditions, respectively, in the reactor system to perform steady-state and transient calculations.

As one can see, TRACE is a flexible tool which provides solutions for a large number of thermal-hydraulic problems. However, its use in the present research has been limited to the analysis of the reactor core with appropriate boundary conditions

(primary and secondary sides are not taken into account), the main goal being to investigate GFR core transient behavior with the innovative plate-type fuel. Having the new fuel model integrated into the FAST code system clearly allows for easy extension of the calculating domain from the reactor core to the whole plant.

With the complexity of the problem limited by the fact that only just the core has been modeled, the principal TRACE model components currently employed are:

- FILL

- BREAK

- PIPE

- PLENUM

- HEAT STRUCTURE

- POWER

These components are described below in more detail.

2.4.1   FILL and BREAK

The FILL and BREAK components are used to impose boundary conditions at 1D hydraulic-component junctions.

In the present case, a BREAK component is used to specify the coolant pressure in the upper plenum, while a FILL component is used to specify the coolant mass flowrate and temperature at the core inlet.

2.4.2   PIPE

The PIPE component models coolant flow in a 1D tube, channel, duct, or pipe. A PIPE component can be used with only BREAK- and/or FILL-component boundary conditions to model 1D flow in a pipe, or it can be used as a connecting pipe between other components to model a reactor system or experimental facility.

The output for a PIPE component includes the pressures, coolant temperatures, liquid and gas temperatures, densities, velocities, wall-friction factors, etc.

2.4.3 PLENUM

The PLENUM component, which models the thermal-hydraulics of a volume connected to an arbitrary number of 1D hydraulic components, is a single-cell component that the user can either set up as a momentum sink (where all inflow momentum is converted to a coolant pressure rise) or for transporting momentum across the cell from one side to the other side.

2.4.4 HEAT STRUCTURE

The Heat Structure (HTSTR) component evaluates the dynamics of conduction, convection, and gas-gap radiation heat transfer in a fuel element or structure hardware element. The heat generation in the heat structures (if there is any) is imposed and must be specified by the POWER component.

The heat-transfer modeling in an HTSTR-component is in either ROD cylindrical (r, z), or SLAB Cartesian (x, z), 2D geometry. The following general equation describes the heat-conduction process in an arbitrary geometry:

$$\rho c_p \frac{\partial T}{\partial t} + \nabla \cdot \overline{q} = q''' \,, \qquad\qquad \textbf{Eq. 2.7}$$

where

ρ: density,

c_p: specific heat,

T: temperature,

$\overline{q}$:   heat flux vector,

q''':   heat generation rate per unit volume.

The heat flux $\overline{q}$ can be expressed in terms of the temperature gradient by Fourier's law of conduction [20], viz.

$$\overline{q} = -k\nabla T \qquad\qquad \textbf{Eq. 2.8}$$

where k stands for the thermal conductivity.

Thus Eq. 2.7 becomes

$$\rho c_p \frac{\partial T}{\partial t} = \nabla \cdot (k \nabla T) + q'''$$

Eq. 2.9

The time history of the structural temperatures is obtained from a solution of the heat conduction equation applied to the different geometries (fuel rods, cylindrical walls, slabs, etc.).

In the present work, slab geometry is of principal interest since, basically, the fuel element has a plate form, as shown in Fig. 2.5. The central part of the slab is the homogenized honeycomb structure (fuel zone) where the heat is generated. The homogenization procedure is described in Section 3.3. The cladding wall is separated from the fuel zone by a gas gap and is cooled by helium. Only half of a plate needs to be modeled due to symmetry. The calculating nodes are located as indicated in Fig. 2.5.
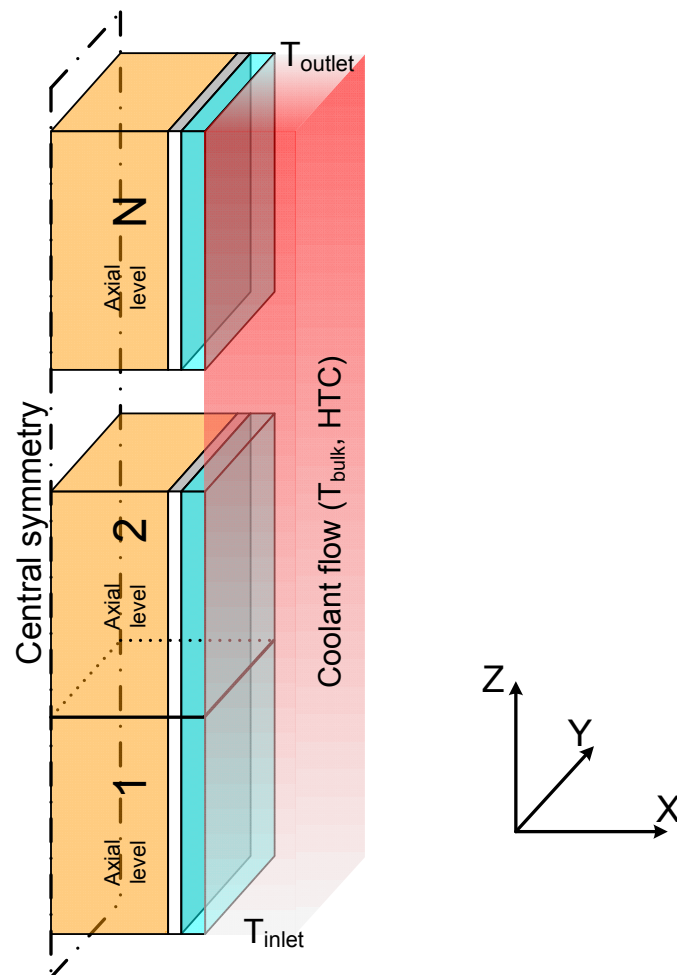
Fig. 2.5. The GFR fuel plate model in TRACE and the coordinate system

The heat transfer is calculated along X and Z directions according to the coordinate system shown in Fig. 2.5. The faces perpendicular to the Y-axis are assumed to be adiabatic, and the width is only used to calculate the material volumes and heat transfer areas necessary for the analysis.

An important parameter which influences the resulting temperature field is the gas-gap conductance. This incorporates the gas thermal conductivity and the radiation heat transfer, and also accounts for the roughness of the surfaces.

Two options are available in TRACE for the fuel-cladding gap conductance. One can either use the initial gap conductance throughout the calculation, or employ a thermal-expansion model to modify the initial gap-conductance value.

The expansion model is elaborated for the traditional pellet-cladding layout (cylindrical fuel rods) and for the materials used in a PWR, i.e. zircaloy for cladding and $(U, Pu)O_2$ for the fuel. A modification has accordingly been introduced in TRACE, so that thermal and expansion models for the gas-gap thermal conductivity can be separated. This is regulated by a special flag through the input. When the GFR plate fuel option is chosen, the expansion is no longer calculated and the gas gap heat transfer coefficient (HTC) is obtained as:

$$h_{gas} = \frac{k_{gas}}{\Delta r_{gap} + \delta_r},$$

Eq. 2.10

where:

k_{gas}: gas-gap thermal conductivity,

Δr_{gap}: fuel-cladding gas-gap width,

δ_r: factor that includes the mean surface roughness of the fuel and the cladding, plus the temperature-jump distances (a built-in constant value of $4.4 \cdot 10^{-6}$ m is used in TRACE).

The heat sink from the heat structure can be modeled in different ways. Thus, the HTSTR element may have an inner surface, outer surface, or both inner and outer surfaces where convection heat transfer is evaluated. Boundary conditions include:

- adiabatic heat transfer surface, where zero heat flux is specified to model the symmetry,

- user-specified heat transfer coefficients and coolant temperatures,

- a heat-transfer surface coupling to hydraulic-component cells that are input-specified, heat-transfer coefficients and temperatures being evaluated by the TRACE hydrodynamic solution for the coolant.

The latter variant has been used in the present analysis. The wall-to-gas heat-transfer coefficient is defined in TRACE as the maximum between the values for forced-convection laminar and turbulent flows:

$$Nu = \max\left(Nu_{laminar}; Nu_{turbulent}\right)$$

Eq. 2.11

The coefficient for laminar-flow convection is given by the maximum between the correlations for low Reynolds numbers (Kim & Li model) [21] and high Reynolds numbers (El-Genk et al. model) [22]. The Churchill superposition method [23] is used to take account of forced and natural convection effects:

$$Nu_{laminar} = \left[\left(\max\left(Nu_{lowRE}; Nu_{hi\,Re}\right)\right)^3 + \left(0.7 \cdot \left(Gr \cdot Pr\right)^{1/4}\right)^3\right]^{1/3}$$

$$Nu_{lowRE} = -5.6605 \cdot pdrat^2 + 31.061 \cdot pdrat - 24.473$$

$$Nu_{hi\,Re} = \left(2.97 - 1.76 \cdot pdrat\right) \cdot Re^{0.56 \cdot pdrat - 0.3} \cdot Pr^{0.33}$$

Eq. 2.12

The coefficient for turbulent-flow convection is given by the El-Genk et al. model [22], which accounts for the entrance-length effect of Mills [24], as also the effects of variable properties due to the near-wall temperature profile

$$Nu_{turbulent} = \left(0.028 \cdot pdrat - 0.006\right) \cdot Re^{0.8} \cdot Pr^{0.33} \cdot \left(\frac{T_{wall}}{T_{gas}}\right)^n \cdot \left[1 + \frac{2.4254}{\max\left(3.0; L_{entrance}\right)^{0.676}}\right]$$

$$n = \begin{cases} -\left[\log_{10}\left(\dfrac{T_{wall}}{T_{gas}}\right)\right]^{1/4} + 0.3, & \text{for } T_{wall} > T_{gas} \\ -0.36, & \text{for } T_{wall} \leq T_{gas} \end{cases}$$

Eq. 2.13

To simulate heat exchange with stagnant coolant, the Nusselt number is limited from below by a value of 2, so that:

$$Nu_{turbulent} = \max\left(Nu_{turbulent}; 2.0\right)$$

Eq. 2.14

The heat transfer coefficient is given by:

$$\alpha = \frac{Nu \cdot \lambda_{gas}}{D_h}$$

Eq. 2.15

In these equations,

pdrat: pitch-to-diameter ratio (set to a constant value 1.33 in the code)

40

Gr: Grashof number,

Re: Reynolds number,

Pr: Prandtl number,

Nu: Nusselt number,

T_{wall}:   fuel element surface temperature,

T_{gas}:   coolant bulk temperature,

$L_{entrance}$:   entrance length (set to $1 \cdot 10^{6}$),

λ_{gas}:   coolant thermal conductivity,

D_h: hydraulic diameter.

Although these models were developed for pin geometry, it was assumed that they provide heat exchange boundary conditions which are accurate enough for the purposes of the current study, focused mainly on the fuel behaviour modeling.

2.4.5   POWER

The POWER component is used to determine the core power evolution by either of two methods. In the first method, the power is specified to be a constant or to be defined by a power table (e.g. versus time). Values between entries in the table are determined by linear interpolation. In the second method, the power is determined from the solution of the point-reactor-kinetics equations. These equations specify the time behavior of the core power level via reactivity, which is the sum of programmed reactivity and feedback reactivity. The programmed reactivity is user-specified and is used to simulate control rod movement. The feedback reactivity is evaluated based on changes in the core-averaged fuel temperature, coolant density, etc. with the use of the reactivity coefficients.

The original TRACE code was modified at PSI to introduce the reactivity changes specific for fast-spectrum cores, i.e. core axial and radial expansion effects. Both of these effects increase the neutron leakage and thus insert negative reactivity. The evaluation of the corresponding reactivity coefficients was described in Section 2.3 as part of the general overview of the ERANOS code. There it was mentioned how, in the case of the GFR core, fuel deformation gets accommodated by the free space within a cell so that the axial expansion of the GFR fuel plate is mainly determined by the thermal deformation of the SiC matrix. The modifications made in TRACE allow the choice between two options, viz. having the axial expansion driven either by fuel

or by cladding. This is user defined via selection of the appropriate value for the corresponding flag,

If the GFR option is chosen, then the axial core expansion reactivity effect during a time step is calculated as:

$$\rho_{axial}(t+\Delta t) = \rho_{axial}(t) + \left(\frac{\partial \rho}{\partial T}\right)_{clad} \cdot \left[T_{clad}(t+\Delta t) - T_{clad}(t)\right],$$

Eq. 2.16

where

$\rho_{axial}(t+\Delta t)$: axial core expansion reactivity at the end of a time step,

$\rho_{axial}(t)$: axial core expansion reactivity at the beginning of a time step,

$\left(\dfrac{\partial \rho}{\partial T}\right)_{clad}$: axial core expansion reactivity coefficient,

$T_{clad}(t+\Delta t)$: average cladding temperature at the end of a time step,

$T_{clad}(t)$: average cladding temperature at the beginning of a time step.

Also as mentioned in Section 2.3, the radial core expansion is driven by thermal expansion of the core support structure (diagrid) and can be approximated by the coolant inlet temperature and the diagrid material thermal expansion coefficient. The reactivity effect is calculated as:

$$\rho_{radial}(t+\Delta t) = \rho_{radial}(t) + \left(\frac{\partial \rho}{\partial T}\right)_{diagrid} \cdot \left[T_{diagrid}(t+\Delta t) - T_{diagrid}(t)\right],$$

Eq. 2.17

where

$\rho_{radial}(t+\Delta t)$: radial core expansion reactivity at the end of a time step,

$\rho_{radial}(t)$: radial core expansion reactivity at the beginning of a time step,

$\left(\dfrac{\partial \rho}{\partial T}\right)_{diagrid}$: radial core expansion reactivity coefficient,

$T_{diagrid}(t+\Delta t)$: average cladding temperature at the end of a time step,

$T_{diagrid}(t)$: average cladding temperature at the beginning of a time step.

The point-reactor kinetics equations are a coupled set of (*I+1*) first-order differential equations, defining the total fission power *P* and the delayed neutron precursor concentrations *C*$_i$ as a function of time. These equations are given by

$$\frac{dP}{dt} = \frac{\rho - \beta}{\Lambda} \cdot P + \sum_{i=1}^{I} \lambda_i C_i$$ **Eq. 2.18**

$$\frac{dC_i}{dt} = -\lambda_i C_i + \frac{\beta_i P}{\Lambda} \quad \text{for} \quad i = 1,2,...,I$$ **Eq. 2.19**

where

P: thermal power (W) that results from fission occurring at time *t*,

T: time (s),

ρ: neutronic reactivity (including both programmed reactivity and feedback reactivity)

β: total fraction of delayed neutrons,

β$_i$: fraction of delayed neutrons in group *i*,

Λ: effective prompt-neutron lifetime (s),

λ$_i$: decay constant for the delayed-neutron precursors in group *i* (1/s),

C$_i$: power of the delayed-neutron precursor concentration in group *i* (W),

I: number of delayed-neutron groups.

The decay heat is evaluated according to the following equations:

$$\frac{dH_j}{dt} = -\lambda_j^H H_j + E_j P \quad \text{for} \quad j = 1,2,...,J ,$$ **Eq. 2.20**

where,

P: solution of Eqs. 2.18 and 2.19,

H$_j$: energy of the decay-heat precursor concentration in group j, W·s,

λ_j^H: decay constant for decay-heat group j,

E$_j$: effective energy fraction of decay-heat group j,

J: number of decay heat groups.

After solving each jth equation represented by Eq. 2.20 for the decay-heat group concentration H_j, the code calculates the total thermal power generated in the reactor-core fuel at time *t*. The total power comprises nuclear fission and fission-product decay as given by

$$P_{eff} = \left(1 - \sum_{j=1}^{J} E_j \right) \cdot P + \sum_{j=1}^{J} \lambda_j^H H_j \qquad \textbf{Eq. 2.21}$$

In order to perform the analysis, the user input has to contain the following information:

- number of the delayed-neutron groups, *I*,

- delayed-neutron parameters, λ_i and β_i,

- number of the decay-heat groups, *J*,

- decay-heat parameters: λ_j^H and E_j.

Moreover a power history (for t < 0) has to be input to calculate the initial precursors concentrations $C_i(0)$ and decay-heat concentrations $H_j(0)$.

If the power history is not specified then the code sets time derivatives $\dfrac{dC_i}{dt}$ and $\dfrac{dH_j}{dt}$ to zero and calculates the initial values from the following:

$$C_i(0) = \frac{\beta_i}{\lambda_i \Lambda} \cdot P(0) \qquad \textbf{Eq. 2.22}$$

$$H_j(0) = \frac{E_j}{\lambda_j^H} P(0) \qquad \textbf{Eq. 2.23}$$

where *P(0)* is the initial power specified through input.

2.5   PARCS CODE

PARCS is a three-dimensional (3D) reactor core simulator, which solves the multi-group neutron diffusion or SP3-transport equations, in square and hexagonal geometries, both for steady state and time-dependent conditions [12]. In the context

44

of the FAST code system, PARCS is used to simulate the 3D neutron kinetics at each time step, i.e. to provide results for the 3D fields of neutron fluxes, power and concentrations of delayed-neutron precursors. For the purpose, the code is coupled directly to the thermal-hydraulics system code TRACE which, during the transient calculation, provides the temperature and flow field information to PARCS for calculation of the change in multi-group cross sections.

The original cross-section parameterization in PARCS was developed for light water reactor (LWR) applications, and this has been extended for fast-spectrum system analysis [7]. In particular, the dominant reactivity feedback effects in LWR transients are the Doppler effect and the change in coolant (moderator) density and temperature, while in fast-spectrum systems, other feedback effects are of equal importance, e.g. fuel and core structure thermal expansion changes both the core dimensions and the effective fuel density, influencing the neutron leakage and hence core reactivity. The absence of boron regulation and a different functional dependence of Doppler reactivity on the fuel temperature are two other distinctive features of fast-spectrum cores compared to thermal reactor cores.

The original PARCS procedure to recalculate the macroscopic cross-sections is:

$$\Sigma(T_F, \rho_M, T_M, B) = \Sigma_0 + \left(\frac{\partial \Sigma}{\partial Z}\right)_{Z_0} \cdot (Z - Z_0) + \left(\frac{\partial \Sigma}{\partial \sqrt{T_F}}\right)_{T_{F0}} \cdot \left(\sqrt{T_F} - \sqrt{T_{F0}}\right) +$$
$$+ \left(\frac{\partial \Sigma}{\partial \rho_M}\right)_{\rho_{M0}} \cdot (\rho_M - \rho_{M0}) + \left(\frac{\partial \Sigma}{\partial T_M}\right)_{T_{M0}} \cdot (T_M - T_{M0}) + \left(\frac{\partial \Sigma}{\partial B}\right)_{B_0} \cdot (B - B_0)$$

, **Eq. 2.24**

where

Σ: the macroscopic cross-section,

Z: the control rod position,

T_F: the fuel temperature,

ρ_M: the moderator density,

T_M: the moderator temperature,

B: the boron concentration,

with the subscript "0" referring to reference conditions.

This procedure was modified to take account of the mentioned effects, essential for fast reactors, such that [7]:

$$\Sigma\left(T_F, \rho_C, R, H\right) = \Sigma_0 + \left(\frac{\partial\Sigma}{\partial Z}\right)_{Z_0} \cdot \left(Z - Z_0\right) + \left(\frac{\partial\Sigma}{\partial \ln T_F}\right)_{T_{F0}} \cdot \left(\ln T_F - \ln T_{F0}\right) +$$

$$+ \left(\frac{\partial\Sigma}{\partial \rho_C}\right)_{\rho_{C0}} \cdot \left(\rho_C - \rho_{C0}\right) + \left(\frac{\partial\Sigma}{\partial R}\right)_{R_0} \cdot \left(R - R_0\right) + \left(\frac{\partial\Sigma}{\partial H}\right)_{H_0} \cdot \left(H - H_0\right) \qquad , \quad \textbf{Eq. 2.25}$$

where

ρ_C: coolant density,

R: average core radius,

H: average core height.

2.6   FRED CODE

The transient thermal-mechanics code FRED [13, 14, 15], originally developed for modeling the transient behavior of LWR fuel rods, forms part of the FAST code system in order to calculate (in cylindrical geometry) the transient coupled changes in the fields of temperature, heat flux, stress, strain and failure probability for structural elements such as fuel rods, heat exchanger tubes, reactor vessel, etc. The library of thermo-mechanical material properties includes data for Zry, Zr-1%Nb, several types of stainless steel, UO_2 and MOX.

The following subsections describe the various algorithms implemented in FRED, in terms of:

- fuel rod nodalization scheme,

- thermal model,

- mechanical model,

- solution of the equations,

- coupling with TRACE.

2.6.1   Fuel rod nodalization scheme

A three-dimensional cylindrical geometry is used in the fuel rod nodalization scheme. The calculational nodes are located only in the active part of the fuel rod.

The scheme of division of the calculated region into control volumes in the radial, tangential and axial directions, as well as the location of the calculational nodes for temperature, is indicated in Fig. 2.6. The control volume boundaries are shown with solid lines and the material boundaries with dashed. A uniform distribution is assumed circumferentially: $\Delta\theta = 2\pi / n_\theta$. An important feature of the scheme is a coincidence of the boundaries between materials with the temperature nodes.
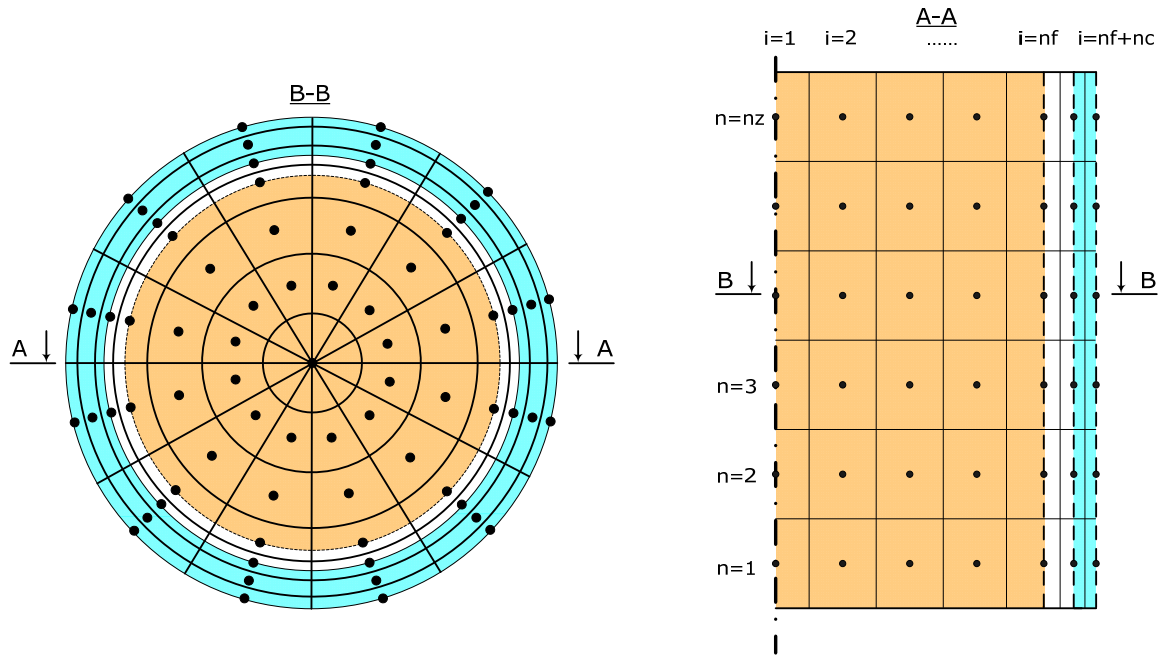
Fig. 2.6. FRED control volumes and distribution of calculational nodes for temperature

2.6.2 FRED thermal model

The differential equation for heat transfer is solved by the FRED model in cylindrical geometry, accounting for radial, axial and azimuthal heat fluxes:

$$\rho c_p \frac{\partial T}{\partial \tau} = -\frac{1}{r}\frac{\partial}{\partial r}\left(\lambda r \frac{\partial T}{\partial r}\right) - \frac{1}{r}\frac{\partial}{\partial \theta}\left(\lambda \frac{1}{r}\frac{\partial T}{\partial \theta}\right) - \frac{\partial}{\partial z}\left(\lambda \frac{\partial T}{\partial z}\right) + q_v \qquad \textbf{Eq. 2.26}$$

where

ρ: density (kg/m^3),

c_p: specific heat (J/kg·K),

λ: thermal conductivity (W/m·K),

q_V: power density (W/m^3),

r,θ,z: coordinates in cylindrical geometry (m),

τ: time (s).

At each time step, the power density distribution is calculated either with the TRACE point-kinetics model or PARCS spatial kinetics model and sent to the FRED model.

Eq. 2.26 shows the balance of heat in an infinitesimal volume. Its right part contains the heat produced in the volume minus the heat flowing out of the volume across the surface. For finite volumes, the heat fluxes can be calculated explicitly, and the corresponding system of ordinary differential equations (ODE) can be derived. An ODE for the i-th control volume can be written as follows:

$$\rho^i c_p^i \frac{dT^i}{dt} = \sum_j \frac{q^{j \to i} \cdot S^{ji}}{V^i} + q_V^i \qquad\qquad \textbf{Eq. 2.27}$$

where

$q^{j \to i}$: heat flux between volumes j and i (W/m^2),

S^{ji} : heat exchange area between volumes j and i (m^2),

q_V^i : power density in the volume i (W/m^3),

V^i: volume i (m^3).

The sum in Eq. 2.27 is taken over all adjacent control volumes (nodes), while the heat flux between control volumes i and j is determined as:

$$q^{j \to i} = \lambda^{ji} \frac{(T^j - T^i)}{\Delta^{ji}}, \qquad\qquad \textbf{Eq. 2.28}$$

where

λ^{ji} : thermal conductivity of the material between centers of volumes j and i (W/(m·K)).

Δ^{ji} : distance between the centers of volumes j and i (m).

The gas-gap heat conductance in both open and closed gap regimes is calculated according to the Ross and Stoute model [25]:

48

$$\alpha_g = \frac{\lambda_g}{\Delta_g + C(\rho_f + \rho_c) + (g_f + g_c)} + \frac{\tilde{\lambda} P_c}{a_0 \tilde{\rho}^{0.5} H} + \alpha_{rad},$$

Eq. 2.29

where

λ_g :   thermal conductivity coefficient of the gas mixture (W/(m·K)),

Δ_g: fuel-clad gap width (m),

C: constant empirical parameter,

ρ_f, ρ_c: average roughness at the outer fuel and inner cladding surfaces, respectively (m),

g_f, g_c: temperature jump distance terms at the outer fuel and inner cladding surface, respectively(m),

$\tilde{\lambda}$:   effective thermal conductivity at the pellet-cladding contact (W/(m·K)),

P_c: contact pressure (Pa),

a_0:   empirical function of fuel roughness,

$\tilde{\rho}$:   effective roughness of fuel and cladding surfaces (m),

H: Meyer hardness of cladding (Pa),

α_{rad}:   heat conductance due to thermal radiation (W/(m^2·K)).

2.6.3   FRED mechanical model

This section gives an overview of the algorithms used for the fuel pin mechanical analysis in the FRED code [13, 15].

The mesh of the mechanical model is identical to that of the thermal model (Fig. 2.6), so that the temperatures can be easily transferred, node by node, as body load for mechanical analysis and for material properties calculation.

Inner and outer gas pressures are used as boundary conditions. The outer pressure is provided by the thermal-hydraulics code (TRACE), and the inner pressure is calculated as:

$$P = \left(\frac{P^0 V^0}{293} + \mu_{FGR} R \right) \frac{T}{V},$$

<div align="right">**Eq. 2.30**</div>

where

P^0, V^0: gas pressure and free volume at fuel rod manufacturing time,

μ_{FGR}: amount of fission gas released from the fuel into the free volume (moles),

R: universal gas constant (J/mol·K).

The gas volume V and the temperature T in the fuel-rod free volume are determined, while taking into account the fuel rod deformation, as follows:

$$V = V_p + \sum_{n=1}^{NZ} (V_{1n} + V_{2n} + V_{3n}),$$

<div align="right">**Eq. 2.31**</div>

$$T = \frac{V}{\dfrac{V_p}{T_p} + \sum_{n=1}^{N_z} \left(\dfrac{V_{1n}}{T_{1n}} + \dfrac{V_{2n}}{T_{2n}} + \dfrac{V_{3n}}{T_{3n}} \right)},$$

<div align="right">**Eq. 2.32**</div>

where

V_p, T_p: volume and temperature of gas in the gas plenum,

V_{1n}, V_{2n}, V_{3n}: volume of gas in the central void, open porosity in fuel and fuel-clad gap, respectively, in axial slice n,

T_{1n}, T_{2n}, T_{3n}: temperature of gas in the central void, open porosity in fuel and fuel-clad gap, respectively, in axial slice n,

N_Z: number of axial calculational slices.

The gas temperature in the gas plenum is assumed equal to the temperature of the adjacent hydraulic volume. This temperature is sent to FRED by TRACE. The volume of open porosity is calculated by the correlation recommended in the MATPRO-V11 library [26].

The determination of the clad and fuel stress-strain condition includes a calculation of radial distributions for stresses and deformations for each axial slice (1.5D approximation).

50

Tangential, radial and axial components of the total clad and fuel deformations are calculated taking into account elastic and plastic deformation, creep, thermal expansion and swelling under the followings assumptions:

- these components are additive,

- the total axial deformation is constant over the fuel radius (thickness of each axial slice remains constant with radius),

- the total axial deformation is constant over the cladding radius,

- there is no slip between the fuel and cladding in the pellet cladding mechanical interaction (PCMI) regime,

- the material mechanical properties are assumed isotropic when creep and plastic deformation is calculated.

The equations are solved level-wise. The radial meshing and the position of the nodes, where stresses and deformations are calculated, are shown in Fig. 2.7.
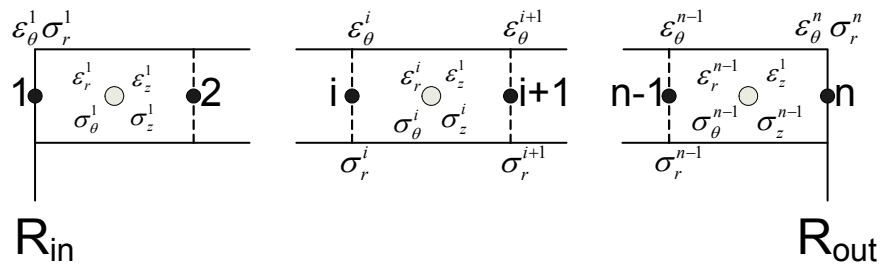
Fig. 2.7. Radial meshing for the mechanical problem

The system of equations for each level includes Hooke's laws, strain compatibility and stress equilibrium equations:

Hooke's laws:

$$\varepsilon_\theta(r,z) = \frac{1}{E}\left(\sigma_\theta(r,z) - \nu(\sigma_z(r,z) + \sigma_r(r,z))\right) + \varepsilon_\theta^{TCP}(r,z) \qquad \text{Eq. 2.33}$$

$$\varepsilon_r(r,z) = \frac{1}{E}\left(\sigma_r(r,z) - \nu(\sigma_\theta(r,z) + \sigma_z(r,z))\right) + \varepsilon_r^{TCP}(r,z) \qquad \text{Eq. 2.34}$$

$$\varepsilon_z(z) = \frac{1}{E}\left(\sigma_z(r,z) - \nu(\sigma_\theta(r,z) + \sigma_r(r,z))\right) + \varepsilon_z^{TCP}(r,z) \qquad \text{Eq. 2.35}$$

where

$\varepsilon_\theta^{TCP}, \varepsilon_r^{TCP}, \varepsilon_z^{TCP}$:   tangential, radial and axial components of fuel and cladding thermal-viscous-plastic deformation (m/m),

$\sigma_\theta, \sigma_r, \sigma_z$:   tangential, radial and axial components of the fuel and cladding stress (Pa),

E :   Young modulus of the fuel or cladding material (Pa),

ν :   Poisson's ratio of the fuel or cladding material.

The strain compatibility (Eq. 2.36) and stress equilibrium (Eq. 2.37) equations are used to make the system of equations complete:

$$\frac{d\varepsilon_\theta(r,z)}{dr} = \frac{\varepsilon_r(r,z) - \varepsilon_\theta(r,z)}{r} \qquad \text{Eq. 2.36}$$

$$\frac{d\sigma_r(r,z)}{dr} = \frac{\sigma_\theta(r,z) - \sigma_r(r,z)}{r} \qquad \text{Eq. 2.37}$$

Effective stress is calculated by the Hill equation:

$$\sigma = \sqrt{0,5(\sigma_\theta - \sigma_z)^2 + 0,5(\sigma_z - \sigma_r)^2 + 0,5(\sigma_\theta - \sigma_r)^2} \qquad \text{Eq. 2.38}$$

The pressure boundary conditions are applied as shown in Fig. 2.8. The inner pressure P_{in} is determined by the free volume, temperature field and fission gas release. P_{out} is the coolant pressure.
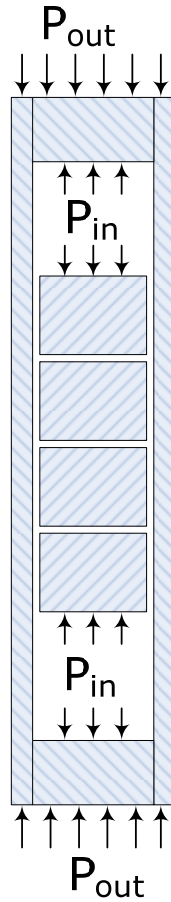
Fig. 2.8. Schematic sketch of the pressure application in the fuel rod mechanical model.

Boundary conditions in open-gap regime

The boundary conditions for each axial slice of the <u>fuel zone</u> are defined by the following equations:

$$\left.\frac{d\sigma_r}{dr}\right|_{r=0} = 0 \qquad\qquad \textbf{Eq. 2.39}$$

$$\sigma_r\left(R_{fuel}, z\right) = -P_{in} \qquad\qquad \textbf{Eq. 2.40}$$

The Eq. 2.39 can be rewritten as follows according to the definition Eq. 2.37:

$$\sigma_r\left(0, z\right) - \sigma_\theta\left(0, z\right) = 0 \qquad\qquad \textbf{Eq. 2.41}$$

The axial stress balance is determined by the inner rod pressure:

$$2\int_{0}^{R_{fuel}} \sigma_z(r,z)rdr = -P_{in}R_{fuel}^2$$ **Eq. 2.42**

The boundary conditions for each axial slice of the <u>cladding zone</u> in the open fuel-clad gap regime are defined by the following equations:

$$\sigma_r(r_i,z) = -P_{in},$$ **Eq. 2.43**

$$\sigma_r(r_o,z) = -P_{out},$$ **Eq. 2.44**

and the integral equation for the balance of axial stresses (see Fig. 2.8):

$$2\int_{r_i}^{r_o} \sigma_z(r,z)rdr = P_{in}R_{clad,inner}^2 - P_{out}R_{clad,outer}^2$$ **Eq. 2.45**

In Eqs. 2.39-2.45:

P_{in}:   gas pressure inside fuel rod,

P_{out}:   coolant pressure,

$R_{clad,inner}$ and $R_{clad,outer}$:   inner and outer cladding radii,

R_{fuel}:   fuel pellet radius.

Boundary conditions in closed-gap regime

The open gas-gap regime boundary conditions are used before the moment when the fuel pellet outer radius is equal to the cladding inner radius. Following the contact occurrence, the boundary conditions are modified as indicated below. These are derived with the assumption of no-slip between the pellet and cladding. This means that, in contact regime, increment of axial and tangential deformations during a given time step are the same for fuel and cladding (schematically shown in Fig. 2.9):

$$\varepsilon_{z,clad}^{i+1} - \varepsilon_{z,fuel}^{i+1} = \varepsilon_{z,clad}^{i} - \varepsilon_{z,fuel}^{i},$$ **Eq. 2.46**

$$\varepsilon_{\theta,clad}^{i+1} - \varepsilon_{\theta,fuel}^{i+1} = \varepsilon_{\theta,clad}^{i} - \varepsilon_{\theta,fuel}^{i},$$ **Eq. 2.47**

where

$\varepsilon_{x,clad}^{i}$:   cladding axial deformation at time step i,

$\varepsilon_{x,clad}^{i+1}$:   cladding axial deformation at time step i+1,

54

$\varepsilon^i_{x,clad}$:   fuel axial deformation at time step i,

$\varepsilon^{i+1}_{x,clad}$:   fuel axial deformation at time step i+1,

x: stands for either z for axial deformation or θ for tangential.

It has to be mentioned that Eq. 2.46 and Eq. 2.47 have to be used only for the nodes, located on the contacting surfaces i.e. the last radial nodes in fuel zone (nodes, corresponding to the fuel outer surface) and first radial nodes in cladding (nodes, corresponding to the cladding inner surface).

The integral equation for the balance of axial stresses in closed-gap regime can be written as:

$$2 \int_o^{R_{fuel,outer}} \sigma_z(r,z)rdr + 2 \int_{R_{clad,inner}}^{R_{clad,outer}} \sigma_z(r,z)rdr = -P_{out}R^2_{clad,outer} \,, \qquad \textbf{Eq. 2.48}$$

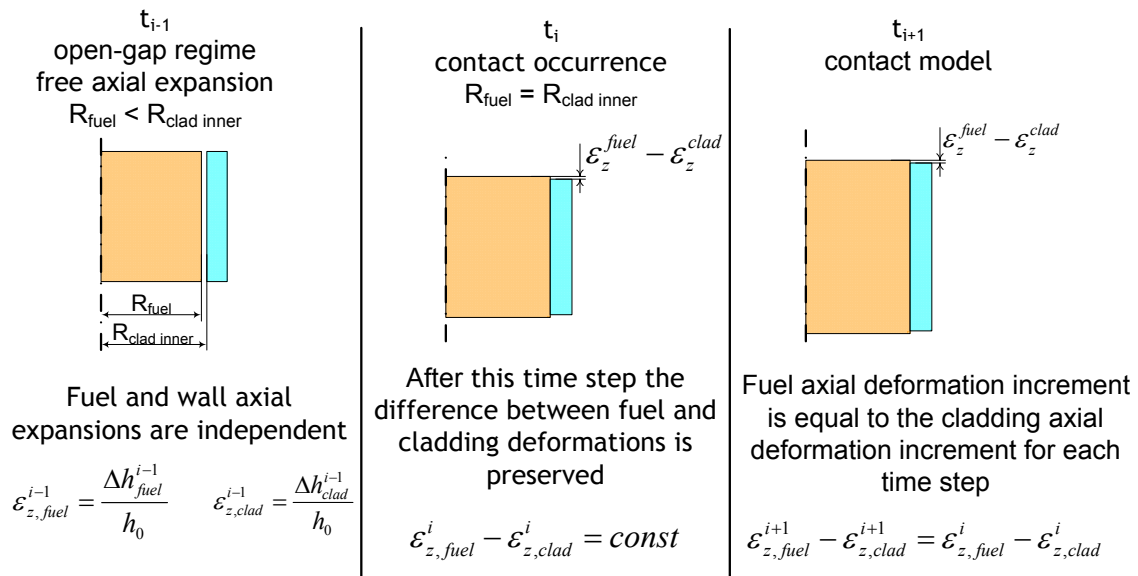| t_{i-1} open-gap regime free axial expansion $R_{fuel} < R_{clad\ inner}$	t_i contact occurrence $R_{fuel} = R_{clad\ inner}$	t_{i+1} contact model
Fuel and wall axial expansions are independent $\varepsilon^{i-1}_{z,fuel} = \dfrac{\Delta h^{i-1}_{fuel}}{h_0} \qquad \varepsilon^{i-1}_{z,clad} = \dfrac{\Delta h^{i-1}_{clad}}{h_0}$	After this time step the difference between fuel and cladding deformations is preserved $\varepsilon^i_{z,fuel} - \varepsilon^i_{z,clad} = const$	Fuel axial deformation increment is equal to the cladding axial deformation increment for each time step $\varepsilon^{i+1}_{z,fuel} - \varepsilon^{i+1}_{z,clad} = \varepsilon^i_{z,fuel} - \varepsilon^i_{z,clad}$

Fig. 2.9. Schematic of the contact model algorithm

During contact, the radial stress is continuous at the pellet-cladding contact surface:

$$\sigma_r\left(R_{fuel},z\right) = \sigma_r\left(R_{clad,inner},z\right) \qquad \textbf{Eq. 2.49}$$

and the outer surface boundary condition is determined in the same way as when the gap is open.

The contact pressure under conditions of the closed gap is assumed to be equal to the radial stress component on the inner clad surface, with opposite sign:

$$\sigma_{contact} = -\sigma\left(R_{fuel}, z\right)$$ **Eq. 2.50**

The criterion for the gap re-opening is decrease of the contact pressure below the gas pressure inside the fuel rod.

The radial distribution of the components of the thermal-viscous-plastic deformation, included in the right-hand sides of Eqs. 2.33-2.35, is determined for each axial slice under the assumption that all elements are additive:

$$\varepsilon_i^{TCP}(r,z) = \varepsilon_i^T(r,z) + \varepsilon_i^C(r,z) + \varepsilon_i^P(r,z),$$ **Eq. 2.51**

where $i = \theta, r, z$,

$\varepsilon_i^T(r,z)$:   clad thermal expansion,

$\varepsilon_i^C(r,z)$:   clad creep,

$\varepsilon_i^P(r,z)$:   clad plastic deformation.

Creep components are determined by time integration of equations written according to the Prandtl-Reuss flow rules, with the use of empirical correlations for the effective creep rate [27]:

$$\frac{d\varepsilon_i^C(r,z)}{dt} = \frac{3}{2} \frac{A\sigma^\eta(r,z)\exp(-Q/RT(r,z))}{\sigma(r,z)}\left(\sigma_i(r,z) - \sum_{j=1}^{3}\sigma_j(r,z)\right),$$ **Eq. 2.52**

where $i = \theta, r, z$,

$\sigma(r,z)$:   effective stress (Pa),

R: universal gas constant (J/mol·K),

$T(r,z)$:   clad temperature (K),

A, Q and η: empirical constants.

To calculate clad plastic deformation components, the uniaxial plastic deformation curve based on experimental data [26, 28] is integrated in time with respect to effective deformation.

$$\frac{d\varepsilon}{dt} = 10^{-3}\left(\frac{\sigma}{K \cdot \varepsilon^n}\right)^m,$$

Eq. 2.53

Where

ε: effective deformation,

K: strength coefficient,

n: strain hardening exponent,

m: strain rate sensitivity exponent.

The coefficients used in Eq. 2.53 are empirical functions of temperature and neutron fluence. The clad plastic deformation in a node begins when the following condition is met in this node:

$$\sigma = E\varepsilon,$$

Eq. 2.54

where

σ: effective stress (Eq. 2.38),

E: Young modulus,

ε: effective deformation calculated from Eq. 2.53.

After start of plasticity, the effective plastic deformation is determined at each time step as

$$\varepsilon^P = \varepsilon - \sigma / E$$

Eq. 2.55

The components of plastic deformation are determined by time integration of equations written according to the Prandtl-Reuss flow rules:

$$\frac{d\varepsilon_i^P(r,z)}{dt} = \frac{3}{2}\frac{d\varepsilon/dt}{\sigma(r,z)}\left(\sigma_i(r,z) - \sum_{j=1}^{3}\sigma_j(r,z)\right),$$

Eq. 2.56

where

$i = \theta, r, z$,

$d\varepsilon/dt$:   effective deformation rate, calculated from Eq. 2.53.

The plastic deformation stops when the following condition is met:

$$\sigma < E(\varepsilon - \varepsilon_{old}^P),$$

<div align="right">**Eq. 2.57**</div>

where

ε_{old}^P : effective plastic deformation, calculated at previous time step.

The cladding nodalization scheme for n control volumes distributed between the inner and outer radii, and the disposition of the calculational nodes for the stress and deformation components, are shown in Fig. 2.7.

The discretization of Eqs. 2.33-2.37 and Eqs. 2.39-2.49, for the chosen nodalization scheme, results in the following set of equations for each axial slice:

Hooke's laws:

$$E\frac{\varepsilon_\theta^i + \varepsilon_\theta^{i+1}}{2} - \sigma_\theta^i + v\left(\frac{\sigma_r^i + \sigma_r^{i+1}}{2} + \sigma_z^i\right) = E\varepsilon_\theta^{TCPi}, \; i = 1,...,n-1$$

<div align="right">**Eq. 2.58**</div>

$$E\varepsilon_r^i - \frac{\sigma_r^i + \sigma_r^{i+1}}{2} + v\left(\sigma_\theta^i + \sigma_z^i\right) = E\varepsilon_r^{TCPi}, \; i = 1,...,n-1$$

<div align="right">**Eq. 2.59**</div>

$$E\varepsilon_z - \sigma_z^i + v\left(\sigma_\theta^i + \frac{\sigma_r^i + \sigma_r^{i+1}}{2}\right) = E\varepsilon_z^{TCPi}, \; i = 1,...,n-1$$

<div align="right">**Eq. 2.60**</div>

Strain compatibility:

$$(r^{i+1} - r^i)\varepsilon_r^i + r^i\varepsilon_\theta^i - r^{i+1}\varepsilon_\theta^{i+1} = 0, \; i = 1,...,n-1$$

<div align="right">**Eq. 2.61**</div>

Stress equilibrium:

$$(r^{i+1} - r^i)\sigma_\theta^i + r^i\sigma_r^i - r^{i+1}\sigma_r^{i+1} = 0, \; i = 1,...,n-1$$

<div align="right">**Eq. 2.62**</div>

Zero derivative of the radial stress at the pellet centre:

$$\sigma_r^1 - \sigma_\theta^1 = 0$$

<div align="right">**Eq. 2.63**</div>

Boundary conditions at the fuel outer and cladding inner surfaces in open- and closed-gap regimes:

$$\begin{cases} \sigma_r^{nf} = -P_{in} \\ \sigma_r^{nf+1} = -P_{in} \end{cases} \text{ or } \sigma_r^{nf} = \sigma_r^{nf+1} \text{ (in closed gap regime)}$$

<div align="right">**Eq. 2.64**</div>

Boundary conditions on cladding outer surface:

$$\sigma_r^{nf+nc} = -P_{out}$$

Eq. 2.65

Joint fuel-cladding axial and tangential deformations in closed-gap regime:

$$\varepsilon_z^{nf+1} - \varepsilon_z^{nf} = \varepsilon_{z,old}^{nf+1} - \varepsilon_{z,old}^{nf},$$

Eq. 2.66

$$\varepsilon_\theta^{nf+1} - \varepsilon_\theta^{nf} = \varepsilon_{\theta,old}^{nf+1} - \varepsilon_{\theta,old}^{nf},$$

Eq. 2.67

Axial forces balance for the fuel pellet in open-gap regime:

$$\sum_{i=1}^{nf-1} \sigma_z^i \cdot \left[\left(r^{i+1}\right)^2 - \left(r^i\right)^2\right] = -P_{in} R_{fuel}^2$$

Eq. 2.68

Axial forces balance for the fuel cladding in open-gap regime:

$$\sum_{i=nf+1}^{nf+nc-1} \sigma_z^i \cdot \left[\left(r^{i+1}\right)^2 - \left(r^i\right)^2\right] = P_{in} R_{clad,inner}^2 - P_{out} R_{clad,outer}^2$$

Eq.

2.69

Axial forces balance in closed-gap regime:

$$\sum_{i=1}^{nf-1} \sigma_z^i \cdot \left[\left(r^{i+1}\right)^2 - \left(r^i\right)^2\right] + \sum_{i=nf+1}^{nf+nc-1} \sigma_z^i \cdot \left[\left(r^{i+1}\right)^2 - \left(r^i\right)^2\right] = -P_{out} R_{clad,outer}^2$$

Eq.

2.70

where

nf: number of nodes in the fuel pellet,

nc: number of nodes in cladding,

2.6.4   Solution of the equations

The resulting system of equations per each axial level in matrix formulation can be written as follows:

$$\begin{vmatrix} a_1^1 & a_1^2 & a_1^3 & \dots & a_1^{5n-2} \\ a_2^1 & a_2^2 & a_2^3 & \dots & a_2^{5n-2} \\ a_3^1 & a_3^2 & a_3^3 & \dots & a_3^{5n-2} \\ \dots & \dots & \dots & \dots & \dots \\ a_{5n-2}^1 & a_{5n-2}^2 & a_{5n-2}^3 & \dots & a_{5n-2}^{5n-2} \end{vmatrix} \times \begin{vmatrix} \varepsilon_\theta^1 \\ \vdots \\ \varepsilon_\theta^n \\ \varepsilon_r^1 \\ \vdots \\ \varepsilon_r^{n-1} \\ \varepsilon_z \\ \sigma_\theta^1 \\ \vdots \\ \sigma_\theta^{n-1} \\ \sigma_r^1 \\ \vdots \\ \sigma_\theta^n \\ \sigma_z^1 \\ \vdots \\ \sigma_z^{n-1} \end{vmatrix} = \begin{vmatrix} b_1 \\ b_2 \\ b_3 \\ \vdots \\ b_{5n-2} \end{vmatrix}$$

Eq. 2.71

where

a_i^j: known coefficients coming from the left side of Eqs. 2.58-2.70,

b_i^j: known coefficients coming from the right side of Eqs. 2.51-2.58.

The set of (5n-2) linear algebraic Eqs. 2.58-2.70 is solved with standard methods of LU-decomposition and back substitution [29] with respect to components of the total deformation and stresses. The resulting vector has the form:

$$\{\varepsilon_\theta^1,...,\varepsilon_\theta^n,\varepsilon_r^1,...,\varepsilon_r^{n-1},\varepsilon_z,\sigma_\theta^1,...,\sigma_\theta^{n-1},\sigma_r^1,...,\sigma_r^n,\sigma_z^1,...,\sigma_z^{n-1}\}^T.$$

The set of ordinary differential equations (ODEs) includes Eq. 2.26 for fuel and cladding temperatures, Eq. 2.52 for creep components, Eq. 2.53 for effective deformation and Eq. 2.56 for plastic deformation components. Such a system of ODEs is solved for each fuel rod, or other structural element, using the standard subroutine LSODES [30].

The set of linear equations Eqs. 2.58-2.70 is solved, at each time step, in an iteration cycle with the recalculation of gas pressure inside the fuel rod. This is necessary due to the changes in fuel rod geometry, calculated as:

$$r^i = r_0^i(1+\varepsilon_\theta^i),$$

Eq. 2.72

$$\Delta z^j = \Delta z_0^j (1 + \varepsilon_z^j) ,$$ <div style="text-align: right;">**Eq. 2.73**</div>

where

r_0^i :   radial position of node i before deformation,

r^i :   radial position of node i after deformation,

Δz_0^j :   height of the j-th axial level before deformation,

Δz^j :   height of the j-th axial level after deformation,

2.6.5   Coupling with the TRACE code

In the framework of the FAST code system, FRED has been coupled to TRACE as a subroutine. Thereby, it has its own internal time integration scheme (LSODES) and has the option to divide the TRACE time-step into sub-steps if convergence is not obtained.

When simulating a fuel pin, identical representative heat structures are specified in both the TRACE and FRED input decks. At each time step, TRACE performs the thermal-hydraulics calculations of temperatures in heat structures and power distributions (with point-kinetics approximation), and sends to FRED the axial distribution of the power density, clad-to-coolant heat exchange coefficient, coolant temperature and coolant pressure for all simulated fuel pins. When a 3D reactor kinetics solution is necessary, PARCS is used for calculation of the power distribution.

With these data, FRED calculates fuel rod properties, temperatures and stress-strain conditions for the same time step as TRACE, and sends back to TRACE the temperature distribution in the fuel pin. Temperatures in the heat structures calculated by TRACE are then overwritten by these FRED data and used as initial conditions for the calculation of thermal-hydraulics and reactivity feedbacks for the next time step.

In addition (when the 3D reactor kinetics option is used), the FRED code sends to PARCS the core height and radius, as well as fuel temperatures, to re-calculate the macroscopic cross sections of the corresponding materials. In the case of the point kinetics option, the same information is sent to TRACE for calculation of the reactivity feedbacks.

2.7 FINITE ELEMENT ANALYSIS AND THE ANSYS CODE

2.7.1 Historical review of the finite element method (FEM)

The finite-element method (FEM) originated from the need for solving complex elasticity, structural analysis problems in civil engineering and aeronautical engineering. Its development can be traced back to the work of Alexander Hrennikoff (1941) and Richard Courant (1942). While the approaches used by these pioneers are dramatically different, they share one essential characteristic: mesh discretization of a continuous domain into a set of discrete sub-domains. Hrennikoff's work discretizes the domain by using a lattice analogy, while Courant's approach divides the domain into finite triangular subregions for solution of second order elliptic partial differential equations (PDEs) that arise from the problem of torsion of a cylinder. Courant's contribution was evolutionary, drawing on a large body of earlier results for PDEs developed by Rayleigh, Ritz, and Galerkin.

Development of FEM began in earnest in the middle to late 1950s for airframe and structural analysis and gathered momentum at the University of Stuttgart through the work of John Argyris and at Berkeley through the work of Ray W. Clough in the 1960s for use in civil engineering. The method was provided with a rigorous mathematical foundation in 1973 with the publication of Strang and Fix's "An Analysis of The Finite Element Method", and has since been generalized into a branch of applied mathematics for numerical modeling of physical systems in a wide variety of engineering disciplines, e.g. electromagnetism and fluid dynamics.

The first book on FEM was published in 1967 by Zienkiewicz and Chung [31]. The development of the finite element method in structural mechanics is often based on an energy principle, e.g. the virtual work principle or the minimum total potential energy principle, which provides a general, intuitive and physical basis that has a great appeal to structural engineers. According to this principle, the original problem is represented by an equivalent variational formulation. The solution is approximated by a combination $\sum q_j \varphi_j$ of predefined shape functions $\varphi_j(x)$. The coefficients q_j are to be found by the solution of the system of discrete equations, which is formed according to the variational principle corresponding to the problem.

The major development has been done in the definition of the shape functions: these are piecewise polynomials in FEM. Each function $\varphi_j(x)$ is zero over the whole domain, except in the vicinity of a given node. In this region, $\varphi_j(x)$ is comprised of low order polynomials and the calculations become trivial [32].

The certain advantage of finite elements modeling is the inherent ability to handle complex domains and boundary conditions. Moreover, the precision over a certain

domain can also be controlled by meshing, which is important in the case of geometrical or other inhomogeneities. The mesh can be refined in the region of interest and broadened where the precision is less important.

The major drawback of the method is the meshing process, i.e. the division of a domain into a finite number of subregions (finite elements). There is no clear guideline about the dimensions of the elements, which would provide a solution of desired accuracy, the choice often being made on the basis of experience or expert opinion.

2.7.2 General description

ANSYS is the original (and commonly used) name for ANSYS Mechanical or ANSYS Multiphysics, general purpose, finite-element analysis software. ANSYS, Inc actually develops a complete range of Computer Aided Engineering (CAE) products, but is perhaps best known for ANSYS Mechanical and ANSYS Multiphysics [33].

ANSYS Mechanical and ANSYS Multiphysics are self-contained analysis tools incorporating pre-processing (geometry creation, meshing), solver and post-processing modules in a unified graphical user interface. ANSYS is a general purpose, finite-element modeling package, for numerically solving a wide variety of mechanical problems. These problems include: static/dynamic structural analysis (both linear and non-linear), heat transfer and fluid problems, as well as acoustic and electro-magnetic problems.

The software is used to analyze a broad range of applications. ANSYS Mechanical can consider both structural and material non-linearities. ANSYS Multiphysics includes solvers for thermal, structural, CFD, electromagnetics and acoustics problems, and can simulate the corresponding physics phenomena in a coupled manner in order to address multi-disciplinary applications. ANSYS software is also used in civil engineering (ANSYS/CivilFEM), electrical engineering, physics and chemistry.

Though ANSYS can provide solutions for a variety of applications, its use in the present research is limited to thermal, structural and coupled analysis. Accordingly, these capabilities are described below in more detail.

Structural analysis

Structural analysis is probably the most common application of the finite element method, as it implies a large variety of different applications in various fields.

Several kinds of structural analysis can be performed with the ANSYS software:

- *Static Analysis* – Used to determine displacements, stresses, etc. under static loading conditions. ANSYS can carry out both linear and nonlinear static analyses. Nonlinearities can include plasticity, stress stiffening, large deflection, large strain, hyper-elasticity, contact surfaces, and creep.

- *Transient Dynamic Analysis* – Used to determine the response of a structure to arbitrarily time-varying loads. All nonlinearities mentioned above under Static Analysis are allowed.

- *Buckling Analysis* – Used to calculate buckling loads and determine the buckling mode shape. Both linear (eigenvalue) buckling and nonlinear buckling analyses are possible.

In addition to the above types, several other special-purpose analyses are available, e.g. fracture mechanics, composite material analysis, fatigue, and both p-method and beam analyses.

ANSYS structural analysis includes contact modeling. It can also be used if the contact status and place of contact are not known a priori, i.e. it can track the contact closure and reopening automatically.

Thermal analysis

ANSYS is capable of both steady-state and transient thermal analysis of any solid with thermal boundary conditions.

Steady-state thermal analyses yield the effects of steady thermal loads on a system or component. Users often perform a steady-state analysis before doing a transient thermal analysis, to help establish initial conditions. A steady-state analysis can also be the last step of a transient thermal analysis, performed after all transient effects have diminished. ANSYS can be used to determine temperatures, thermal gradients, etc., which result in an object due to thermal loads of various types, including the following:

- convection,

- radiation,

- heat flow rates,

- heat fluxes (heat flow per unit area),

- heat generation rates (heat flow per unit volume),

- constant temperature boundaries.

64

A steady-state thermal analysis may be either linear, with constant material properties, or nonlinear, with material properties that depend on temperature. The thermal properties of most materials vary with temperature. This temperature dependency being appreciable, the analysis becomes nonlinear. Radiation boundary conditions also make the analysis nonlinear. Transient calculations are time dependent, and ANSYS can both solve the corresponding equations and post-process the results.

Thermal conductivity can be calculated for places of contact. Thermal conductance can be either fixed or dependent on certain parameters, e.g. temperature, contact pressure, etc.

Coupled Fields

A coupled-field analysis is an analysis that takes into account the interaction (coupling) between two or more disciplines (fields) of engineering. A thermal/structural analysis, for example, handles interaction between structural and thermal fields: it solves for the deformations and stresses resulting from an applied temperature field, and vice versa. Other examples of coupled-field analyses are piezoelectric analysis, thermal-electric analysis, and fluid-structure analysis.

The application of ANSYS in the present research is limited to thermal/structural coupled analysis.

REFERENCES

1.   A Technology Roadmap for Generation IV Nuclear Energy Systems: Technical Roadmap Report, December, 2002

2.   P. Martin, N. Chauvin, J.C. Garnier, M. Masson, P. Brossard, P. Anzieu, "Gas Cooled Fast Reactor System: Major Objectives and Options for Reactor, Fuel and Fuel Cycle", Proceedings of GLOBAL 2005, Paper No. IL002, Tsukuba, Japan, Oct 9-13, 2005

3.   J.C. Garnier, C. Bassi, M. Blanc, J.C. Bosq, N. Chauvin, P. Dumaz, J.Y. Malo, B. Mathieu, A. Messié, L. Nicolas, A. Ravenet, "Contribution to GFR design option selection", Proceedings of ICAPP '06, Paper 6147, Reno, NV USA, June 4-8, 2006.

4.   N. Chauvin, J.Y. Malo, J.C. Garnier, F. Bertrand, J.C. Bosq, A. Ravenet, D. Lorenzo, M. Pelletier, J.M. Escleine, I. Munoz, JM. Bonnerot, "GFR Fuel And Core Pre-Conceptual Design Studies", Proceedings of GLOBAL 2007, Boise, Idaho, USA, Sept. 9-13, 2007.

5.   J.C. Bosq, Y. Peneliau, G. Rimpault, M. Vanier, "Fine 3D neutronic characterization of a gas-cooled fast reactor based on plate-type subassemblies", PHYSOR-2006, Vancouver, BC, Canada, September 10-14, 2006

6.   P. Dumaz, P. Allegre, C. Bassi, T. Cadiou, A. Conti, J.C. Garnier, J.Y. Malo, A. Tosello, "Gas-cooled fast reactors—Status of CEA preliminary design studies", Nuclear Engineering and Design 237 (2007) 1618–1627, 2007

7.   K. Mikityuk, S. Pelloni, P. Coddington, E. Bubelis, R. Chawla. "FAST: An advanced code system for fast reactor transient analysis", Annals of Nuclear Energy. 32, 15, 1613-1631 2005

8.   G. Rimpault et al., "The ERANOS Data and Code System for Fast Reactor Neutronic Analyses", Int. Conf. on the New Frontiers of Nuclear Technology: Reactor Physics, Safety and High-Performance Computing, PHYSOR 2002, Seoul, Korea (2002)

9.   G. Rimpault, "ERANOS: Manuel des méthodes, le code de cellule ECCO", Rapport Technique, CEA, SPRC/LEPh 97-001 (1997)

10. G. Palmiotti et al., "VARIational Anisotropic Nodal Transport for Multidimensional Cartesian and Hexagonal Geometry Calculation", Argonne National Laboratory Report, ANL-95/40 (1995)

11. J.Y. Doriath, et al., "ERANOS1: The Advanced European System of Codes for Reactor Physics", International Conference on Mathematical Methods and Supercomputing in Nuclear Applications, Karlsruhe, Germany, 1993.

12. H.G. Joo et al. "PARCS, A Multi-Dimensional Two-Group Reactor Kinetics Code Based on the Nonlinear Nodal Method", Technical Report, PU/NE-98-26, Purdue University, 1998

13. K. Mikityuk, et al. "LOOP2: Comprehensive Transient Code for Advanced Nuclear Reactors", Proc. of PHYSOR 2002, Seoul, Korea, October 7-10, 2002

14. K. Mikityuk. "Modifications made in the TRAC-M/AAA code, including introduction of the FRED fuel rod model", PSI Report TM-41-03-18, June 2003 (2003)

15. K. Mikityuk and P. Fomitchenko, "FRED: Calculational Model of Fuel Rod Behavior Under Accident Conditions Coupled with RELAP5/MOD3", Proc. of 8th International Conference on Nuclear Engineering (ICONE-8), Baltimore, MD USA, 2000

16. F. Odar, C. Murray, R. Shumway, M. Bolander, D. Barber, J. Mahaffy. "TRACE V4.0 USER'S MANUAL" U.S. Nuclear Regulatory Commission, Office of Nuclear Regulatory Research, 2003.

17. G. Rimpault, "Algorithmic Features of the ECCO Cell Code for Treating Heterogeneous Fast Reactor Subassemblies", International Topical Meeting on Reactor Physics and Computations, Portland, Oregon, May 1-5, 1995.

18. C.J. Dean, C.R. Eaton, P. Peerani, P. Ribon, G. Rimpault, "Production of Fine Group Data for the ECCO Code, International Conference on the Physics of Reactors : Operation, Design and Computation", PHYSOR'90 International Conference, Marseille, France, April 23-27, 1990.

19. E. Fort, W. Assal, G. Rimpault, J. Rowlands, P. Smith, R. Soule, "Realisation and Performance of the Adjusted Nuclear Data Library ERALIB1 for Calculating Fast Reactor Neutronics", PHYSOR'96 International Conference, Mito, Japan, 1996.

20. G.B. Wallis, "One Dimensional Two-Phase Flow", McGraw-Hill, Inc., New York, 1969.

21. J.H. Kim, W.H. Li. "Heat transfer in laminar flow along circular rods in infinite square arrays". Journal of Heat Transfer, Vol.: 110:1, 1988

22. M.S. El-Genk, Bingjing Su, Zhanxiong Guo. "Experimental studies of forced, combined and natural convection of water in vertical nine-rod bundles with a square lattice". International Journal of Heat and Mass Transfer, Volume 36, Issue 9, Pages 2359-2374, 1993

23. S.W. Churchill, R. Usagi. "A General Expression for the Correlation of Rates of Transfer and Other Phenomena", American Institute of Chemical Engineers, Vol.18, pp. 1121-1128, 1972

24. D.K. Edwards, V. E.Denny, A. F.Mills. "Transfer processes : an introduction to diffusion, convection, and radiation, ed. 2". Washington a.o.: Hemisphere Publishing Corporation; New York a.o.: McGraw-Hill, 1979

25. A.M. Ross and R.L. Stoute, 1962, "Heat Transfer Coefficient Between UO2 and Zircaloy-2", AECL-1552.

26. D.L. Hagrman, et al., 1980, "MATPRO-Version 11 (revision 1): A Handbook of Material Properties for Use in the Analysis of Light Water Reactor Fuel Rod Behavior", NUREG/CR-0497 TREE-1280, Rev 1.

27. Khan, A.S., and Huang, S. "Continuum Theory of Plasticity". John Wiley and Sons, Inc., New York, 1995.

28. L. Yegorova, et.al. "Data Base to Characterize Behavior of High-Burnup Fuel Rods with Zr-1%Nb Cladding and UO2 Fuel (VVER Type)", International Agreement Report NUREG/IA-0156, 1999

29. W.H. Press, B.P. Flannery, S.A. Teukolsky, W.T. Vetterling. Numerical Recipes. The Art of Scientific Computing. Cambridge University Press. 1986.

30. C. Hindmarsh, "ODEPACK, A Systematized Collection of ODE Solvers," in Scientific Computing, R. S. Stepleman et al. (eds.), North-Holland, Amsterdam, 1983 (vol. 1 of IMACS Transactions on Scientific Computation), pp. 55-64. Also available as LLNL Report UCRL-88007, August 1982.

31. O.C. Zienkiewicz and Y.K. Cheung, The finite element method in structural and continuum mechanics. , McGraw-Hill, London, 1967.

32. G. Strang, G.J. Fix, An Analysis of The Finite Element Method, Prentice-Hall, Inc., Englewtfod Cliffs, N. J.,1973

33. ANSYS Basic Analysis Guide, ANSYS Release 9.0, ANSYS, Inc., November 2004

3 DEVELOPMENT OF THE THERMO-MECHANICAL MODEL FOR PLATE-TYPE GFR FUEL

This chapter is devoted to the description of the algorithms, which have currently been developed for the thermo-mechanical modeling of advanced GFR plate-type fuel (see Section 2.1).

Section 3.1 provides the geometrical specifications for the reference fuel design considered, as well as for the corresponding reactor core. The necessary extension of the materials database is presented in Section 3.2. Limitations of the existing simulation tools (as described in the previous chapter) are discussed in the context of thermal modeling in Section 3.3, while Section 3.4 presents an overview of the currently developed calculational scheme. Elaboration of the thermal part of the new fuel model is described in Section 3.5, and that of the mechanical part – in Section 3.6. Section 3.7 presents the consideration of burnup effects, and finally, Section 3.8 gives a short summary of the present chapter.

3.1 REFERENCE GFR FUEL DESIGN CONSIDERED

In the context of Fig. 2.2, which illustrates the general layout of the advanced plate-type fuel proposed for the Generation IV GFR, the following parameters need to be fixed for a given reference design of fuel assembly and reactor core:

- plate dimensions (thickness, width and height),

- thickness of the lateral walls enclosing the honeycomb mesh,

- thickness of the honeycomb mesh walls,

- pitch of the honeycomb structure,

- fuel pellet radius and height,

- number of plates within the assembly,

- hexcan wrapper thickness and across flats,

- fuel assembly pitch and the number of assemblies within the core.

The reference GFR design, which has been chosen for the present research, is the so-called 06/04 GFR design. This has been established by the French Commissariat à l'Energie Atomique (CEA) on the basis of detailed neutronic and thermal-hydraulic considerations [1 – 6]. The corresponding geometrical specifications – at the level of fuel pellet, honeycomb structure, fuel plate, assembly and core – are given in Table 3.1.

Minimal radial gap (mentioned in this table) refers to the minimal distance between fuel and a wall for the case of their concentric arrangement (δ in Fig. 3.1). The pellet is assumed to be centralized within the hexagonal SiC cell in this manner by means of appropriate "spacers" designed into the inner cell walls (not shown in the figure).
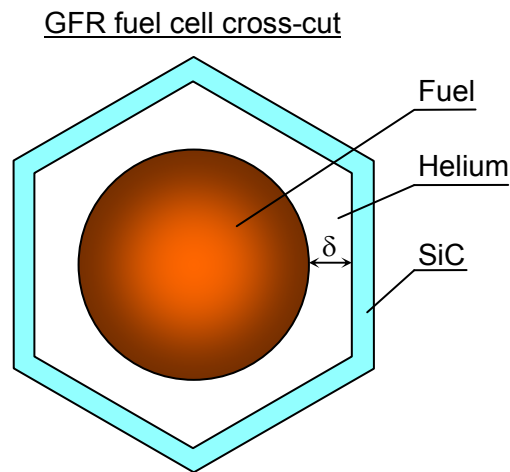
GFR fuel cell cross-cut

Fig. 3.1. GFR fuel cell cross-cut, indicating the choice of the radial gap

Table 3.1. Geometrical characteristics of the 2400 MW$_{th}$ (06/04 design) GFR fuel and core

Parameter	Value
Fuel pellet	
Pellet height, mm	4.9
Pellet radius, mm	5.6
Axial gaps, mm	2 x 0.05
Minimal radial gap (symmetric pellet arrangement within a cell), mm	0.75
Honeycomb structure	
Inner across-flats distance, mm	12.7
Honeycomb wall thickness, mm	1.3
Fuel plate	
Thickness, mm	7
Height, mm	1560
Width, mm	120
Lateral wall thickness, mm	1
Fuel assembly	
Outer across flat, mm	211
Hexcan wrapper thickness, mm	1.5
Pitch, mm	214
Plates per assembly	27
Distance between plates, mm	4.57
GFR core	
Thermal power, MW	2400
Number of fuel assemblies	387
Number of channels reserved for control rods	33
Height, m	1.56
Diameter, m	4.44

3.2　GFR MATERIALS DATABASE

As mentioned earlier, the reference option for the GFR fuel composition is (U, Pu)C. The reference matrix materials are SiC and fiber-reinforced SiC (SiC$_f$/SiC).

Carbide fuel is not in significant use in the nuclear industry currently. It has, however, been extensively studied in the past [6-10], as a possible substitute for widely used UO$_2$, the main incentives being its higher density (around 13-14 g/cm^3) and high thermal conductivity (around 20 W/(m·K)) [6, 7].

The vast majority (>80%) of commercial nuclear power plants today use water as a coolant and moderator. As carbide fuel reacts with water, the more inert UO$_2$ has throughout been the reference fuel composition. The start of the Gen-IV program [11] has now focused attention on the development of gas, lead and sodium cooled reactors, for which carbide and nitride fuels can be deployed to considerably greater potential advantage than oxide [6, 7].

For the corresponding studies, the development of an adequate fuel properties database becomes an important issue. This also refers to the cladding materials, considering that the application of materials such as SiC$_f$/SiC composites in nuclear reactors was never considered previously. Certain steps in this direction, however, have been taken in the context of fusion reactor applications [12-15].

The essential material characteristics of interest and their impact on reactor behavior are described below. The various materials properties, relevant to the GFR and hence essential for the present work, have been collected from the open literature and are presented in Appendix A.

Essential properties for thermal calculations

Density

In the context of time-dependent calculations, the density, together with the specific heat (see below), determines the stored energy of the material which can be potentially released during accidents and transients.

Specific heat

The specific heat is needed for time-dependent temperature calculations, since both the stored energy and temperature change rate depend on the specific heat. It is important in reactor transient analysis to have an accurate estimation of the material

specific heat, because the severity of the transient is greatly affected by the initial stored energy of the fuel and the rate of temperature increase.

Thermal conductivity

The thermal conductivity is needed to predict the temperature distribution within the fuel during reactor operation. This property, as well as the closely associated characterization of fuel material porosity and sintering, is crucial for accurate predictions of the fuel behavior in both steady state and during off-normal transients, because the fuel behavior is strongly dependent on the temperature.

Melting point

The melting point is important for the consideration of accident consequences. It determines the permissible temperature margins to prevent fuel and cladding destruction.

Essential properties for mechanical calculations

Thermal expansion

The thermal expansion describes the dimensional changes in materials caused by changes in temperature. For instance, for the first GFR fuel options (BISO or TRISO coated particles dispersed in matrix) [16, 17], fuel dimensional changes together with the coating thermal expansion determine the porous carbon layer thickness, which due to the relatively low thermal conductivity determines the temperature level. For the plate-type dispersed fuel option (see Fig. 2.2), the fuel thermal expansion will influence both the gas gap size and the pressure of the helium in the free volume and therefore the heat transfer to the cladding and to the coolant. In the case of gas gap closure, the fuel/clad system thermal expansion strictly determines the stress-strain conditions and the integrity of the fuel element. The fuel and clad expansions influence also the core reactivity due to the change in the neutron leakage.

Yield stress

The yield point on a typical stress-strain curve separates regions of elastic and plastic deformations. If the stress reaches this point (the yield stress) and if the material has the possibility of plasticization, stresses can be relaxed by the flow of material and the deformation beyond this point is not recovered when the load is removed.

<u>Young's and shear modulus</u>

Elastic moduli are required to relate stress components to strain components in the elastic region by the generalized form of the Hooke's law. In practice, materials are frequently assumed to be isotropic. In this case, only two independent elastic moduli (i.e. Young's modulus and the shear modulus) are needed to describe the relation between elastic stress and strain, below the yield point.

The Hooke's law is given by

$$\varepsilon_{ii} = \frac{1}{E} \cdot \left[\sigma_{ii} - v \cdot (\sigma_{jj} + \sigma_{kk}) \right]$$

$$\varepsilon_{ij} = \frac{\sigma_{ij}}{G} \qquad \qquad , \qquad \qquad \textbf{Eq. 3.1}$$

$$G = \frac{E}{2 \cdot (1+v)}$$

where:

v: Poisson's ratio (see below),

ε: deformation component,

σ: stress components,

G: shear modulus;

i, j, k: indices of the directions in the chosen coordinate system.

<u>Poisson's ratio</u>

The elastic constants are usually expressed in terms of Young's modulus, the shear modulus and Poisson's ratio. They are not independent, and Poisson's ratio can be related to Young's modulus and the shear modulus as follows:

$$v = \frac{E}{2 \cdot G} - 1, \qquad \qquad \textbf{Eq. 3.2}$$

where:

v: Poisson's ratio,

E: Young's modulus,

G: shear modulus.

Poisson's ratio determines the dependence of the material deformations in different directions (e.g. the extension of the material in X-direction causes constrictions along Y and Z directions, etc.).

As mentioned earlier, the various materials properties, which have been collected from the literature for use in the present work, are presented in Appendix A.

3.3 THERMAL ANALYSIS OF THE GFR FUEL, LIMITATIONS OF THE AVAILABLE TOOLS

The present section describes attempts to analyze the GFR plate-type fuel with the numerical tools described in Chapter 2. Thermal-hydraulic modeling is done by means of the TRACE code, which performs heat transfer calculation within a plate. The plate is divided into axial levels, each of which is treated independently by solving a 1D heat transfer equation. Such an approach involves homogenization of the inner honeycomb structure.

3D analysis is performed by ANSYS for only one cell within the honeycomb structure, with the boundary conditions provided by TRACE analysis. As the boundary conditions are not geometry dependent, the comparison of 1D and 3D solutions simply reveals the effect of homogenization on the results. The whole-plate 3D modeling would be too time-consuming and was therefore not performed.

The following subsection describes the 1D and 3D models, while Subsection 3.3.2 compares the results obtained, thereby underlining the need for the development of a new 2D thermal model.

3.3.1   Description of 1D and 3D models

The comparative analysis of 1D and 3D models is done for different cell and pellet sizes, in order to see the effect of the GFR fuel geometry on the temperature field. As mentioned above, a 3D cell was modeled by the ANSYS code, the 1D heat transfer within the plate being analyzed with TRACE.

One of the 3D model assumptions is the coaxial arrangement of a pellet and a hexagonal cell. This permits the reduction of the dimensionality (in terms of the total number of nodes) by allowing one to model a 60° (or 30°) sector of a cell with adiabatic boundary conditions. The geometry of a cell (60° sector) is shown in Fig. 3.2a. Fig. 3.2b shows the geometry with the inner zone homogenized and is simply meant to illustrate the homogenization procedure when the heat transfer is calculated in 1D.
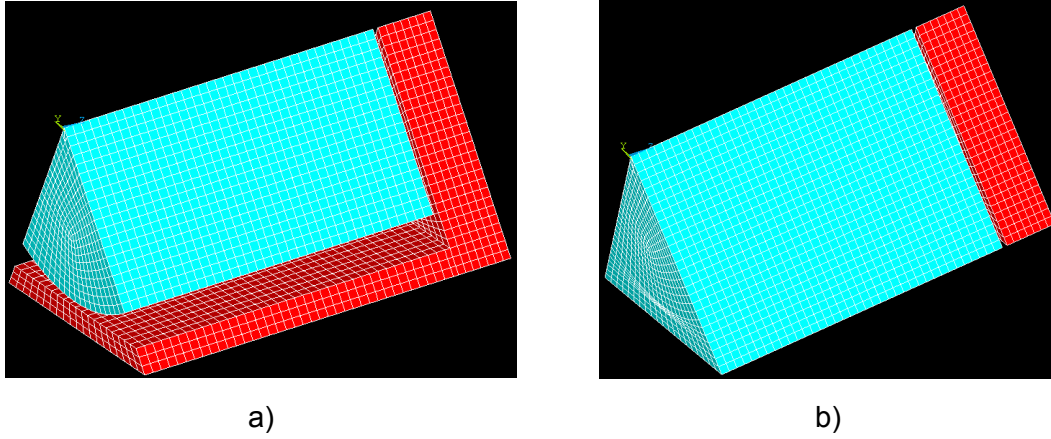
a)   b)

Fig. 3.2. a) Original (heterogeneous) and b) simplified (homogeneous) cell geometries

Effectively, the inner zone of a fuel plate – fuel, radial gas gap and SiC wall – is homogenized with the following assumptions about the homogeneous-zone properties:

- thermal conductivity is equal to that of pure fuel: $\lambda_{\text{hom}} = \lambda_{fuel}$

- density and specific heat are averaged as follows:

$$\rho_{\text{hom}} = \frac{\rho_{fuel} \cdot V_{fuel} + \rho_{He} \cdot V_{He} + \rho_{SiC} \cdot V_{SiC}}{V_{fuel} + V_{He} + V_{SiC}}$$

$$c_p^{\text{hom}} = \frac{\rho_{fuel} \cdot V_{fuel} \cdot c_{p,fuel} + \rho_{He} \cdot V_{He} \cdot c_{p,He} + \rho_{SiC} \cdot V_{SiC} \cdot c_{p,SiC}}{\rho_{fuel} \cdot V_{fuel} + \rho_{He} \cdot V_{He} + \rho_{SiC} \cdot V_{SiC}}$$

Eq. 3.3

- power deposition (P) is the same for the homogeneous and heterogeneous cells, so that the heat generation rate (q_V) is to be adjusted as follows:

$$q_{V\,\text{het}} = \frac{P}{V_{fuel}}$$

$$q_{V\,\text{hom}} = \frac{P}{V_{fuel} + V_{He} + V_{SiC}}$$

Eq. 3.4

- the external boundary conditions, represented by bulk coolant temperature and heat exchange coefficient, are the same for the heterogeneous and homogeneous cells.

The various calculations carried out for the 1D/3D comparisons have all employed the same boundary conditions. These are given in Table 3.2. Although chosen somewhat arbitrarily, the various numerical values are quite representative of the 2400 MW$_{\text{th}}$ GFR core.

Table 3.2. Boundary conditions for the 1D and 3D models comparisons

Parameter	Value
Heat generation rate in the fuel pellet (3D geometry), MW/m^3	500
Heat exchange coefficient, W/(m$^2\cdot$K)	6000
Bulk coolant temperature, K	820

Major attention is paid to the temperature field within a 3D cell and to the heat flows through radial and axial fuel pellet boundaries. The parameters traced during the analysis are:

- peak fuel temperature,

- average fuel temperature,

- peaking factor as the ratio of the above mentioned temperatures,

- axial-to-radial heat flow ratio.

The conductivity of SiC at operating temperatures is quite high, so that the thermal resistance of the He in the gap has the major influence on the fuel temperature. The latter's thermal conductivity is less than 1 W/(m·K). The other important parameters are the fuel pellet size and composition. The thermal conductivity of (U, Pu)C is about 20 W/(m·K). As mentioned, the influence of pure SiC on the temperature field is not very significant due to its high thermal conductivity and low wall thickness. This statement would need to be refined if SiC$_f$/SiC were considered as cladding.

Hence, it is appropriate here to conduct the comparative 1D/3D calculations with different combinations of the pellet radius and the radial gas gap, as these parameters are most likely to be changed during future fuel design improvements. The range of parameter values chosen for the investigations is given in Table 3.3, all possible combinations of these values having been considered.

Table 3.3. Variation of parameters

Pellet radius, mm	Minimal radial gap, μm	Cell wall thickness, mm
1.6 2.6 3.6 4.6 5.6	50 150 250 350 450 550 650 750	0.2

The GFR fuel pellet, in reality, is cooled on all sides. This represents one of the principal limitations with the 1D model, where fuel is cooled only from across the axial boundaries (flat ends). The cooling scheme is illustrated in Fig. 3.3, with the arrows indicating the direction of the heat flow.
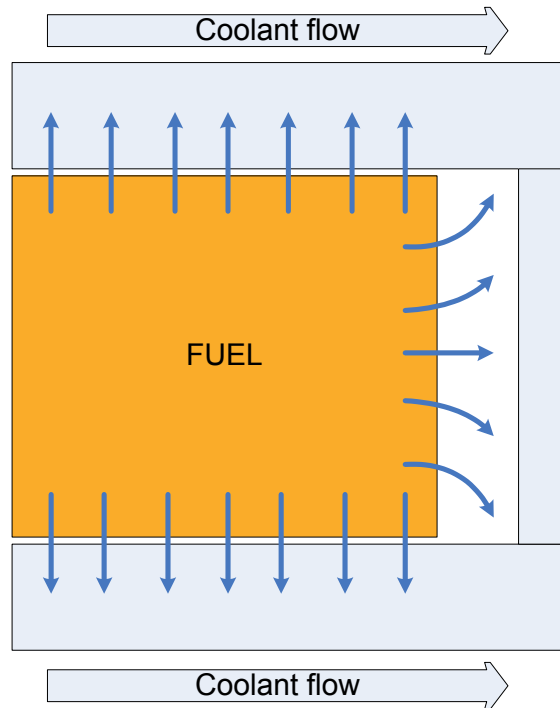
Fig. 3.3. Heat flow in the heterogeneous (3D) cell

There are two competing effects that can be expected to determine the differences between the 1D/3D results, viz.

- power density, which is higher in the heterogeneous cell as the fuel volume is smaller. This effect increases the fuel temperature in the detailed analysis,

- heat exchange area, which is larger in the heterogeneous cell as the pellet is cooled over the whole surface.

Thus, more intensive heat production competes with more effective cooling. It is a priori clear that, in the extreme case of an infinite radial gap, there would be no heat flow in that direction and the radial pellet boundary would be almost adiabatic. As a result, temperatures would be higher in the 3D calculation.

The study of differences between the 1D and 3D heat transfer schemes clearly serves to help understand the GFR fuel thermal behavior in a general sense and can also be expected to lead to recommendations/limitations of the 1D model's usage. The latter aspect is particularly important since nearly all the available system codes (TRACE, RELAP, CATHARE etc.) apply a 1D approach.

3.3.2   Results comparisons, need for the new model development

The results obtained applying the 1D and 3D thermal models are summarized in Tables 3.4 to 3.7. Table 3.4 shows the peak fuel temperatures predicted by the two models, while Table 3.5 shows the corresponding differences. Tables 3.6 and 3.7 provide analogous information in terms of the average fuel temperature.

It can be easily seen that, in most cases, temperatures predicted by the 3D model are higher than for the homogeneous fuel cell. Moreover, for the larger radial gaps (more than 0.3 mm), the temperature difference depends only slightly on the fuel pellet size.

Table 3.4. Peak fuel temperature for the 1D and 3D cells

R_{fuel}, mm \ δ, μm	Geom	50	150	250	350	450	550	650	750
1.6	3D	1071.1	1089.4	1097.1	1100.4	1101.6	1101.5	1100.8	1099.7
	1D	1155.1	1121.4	1092.3	1067.0	1044.8	1025.3	1008.0	992.6
2.6	3D	1139.1	1156.2	1162.2	1164.2	1164.2	1163.2	1161.6	1159.7
	1D	1192.6	1167.9	1145.5	1125.1	1106.4	1089.2	1073.5	1059.0
3.6	3D	1181.9	1195.1	1199.2	1200.1	1199.5	1198.1	1196.3	1194.3
	1D	1210.6	1191.9	1173.9	1157.1	1141.4	1126.7	1112.9	1100.0
4.6	3D	1210.7	1220.4	1222.4	1222.6	1221.7	1220.2	1218.4	1216.5
	1D	1221.7	1206.5	1191.5	1177.3	1163.9	1151.2	1139.1	1127.6
5.6	3D	1231.2	1237.5	1239.2	1239.0	1238.0	1236.6	1235.0	1233.3
	1D	1229.0	1215.6	1203.5	1191.2	1179.5	1168.4	1157.7	1147.4

Table 3.5. Difference between fuel peak temperatures ($T_{3D} - T_{1D}$)

R_{fuel}, mm \ δ, μm	50	150	250	350	450	550	650	750
1.6	-84.0	-32.0	4.7	33.4	56.8	76.2	92.8	107.1
2.6	-53.5	-11.8	16.7	39.2	57.9	74.0	88.1	100.7
3.6	-28.7	3.2	25.3	43.0	58.1	71.4	83.4	94.3
4.6	-10.9	13.9	30.9	45.3	57.8	69.0	79.3	88.9
5.6	2.2	21.9	35.7	47.8	58.5	68.2	77.3	85.9

Table 3.6. Average fuel temperature for the 1D and 3D cells

δ, µm / R_{fuel}, mm	Geom	50	150	250	350	450	550	650	750
1.6	3D	1052.4	1068.1	1073.9	1075.9	1076.0	1075.1	1073.7	1072.0
	1D	1131.3	1100.1	1073.0	1049.4	1028.8	1010.6	994.4	980.1
2.6	3D	1110.7	1126.4	1131.6	1133.0	1132.5	1131.1	1129.2	1127.1
	1D	1166.2	1143.3	1122.5	1103.4	1086.1	1070.1	1055.5	1042.0
3.6	3D	1146.1	1159.3	1163.4	1164.2	1163.6	1162.1	1160.3	1158.2
	1D	1182.9	1165.5	1148.8	1133.2	1118.6	1104.9	1092.1	1080.1
4.6	3D	1169.4	1180.2	1182.7	1183.1	1182.4	1181.0	1179.3	1177.4
	1D	1193.1	1179.0	1165.1	1151.9	1139.5	1127.7	1116.4	1105.8
5.6	3D	1185.6	1193.8	1196.3	1196.5	1195.8	1194.5	1193.0	1191.3
	1D	1199.9	1187.5	1176.2	1164.8	1154.0	1143.6	1133.7	1124.2

Table 3.7. Difference between fuel average temperatures ($T_{3D} - T_{1D}$)

δ, µm / R_{fuel}, mm	50	150	250	350	450	550	650	750
1.6	-79.0	-32.0	0.9	26.4	47.2	64.5	79.2	91.9
2.6	-55.5	-16.9	9.2	29.5	46.5	61.0	73.8	85.1
3.6	-36.8	-6.2	14.6	31.1	45.0	57.2	68.1	78.1
4.6	-23.7	1.1	17.6	31.2	42.9	53.3	62.8	71.6
5.6	-14.3	6.4	20.1	31.7	41.8	50.9	59.3	67.1

As shown by the analysis, the discrepancy between 1D and 3D models can be quite high. For the given boundary conditions (Table 3.2), the temperature difference can be almost 100°C (higher or lower, depending on the geometry). Thus, it is seen that the geometrical complexity of the heat transfer significantly affects the within-pellet temperature distribution and needs to be taken into account. Stand-alone use of the 1D model cannot provide reliable results, as it does not take the inner structure into account. Detailed investigations of the heat transfer in the GFR fuel and the reasons causing the shown differences are presented in Section 4.3.

On the other hand, a detailed 3D analysis would be too costly in terms of CPU time. What is required is a fast-working model, which takes inner fuel structure into

account and can work in parallel (via on-line information exchange) with the thermal-hydraulic code to provide the temperature field in a reliable manner.

Moreover, a 1D model cannot be used for modeling the fuel mechanics, i.e. pellet and cell deformations in open and closed gap regimes, swelling, etc. A mechanical analysis would require even more CPU time for a 3D model, as the number of degrees of freedom is much higher, for a given number of nodes, than in the case of thermal analysis.

From the above, it clearly appears that a 2D cylindrical (R-Z) representation of the GFR fuel cell offers a promising solution for resolving the conflicting requirements. On the one hand, its complexity would be much lower than that of a 3D cell and hence computing times much lower. On the other hand, it would be able to take the inner structure more accurately into account, the calculating geometry and the heat flow being similar to those shown in Fig. 3.3.

3.4   OVERVIEW OF NEW CALCULATIONAL SCHEME

3.4.1   General concept

The previous section underlined the need for the development of a new model for the GFR fuel, which would enable, in a reliable and efficient manner, the following types of analysis:

- thermal analysis,

- mechanical analysis (coupled with the thermal solution),

- peculiarities of the nuclear fuel behavior under irradiation: swelling, fission gas release and the corresponding changes in material properties,

- coupling with the thermal-hydraulic/neutron-kinetic code which should provide the boundary conditions and evaluate the heat generation rate distribution in the core (point or 3D kinetics model).

The standard numerical tools which are available have been described in Chapter 2. The thermal-hydraulic code is TRACE. It can be used to analyze the overall system's performance. This includes not only the core, but also heat exchangers, piping, pumps, safety systems, etc. In the present work, the TRACE modeling is restricted to the static and dynamic analysis of the reactor core, the primary and secondary sides being accounted for via fixed boundary conditions for the core.

At the beginning of the study TRACE was coupled with the FRED code, which provided the thermo-mechanical solution for traditionally designed fuel (cylindrical fuel rods). The basic approach taken was to analyze the algorithms implemented in FRED, as also its coupling with TRACE, and to extend the corresponding calculational scheme to the GFR plate-type fuel analysis via implementation of a 2D FRED model.

The main incentives for having a reliable description of the temperature field within the pellet and matrix are the following:

- precise Doppler feedback calculation, as one of the most important reactivity feedbacks for the GFR [18, 19],

- accurate calculation of the core axial expansion (and the corresponding reactivity feedback), driven by the matrix thermal expansion,

- coupled thermal mechanical calculation of the fuel behavior,

- development of safe-operation criteria for the proposed fuel,

- elaboration of the recommendations for simplified 1D analysis.

3.4.2   Modified FRED/TRACE coupling scheme

The original FRED/TRACE coupling is quite simple and straightforward. Identical fuel rods are specified in both FRED and TRACE, with "identity" implying:

- same fuel pellet, inner and outer cladding radii,

- same height and axial division scheme for the fuel rod,

- same radial nodalization scheme.

Usage of identical meshes in the two codes allows the temperatures to be simply transferred, node by node, from FRED to TRACE. More details about the TRACE/FRED coupling scheme are given in Subsection 2.6.5. In principle, TRACE itself could be used for the thermal fuel analysis. However, its coupling with FRED provides a much better estimate of the temperature field, due to inclusion of the mechanics in FRED as well as the greater flexibility in specifying materials properties.

The original coupling scheme would clearly be inapplicable to a 2D FRED model for the GFR fuel, since the 2D temperature field obtained would not match the 1D TRACE temperature field. Accordingly, an appropriate temperature averaging and transfer (from FRED to TRACE) procedure has to be elaborated, incorporating logics

which helps to reduce the number of cells analyzed. The latter aspect is particularly important due to the huge number of individual cells involved. A simple estimate shows that for the reference GFR design, a plate corresponds to about 1000 cells, which results in 10^7 for the whole core. With, say, 100 nodes per cell and account being taken of thermal and mechanical degrees of freedom (DOF) for each node, one would clearly have an insurmountable problem in terms of CPU time, if such detailed consideration were necessary.

The main goals for the new model can thus be summarized as:

- reduction of the real geometry from 3D to 2D,

- reduction of problem dimensionality (total number of DOFs),

- elaboration of the appropriate temperature averaging procedure to apply a 2D temperature field (provided by FRED) to the 1D TRACE model.

As mentioned, the fuel plate is modeled in TRACE by a slab with the inner zone homogenized. The slab is divided into several axial levels, each of which is coupled with coolant as heat sink.

It was decided to correlate each axial level with just one cell which has to be modeled by FRED. Thus the total amount of cells to be treated by FRED equals the number of fuel plates specified in the TRACE input (number of different heat structures) times the number of axial divisions per assembly. Such an approach assumes no heat exchange between adjacent cells (zero heat flux on the radial boundaries). This assumption is valid if axial heat fluxes can be neglected. To accomplish the cell calculation, boundary conditions from the corresponding heat structure axial level have to be used, viz.

- bulk coolant temperature,

- clad-to-coolant heat exchange coefficient,

- heat generation rate (has to be adjusted according to Eq. 3.4)

The next assumption concerns the cell geometry. The 3D hexagonal cell is approximated in FRED by the cylindrical geometry, in that the element volumes are preserved. With an axial symmetry assumed, the model corresponds to 2D R-Z geometry.

The scheme below (Fig. 3.4) shows the data exchange and the geometry reduction in the coupled TRACE/FRED calculations.
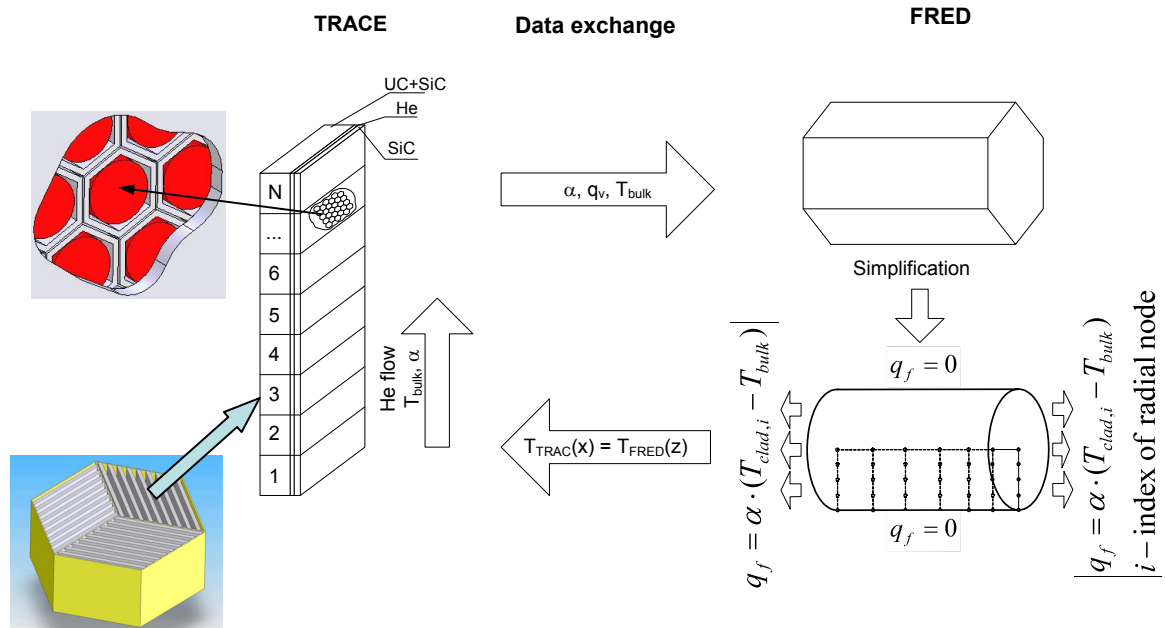
Fig. 3.4. Flowchart of the calculating procedure

The following are the main features of this simple coupling scheme:

- The FRED code is included in the TRACE code as a subroutine, which calculates the temperature field in each simulated fuel cell.

- Core channels and 1D heat structures, simulating representative fuel elements, are specified in the TRACE input deck.

- 2D fuel cells, each representing the corresponding axial level of the TRACE heat structure, are specified in the FRED input deck.

The homogenization of the inner structure for the TRACE simulation is shown schematically in Fig. 3.5. Longitudinal and transversal cell cross-sections are indicated on the left and the homogenized cell on the right, the properties of the inner zone being modified according to Eq. 3.4. These assumptions help to preserve the total mass of the fuel and therefore the potential energy, which are important for the transient analysis.
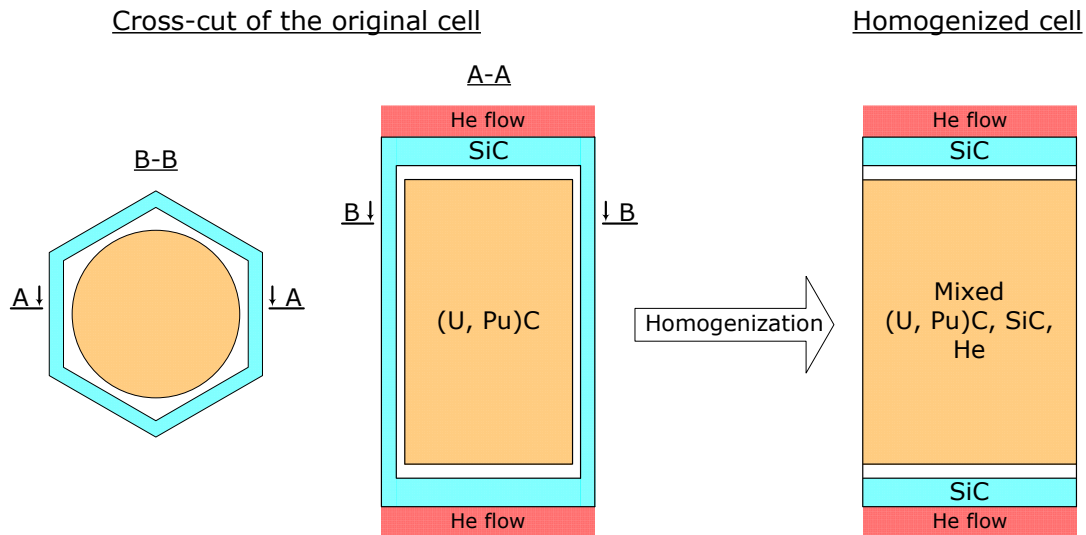
Fig. 3.5. Homogenization procedure for the TRACE calculations of the GFR fuel

Finally, the coupled codes perform the calculation as follows. At each time step, four successive steps are taken (only a point-kinetics option is presented here, but a similar scheme is used when 3D kinetics is simulated with the PARCS code):

- TRACE performs hydraulic and power calculations for the time step Δt, using the distribution of temperature in the cells obtained from the FRED model at the previous time step (the temperature distribution is used by TRACE for reactivity feedback calculations),

- TRACE transfers to FRED a coolant bulk temperature, heat exchange coefficient and power density for each axial level of all the core heat structures,

- FRED calculates the change in the cell material properties and temperatures for the same time step Δt, using the heat generation and heat transfer conditions obtained from TRACE.

- FRED transfers to TRACE the averaged temperature distribution across the cell (the number of nodes across the plate in the TRACE heat structure axial layer should match the number of the corresponding nodes in the FRED cell). Temperatures in the heat structures calculated by TRACE are overwritten by FRED data.

Then, these four steps are repeated for the next time step.

This coupling scheme is a non-iterative, fast running procedure that obtains heat transfer boundary conditions for the FRED cell model from TRACE and returns to

TRACE temperatures in the heat structures calculated in an appropriate manner (see next subsection). The FRED module includes its own internal time integration scheme and has the option to divide the TRACE time-step into sub time-steps if convergence is not obtained.

3.4.3   Temperature transfer from FRED to TRACE

As mentioned earlier, the 2D temperature field calculated by FRED needs to be appropriately correlated with the 1D field needed by TRACE. The data exchange scheme which has chosen for the temperature averaging is shown in Fig. 3.6, the general formula used being:

$$T(z) = \frac{\int_S T(r,z) \cdot r^2 \cdot dr}{\int_S r^2 \cdot dr} \qquad \text{Eq. 3.5}$$
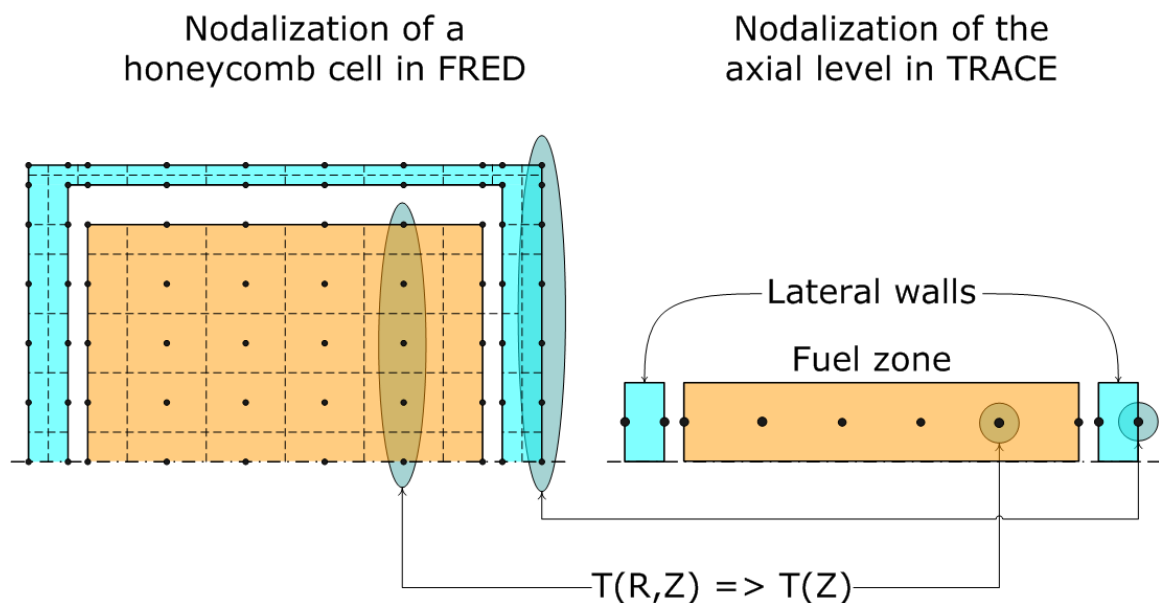
Fig. 3.6. Temperature transfer from FRED to TRACE

The integration area choice is important, since the resulting temperature is used for the point-kinetics calculation. In the fuel zone, the temperature is averaged only over the fuel area, without taking the radial wall and gap into account. This is done to preserve the average fuel temperature which is used for the Doppler-effect

estimation (which is very strong and is one of the most important feedbacks). In the lateral walls zone, the temperature is averaged over the whole area.

3.5 ELABORATION OF THE THERMAL GFR FUEL MODEL ON BASIS OF THE FRED CODE ALGORITHMS

The present chapter describes the first part of the FRED code extension, viz. the temperature field calculation within a honeycomb cell. As shown earlier, a full 3D model of the GFR honeycomb structure, taking into account heat exchange with neighboring cells is quite a complicated task, so that several assumptions have had to be made. The first one is the approximation of the hexagonal cell (3D treatment required) by a 2D cylindrical one, with preservation of materials masses.

3.5.1 Development of the model

As mentioned, the 2D model has not been created from scratch, but is based on available tools, namely the 1D FRED (fuel pin thermal-mechanics) and TRACE (reactor thermal-hydraulics with point kinetics included). Such an approach significantly reduces the development time needed, since solutions are used which have been successfully tried with other types of nuclear fuels and reactors. In the present case, only minor modifications were made to the TRACE code. Most of the development work was in terms of adapting the FRED algorithms for application to the plate-type GFR fuel.

Validation of the new computational routines has been done on the basis of finite element calculations (performed by ANSYS), and these are described in Chapter 4.

Material properties

As described in Section 3.2, an important initial task has been the extension of the material properties database, such as to incorporate new entries specific for the GFR fuel, e.g. (U, Pu)C, SiC and SiC$_f$/SiC. The properties are specified either in tabulated form or as formulas where available. Moreover, the possibility has been provided to add new user-specified materials (from external files).

Geometry reduction

The original thermal module of FRED solves the heat transfer equation in cylindrical coordinates according to the algorithms described in Chapter 2. This is an important reason for choosing cylindrical geometry as basis for the current model. Such an approach can, as mentioned, still approximate the heterogeneous cell structure but

significantly reduces the model complexity and number of degrees of freedom in the model.

In contrast to traditional fuel, the axial heat transfer (along the fuel pellet's rotational-symmetry axis) is the predominant effect in the GFR cell and has to be always taken into account by the FRED model. An adequate geometry transition procedure has to be elaborated in going from the hexagonal cell to the cylindrical. This is illustrated in Fig. 3.7.
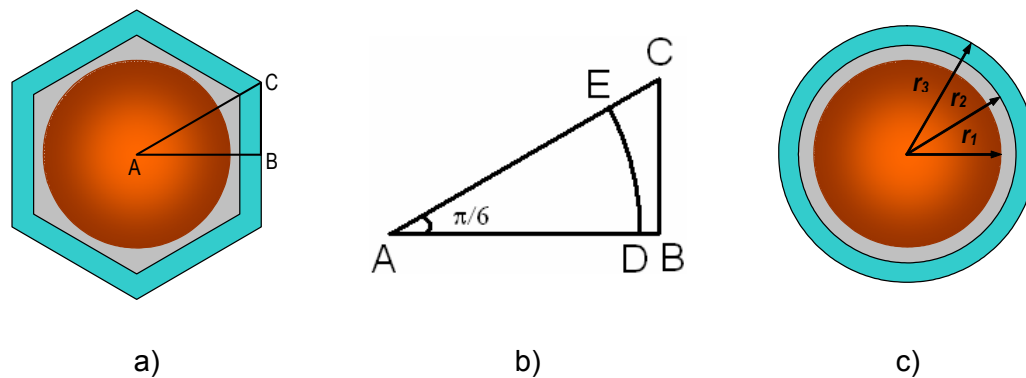

Fig. 3.7. Illustration of the averaging procedure: a) the full cross-section of the hexagonal cell, b) the smallest representative part due to symmetry, c) the equivalent cylindrical cell

Fig. 3.7a shows the original cell cross-cut. The inner circle is the fuel zone, the area between the fuel and the hexagonal wall is filled with gas (helium). Fig. 3.7c shows the result of the geometry reduction, i.e. the cross-cut of the cylindrical cell. The consistency of the two models is achieved by the preservation of the materials volumes.

According to Fig. 3.7b, the following values can be derived through simple trigonometric relations:

$$r_1 = r_{fuel} = AD$$

$$r_2 = r_{clad,inner} = AB \cdot \sqrt{\frac{2\sqrt{3}}{\pi}}$$

$$r_3 = r_{clad,outner} = \left(AB + \delta_{clad}\right) \cdot \sqrt{\frac{2\sqrt{3}}{\pi}}$$

Eq. 3.6

where

r_1, r_2, r_3 :   dimensions of the equivalent cylindrical cell (Fig. 3.7c),

δ_{clad} :   wall thickness of a hexagonal cell.

Fuel-coolant heat exchange

The original FRED model assumes the removal of heat from the radial fuel boundary. The typical calculating geometry and the nodalization scheme are shown in Fig. 3.8a. In contrast to this scheme, the cooling of the GFR cell takes place on the axial boundaries (see Fig. 3.8b), as the pellets are horizontally oriented within a plate. Here, the radial boundary is adiabatic, in accordance with the adopted assumption of no axial heat transfer within a plate.

Thus, the main modifications made in the original code relate to the effective introduction of new cladding layers on the top and on the bottom of the fuel pellet, and to the heat transfer from the top and bottom flat ends. The heat flux from the radial surface is assumed zero.
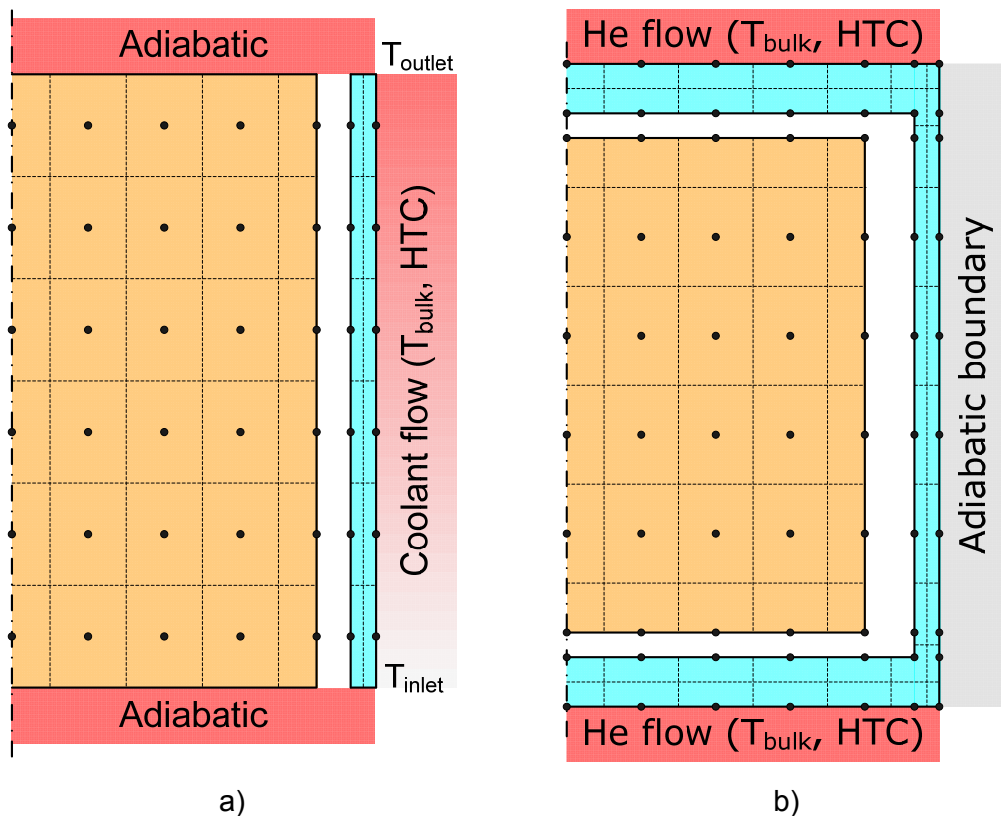
Fig. 3.8. Nodalization scheme for the FRED calculations: a) conventional fuel pin scheme, b) GFR (modified) scheme

The thermal boundary conditions are in terms of bulk coolant temperature, heat transfer coefficient (HTC) and a heat generation rate. As a matter of fact, the heat

sink from the axial boundary is specified by a heat flux, and not by a constant surface temperature. Hence, a radial temperature distribution may be simulated on the flat ends.

The heat generation rate is adjusted according to the same logic as was used to compare 1D and 3D solutions: the powers deposited in the 1D and 3D cells are the same.

The power density distribution within the plate is calculated via the TRACE point kinetics (or the PARCS spatial kinetics) model and sent to FRED at each time step, with the following formula being used to obtain the heat generation rate in a pellet:

$$q_V^{FRED} = q_V^{TRACE} \cdot \frac{r_{clad,outer}^2}{r_{fuel}^2}$$

Eq. 3.7

One of the most significant effects is the heat transfer through the axial gas gaps. The algorithm to calculate this is the same as that for the radial gap (see Section 2.6.2).

Nodalization

The nodalization scheme needs to be adjusted due to the additional material (compared to the original model), above and below the fuel pellet. Moreover, the lateral walls, which close the inner honeycomb structure, need to be modeled. The nodes are distributed in the same manner as in the pellet and the radial wall. For accurate heat transfer analysis, the first and last rows in the fuel and lateral walls are put exactly on the material boundaries.

For better understanding, the corresponding nodalization scheme with the indication of boundary conditions is shown in Fig. 3.8b.

Coupling

The general idea about the flow of information between TRACE and FRED was given in Fig. 3.4. Fig. 3.9 provides more specific details illustrating the coupling of the two codes. As one can see, each axial level in TRACE is separated from the others and is characterized by its geometry, materials and boundary conditions. A unique FRED cell is correlated with a particular heat-structure axial level in TRACE. The corresponding boundary conditions are fed to FRED, and the resulting temperature field overwrites that calculated by TRACE itself.
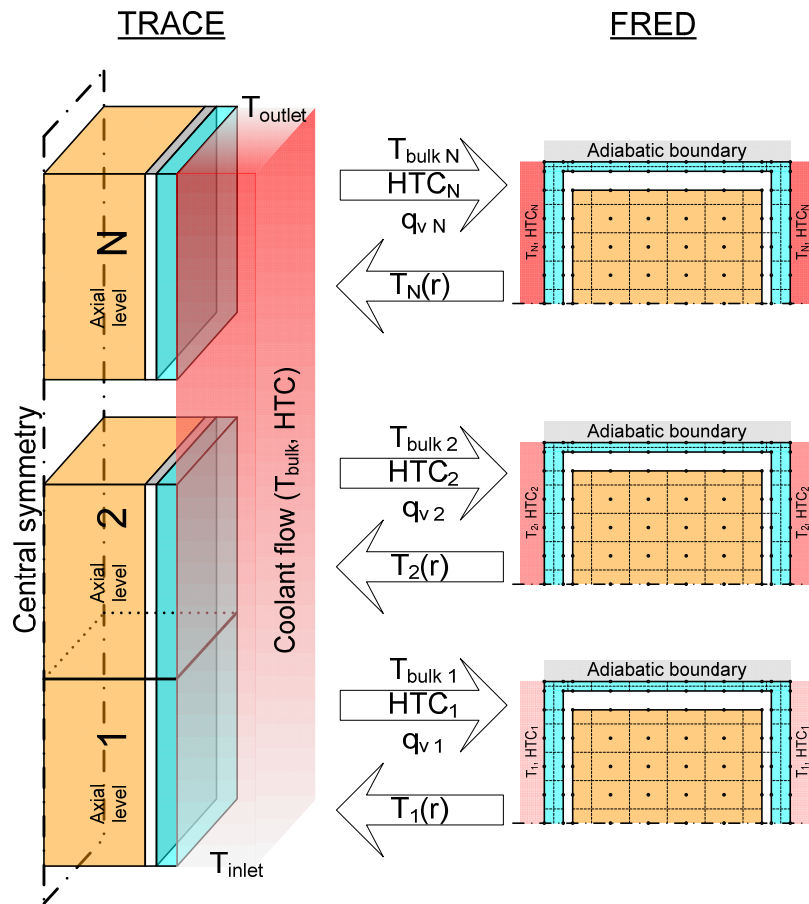
Fig. 3.9. TRACE-FRED coupling

3.5.2 Radial gas gap issues

The gas-gap heat conductance is calculated according to the Ross and Stoute model [20]. In the open-gap regime, it can be rewritten as follows:

$$\alpha_g = \frac{\lambda_g}{\Delta_g + C(\rho_f + \rho_c) + (g_f + g_c)} + \alpha_{rad}$$

Eq. 3.8

where

λ_g :   thermal conductivity coefficient of the gas mixture (W/(m·K)),

Δ_g: fuel-clad gap width (m),

ρ_f, ρ_c: average roughness at the outer fuel and inner cladding surfaces, respectively (m),

C: constant empirical parameter,

g_f, g_c: temperature-jump distance terms at the outer fuel and inner cladding surface, respectively(m),

α_{rad}:   heat conductance due to thermal radiation (W/(m^2·K)).

The temperature drop across the gap is calculated as

$$\Delta T = \frac{q_f}{\alpha_g}$$ **Eq. 3.9**

where q_f is the heat flux, W/m^2.

Thus, the temperature change through the gap is mainly affected by the gap size Δ_g.

Radial contact does not occur over the entire pellet surface, the cylindrical pellet touching the hexagonal wall only at certain points as shown in Fig. 3.10. Thus, the term reflecting the contact conductance can be neglected for radial gap closure.

Points of contact
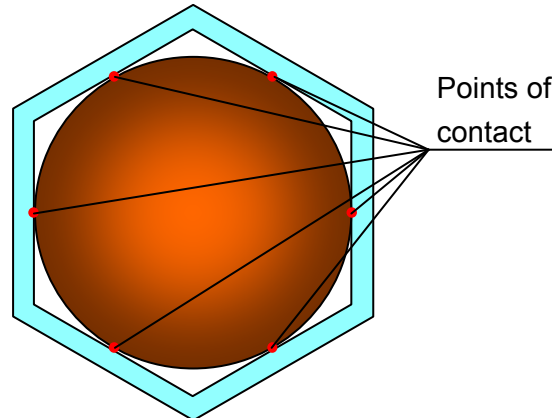
Fig. 3.10. GFR fuel pellet in contact with the hexagonal cell wall

The FRED model operates with the averaged value of the gas gap, which can never be zero (see Fig. 3.10). Hence, the temperature change across the gap is affected by the cell and pellet dimensions (radiation heat transfer) and the average value of the gas gap. The latter is the more significant effect and requires special attention.

There can be two different ways to calculate the average gap value:

- "simple" geometrical averaging, based on the same approach as used in Eq. 3.6:

$$\Delta_g = \frac{1}{\pi/6} \int_0^{\pi/6} \Delta_g(\vartheta) d\vartheta \qquad \text{Eq. 3.10}$$

- "advanced" averaging, with the averaging made in terms of the reciprocal gap width:

$$\left(\frac{1}{\Delta}\right)_{average} = \frac{1}{\pi/6} \int_0^{\pi/6} \frac{d\vartheta}{\Delta_g(\vartheta)} \qquad \text{Eq. 3.11}$$

For "simple" averaging, one could just use the formula

$$\Delta_g = r_2 - r_1 \qquad \text{Eq. 3.12}$$

where r_2 and r_1 are the inner-cell and pellet radii, respectively, as calculated using Eq. 3.6.

The advanced procedure is more complicated. Firstly, one should determine the dependence of the gap thickness on the azimuthal angle. According to Fig. 3.7b, this can be written as:

$$\Delta_g(\vartheta) = \frac{AB}{\cos(\vartheta)} - AD \qquad \text{Eq. 3.13}$$

Then, the following integral should be calculated:

$$\left(\frac{1}{\Delta}\right)_{eff} = \frac{1}{\pi/6} \int_0^{\pi/6} \frac{d\vartheta}{\Delta_g(\vartheta)} = \frac{1}{\pi/6} \int_0^{\pi/6} \frac{d\vartheta}{\dfrac{AB}{\cos(\vartheta)} - AD} \qquad \text{Eq. 3.14}$$

The effective gap width in terms of the cylindrical cell dimensions, using Eq. 3.6, can be expressed as:

$$\left(\frac{1}{\Delta}\right)_{eff} = \frac{1}{\pi/6} \int_0^{\pi/6} \frac{d\vartheta}{\dfrac{r_2\sqrt{\pi}}{\sqrt{2\sqrt{3}\cdot\cos(\vartheta)}} - r_1} \qquad \text{Eq. 3.15}$$

The integral can be evaluated as follows:

$$\Delta_{eff} = \left\{ \frac{1}{\pi/6} \cdot \left[f\left(\frac{\pi}{6}\right) - f(0) \right] \right\}^{-1}$$

<div align="right">**Eq. 3.16**</div>

where

$$f(\vartheta) = \frac{2 \cdot \left(r_2 \sqrt{2\pi\sqrt{3^3}} \cdot \arctan\left(\frac{\left(r_2 \sqrt{2\pi\sqrt{3^3}} + 6r_1 \right) \cdot \tan\left(\frac{\vartheta}{2}\right)}{\sqrt{6r_2^2 \pi\sqrt{3} - 6r_1^2}} \right) \right) - \tan\left(\frac{\vartheta}{2}\right) \cdot \sqrt{6r_2^2 \pi\sqrt{3} - 6r_1^2}}{\sqrt{6r_2^2 \pi\sqrt{3} - 6r_1^2}}$$

It should be mentioned that the average gap width as calculated above is not used to derive the equivalent FRED cell geometry, but only to calculate heat transfer across the radial gap. The Δ_g value effectively appears only in the Ross-Stoute formula, and nowhere else.

Both "simple" and "advanced" averaging approaches have been applied, in order to assess the influence of the averaging procedure and to define the variant which gives better correspondence with the original 3D geometry (see Chapter 4).

3.6 ELABORATION OF THE MECHANICAL GFR FUEL MODEL ON BASIS OF THE FRED CODE ALGORITHMS

This section describes the extension of the FRED mechanical module for the honeycomb-cell analysis to simulate the fuel deformation arising from multiple effects. This thus represents completion of the work undertaken to develop the new coupled thermo-mechanical procedure for analyzing plate-type GFR fuel. The important incentives for implementing this procedure within the FAST code system are being able to model:

-   evolution of the fuel-matrix gas gaps, which has the major influence on the temperature field; its accurate evaluation is important for the Doppler-effect calculation, one of the main GFR feedbacks [18, 19],

-   core axial expansion, based on the calculated cladding deformations and used for the corresponding feedback estimation.

3.6.1 Development of the model

The mechanical analysis is coupled with the thermal one. The nodalization schemes for both are the same (see Fig. 3.11), so that no interpolation is needed in transferring the temperature field for its use as load for the mechanical analysis. The basic principles of the mechanical analysis described in Subsection 2.6.3 are not changed. Thus, the 1.5D approach is still used, but with certain specific features introduced to account for the GFR fuel peculiarities. These are mainly:

- no gas plenum; the inner gas pressure is unique for each cell and depends on the free volume, inner gas temperature distribution and fission gas release,

- gap closure occurs on the axial flat end of the pellet, radial gap closure is unlikely and has to be excluded by design.

The radial independence of axial deformation is preserved, i.e. axial contact occurs over the whole surface.

R_{fo} – outer fuel radius
R_{ci} – inner cell radius
R_{co} – outer cell radius
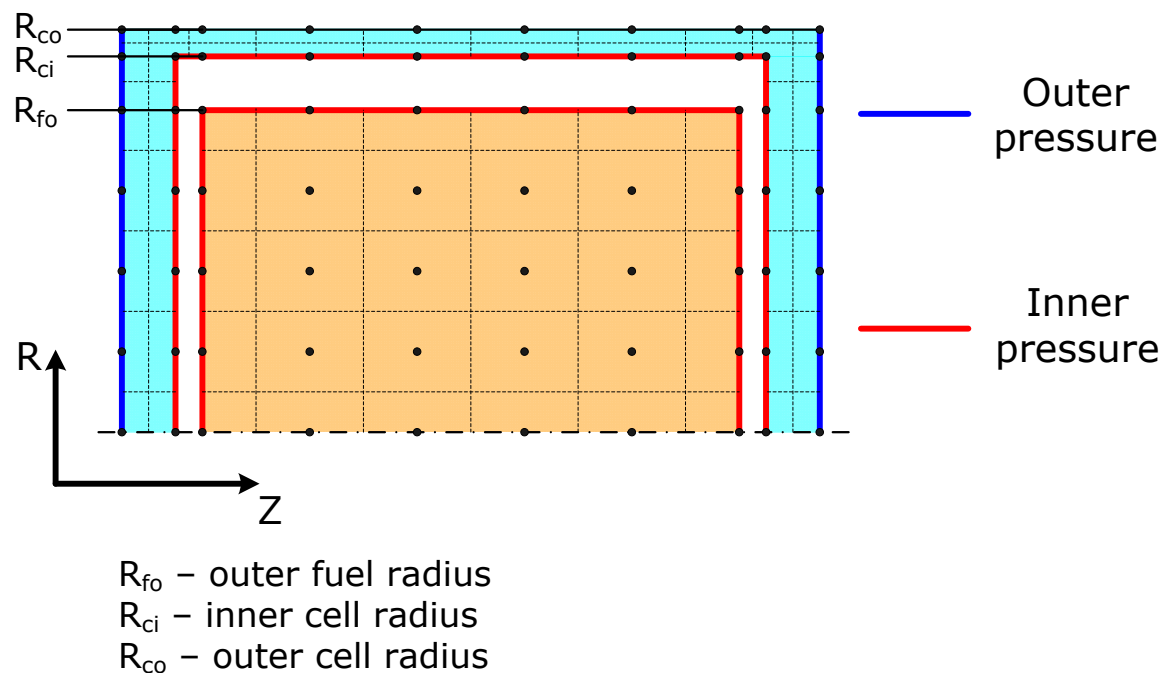
Fig. 3.11. Nodalization, coordinate system and the loading in the mechanical problem

Major modifications have been done for the boundary conditions, especially after axial contact occurrence. The application of the boundary conditions and the notation of the radii used in the formulas below are shown in Fig. 3.11.

The following boundary conditions are applied in open-gap regime

$$\int_{0}^{R_{fo}} \sigma_z(r,z) \cdot 2r \cdot dr = P_i \cdot R_{fo}^2 \qquad \text{Eq. 3.17}$$

$$\int_{R_{ci}}^{R_{co}} \sigma_z(r,z) \cdot 2r \cdot dr = P_o \cdot R_{co}^2 - P_i \cdot R_{ci}^2 \qquad \text{Eq. 3.18}$$

$$\sigma_r(R_{fo},z) = \sigma_r(R_{ci},z) = -P_i \qquad \text{Eq. 3.19}$$

$$\left. \frac{\partial \sigma_r(r,z)}{\partial r} \right|_{r=0} = 0 \qquad \text{Eq. 3.20}$$

$$\left. \frac{\partial \sigma_r(r,z)}{\partial r} \right|_{r=R_{co}} = 0 \qquad \text{Eq. 3.21}$$

According to Eq. 2.35 (stress equilibrium equations) the last two equations are equivalent to

$$\sigma_r(R_{co},z) = \sigma_\theta(R_{co},z) \qquad \text{Eq. 3.22}$$

$$\sigma_r(0,z) = \sigma_\theta(0,z) \qquad \text{Eq. 3.23}$$

In Eqs. 3.17 - 3.19,

P_i: inner gas pressure,

P_o: outer pressure (coolant pressure).

The outer pressure is passed over to FRED from the TRACE calculations, and the inner is calculated at each time step for each specified cell with account being taken of the temperatures, cell and fuel deformations and the fission gas release (if the burnup option is switched on; see the next section).

The value of the axial and radial gas gaps are recalculated at each time step.

As soon as the axial gap closes, the boundary conditions are changed as described below. The precise treatment of contact is impossible due to the inherent limitations of the 1.5D procedure. The equations contain no information about the influence of axial levels on each other. Thus, axial expansion of the fuel can be correlated only with the axial level of the radial wall. This is done as shown in Fig. 3.12. After the gap closure, the rate of the axial expansions of fuel and wall are identical, so that the difference between their axial deformations stays constant with time.
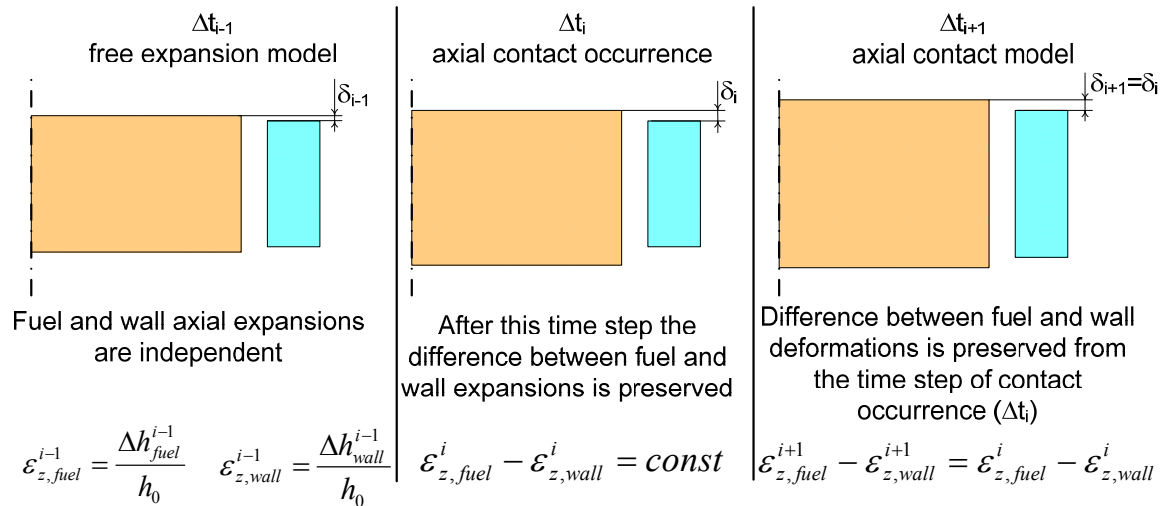
Δt_{i-1} free expansion model	Δt_i axial contact occurrence	Δt_{i+1} axial contact model
Fuel and wall axial expansions are independent	After this time step the difference between fuel and wall expansions is preserved	Difference between fuel and wall deformations is preserved from the time step of contact occurrence (Δt_i)
$\varepsilon^{i-1}_{z,fuel} = \dfrac{\Delta h^{i-1}_{fuel}}{h_0} \quad \varepsilon^{i-1}_{z,wall} = \dfrac{\Delta h^{i-1}_{wall}}{h_0}$	$\varepsilon^{i}_{z,fuel} - \varepsilon^{i}_{z,wall} = const$	$\varepsilon^{i+1}_{z,fuel} - \varepsilon^{i+1}_{z,wall} = \varepsilon^{i}_{z,fuel} - \varepsilon^{i}_{z,wall}$

Fig. 3.12. Axial expansion models

The contact pressure is calculated as the average axial stress on the contacting fuel surface:

$$\sigma_{contact} = \frac{\displaystyle\int_{o}^{R_{fo}} \sigma_z(r) \cdot r \cdot dr}{\displaystyle\int_{o}^{R_{fo}} r \cdot dr} \qquad \textbf{Eq. 3.24}$$

When this pressure goes below the inner gas pressure, the "axial contact model" is switched to the "free expansion model" which means that the gas gap is reopened.

3.7   BASE-IRRADIATION CALCULATION

Base-irradiation analysis is a thermo-mechanical fuel analysis as a function of burnup. The phenomena, which need to be taken into account during a base-irradiation calculation, are:

-   changes of the fuel and cladding volumes under neutron irradiation (swelling, densification, creeping, cracking, etc.),

-   generation and release of fission gases: this leads to degradation of the fuel and the gas-gap thermal conductivity. Moreover, the fission gas release (FGR) rate depends on the fuel temperature and burnup, as the fuel structure may change and cracking can occur,

100

- changes of the fuel and cladding thermal and mechanical properties with irradiation,

- fuel-cladding mechanical interaction, if any.

The fuel behavior also depends on the power history during base irradiation.

The FRED model accounts for a number of the above phenomena: correlations for swelling and FGR, as well as the burnup dependence of the material properties (when the data are available), are embedded into the material properties database.

The power history is provided by the neutronics/thermal-hydraulics code. The burnup is calculated for each axial level of the fuel, based on its heat generation rate and the operation time, as follows:

$$BU_{i+1} = BU_i + \frac{q_V \cdot \Delta t_i}{\rho_{fuel}}$$ **Eq. 3.25**

where

BU_i: burnup the beginning of time-step i,

BU_{i+1}:   burnup at the end of time-step i,

q_V: heat generation rate,

Δt_i: length of the time-step i,

ρ_{fuel}:   fuel density.

Correlations for swelling and fission gas release of UC and (U, Pu)C [6] have been integrated into the extended FRED material properties database (see Appendix A).

It is seen that the accounting for burnup effects on materials characteristics is inherent to FRED and, as such, no modifications have been necessary to the code itself. The base-irradiation calculations provide initial conditions for the transient analysis in terms of irradiated fuel geometry, material properties, gap conductance, inner gas pressure, possible pellet-cladding mechanical interaction, etc. It is very important that, for consistent base-irradiation analysis, a single calculational tool, with the same basic models and database, is used for both steady-state and transient conditions.

During the coupled TRACE/FRED execution, however, it was found that the smallest time steps generated by TRACE are ~ 1min. The time scale of the base-irradiation analysis, on the other hand, is several years (fuel residence time in the core). Since

analysis with such small time-steps would be unacceptably time consuming, the coupling scheme was modified to enable coupled base-irradiation analysis to be performed. The flowchart developed is shown in Fig. 3.13.

As can be seen from the figure, once TRACE has calculated steady-state thermal-hydraulic conditions, control is passed over to a special module which generates sufficiently large time steps while preserving the steady-state boundary conditions. In the input file, the user specifies t_{ss} as the time at which one switches over to the standalone FRED calculation, i.e. when the current time $t_{current}$ is greater than this value, TRACE execution is bypassed and the calculation is done by FRED only.

The described scheme is applicable when the reactor power remains constant. This assumption is quite adequate for the present stage of conceptual design studies.

An example of a base-irradiation calculation for the GFR fuel will be given in Chapter 4. The initial conditions for end-of-cycle transients, discussed in Chapter 5, have also been calculated by FRED using the described scheme.

TRACE

Δt_{TRACE}, T_{bulk}, q_v, α

Check for time:
$t_{current} < t_{ss}$

Next Time step

YES   NO

FRED
Δt_{TRACE}, T_{bulk}, q_v, α

TRACE calculated temperature field is overwritten by the FRED code results

Δt_{TRACE} – time step generated by TRACE

t_{ss} – specified time to start the base irradiation calculation

$t_{current}$ – current time

$t_{base-irr}$ – specified time for end of analysis

Control is passed over to the new burnup module

$\Delta t = 1$ day, T_{bulk}, q_v, α are taken from the last time step

FRED   YES

$t_{current} < t_{base-irr}$

NO

STOP

Normal operation of the coupled TRACE/FRED codes

Burnup calculation

Fig. 3.13. Flow-chart of the burnup analysis procedure

102

3.8   SUMMARY

This chapter describes the development of the coupled thermo-mechanical procedure for plate-type GFR fuel analysis.

To reduce the overall effort needed, an approach analogous to that used in the FRED code for traditional fuel has been adopted. The algorithms were modified to account for the high degree of heterogeneity characteristic of the plate-type fuel layout. The FRED code input data contains all the information needed to adequately describe the inner structure of the fuel, while TRACE is used to analyze the system's thermal-hydraulics and to provide the boundary conditions for the thermo-mechanical calculations. An improved estimation of the temperature field can thus be achieved.

The thermo-mechanical analysis can also be done as a function of burnup. The developed model includes the consideration of the burnup dependence of materials properties, as well as of important phenomena such as fuel swelling and fission gas release. It should be mentioned that certain data are still missing in the latter context (see Appendix A), but these could of course be easily embedded into the currently extended FRED materials database when available.

As mentioned, the FRED code runs independently and only needs the continuous feed of boundary conditions from TRACE or similar codes. It has a separate input file to describe the fuel and honeycomb geometry, the number of cells to be calculated, options for thermo-mechanical and burnup calculations, etc. More details on the input file structure are given in Appendix B.

REFERENCES

1. P. Martin, N. Chauvin, J.C. Garnier, M. Masson, P. Brossard, P. Anzieu, "Gas Cooled Fast Reactor System: Major Objectives and Options for Reactor, Fuel and Fuel Cycle", Proceedings of GLOBAL 2005, Paper No. IL002, Tsukuba, Japan, Oct 9-13, 2005

2. J.C. Garnier, C. Bassi, M. Blanc, J.C. Bosq, N. Chauvin, P. Dumaz, J.Y. Malo, B. Mathieu, A. Messié, L. Nicolas, A. Ravenet, "Contribution to GFR design option selection", Proceedings of ICAPP '06, Paper 6147, Reno, NV USA, June 4-8, 2006.

3. N. Chauvin, J.Y. Malo, J.C. Garnier, F. Bertrand, J.C. Bosq, A. Ravenet, D. Lorenzo, M. Pelletier, J.M. Escleine, I. Munoz, J.M. Bonnerot, "GFR Fuel And Core Pre-Conceptual Design Studies", Proceedings of GLOBAL 2007, Boise, Idaho, USA, Sept. 9-13, 2007.

4. J.C. Bosq, Y. Peneliau, G. Rimpault, M. Vanier, "Fine 3D neutronic characterization of a gas-cooled fast reactor based on plate-type subassemblies", PHYSOR-2006, Vancouver, BC, Canada, September 10-14, 2006

5. P. Dumaz, P. Allegre, C. Bassi, T. Cadiou, A. Conti, J.C. Garnier, J.Y. Malo, A. Tosello, "Gas-cooled fast reactors—Status of CEA preliminary design studies", Nuclear Engineering and Design 237 (2007) 1618–1627, 2007

6. T. Preusser. "Modelling of carbide fuel rods". Nucl. Technology, 57 (1982), 343-371 and T. Preusser. Dissertation, KfK-Bericht 3426 (1982).

7. Y.S. Touloukian et al. Thermophysical properties of matter (Volumes 2, 5, 13). IFI/PLENUM - New York-Washington, 1977.

8. P. Werner, H. Blank. "Mechanical properties of advanced fuels under compressive deformation". Nucl. Technol., 52 (1981), 73-85.

9. T.L. George, K. Peddicord. "SPECKLE-III. A computer code for calculating the thermal-mechanical behaviour of sphere-pac fuel pins". OSU-EIR-64, Oregon State University – Eidg. Inst. für Reaktorforschung, (1982)

10. A. Padel, Ch. de Novion. "Constantes élastiques des carbures, nitrures et oxides d'uranium et de plutonium". J. Nucl. Mater., 33 (1969), 40-51

11. A Technology Roadmap for Generation IV Nuclear Energy Systems: Technical Roadmap Report, December, 2002

12. M. Ferraris, M. Salvo, V. Casalegno, A. Ciampichetti, F. Smeacetto, M. Zucchetti, "Joining of machined SiC/SiC composites for thermonuclear fusion reactors", Journal of Nuclear Materials (2008), doi: 10.1016/j.jnucmat.2008.02.020

13. T. Shimoo, H. Takeuchi, K. Okamura, "Thermal Stability of Polycarbosilane-Derived Silicon Carbide Fibers under Reduced Pressures", J. Am. Ceram. Soc., 84, 3, 566–70 (2001).

14. R.H. Jones et al., "Recent advances in the development of SiC/SiC as a fusion structural material", Fusion Engineering and Design, 41, 15–24 (1998).

15. Proceedings of IEEE,Vol 70,No.5,May 1982, p.421.

16. M.K. Meyer, N. Chauvin, Overview of gas fast reactor inert matrix fuel candidates. Global 2003, New Orleans, LA, November 16–20, 2003.

17. A. Nosek, J. Conzen, H. Doescher, C. Martin, J. Blanchard, "Thermomechanics of Candidate Coatings for Advanced Gas Reactor Fuels", Journal of Nuclear Materials 371 (2007) 288–303, 2007

18. S.Pelloni, E. Bubelis, K. Mikityuk, P. Coddington, "Calculations of Reactivity-initiated Transients in Gas-cooled Fast Reactors Using the Code System FAST", Annals of Nuclear Energy, Volume 33, Issue 6, Pages 499-509, April 2006

19. H. Choi, G. Rimpault, and J.C. Bosq, "A Physics Study of a 600-MW(thermal) Gas-Cooled Fast Reactor", Nuclear Science and Engineering, 152, 204–218 (2006)

20. A.M. Ross and R.L. Stoute, "Heat Transfer Coefficient between UO_2 and Zircaloy-2", AECL-1552, 1962.

4 BENCHMARKING OF THE 2D FRED MODEL AND SUPPLEMENTARY 3D INVESTIGATIONS

This chapter describes use of the general-purpose finite element analysis code ANSYS (see Section 2.7) for benchmarking the currently developed algorithms for plate-type GFR fuel.

In Section 4.1, the benchmarking of the thermal part of the thermo-mechanical modeling is presented, while that for the mechanical part is presented in Section 4.2. Section 4.3 describes a series of supplementary studies, which have been carried out for the GFR fuel using the 3D modeling capability provided by ANSYS. Finally, Section 4.4 gives a short summary of the present chapter.

4.1 BENCHMARKING OF THE THERMAL MODEL

As mentioned earlier, the lack of experimental data for plate-type GFR fuel has necessitated that benchmarking of the 2D thermo-mechanical model, presented in the previous chapter, be carried out against detailed 3D finite-element modeling using the ANSYS code [1]. A detailed description of the 3D ANSYS model and the calculating methodology used to benchmark the thermal model is given in Appendix C.

For benchmarking the thermal model, the 2D/3D comparisons have been done for temperature distributions along arbitrarily chosen positions within a unit cell. The boundary conditions and the heat generation rate were identical in the two cases, both models assuming that the pellet is concentric with the hexagonal cell walls. For a 2D geometry, this results in independence of the temperature on the angular position. A 3D calculation domain can be reduced to a 30° half-height sector (Fig. 4.1), with adiabatic conditions on all surfaces except that in contact with coolant. As the fuel is cylindrical and the radial wall is hexagonal, the gas gap has angular dependence. This is minimal at 0°, and maximal at 30° (see Fig. 3.7b). The temperature variations along these directions would be slightly different, so that the 3D modeling results are represented by two curves, one of which corresponds to the minimal radial gap (0° direction) and the other to the maximal (30° direction).

As mentioned, the comparison of the temperature field is done for several positions within the cell. These are shown in Fig. 4.1 as blue lines. Path 1 refers to the line coincident with the pellet rotational axis. Path 2 refers to the radial pellet boundary. Path 3 is the inner surface of the hexagonal cell wall. The temperature change across the hexagonal wall is very small due to the high SiC thermal conductivity and

small thickness of the wall. For this reason, the temperature variation along the outer cell surface has not been considered.
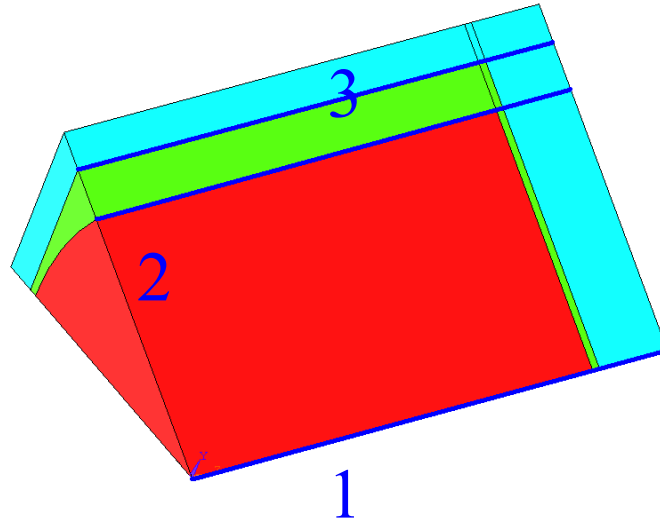
Fig. 4.1. 3D calculating domain and the paths along which the temperature distributions have been compared

The figures below (Fig. 4.2 - Fig. 4.4) show the temperature distributions along the different paths. As described in Chapter 3, there are two different approaches to model the heat transfer across the radial gas gap. These imply different gap averaging techniques: "simple" and "advanced" according to the used terminology. The a) variants of the plots show the results obtained with the "simple" averaging technique. The b) variants are the results of "advanced" averaging.

a)   b)
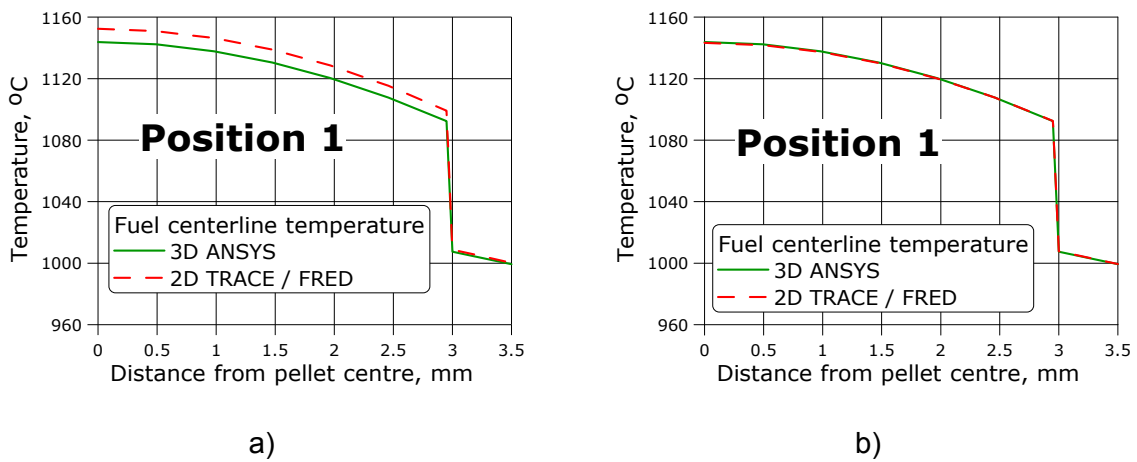
Fig. 4.2. Temperature field along path 1 for a) "simple" and b) "advanced" radial gap averaging procedures
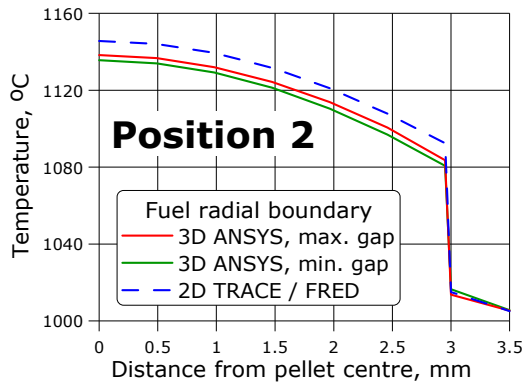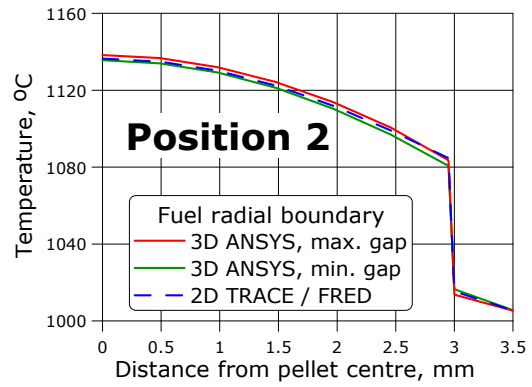
Fig. 4.3 Temperature field along path 2 for a) "simple" an b) "advanced" radial gap averaging procedures
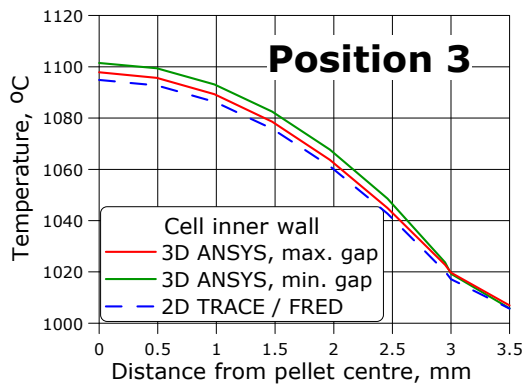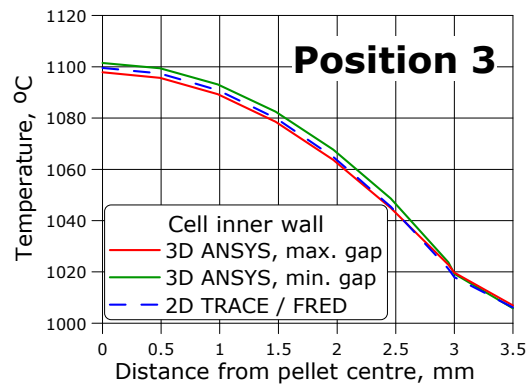
Fig. 4.4. Temperature field along path 3 for a) "simple" and b) "advanced" radial gap averaging procedures

As seen in Fig. 4.2 - Fig. 4.4, the "advanced" gap averaging technique leads to better agreement of the simplified model results with the reference solution. For this reason, it has been chosen as the basic option to calculate the radial gap heat transfer. It can also be concluded, from the figures, that the 2D FRED model indeed provides an accurate solution for the temperature field. This is important in the view of the recent trend to use "best estimate" calculations for safety assessment, instead of adopting a conservative approach as in the past.

4.2   BENCHMARKING OF THE MECHANICAL MODEL

As done in the case of the thermal model benchmarking, results obtained using the 2D mechanical model have been benchmarked against a series of calculations performed using ANSYS. The 2D/3D comparisons have been made for pellet deformations and stresses in both open and closed gap regimes. As mentioned earlier, accurate calculations of the material displacements are especially important for GFR safety analysis, because of the core axial expansion reactivity effect.

The geometry of the hexagonal GFR cell, used as reference for the benchmarking comparisons, corresponds to the reference design dimensions [2, 4, 5, 6] provided in Table 3.1. The ANSYS model employed is shown in Fig. 4.5, a more detailed description being given in Appendix C. This is effectively, in volumetric terms, a 1/24 representation of the whole cell (30° sector of ½ cell height), with symmetry boundary conditions applied as necessary. The red lines in Fig. 4.5a show the shape of the outer and inner boundaries of the cell walls (hexagons), as also of a fuel pellet (circle).

(a)   (b)
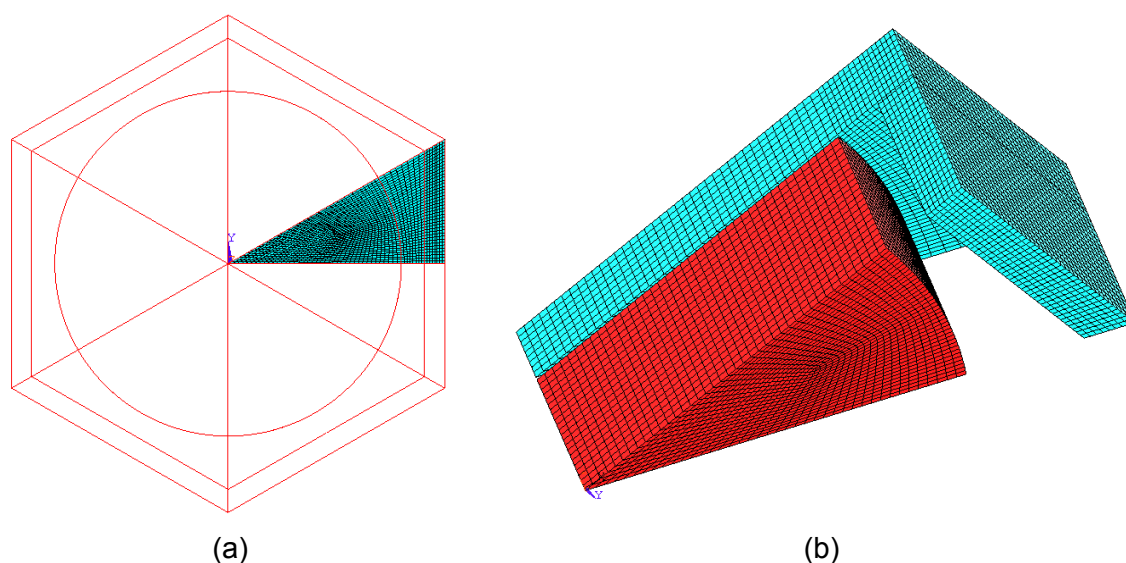
Fig. 4.5. Geometry of the reference cell used for benchmarking: (a) view from above, (b) isometric view

As the FRED model contains a number of strong assumptions, the benchmarking has been considered in two stages. First, simplifying assumptions were introduced into the ANSYS model to make it more directly comparable with the FRED model, thus aiming to validate the developed algorithm itself.

The corresponding simplifications are principally:

110

- zero friction coefficient between fuel and axial wall during contact,

- axial cladding wall (exposed to coolant) remains flat during deformation.

For the next stage, the simplifying assumptions were removed, so that ANSYS could model the fuel behavior as realistically as possible. This allowed one to have an in-depth understanding of the effects which are not taken into account in the developed FRED model, and thereby to identify its applicability limits.

The total deformation is comprised of the thermal expansion and the deformations from the gas pressure and pellet-matrix interaction (in the closed gap regime). The predicted temperature field has a significant influence on the results. The FRED and ANSYS models pre-calculate the temperature distribution in the cell independently [6], and then impose this as a body load for the mechanical analysis. The thermal boundary conditions, which have been used for the GFR cell in the comparisons, are as follows:

- heat generation rate in the fuel pellet: 400 MW/m^3,

- clad-coolant heat exchange coefficient: 6624 W/m^2·K,

- bulk coolant temperature: 1074 K

The plots below show, for both open and closed gap regimes, the increase in the fuel pellet height, the fuel radius and the plate thickness (referred to as cell height). For the sake of simplicity, the axial gap closure was forced by increasing the thermal expansion coefficient to simulate the additional deformation due to fuel swelling. The more detailed ANSYS analysis of the fuel pellet axial deformation shows that, for a given axial level, this has a radial dependence. This is one of the major differences with respect to the present FRED model, where axial deformation is considered to be radially independent.

Fig. 4.6a compares the simplified-ANSYS and FRED results for the axial pellet deformation as a function of radius, while Fig. 4.6b gives the changes in pellet radius for different axial levels. As one can see, the correspondence between the two sets of results is quite good in each case. This means that geometry change is well predicted by the 2D FRED model. The discrepancy of about 2 μm obtained for the pellet and cell heights can be explained by the small differences between the temperature fields predicted by the models, as also by the relatively large differences in the computational-mesh discretization (the mesh used in FRED is much coarser).
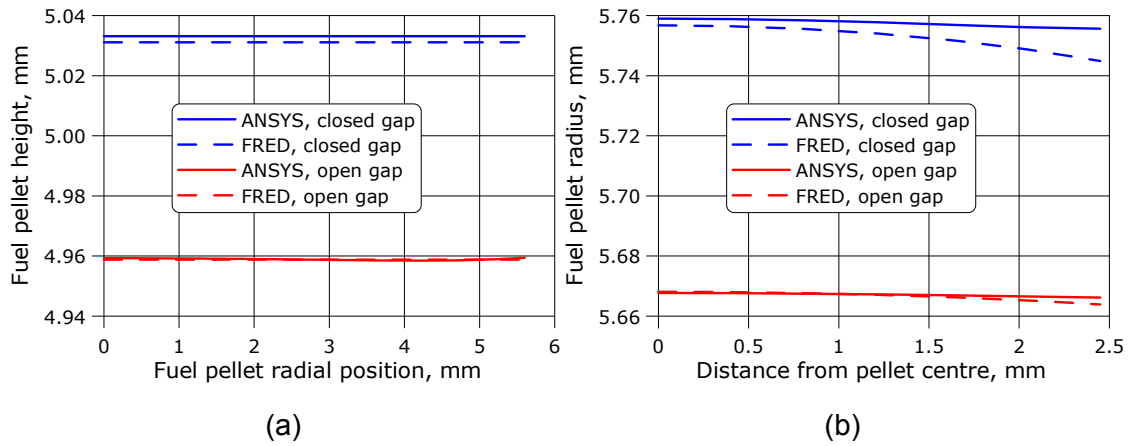
Fig. 4.6. (a) Fuel pellet elongation and (b) radial deformation, calculated by FRED and ANSYS for open and closed gap regimes

The radial variations of the cell height (plate thickness) and axial gas gap are shown in Fig. 4.7a and Fig. 4.7b, respectively.
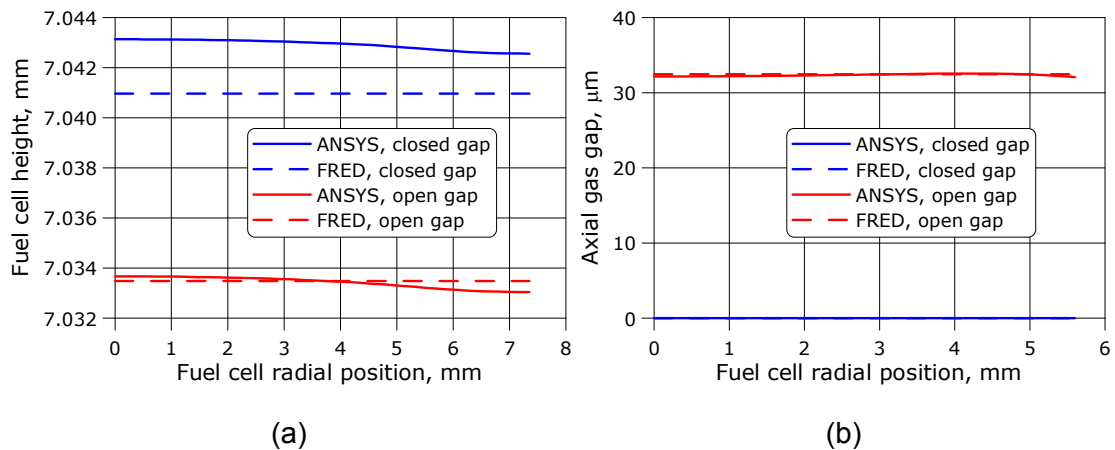

Fig. 4.7. (a) Cell height (b) axial gas gap, calculated by FRED and ANSYS for open and closed gap regimes

The FRED and ANSYS results for the axial stress distribution in the fuel pellet are compared in Fig. 4.8 (stresses are presented here for the pellet half-height plane), as also in Table 4.1. As can be seen, the 3D model predicts quite a strong dependence on the radial position, while the FRED results are significantly flatter. This can be explained by the usage of a 1.5D approach in FRED, which implies that there is no interference between axial levels. Nevertheless, it is relevant to compare the radially averaged stress values:

112

$$\overline{\sigma}_z = \frac{\int\limits_o^{R_{fuel}} \sigma_z(r) \cdot r \cdot dr}{\int\limits_o^{R_{fuel}} r \cdot dr}$$

The results are listed in Table 4.1. A good agreement is seen to be obtained for the open gap regime, while there is a discrepancy of about 20% for the closed gap. This is acceptable, considering the large difference in computational time needed by the two sets of calculations.
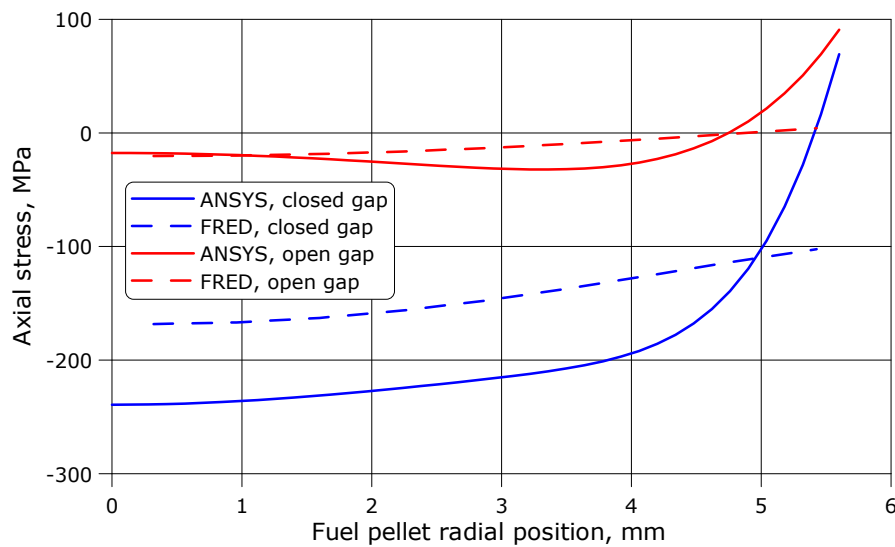
Fig. 4.8. Axial stress distribution

Table 4.1. Comparison of deformed cell parameters

	Open gap		Closed gap	
	ANSYS	FRED	ANSYS	FRED
Fuel outer across flat, mm	14.068	14.067	14.068	14.062
Average axial gap, μm	32	32	0.0	0.0
Average fuel pellet height, mm	4.959	4.959	5.033	5.031
Average fuel cell height, mm	7.033	7.034	7.043	7.041
Average axial stress, MPa	6.47	6.46	161.6	129.4

4.3 3D INVESTIGATIONS OF THE GFR FUEL THERMO-MECHANICAL BEHAVIOR

As shown above, the developed thermo-mechanical FRED model provides a prediction accuracy which is quite comparable to that of the more detailed 3D finite-elements model. In conjunction with its much lower CPU running time, it is thus very attractive for coupled use with TRACE [7] or other system codes. The simplicity of coupling is provided by the fact that all the subroutines are completely independent of the thermal-hydraulic code used, and the only development needed for the coupling is the data exchange between the two codes.

However, the FRED model uses a number of strong assumptions, the most important being:

- 2D geometry,

- radial independence of the axial deformation.

The first approximation could lead to a loss of certain information about the heat transfer. The second one means that the axial fuel-matrix contact appears on the whole pellet surface and the resulting stress distribution is relatively flat which is not the case in reality.

Several detailed analyses have been carried out with the 3D ANSYS model, without making the simplifying assumptions inherent in the FRED modeling. (As previously, the contact closure was forced by increasing the fuel thermal expansion coefficient.) The conducted studies aim at providing an in-depth understanding of the thermo-mechanical behavior of the fuel, pertain to deformation and heat transfer phenomena (Sections 4.3.1 and 4.3.2, respectively). Based on the findings, recommendations are made for simplified 1D modeling of the GFR fuel in Section 4.3.3, while a pellet-size optimization study is presented in Section 4.3.4.

4.3.1 Deformation of the cell and fuel pellet shape optimization

The temperature field within the deformed cell, calculated using the 3D finite-elements method, is shown in Fig. 4.9 (the axial gap is closed).
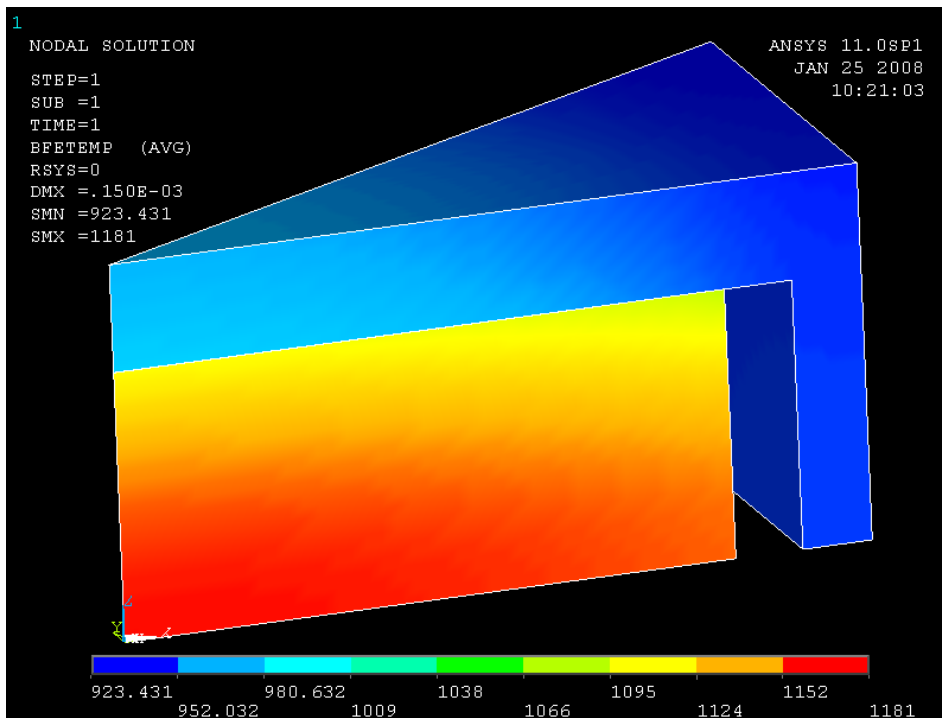
Fig. 4.9. The deformed cell (closed gap regime), with the color scale for showing the temperature distribution

Results for the deformation, in both open and closed gap regimes, are presented in Fig. 4.10(a) for the pellet, and in Fig. 4.10(b) for the cladding (matrix). Fig. 4.11 shows the distance from the pellet centre to the pellet surface and to the lateral wall inner surface, the parts (a) and (b) of the figure corresponding to the open and closed gap regimes, respectively.

As can be seen from the results obtained, the 3D analysis of the GFR fuel reveals a strong radial dependence of the axial deformation. This refers both to fuel and matrix, especially the lateral walls (see Fig. 4.10). An important observation is the local increase of the fuel height at the periphery. This effect forces the gap closure over a relatively narrow zone near the pellet radial boundary (Fig. 4.10, Fig. 4.11b).

Fuel pellet, open gap

Matrix, open gap

Fuel pellet, closed gap

Matrix, closed gap

a)   b)
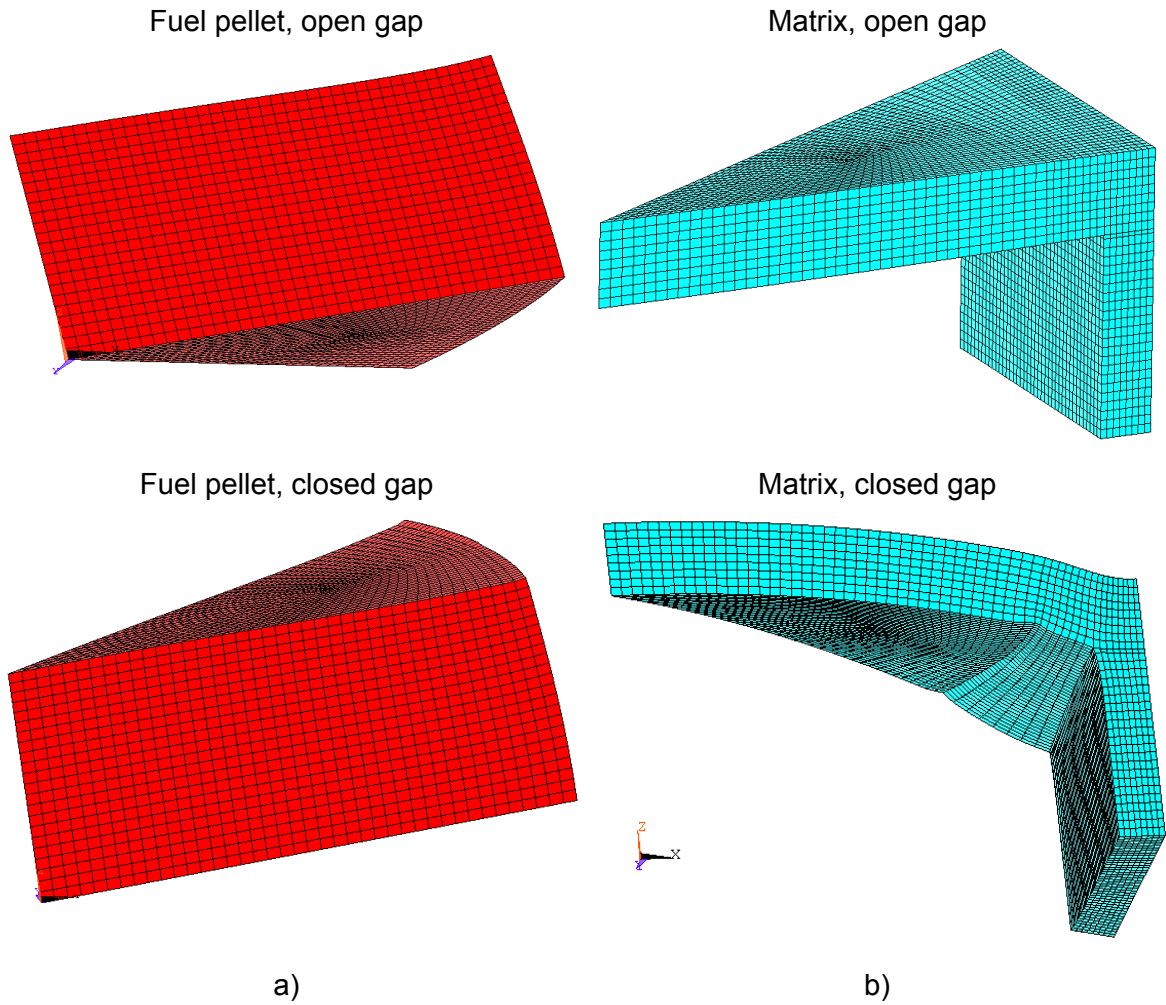
Fig. 4.10. Detailed 3D FE-analysis results obtained with ANSYS for deformation of (a) the pellet and (b) the cladding (matrix), in both open and closed gap regimes. For clarity, the deformations have been increased optically by several orders.

a)   b)
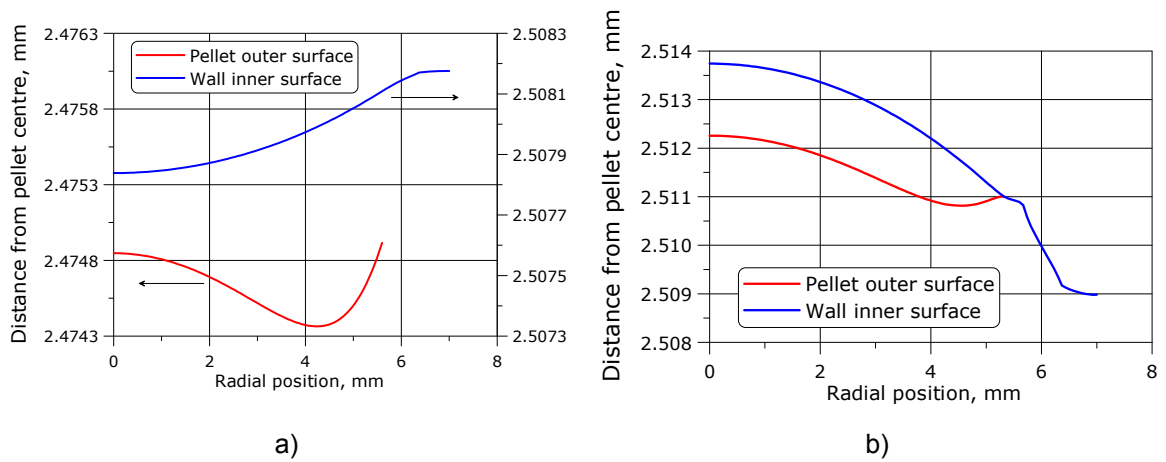
Fig. 4.11. Distance from pellet centre to the pellet surface, and to the lateral wall inner surface, in (a) open gap and (b) closed gap regimes

It needs to be borne in mind that the main purpose of the currently developed 2D FRED model is to provide reliable data for the calculation of the neutronic feedbacks, i.e. fuel temperature for the Doppler effect and fuel plate deformation for the axial core expansion effect. As stated in [8], the axial core expansion is driven by the deformation of the SiC matrix (in open gap regime), rather than that of the fuel as in the case of conventional fuel rods. The precise evaluation of the local stresses is hence not crucial for assessing the parameters relevant for reactivity feedback and, as has been shown in both the above cited reference and in [6], the latter can be very well predicted by the FRED model in spite of its inherent simplifying assumptions.

Though the developed model is thus quite adequate for providing the reactivity feedback related information, the stress concentration at the fuel periphery can only be quantified by 3D analysis of the type allowed by ANSYS. This is an important issue in a more general safety context, since it can lead to possible material failure and therefore has to be avoided. One possible solution is the enhancement of the contact area and reduction of the peak stresses through an appropriate shaping of the fuel pellets. A pellet-height profiling is necessary in order to reduce the cusping of the pellet at its radial boundary. This can be done for instance by raising the pellet height in the middle and decreasing it towards the edges.

Fig. 4.12 compares the standard cylindrical pellet with the modified shape suggested. As can be seen, the adjusted pellet geometry is determined by the single parameter δ. It is evident that the central part of the pellet needs to be raised relative to the outer part, in order to reduce the "peaking" effect. Therefore, negative values of δ are not relevant.
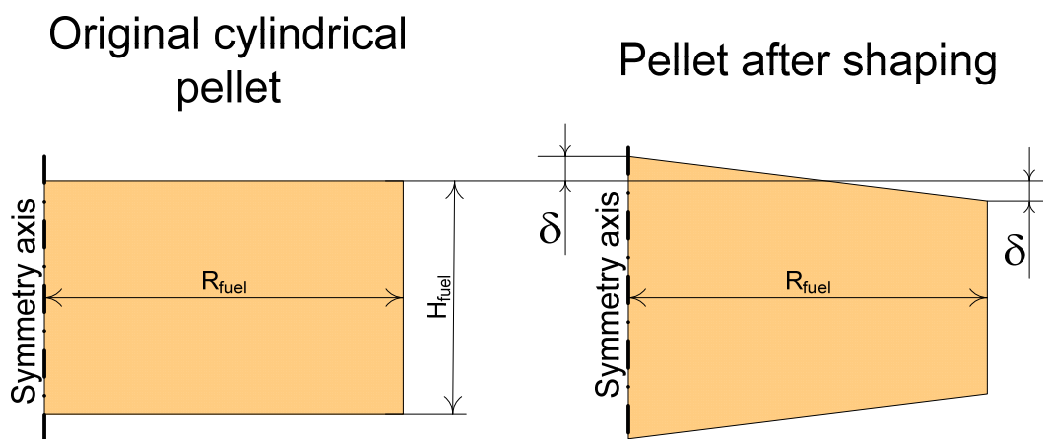
Fig. 4.12. Original and shaped fuel pellet cross-cut

In the currently conducted study using the 3D ANSYS model, δ has been varied over the range 0-10 micrometers in order to find the optimal pellet shape. The following results were sought from the calculations:

- axial gap size as a function of radius,

- contact area,

- axial stress on the pellet axial surface.

The plots for the axial gap size are shown in Fig. 4.13 (for 11 different δ values), while Fig. 4.14 gives the normalized (to the maximal value) axial stress distribution for four different δ values. The numerical values of the parameters of interest, which depend on the pellet shape, are listed in Table 4.2.

As can be seen, even a small change in the pellet geometry has a significant influence on the results affecting the pellet/cladding interaction behavior. The best results are obtained for $\delta=5\mu m$ and $\delta=6\mu m$, with the stress concentration greatly reduced compared to the original cylindrical pellet.
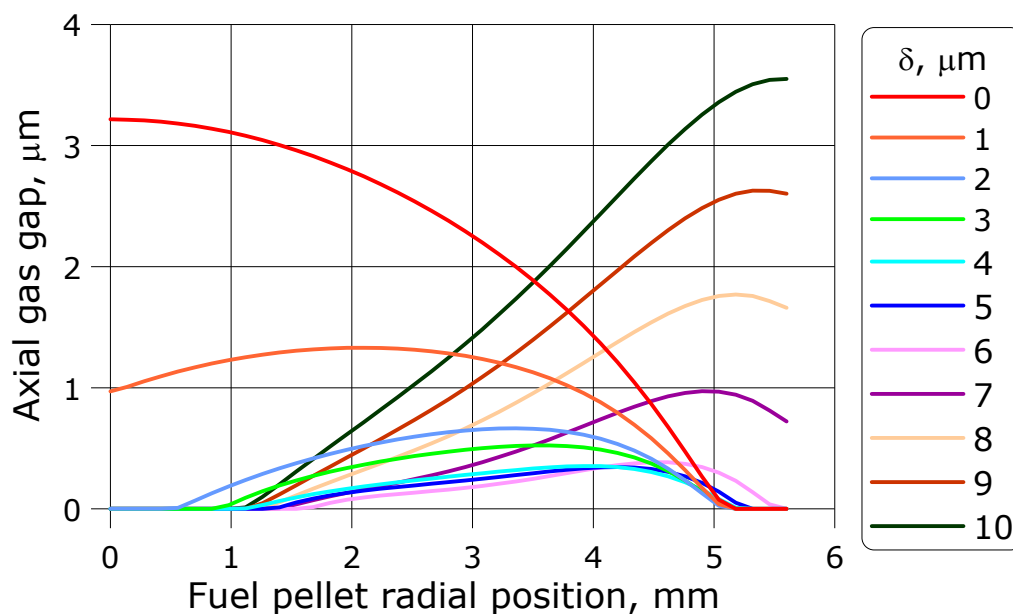
Fig. 4.13. Axial gap size as function of radius for different δ values
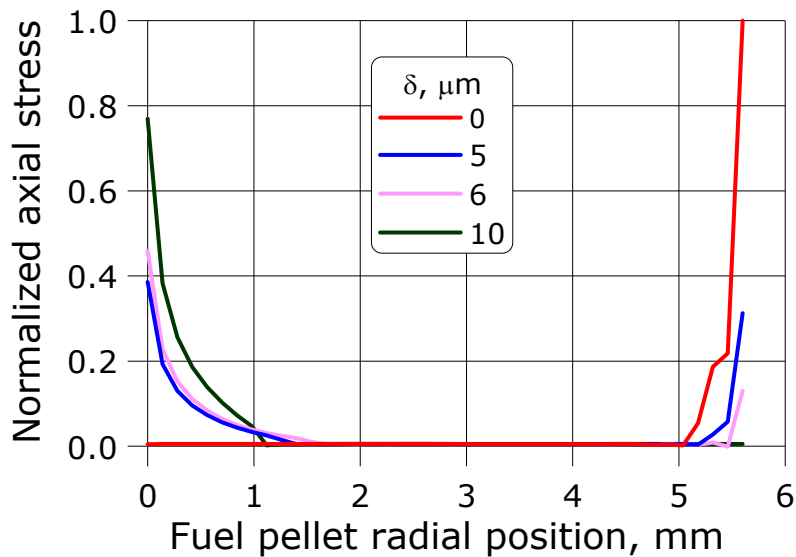
Fig. 4.14. Axial stress distribution for different δ values

Table 4.2. Dependence of parameters of interest on δ

δ	Area averaged gas gap, μm	Average σ_z, MPa	Contact area, %
0	1.43	69.8	16.7
1	0.77	61.5	16.7
2	0.38	53.0	17.5
3	0.30	44.2	19.4
4	0.20	33.8	15.6
5	0.20	25.7	17.8
6	0.22	15.4	10.8
7	0.58	11.9	5.6
8	1.10	12.1	4.5
9	1.62	12.3	3.5
10	2.16	12.6	3.5

It is interesting to note that the pellet shaping procedure described here is the opposite of that used for traditional rodded fuel. Without the pellets being sintered together, the fuel rods undergo so-called "bambooing" [9]. This is due to thermal deformations causing the pellets to get an hourglass shape, which results in greater pellet cladding interaction (Fig. 4.15a). To avoid this, the corners are rounded and a

certain "dishing" is implemented across the flat ends of each pellet. In this situation, the surface becomes flatter upon deformation.

The GFR pellets undergo a similar type of deformation, but with the temperature gradient much higher along the pellet axis, the flat ends become concave rather then convex (Fig. 4.15b). Accordingly, in the GFR case, the fuel pellets have to be initially convex at the flat ends in order to yield a flattening effect upon thermal expansion.

a)   b)
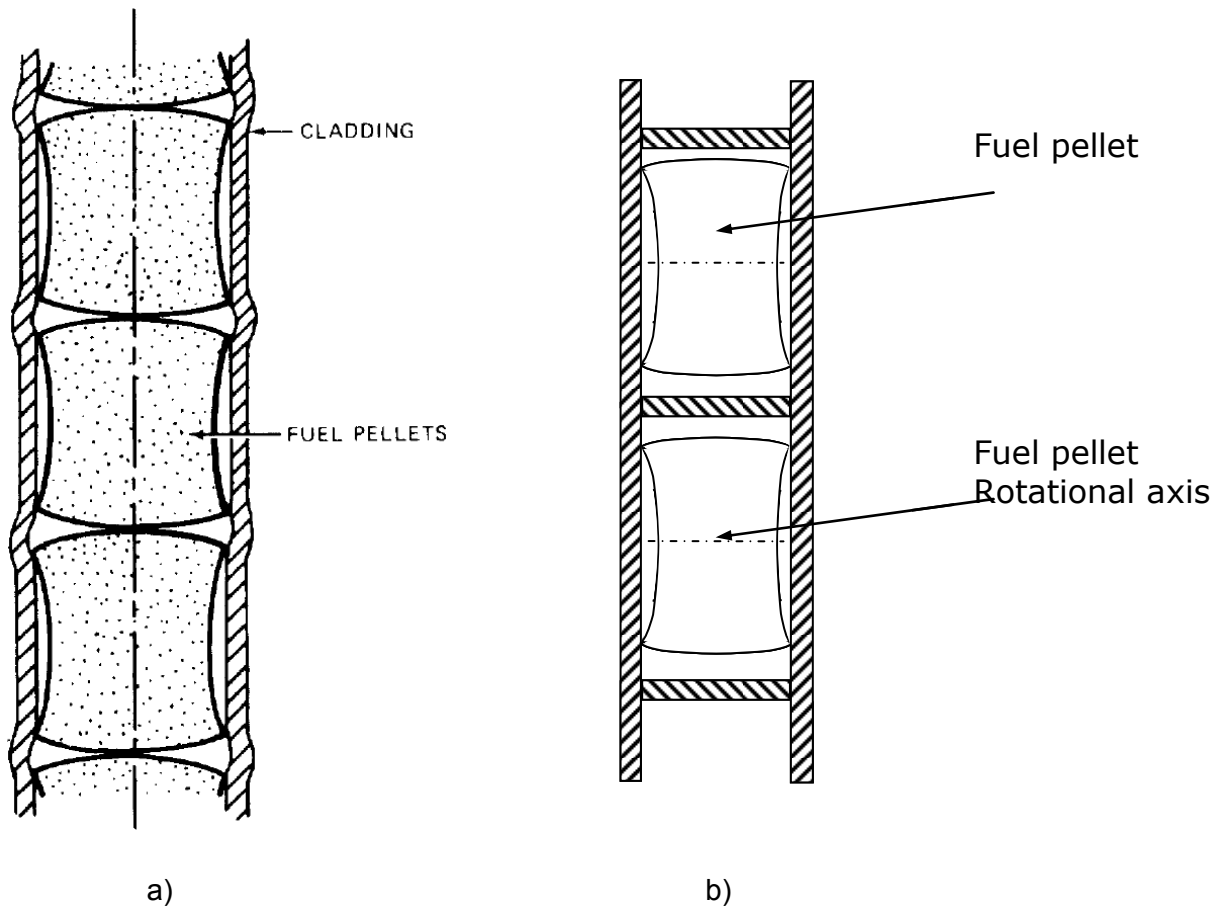
Fig. 4.15. a) LWR fuel pellet and b) GFR fuel pellet after unrestricted thermal deformation

4.3.2   Heat transfer in the cell

The elaboration of a specific fuel design is an evolutionary process, which depends on the consideration of different aspects such as neutronics, thermal-hydraulics and thermo-mechanics. Some of the analysis results can be contradictory, so that understanding the influence of different design parameters on each other is very

important. In order to reduce the overall development effort needed, it is clear that the use of a simple model, which is adequate for describing a particular aspect, can be quite advantageous. In the context of the present research related to plate-type GFR fuel, it would, for example, be useful to demonstrate the possibility of modeling the 3D heat transfer processes in a simplified 1D manner.

The present subsection describes the use of the 3D ANSYS model to better understand the detailed heat transfer processes in the plate-type fuel. Recommendations for applying a 1D treatment are made in the following subsection.

The main difference one has in the heat transfer mechanisms, relative to traditional fuel, is clearly in the prevailing heat flow direction. As standard rodded fuel is cooled on the radial boundary, the temperature has a strong radial dependence. The GFR fuel pellets are cooled mainly across the axial boundaries, which results in an almost uniform radial distribution of the temperature and a strong variation in the axial direction. The radial dependence of the temperature field is in fact not negligible, as the SiC cladding is a good heat conductor and heat flows through the radial gap to the wall and further to the coolant. Thus, the final result depends on the dimensions of the fuel pellet and the matrix inner structure.

The preliminary investigations of the multidimensional heat transfer were described in Section 3.3, as prerequisite for the GFR fuel model development. Different cell and fuel geometries were investigated, and compared against their 1D representation in terms of peak and average fuel temperatures. It was found that the differences between 3D and 1D model predictions tend to asymptotically approach certain values, which depend on the heat generation rate, material properties, geometry and boundary conditions. Such behavior was observed for both the following cases:

- increase of the fuel radius with the preservation of the minimal radial gas gap,

- increase of the radial gas gap with the preservation of the fuel radius.

The present, more detailed investigations of the heat flow have been conducted in order to better understand the GFR plate-type fuel performance. As previously, several cells of different dimensions have been analyzed with the focus on the heat flow from the pellet boundaries. Considerations have been restricted to three different pellet radii (1.6, 3.6 and 5.6 mm), as also to four values of the minimal radial gas gap (50, 150, 250 and 350 μm), all possible combinations being analyzed.

The results are shown in Table 4.3. S_{axial}/S_{radial} is the ratio of the axial to radial fuel pellet surface areas and has been calculated as:

$$\frac{S_{axial}}{S_{radial}} = \frac{2 \cdot \pi \cdot R^2}{2 \cdot \pi \cdot R \cdot H} = \frac{R}{H}$$

121

where

R: pellet radius,

H: pellet height.

q_{axial}/q_{radial} is the ratio of the total heat (in W) extracted from the pellet axial surface to that from the radial surface, and H/D is the height-to-diameter ratio.

Table 4.3. Ratio q_{axial}/q_{radial} for a range of cell and fuel pellet dimensions

R_{fuel}	S_{axial}/S_{radial}	H/D	Minimal radial gap, μm			
			50	150	250	350
1.6	0.327	1.531	0.625	0.973	1.248	1.479
3.6	0.735	0.681	1.846	2.624	3.210	3.686
5.6	1.143	0.438	3.301	4.439	5.261	5.908

The graphical representation of the results, i.e. of the heat flux on the fuel pellet boundaries as calculated by means of the 3D ANSYS model, is shown in Fig. 4.16. - Fig. 4.18. These figures show the results for R_{fuel} values of 1.6, 3.6 and 5.6 mm, respectively.

Two trends can be easily deduced from Table 4.3 and in Fig. 4.16 - Fig. 4.18:

- The heat flow across the axial boundary increases with increase of the radial gas gap.

- The heat flow across the axial boundary increases with increase of the fuel pellet radius.
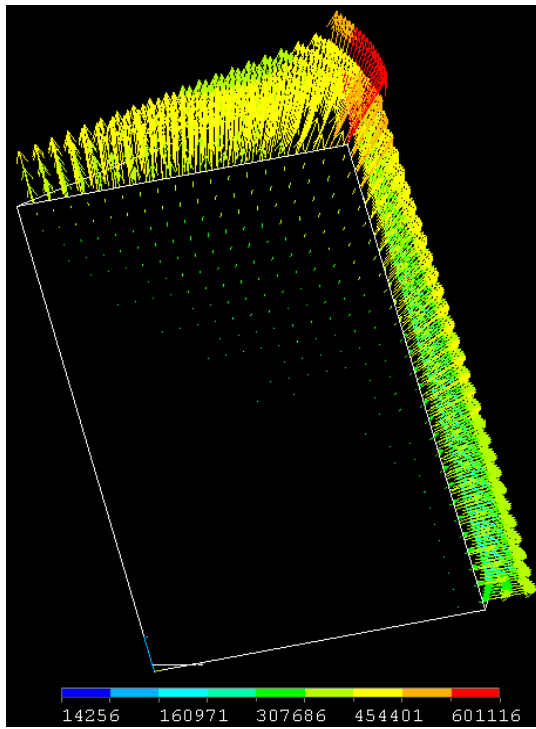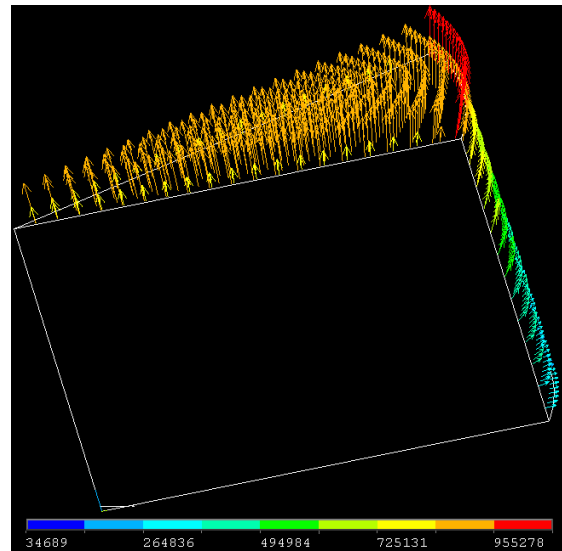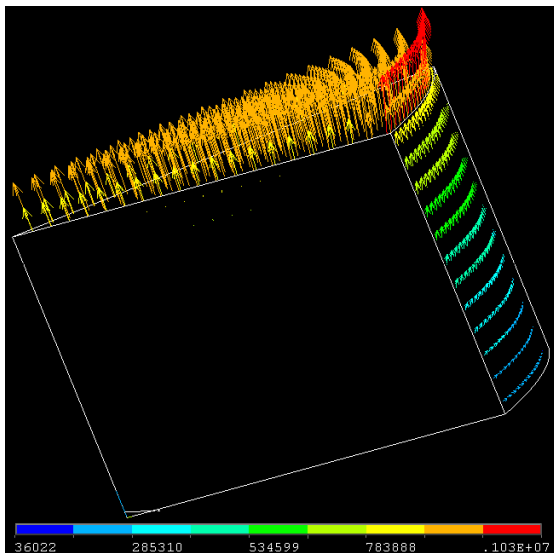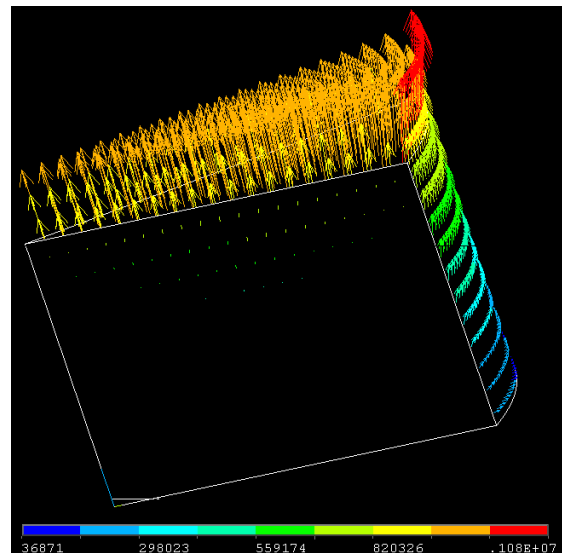
a)
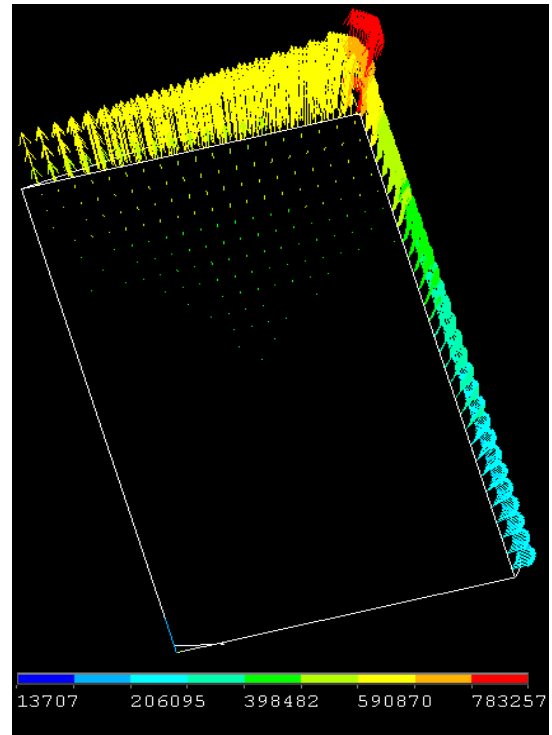
b)
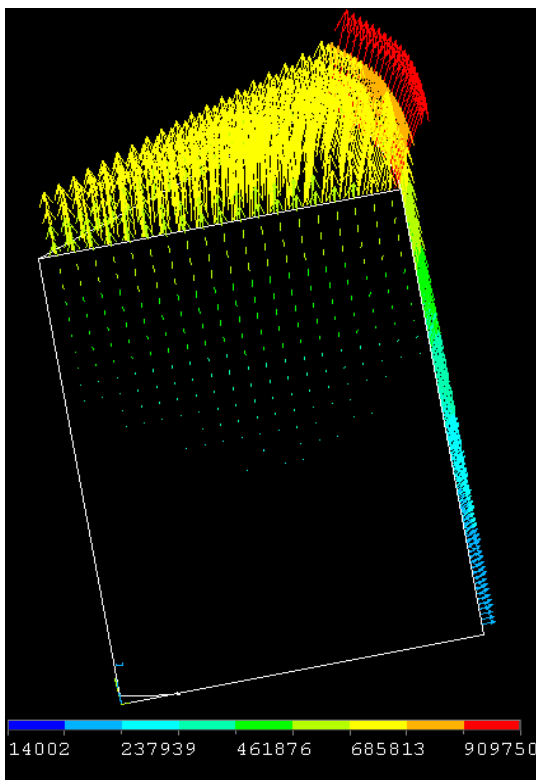
c)
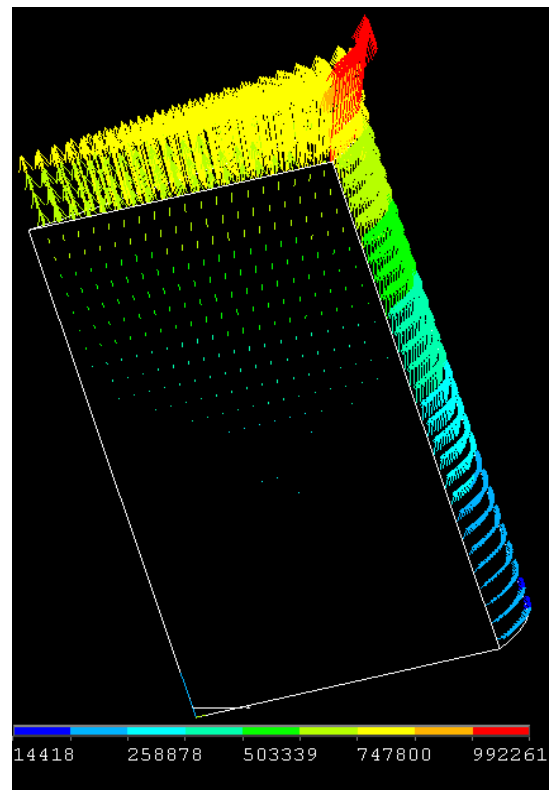
d)

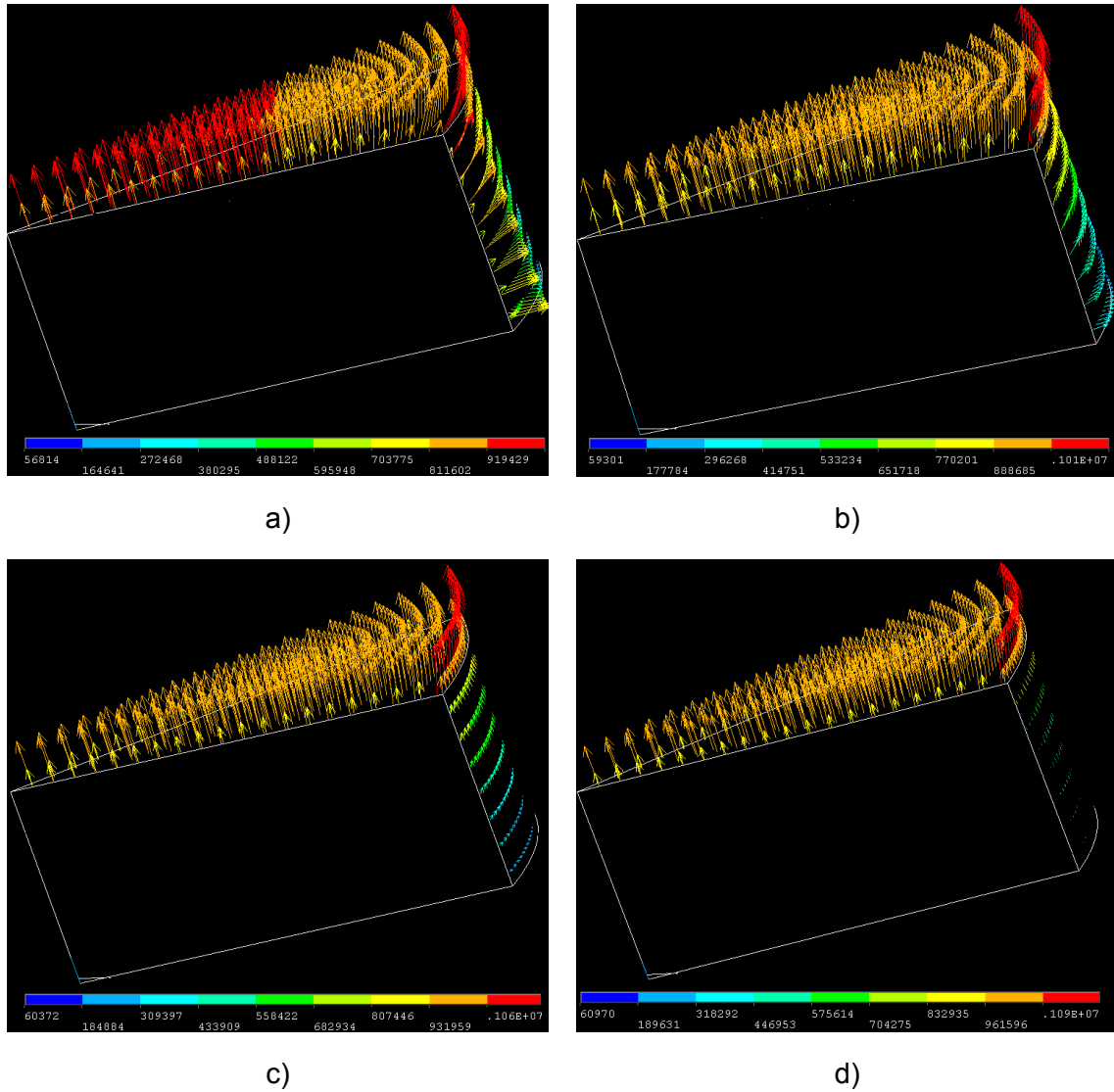**Fig. 4.16. Heat flux on the fuel pellet boundaries for R_{fuel}= 1.6mm and minimal-radial-gap values of a) 50μm, b) 150μm, c) 250μm, d) 350μm.**
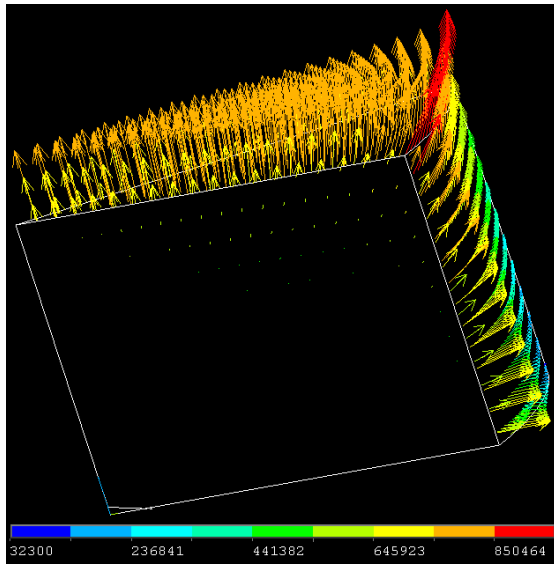
Fig. 4.17. Heat flux on the fuel pellet boundaries for R_{fuel}=3.6mm and minimal-radial-gap values of a) 50μm, b) 150μm, c) 250μm, d) 350μm.

124

Fig. 4.18. Heat flux on the fuel pellet boundaries for R$_{fuel}$=5.6mm and minimal-radial-gap values of a) 50μm, b) 150μm, c) 250μm, d) 350μm.

The most favorable cooling of the fuel pellets is obtained for the highest H/D ratio and smallest radial gas gap value. Conversely, the worst cooling is obtained for the largest radial gas gap and lowest H/D ratio. The pellet height and diameter values for the reference GFR fuel are, in fact, those corresponding to the latter (worst) case. The radial gap [2-6] is even larger (750 μm), implying even lower radial heat transfer. In spite of these features of the reference design, the fuel and cladding thermal conductivities are sufficiently high to provide acceptable margins from the viewpoint of peak temperatures.

4.3.3 Recommendations for 1D modeling

The heat transfer phenomena investigations have shown that, for the reference GFR plate-type cell, the axial heat flux component prevails over the radial one. For the reference GFR fuel design in particular, the radial fuel pellet boundary was shown to be almost adiabatic, resulting in low temperature gradients in the radial direction. Such behavior implies that the temperature field within the cell can be well approximated by a 1D model, which accounts only for the fuel height and lateral wall thicknesses, excluding the inner SiC wall from explicit consideration. This is illustrated in Fig. 4.19. The detailed geometry is shown in Fig. 4.19a. Imposing adiabatic boundary conditions on the pellet's radial surface implies the removal of the indicated material zones indicated by dashed lines in Fig. 4.19b. The latter will be referred to as the 1D ANSYS model, to avoid confusion with the TRACE model. Such a geometry can be analyzed using the 1D heat transfer equation in Cartesian coordinates, as only the axial heat flux has to be considered:

$$\rho c_p \frac{\partial T}{\partial t} = -\frac{d}{dz}\left(\lambda \cdot \frac{dT}{dz}\right) + q_V$$

,

where

ρ: density,

c_p: specific heat,

T: temperature,

λ: thermal conductivity,

q_V :   heat generation rate per unit volume.

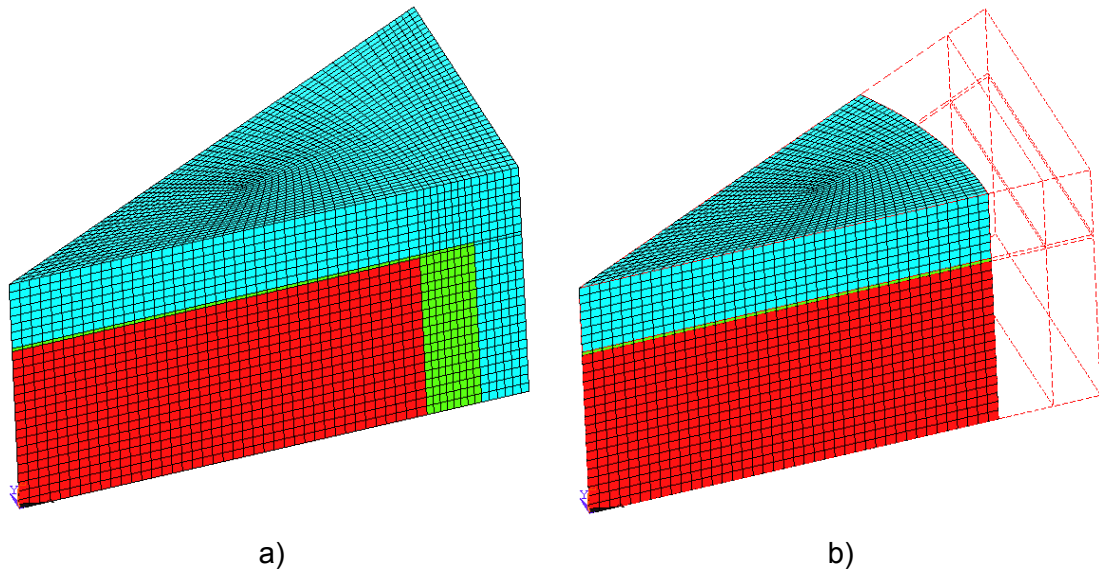a)   b)

Fig. 4.19. Detailed (a) and simplified (b) geometries for thermal analysis

The total heat flux on the 1D model's surface would be higher then that in a real cell, as a smaller area is exposed to coolant while the power production within the cell is preserved. Therefore, heat sink boundary conditions in the form of bulk coolant temperature and heat exchange coefficient are not applicable, as these would lead to higher wall temperatures (higher difference between wall and bulk coolant temperature). This follows from the equation relating the wall and bulk coolant temperature:

$$q_f = \alpha \cdot \left(T_{wall} - T_{bulk} \right),$$

where

α: clad-coolant heat exchange coefficient,

T_{wall}:   wall temperature,

T_{bulk}:   bulk coolant temperature,

q_f: heat flux.

Two alternative approaches can be identified to approximate the 3D results by a 1D model:

-   reduction of the heat flux (or increase of the heat exchange coefficient) by a factor equal to the ratio of the cross-sectional area occupied by fuel to the total cross-sectional area of the cell,

127

- fixing of the wall temperature such that it is equal to the average wall temperature of a 3D model. This value can also be taken from the 1D analysis employing honeycomb structure homogenization as described in Chapter 3.

The latter approach has been chosen currently, as the required wall temperature is provided from the TRACE analysis with a homogeneous plate model [8, 10]. The material properties have been assumed to be constant to reveal the pure effect of the geometry reduction from 3D to 2D. No other assumptions were made about the material properties. Results for the steady state analysis are shown in Fig. 4.20. The boundary conditions for the hottest point in the core have been applied here, viz.:

Heat generation rate: 543 MW/m^3,

Heat exchange coefficient: 6198 W/(m^2·K),

Bulk coolant temperature: 792 °C,

Wall temperature: 916 °C.

The red line shows the temperature distribution along the cell axis, while the blue line is the temperature distribution along the fuel pellet radial boundary. The green line shows the temperature distribution calculated by the 1D ANSYS model (Fig. 4.19b).
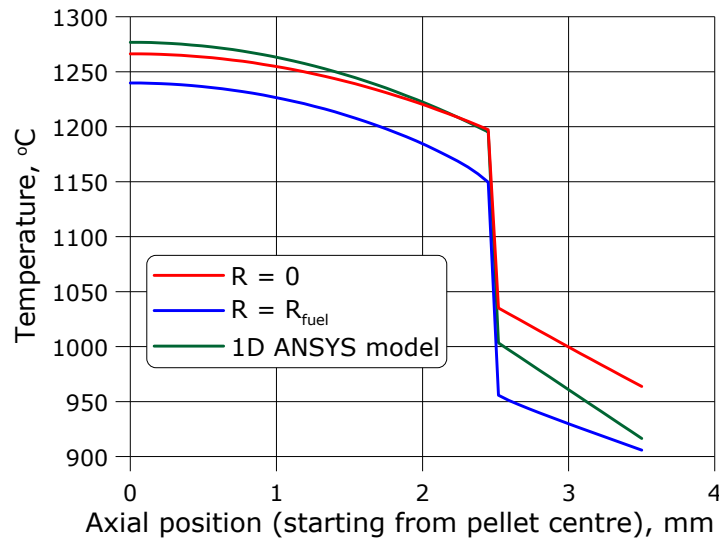

Fig. 4.20. The temperature fields obtained using the 3D and 1D models

It is seen that the peak temperature is overpredicted by only 10°C. In general, the results obtained using the 1D ANSYS model approximate very well the temperature

128

distribution along the pellet axis. The average temperature would be slightly higher, due to the heat sink on the fuel pellet radial boundary having been neglected.

Transient analysis has also been performed to see how the differences between the two models are affected by varying heat generation rate and boundary conditions. The power evolution and other data were taken from the unprotected reactivity insertion accident calculated by TRACE (with the homogenized fuel model) for the GFR [8, 10]. Fig. 4.21 gives the evolution of the boundary conditions for the specific transient case considered. More details on GFR transient analysis are provided in Chapter 5.

The comparison of the 1D and 3D models for the reference transient case has been made in terms of results obtained for certain specific positions, labeled 1 – 8 for the 3D model in Fig. 4.22. The 1D ANSYS results are output in terms of temperatures for the pellet centre, pellet axial surface, and inner and outer surfaces of the lateral wall. The corresponding comparisons are made in Fig. 4.23a – Fig. 4.23d.
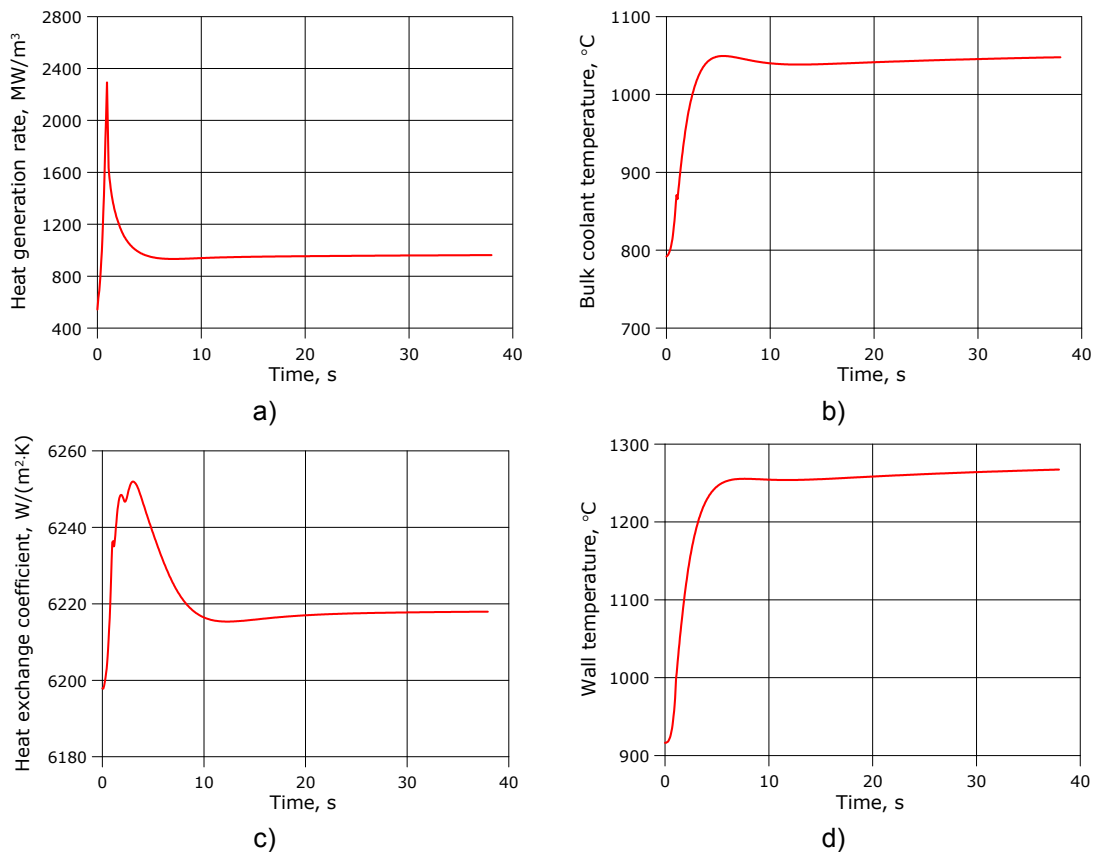

Fig. 4.21. Evolution of boundary conditions during reactivity insertion transient: a) heat generation rate, b) bulk coolant temperature, c) heat exchange coefficient, d) wall temperature
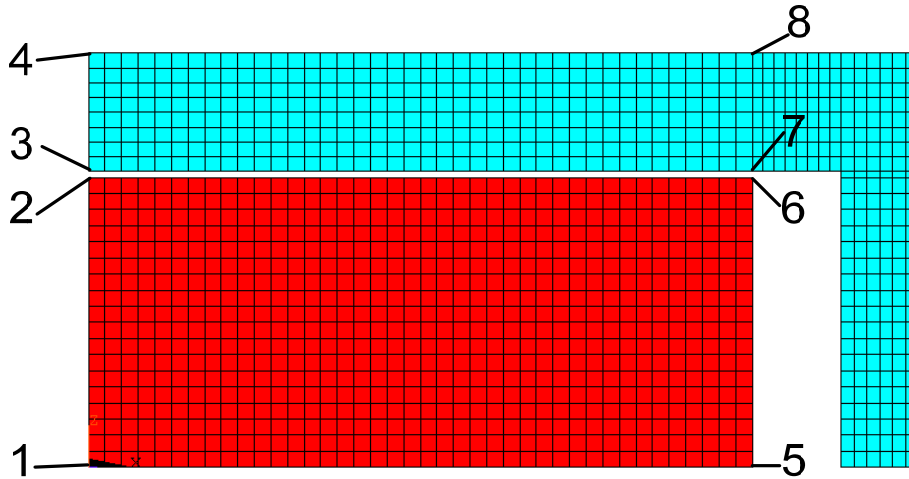
Fig. 4.22. 3D-model positions for the transient results comparison
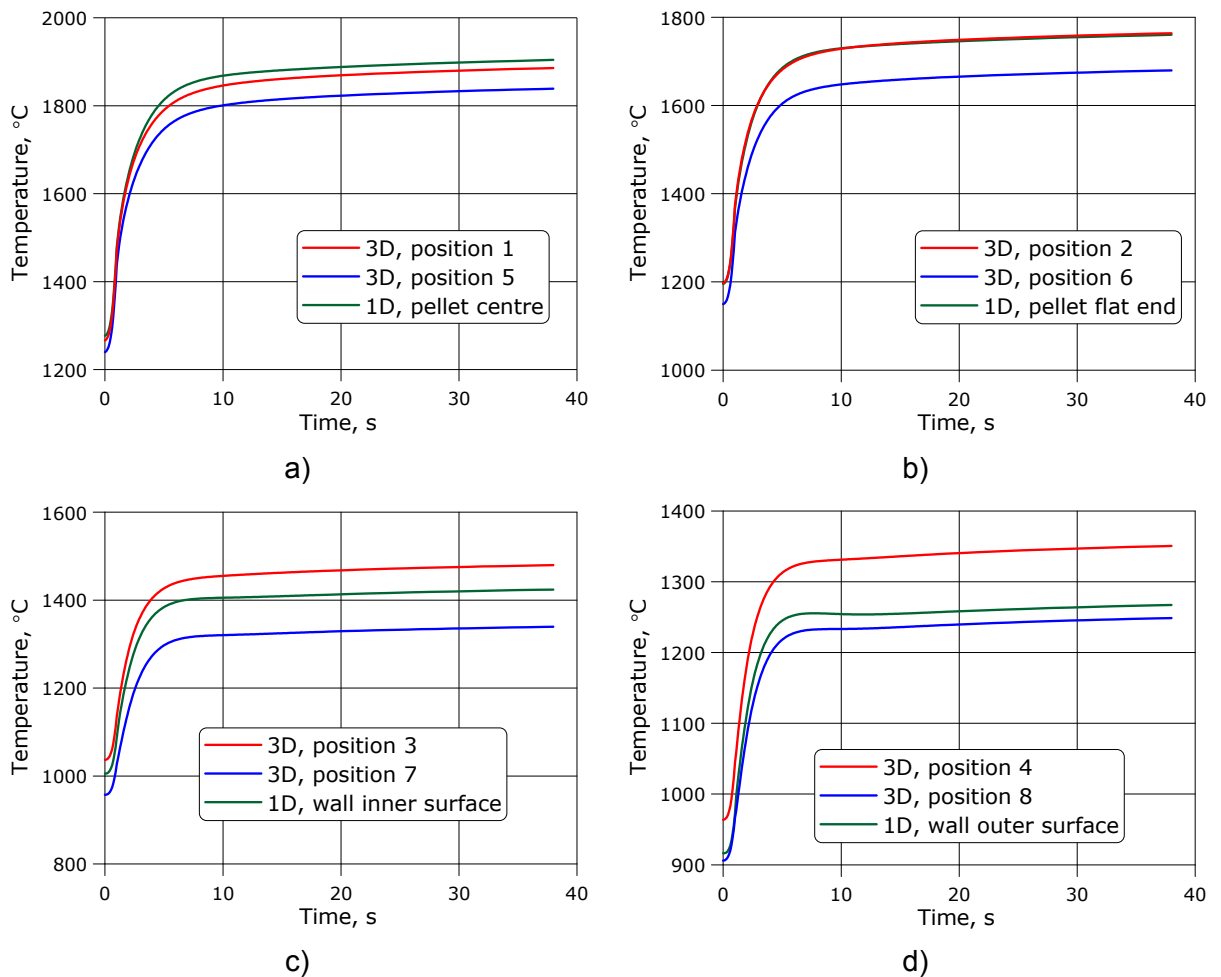

a)

b)

c)

d)

Fig. 4.23. Temperature evolution for certain positions within the cell, calculated by 1D and 3D models

As can be seen, the fuel temperature evolution is well predicted by the 1D model, as for the steady-state case. The two-fold power density increase results in a two-fold increase of the peak temperature overprediction: the difference at the end of the transient is about 20 °C. In general, the temperature evolution for the 1D case is almost identical to that along the cell axis for the 3D model. Thus, the peak fuel temperature is very well predicted by the simplified model. Due to the high fuel thermal conductivity, the *peak* temperature change rate is very similar to the *average* temperature change rate. For a Doppler effect evaluation, therefore, the 1D modeling is quite adequate, a *dT/dt* value being needed rather than the absolute value of temperature.

A larger disagreement is obtained for the cladding temperature, but the 1D model results lie in between those for different radial positions of the 3D cell. This means that the 1D model can be used to calculate the average cladding temperature. In any case, the main limiting parameter for the GFR fuel-design optimization would be the temperature of the fuel rather than that of the cladding.

The considerations that have been made here can not be directly implemented into a 1D model used by a standard systems code such as TRACE or CATHARE. The problem arises from the fact that the heat fluxes within the cell and on the cell surface have currently been calculated using different cross-sectional areas, which is not the case in traditional 1D heat transfer calculation schemes, where the cross-section is supposed to be maintained constant (see Fig. 4.24. and the considerations below). To resolve the problem, one needs to use two different cross-sections in the calculation, viz.

- Within the cell, only the fuel pellet has to be considered, so that the heat generation rate and the cross-section are those of a real fuel pellet,

- On the axial cell boundary, the full cell cross-section area is necessary to calculate the real value of the heat flux and thus the right value for the steady-state wall temperature as indicated below:

$$T_w = \frac{q_V \cdot H_{fuel} \cdot S_{fuel}}{\alpha \cdot S_{cell}} + T_b \, , \qquad\qquad \textbf{Eq. 4.1}$$

where

q_V: heat generation rate,

H_{fuel}:   fuel height,

S_{fuel}:   fuel pellet cross-sectional area,

S_{cell}: cell cross-sectional area,

T_w: wall temperature,

T_b: bulk coolant temperature,

α : clad-coolant heat exchange coefficient.

The standard approach to analyze the homogeneous cell would employ the same cross-sectional area for the fuel zone and the cell boundary. Usage of different areas implies that the heat flux on the pellet axial boundary is higher than that at the cell boundary (the total amount of heat generated is preserved).

The calculation scheme is shown schematically in Fig. 4.24. Dashed lines signify the cross-sectional areas which have to be taken to calculate the within-cell heat fluxes. Solid lines indicate the areas which have to be taken to calculate the heat flux for the wall temperature assessment (according to Eq. 4.1), which is done on the basis of the bulk coolant temperature (T_{bulk}) and the clad-coolant heat transfer coefficient (HTC). As can be seen, the proposed scheme does not assume any smearing of the heat generation and/or heat flux over the whole cell.

As shown earlier, such a calculation scheme very well approximates the fuel peak temperature for the GFR reference fuel geometry. The peculiarity of the design is the negligible radial heat transfer, which allows one to avoid explicit consideration of the radial gas gap and cladding.

Should the fuel design change such that the radial heat transfer can no longer be neglected, one could artificially increase the fuel radius to account for an additional heat sink from the pellet radial boundary. This increase would depend on the heat generation rates, boundary conditions and the geometry. Thus, in principle, multidimensional tables can be generated on the basis of a series of 1D calculations with different cross-sectional areas and their comparison with 3D analysis. Such an approach requires some preparatory work to assemble the necessary "database", but once this is available, the calculation speed can be increased considerably. Moreover, simple correlations for fuel and cladding thermal expansion and for the fuel swelling can be added to the model to account for axial gas-gap changes and corresponding effects on the heat transfer. Such an approach is already implemented in TRACE for modeling LWR fuel. However, this work is out of the scope of the present study but can be considered as its possible continuation.
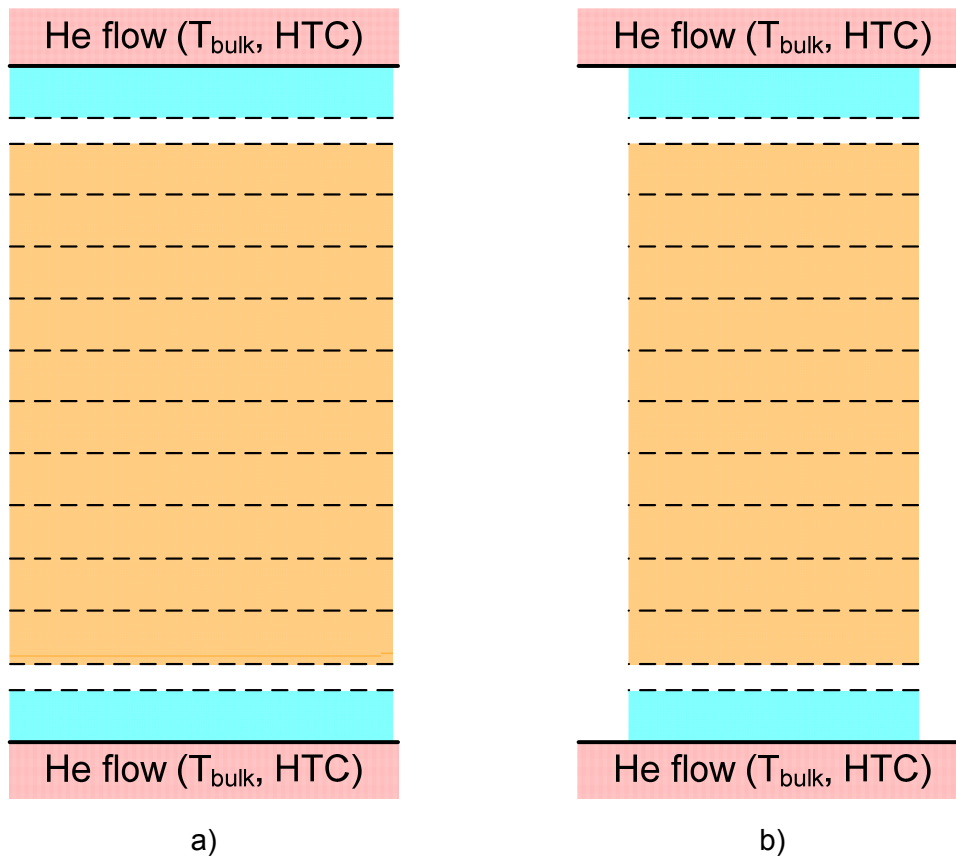
Fig. 4.24. a) Standard and b) adjusted 1D models for the GFR fuel

4.3.4   Pellet size optimization

As described in Section 4.3.1, thermal expansion and swelling of the GFR fuel during irradiation can lead to axial gap closure, which can result in high stresses both in fuel and cladding. It was shown, for the reference fuel design, that optimization of the fuel pellet shape can reduce the peak stresses considerably.

The present subsection uses simple analytical estimations and the 2D FRED model for exploring a potentially more effective approach, viz. of optimizing the pellet size, such that one can maintain an open axial gap throughout the planned residence time of the fuel in the reactor. Clearly, this would be a very effective measure for reducing the fuel failure probability.

The honeycomb structure geometry itself has been kept fixed (with the dimensions corresponding to the hot conditions) in the present study. Furthermore, since the behavior of SiC_f/SiC under neutron irradiation is unknown, it has been assumed that there is no swelling of the structural material and the deformations occur only due to the temperature change.

The optimization of the pellet dimensions needs to consider both thermal expansion and swelling of the fuel (in the open gap regime). The GFR fuel burnup is expected to reach 10% FIMA [11]. This value was chosen for the following analysis.

As shown in Appendix A, the fuel swelling rate increases with temperature, which means that the pellet-cladding interaction is most likely to occur first at the hottest positions in the core. Consequently, the hottest honeycomb cell was chosen for the analysis. The temperature distribution in such a cell is shown in Fig. 4.25. The positions mentioned in the legend correspond to those shown in Fig. 4.1, viz.

-   position 1 is along the cell axis,

-   position 2 coincides with the fuel radial boundary,

-   position 3 coincides with the inner surface of the hexagonal wall of the cell.
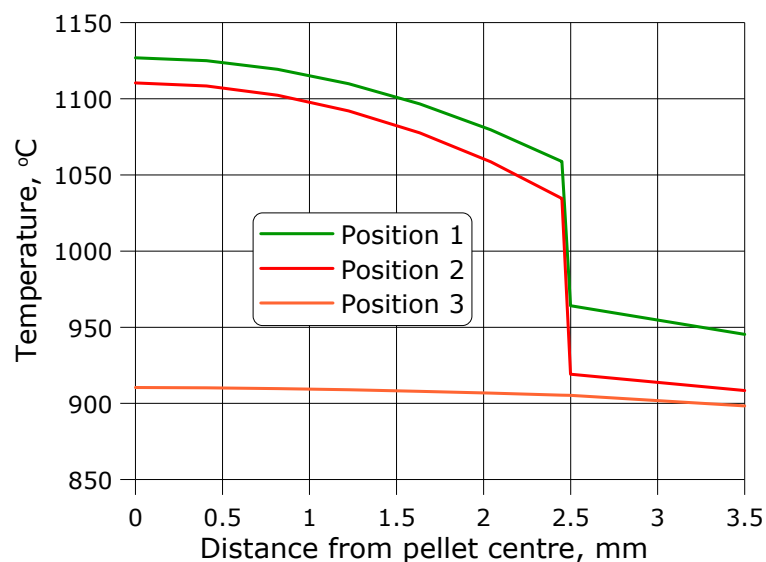

Fig. 4.25. Temperature field for the GFR cell with the highest heat generation rate

As can be seen, the temperature gradients in fuel and cladding are quite low which would result in their almost isotropic thermal expansion. For this reason, it was decided to perform the analysis based on the average material temperatures, viz.

-   fuel pellet temperature: 1100 °C,

-   cladding temperature: 900 °C.

The cell geometry, as also the designations used in the following analysis, are shown in Fig. 4.26. The variables can be briefly described as follows:

h_{fuel}:   fuel pellet height,

R_{fuel}:   fuel pellet radius,

h_{wall}:   distance between the inner surfaces of lateral walls,

h_{cell}:   distance between the outer surfaces of lateral walls (cell height),

δ_{rad}:   minimal radial gas gap (the fuel is supposed to be concentric with the alveola),

δ_{ax}:   axial gas gap, as the cell is supposed to be symmetric with respect to the half-height plane, both axial gaps have got the same value,

d: inner cell across-flats width.

The subscript "0" will be used to signify the given value for cold conditions (20 °C). Values without any subscript refer to the deformed cell.

Clearly, a "hard" fuel pellet contact appears when either δ_{rad} (radial contact) or δ_{ax} (axial contact), or both of them, are equal to zero.
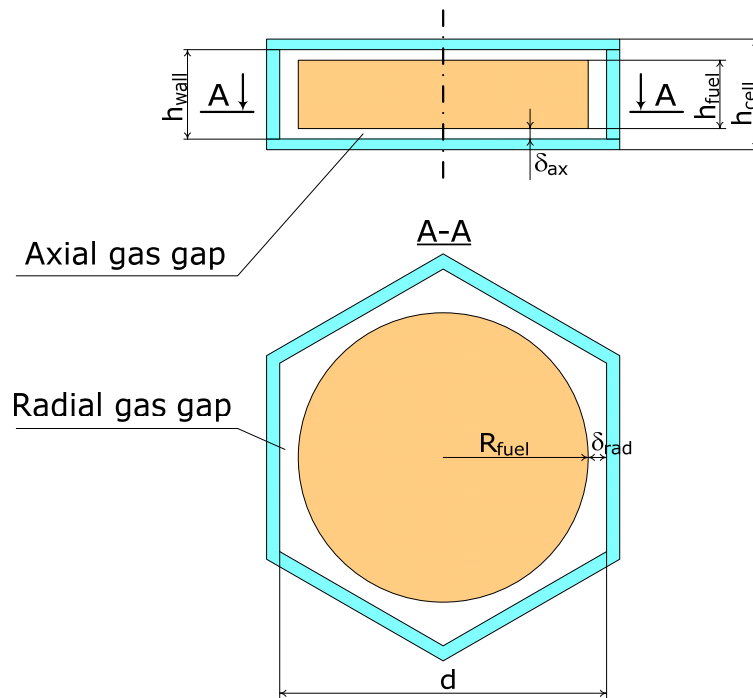

Fig. 4.26. Geometry of a cell and the definition of variables used in the present analysis

The available space to accommodate fuel expansion in the radial direction is determined by the across flats width (see Fig. 4.26):

$$2 \cdot R_{fuel}^{\max} = d$$

The available space to accommodate fuel expansion in the axial direction is determined by the distance between the lateral walls (see Fig. 4.26):

$$h_{fuel}^{\max} = h_{wall}$$

The correlations and tables to calculate the fuel swelling, as well as the fuel and matrix thermal expansion, are presented in Appendix A. The values for the given average temperatures are listed in Table 4.4.

Table 4.4. Coefficients to calculate fuel and cladding expansions for the given average temperatures

Parameter \ Material	Fuel	Cladding
Linear thermal expansion coefficient, $1 \cdot 10^{-6}$/K	11.95	5.56
Swelling, $\Delta V / V$ per 1% burnup	1.9*	--

* This value is quite conservative and corresponds to burnt fuel. Fresh fuel would swell at lower rates (~1.3-1.4%)

According to the given data, the maximal values for the fuel deformations can be evaluated (assuming constant temperatures for the materials).

The maximal theoretical fuel radius is given by:

$$R_{fuel}^{\max} = d_0 \cdot \left(1 + \alpha_{clad} \cdot \Delta T_{clad}\right) \cdot \frac{1}{2}$$

For the reference design parameters (see Chapter 2), this yields:

$$R_{fuel}^{\max} = 12.7 \cdot \left(1 + 5.56 \cdot 10^{-6} \cdot (900 - 20)\right) \cdot \frac{1}{2} = 6.381 mm$$

The maximal theoretical fuel height is given by:

136

$$h_{fuel}^{max} = h_{wall,0} \cdot \left(1 + \alpha_{clad} \cdot \Delta T_{clad}\right)$$

For the reference design parameters, this yields:

$$h_{fuel}^{max} = 5 \cdot \left(1 + 5.56 \cdot 10^{-6} \cdot \left(900 - 20\right)\right) = 5.024 mm$$

As mentioned above, the total relative volumetric fuel deformation is comprised by thermal expansion and swelling:

$$\frac{\Delta V}{V} = \frac{\Delta V_{therm}}{V} + \frac{\Delta V_{swell}}{V}$$

This can be expressed as:

$$\frac{\Delta V}{V} = 3\alpha_{fuel}\Delta T_{fuel} \cdot \left(1 + \alpha_{fuel}\Delta T_{fuel} + \frac{\left(\alpha_{fuel}\Delta T_{fuel}\right)^2}{3}\right) + \frac{\Delta V_{swell}}{V} = 0.225$$

As the fuel deformation is assumed to be isotropic, the radial, axial and tangential components are equal, i.e.

$$\varepsilon_r = \varepsilon_z = \varepsilon_\vartheta = \varepsilon$$

The exact value can be found from the following equation for the total volumetric deformation:

$$\frac{\Delta V}{V} = \left(1 + \varepsilon\right)^3 - 1 = 3\varepsilon \cdot \left(1 + \varepsilon + \frac{\varepsilon^2}{3}\right) = 0.225$$

Thus

$$\varepsilon_r = \varepsilon_z = \varepsilon_\vartheta = \left(1 + \frac{\Delta V}{V}\right)^{\frac{1}{3}} - 1 = 0.07$$

The results of calculation and optimization are summarized in Table 4.5. The initial "cold" fuel pellet dimensions, corresponding to the reference fuel design, are listed in the 1st column. The 2nd column lists the pellet dimensions after theoretically unrestricted swelling and thermal expansion. The limits for axial and radial deformations based on the deformed cell size are listed in the 3rd column, while the adjusted cold pellet dimensions are in the 4th column. The latter correspond the largest pellet which meets the no-fuel-clad-contact requirement for a given cell size. As can be seen, such a pellet would be smaller in height than the original pellet, but have a larger radius. The total volume is greater by 8.7%. Finally, the last column of

Table 4.5 shows the adjusted pellet dimensions with preservation of the original volume. This condition would keep the neutronics characteristics the same, since these depend on the volumetric fuel-to-cladding ratio).

Table 4.5. The initial, deformed and optimized fuel pellet dimensions

	Initial (cold conditions)	After unrestricted expansion	Upper limits for the pellet expansion	Adjusted values (for cold conditions) based on the maximal theoretical expansion	Adjusted dimensions with fuel volume preservation
h_{fuel}, mm	4.9	5.243	5.024	4.695	4.695
R_{fuel}, mm	5.6	5.992	6.381	5.964	5.721
V_{fuel}, mm^3	482.75	591.39	642.65	524.6	482.75
% of the Initial cold pellet volume	100	122.5	133.1	108.7	100

As mentioned earlier, the honeycomb cell size was not modified in the present study. The aim has been to optimize the fuel pellet size for a given honeycomb mesh, such as to have low pellet-cladding mechanical interaction during the entire residence period in the core. This has been shown to be possible, also in conjunction with a significant (8.7 % in the present case) increase in pellet volume. The latter aspect could be used to optimize certain neutronics parameters.

The disadvantage of such a fuel pellet would be the larger axial gaps, which would result in higher fuel temperatures. This can be slightly mitigated by the increased pellet size and correspondingly decreased heat generation rate (The power deposited in a cell has to be preserved).

An analysis has been carried out to assess the deterioration of the heat transfer due to the increased axial gas-gap width. The temperature field was calculated for cells with the optimized fuel pellet size and compared to the reference design solution. The results are shown in Fig. 4.27-Fig. 4.29. All the figures contain 3 curves:

- The red curve corresponds to the reference design solution.

- The blue shows the results for the optimized pellet with fuel volume preservation (column 5 of Table 4.5 and referred to as $V_{pellet} = V_{reference}$ in the figures),

- The green curve shows the results for the optimized pellet with the increased fuel volume (column 4 of Table 4.5 and referred to as $V_{pellet} > V_{reference}$ in the figures).

The temperature distributions are shown along paths 1-3 according to Fig. 4.1. The temperature field is calculated by FRED for steady-state conditions, while accounting for the fuel and matrix deformations.
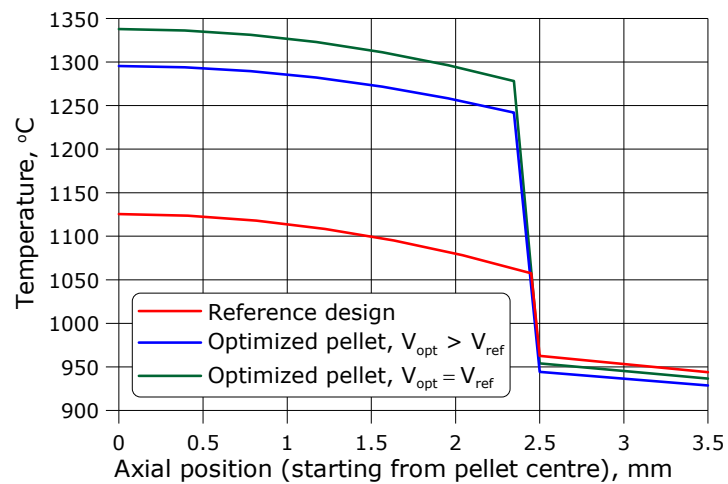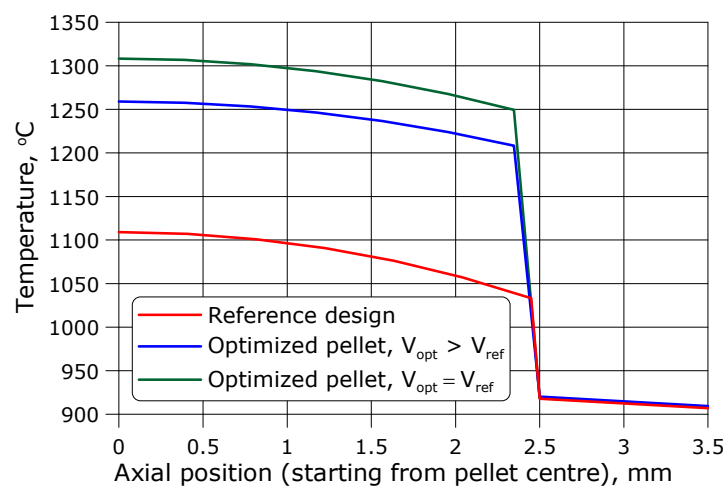

Fig. 4.27. Temperature distributions along path 1

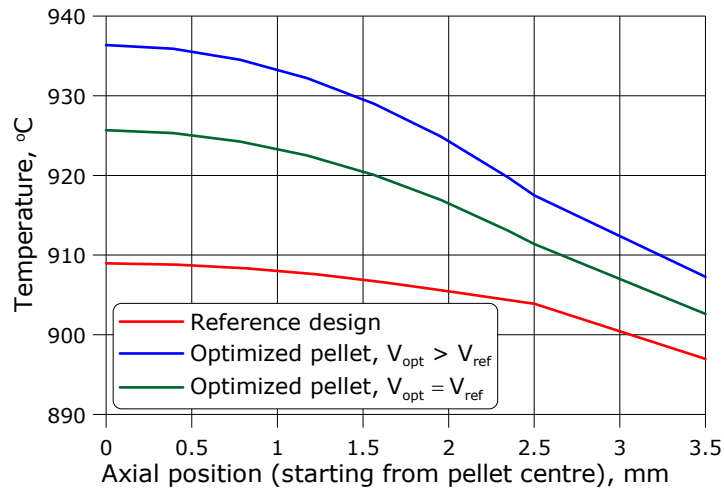**Fig. 4.28. Temperature distributions along path 2**

Fig. 4.29. Temperature distributions along path 3

As expected, the decrease in the pellet height results in higher temperatures due to the significant increase in the axial gas-gap width. This effect is slightly mitigated for the larger pellet volume, the corresponding heat generation rate being lower. (This results in a lower heat flux on the pellet boundaries and therefore in a lower temperature drop across the axial gas gap.)

Summarizing the results, one can conclude that the pellet size optimization has little influence on the cladding temperature (Fig. 4.29) but significantly influences the fuel temperature. For fresh fuel under steady-state conditions, the increase (at the hottest point of the core) is 200°C for the optimized pellet with preserved volume and 150°C for the optimized pellet of larger volume. These values would be lower for colder positions in the core, and the difference will constantly decrease with burnup due to axial gas gap closure. However, the peak fuel temperatures remain well below the design limit of 1600°C. The peak temperatures for the cladding are determined by the stability of the SiC fibers, as the bulk SiC is refractory and can withstand temperatures up to 2800ºC (see Appendix A). According to [13, 14], the thermal stability for SiC fibers is provided only till about 1500ºC, depending on the fabrication procedure and other factors. In any case, the cladding temperatures are also below the limits, and there is a significant margin also for transients.

The higher fuel temperatures for the alternative fuel geometries would result in higher swelling rates, and hence burnup calculations are necessary to more realistically investigate the fuel behavior under irradiation. The calculations have been done with the developed FRED model for the reference fuel design and for the pellet dimensions given in Table 4.5. For simplicity, analysis is performed for the hot

assembly only, as the swelling rates would be highest in this case. The results are shown for the hot spot within the assembly, again for the three cases:

- reference fuel design,

- fuel pellet of adjusted geometry with the fuel volume ($V_{pellet} = V_{reference}$),

- fuel pellet of adjusted geometry with the larger fuel volume ($V_{pellet} > V_{reference}$).

Fig. 4.30 shows the dependence of axial and radial gaps versus burnup. Zero time refers to steady-state operation, so that the initial values of the gaps are smaller then design values, which are specified for cold conditions. As can be seen, the axial gas gap of the reference cell closes at a burnup of 26 MW·d/kg. The radial gap remains open throughout the whole irradiation period. The axial gap closure for the optimized cell with the same volume happens at a burnup of 70 MW·d/kg, while the radial gap always remains open.
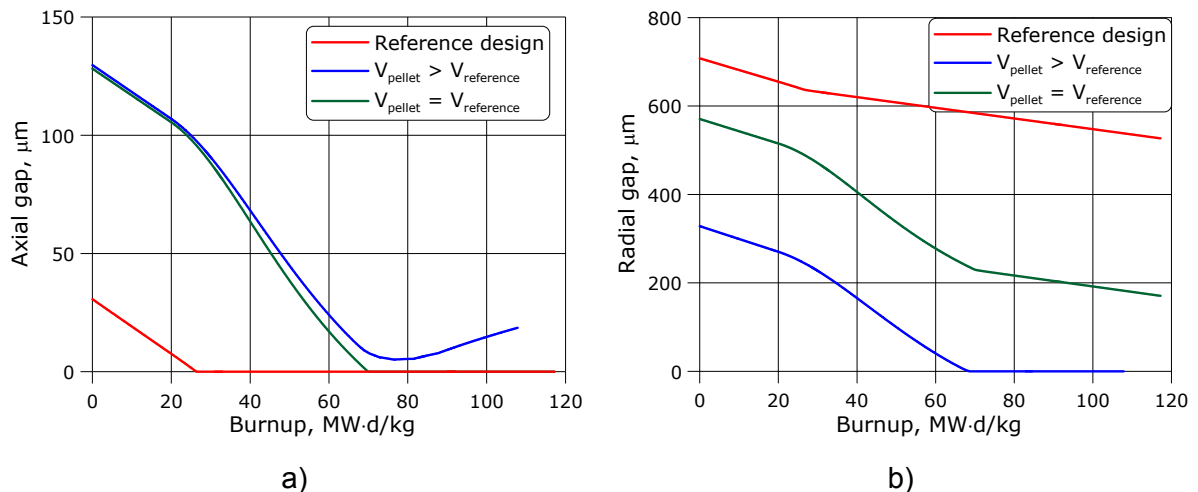
Fig. 4.30. Evolution of the a) axial and b) radial gas gaps during irradiation

The pellet of larger volume has radial contact at a burnup of 70 MW·d/kg. After the radial gap closure, one can observe the slight increase of the axial gas gap and also of the plate thickness. This happens due to the no-slip condition assumed for fuel and cladding during radial contact, which leads to the reduction of the inner SiC wall thickness and corresponding increase of the thickness of the plate. Such a phenomenon is called ratcheting and can be obtained for traditional fuel rods [10]. The no-slip condition has been accepted here as an approximation, as no data is available on pellet-clad interaction for the GFR fuel.
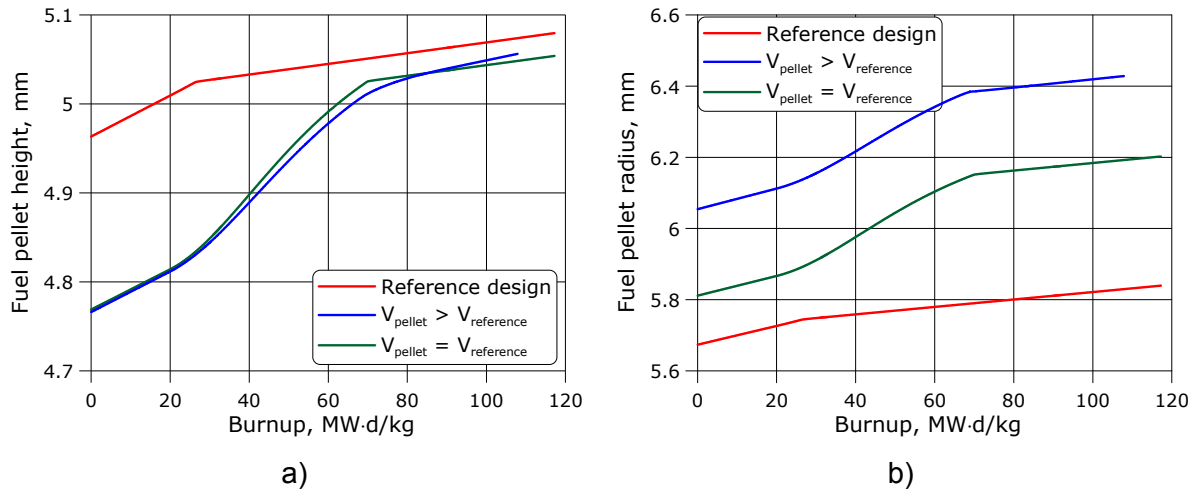
Fig. 4.31. Evolution of the fuel pellet a) height and b) radius during irradiation

Fig. 4.31a,b and Fig. 4.32a show the evolution of the pellet dimensions. Three different regions can be observed, which can be explained by the correlations used for calculation of the swelling. The fuel growth until 2% burnup is only temperature dependent. After 2% (this value is a model parameter and can be changed), gas-bubble swelling leads to larger swelling rates and there is rapid volume growth until the fuel comes in contact with cladding. Following contact closure, the fuel starts to swell into the porosity (according to the model used; see Appendix A for details), which results in lower volume-increase rates.

The correlation used here (see Appendix A) is based on the experimental data for carbide fuel rods and therefore cannot be totally representative of the phenomena occurring in the GFR cell. It can well describe the unrestricted fuel swelling, but the contact behavior is most likely to be quite different. The principal difference in the GFR fuel case is the separation of the pellets from each other and their location within isolated cells with enough free volume to accommodate swelling. Therefore, after contact occurrence (radial or axial), the fuel can continue to swell in the other direction as well as into the porosity. This would result in higher swelling rates during contact. The overall behavior would thus depend on the contact pressure, the availability of free space, the contact surface, and the friction between fuel and cladding.
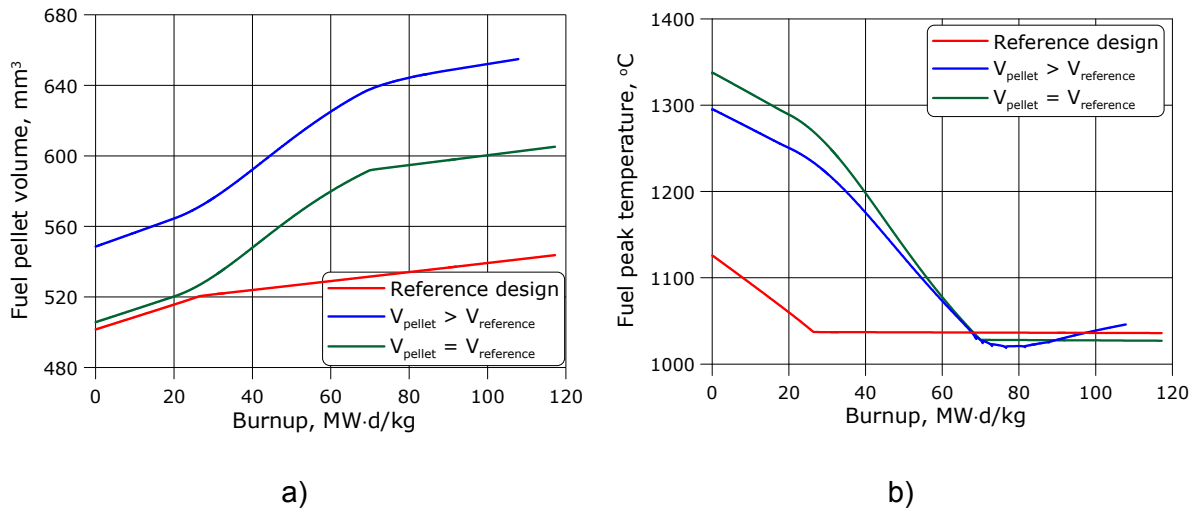
142

Fig. 4.32. Evolution of the fuel pellet a) volume and b) peak temperature during irradiation

The fuel peak temperature is shown in Fig. 4.32b. As expected, the fuel temperature decreases with burnup. A slight increase is obtained for the larger pellet after 70 MW·d/kg, which is the effect of the axial gas-gap thermal conductance.
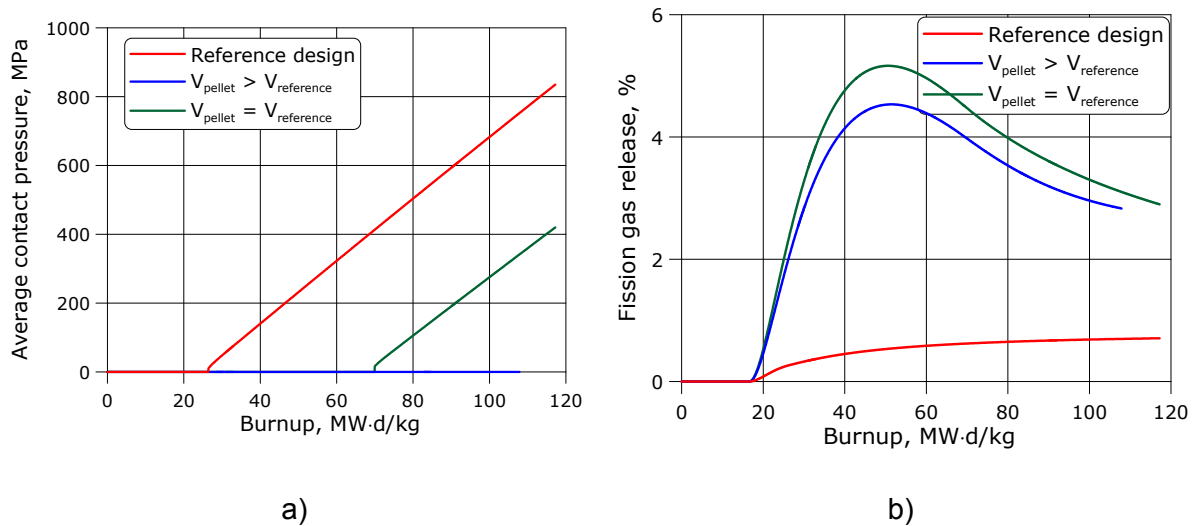

Fig. 4.33. Evolution of the a) contact pressure and b) fission gas release during irradiation

The evolution of the average axial contact pressure is shown in Fig. 4.33a. As can be seen, the pellets of optimized shape produce much less or no pellet-cladding interaction at all. The high value of the contact pressure is a consequence of the

143

model used. Only elastic deformations have currently been taken into account; the plasticity and cracking were not considered.

The total fission gas release (FGR) in percent for a given cell is shown in Fig. 4.33b. For a reference pellet, the FGR rate starts to increase after 20 MW·d/kg burnup according to the correlations given in Appendix A. For the optimized pellets, the FGR rate is determined by competing effects, viz.

- increase of the FGR rate with burnup,

- decrease of the FGR rate when temperatures go down.

Clearly, the higher temperatures at the beginning of cycle lead to higher FGR for the optimized fuel. However, the amount of the fission gas released is not high: less then 1% for the reference design and around 3% for the optimized fuel. Moreover, these are hot-spot values, and the FGR would be significantly lower on the average.

Though the new pellet dimensions do not really fulfill the initial requirement of no gap closure, it has been shown that the reference GFR fuel design has a considerable potential for improvement via simple change of the pellet dimensions. Thus, it was seen that the axial gas gap closure can be delayed up to 70 MW·d/kg (for the pellet with preservation of volume). In this case, there is still quite a large margin till radial gap closure. For the larger-volume pellet, radial gap closure was observed. The used algorithms predict no axial gap closure in this case due to the no-slip approximation. In reality, there will be some slip between the materials, which would result in lower axial deformation rates and further delayed axial gap closure.

For more precise evaluation of the phenomena, an adequate assessment of the contact area and pressures is necessary, including the use of appropriate data on the contact of (U, PU)C with SiC$_f$/SiC. As was mentioned in Chapter 3, the radial contact occurs in the vicinity of the lines of contact of the cylindrical pellet and the hexagonal cell walls. Therefore, a 3D analysis is necessary for detailed radial contact treatment. The presently developed 2D model is adequate for tracing contact occurrence, but not for a quantitative analysis of the contact pressures.

4.4   SUMMARY

The extension of the FRED code, originally intended for rod-type fuel, to the thermo-mechanical analysis of GFR plate-type fuel was described in the previous chapter. A number of quite strong assumptions are inherent to the newly developed FRED model, so that appropriate benchmarking has been necessary. With no appropriate experimental results being available, numerical solutions obtained from 3D finite-element analysis have been used as reference. The benchmarking has served to:

144

- assess the impact of the simplifications on the final results,

- identify the range of applicability of the new model,

- justify use of the model for GFR safety analysis.

A feature of the developed model is that the thermal and mechanical parts are separate, and the user can make a choice between different options. The treatment can be either purely thermal or coupled thermo-mechanical. The benchmarking was divided into two parts. Firstly, the thermal model was verified and then the coupled one.

Benchmarking of the thermal model has shown good agreement between the developed model and the detailed solution. Due to the complex shape of the radial gap, there can be different approaches to calculate the corresponding heat transfer coefficient. One can either base the calculation on the average gap-width value or on the average of the reciprocal gap width. It was shown that the latter provides results which correspond much better to the reference solution. Therefore, this approach was chosen as standard.

Benchmarking of the coupled thermo-mechanical model has shown very good agreement for the deformations of fuel and matrix, both for open and closed gap regimes. However, the reliable prediction of stress distributions is impossible in the frame of a simplified 2D model, due to its inherent simplifications. One can only predict average stress values, which can be used to assess effects such as creep, etc. It must be emphasized that the principal aim of the developed model is not the assessment of fuel integrity but rather, the reliable prediction of the temperature field and of the material deformation from the viewpoint of transient analysis, i.e. with regard to calculating the corresponding reactivity feedbacks.

The benchmarking tool, viz. the 3D finite-elements model, has also permitted certain detailed analyses for obtaining in-depth physical understanding. Thus, the heat transfer phenomena in the GFR cell were analyzed in detail. It was shown that, for certain fuel and cell dimensions, the radial heat flux is considerable, and the detailed model predicts lower fuel temperatures. For the reference design, however, both the pellet radius and the radial gas gap are large enough for the radial heat flux to be low and the heat is mostly transferred in the axial direction.

It has been shown that the temperature field calculated by the 3D model can be approximated quite well by a 1D model, when certain assumptions are made regarding the materials properties averaging and the manner in which the heat generation rate is calculated. This is an important issue, since a 1D GFR-fuel model can be easily set up in system behavior codes such as TRACE or CATHARE. Usage of the 3D model for more detailed understanding of the heat transfer phenomena has

thus resulted in useful recommendations for achieving improved accuracies in fuel temperature predictions with a simplified 1D model.

The 3D model was also used for some detailed investigations of the GFR fuel mechanical behavior, leading to certain recommendations for design improvement. Thus, it was shown that cusping of fuel pellet corners can occur in the axial direction, which would result in stress concentrations leading to possible material failure. Detailed investigations have provided two solutions of the problem. The first is to have an appropriate fuel pellet shape: having convex, rather than flat pellet-ends would enhance the contact area and reduce the peak stress values considerably.

The second way to reduce the pellet-clad interaction is to ensure that the gas gaps in the honeycomb cell remain open throughout the fuel residence time in the reactor. The corresponding calculations for the reference fuel design have shown that the goal can be achieved by decreasing the pellet height while increasing its radius. The disadvantage is the reduced axial-gap size, which would cause higher fuel temperatures at the beginning of cycle. For the hottest point, the differences can reach 150-200°C. However, fuel swelling later drives the temperatures down and, after a certain point, they reach similar values as for the reference design.

REFERENCES

1.   ANSYS Basic Analysis Guide, ANSYS Release 9.0, ANSYS, Inc., November 2004.

2.   J.C. Garnier, C. Bassi, M. Blanc, J.C. Bosq, N. Chauvin, P. Dumaz, J.Y. Malo, B. Mathieu, A. Messié, L. Nicolas, A. Ravenet, "Contribution to GFR design option selection", Proceedings of ICAPP '06, Paper 6147, Reno, NV USA, June 4-8, 2006.

3.   N. Chauvin, J.Y. Malo, J.C. Garnier, F. Bertrand, J.C. Bosq, A. Ravenet, D. Lorenzo, M. Pelletier, J.M. Escleine, I. Munoz, J.M. Bonnerot, "GFR Fuel And Core Pre-Conceptual Design Studies", Proceedings of GLOBAL 2007, Boise, Idaho, USA, Sept. 9-13, 2007.

4.   J.C. Bosq, Y. Peneliau, G. Rimpault, M. Vanier, "Fine 3D neutronic characterization of a gas-cooled fast reactor based on plate-type subassemblies", PHYSOR-2006, Vancouver, BC, Canada, September 10-14, 2006

5.   P. Dumaz, P. Allegre, C. Bassi, T. Cadiou, A. Conti, J.C. Garnier, J.Y. Malo, A. Tosello, "Gas-cooled fast reactors – Status of CEA preliminary design studies", Nuclear Engineering and Design 237 (2007) 1618–1627, 2007

6.   P. Petkevich, K. Mikityuk, P. Coddington, R. Chawla. "Development and benchmarking of a 2D transient thermal model for GFR plate-type fuel", Annals of Nuclear Energy 34, pp. 707-718, 2007.

7.   F. Odar, C. Murray, R. Shumway, M. Bolander, D. Barber, J. Mahaffy. "TRACE V4.0 USER'S MANUAL". U.S. Nuclear Regulatory Commission, Office of Nuclear Regulatory Research, 2003.

8.   P. Petkevich, K. Mikityuk, P. Coddington, R. Chawla. "GFR transient analysis employing a 2D thermo-mechanical model for the plate-type fuel", PHYSOR-2008, Interlaken, Switzerland, September 14-19.

9.   D.R. Olander. "Fundamental Aspects of Nuclear Reactor Fuel Elements", Department of Nuclear Engineering, University of California, Berkeley, 1976.

10. P. Petkevich, K. Mikityuk, P. Coddington, P. Pelloni, R. Chawla. "Comparative Transient Analysis of a Gas-cooled Fast Reactor for Different Fuel Types". Proceedings of ICAPP'06, Paper 6312, Reno, NV USA, June 4-8, 2006

11. D.F. da Cruz, A. Hogenbirk, J.C. Bosq, G. Rimpault, G. Prulhiere, P. Morris, "Neutronic benchmark on the 2400 MW gas-cooled fast reactor design", PHYSOR-2006, Vancouver, BC, Canada, September 10-14, 2006

12. T. Shimoo, H. Takeuchi, K. Okamura, "Thermal Stability of Polycarbosilane-Derived Silicon Carbide Fibers under Reduced Pressures", J. Am. Ceram. Soc., 84, 3, 566–70, 2001

13. R.H. Jones et al., "Recent advances in the development of SiC/SiC as a fusion structural material", Fusion Engineering and Design, 41, 15–24, 1998

14. T. Preusser, "Modelling of Carbide Fuel Rods", Nucl. Technol. 57, 343, 1982

5 APPLICATION OF THE NEW THERMO-MECHANICAL MODEL TO GFR TRANSIENT ANALYSIS

The development and benchmarking of the new thermo-mechanical model for plate-type GFR fuel have been described in the preceding two chapters. The principal features of the model are:

- discretization of the GFR fuel plate into several independent regions and analysis of a single representative honeycomb cell for each of them,

- reduction of the hexagonal geometry to 2D R-Z for calculating the temperature field,

- calculation of the fuel and matrix deformations from the viewpoint of assessing gas pressure, pellet matrix interaction, etc.,

- accounting for the change of the materials properties with burnup,

- calculation of the fuel swelling and fission gas release.

The present chapter is devoted to the application of the developed model to investigations of GFR transient behavior. This has been done in the framework of the PSI coupled code system FAST, the overall calculational methodology for which was described in Chapter 3. The present analysis is aimed at the comparison of two different types of solutions, viz. those obtained using:

- the system code (TRACE) in conjunction with a homogenized model of a fuel plate (1D treatment),

- an explicit coupling of the new FRED model with TRACE, implying a more accurate treatment of the honeycomb structure of the fuel plate (2D analysis).

Following a listing of the types of reference transients considered (Section 5.1), Section 5.2 briefly describes the simulation methodology which has been applied. The transient analysis results are presented for beginning-of-life conditions in Section 5.3, while those for end of cycle are presented in Section 5.4.

5.1   TRANSIENTS ANALYZED

As indicated, the main aim of the present chapter is to underline the improved accuracy in predictions for GFR transient behavior, which are rendered possible by use of the currently developed thermo-mechanical fuel model. For this purpose, comparisons with the simplified 1D model have been made for the calculation of a series of both fast and slow transient types, viz.

- unprotected transient overpower (UTOP),

- unprotected core overcooling (UOVC),

- unprotected loss of heat sink (ULOHS),

- unprotected loss of flow (ULOF).

The UTOP accident event was analyzed to determine the response of the GFR core to a reactivity insertion. The case considered is the insertion of a reactivity of 1 dollar over 1 second (see Fig. 5.1a).

The UOVC transient was calculated to determine the response of the GFR core to a decrease of the inlet coolant temperature. The inlet temperature was decreased by 100 K from the nominal value in 30s (see Fig. 5.1b).

The ULOHS accident event was analyzed to examine the response of the GFR core to an increase of the inlet coolant temperature. The inlet temperature was increased by 100 K from nominal value in 30 s (see Fig. 5.1c).

The ULOF transient was calculated to examine the response of the GFR core to a reduction of the coolant flowrate. The core mass flowrate was specified as a boundary condition: it was assumed to reduce by a factor of 2 every 30 s, while the asymptotic value (the natural circulation level) was set to be 5% of the nominal value (see Fig. 5.1d).
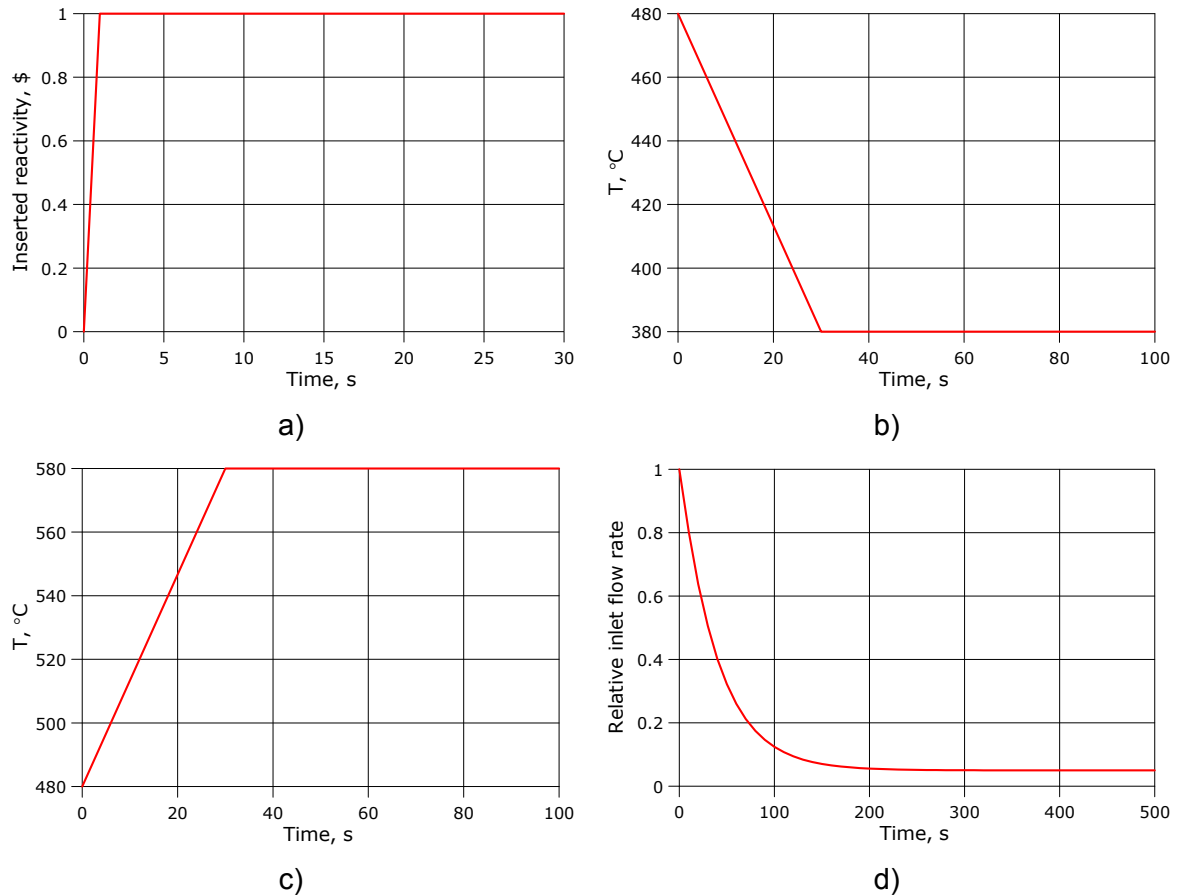
Fig. 5.1. Conditions assumed for the analyzed transients: a) inserted reactivity for UTOP, b) core inlet temperature for UOVC, c) core inlet temperature for ULOHS, d) relative coolant mass flow rate for ULOF (Zero time refers to the steady-state conditions.)

5.2   SIMULATION METHODOLOGY

As mentioned, all the transients were analyzed without scramming the reactor. The reactor's primary and secondary circuits were not taken into account explicitly (they are effectively represented by the core inlet and outlet boundary conditions), the main purpose being to analyze the differences in the results introduced by the differences in modeling the plate-type fuel. The overall calculating scheme is described in Chapter 3 and shown in Fig 3.10.

5.2.1   System modeling

The system modeling was done with the TRACE code [2], which can be either run as stand-alone (1D modeling) or in a coupled mode using the extended FRED code, i.e.

the new version including subroutines for considering the honeycomb structure of the plate-type fuel [3, 4] (2D modeling).

The reactor core was represented in TRACE by 14 parallel channels, one of which represents a hot assembly. The nodalization diagram is shown in Fig. 5.2.
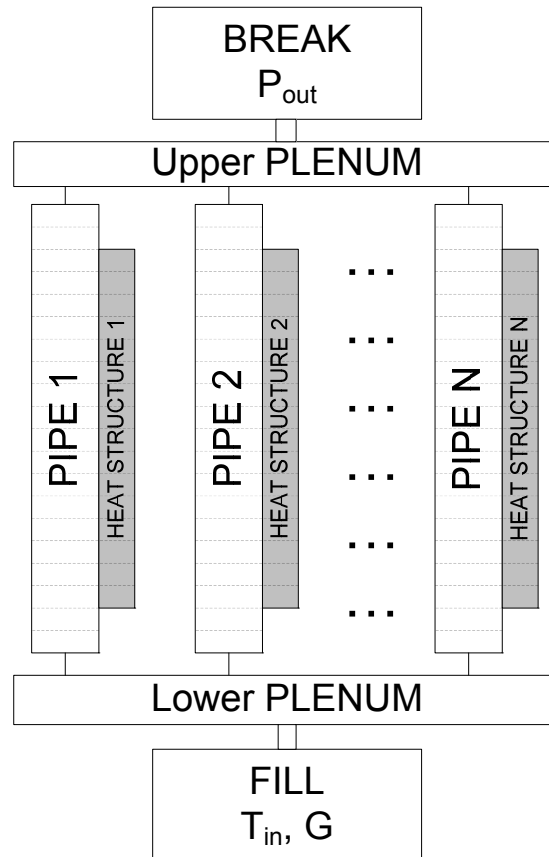

Fig. 5.2. TRACE model nodalization diagram

Each heat structure represents a fuel plate. Its inner zone is homogenized, and the properties are averaged as described in Chapter 3 (Eq. 3.3).

The gas gap conductance is calculated in TRACE as:

$$\alpha = \frac{\lambda}{\delta_{gap} + \delta_r} + \alpha_{rad}$$

where

λ: gas gap thermal conductivity

δ_{gap}:   gas gap width

δ_r: factor including the mean surface roughness.

The radiation heat α_{rad} transfer for the plate geometry is assessed as:

$$\alpha_{rad} = \frac{\sigma \cdot \dfrac{\varepsilon_f \cdot \varepsilon_c}{\varepsilon_f + \varepsilon_c - \varepsilon_f \cdot \varepsilon_c} \cdot \left(T_f^4 - T_c^4\right)}{T_f - T_c}$$

Eq.

5.1

where

σ: Stefan-Boltzmann constant

ε_f, ε_c: fuel and cladding emissivities

T_f, T_c: temperatures of the fuel outer and cladding inner surfaces.

As the emissivities of the GFR materials are not well known, the limiting case was assessed with both fuel and cladding emissivities set equal to 1. For operating conditions and temperatures typical for the GFR, the radiation conductance calculated according to Eq. (5.1) is about 3% of the conductance determined by the gas thermal conductivity. Thus, even such conservative estimations show that the radiation heat transfer has a minor influence on the temperature field and can be neglected. For the same reason, radiation was not taken into account by the FRED model.

5.2.2   Kinetic parameters preparation

The ERANOS (Version 2) code system [5] has been used to perform the steady-state neutronic calculations necessary for the transient analysis, viz. the spatial power distribution, the neutron kinetics parameters, reactivity coefficients, etc. The reactor geometry was simulated using a detailed 3D core model [6]. Core-average reactivity effects were assessed by means of additional calculations for modified core conditions. These include reactivity variations as a result of homogeneous changes of the fuel temperature or of coolant density, as well as those originating from thermo-mechanical expansion of the core in both the radial and axial direction (under the main assumption that the fuel mass is preserved). A more detailed description of the parameters evaluation is provided in Chapter 2. The numerical values used for the kinetics parameters and reactivity coefficients are presented in Table 5.1 [6].

Table 5.1. Kinetics parameters and reactivity coefficients for the GFR core (fresh fuel)

Parameter	Value
Doppler constant[a], pcm[b]	-1797
Core radial expansion, pcm/K	-0.439
Core axial expansion, pcm/K	-0.111
β_{eff}, pcm	385.4
Λ, µs	0.901

[a]   Reactivity assumed to be a logarithmic function of fuel temperature: $\Delta\rho(T_0 \to T) = K_D \cdot \ln(T/T_0)$, where K_D is the Doppler constant, T is the temperature in K

[b]   1 pcm = $10^{-5}\,\Delta(1/k_{eff})$

As seen from Table 5.1, an important feature of the GFR core is that the magnitude of the Doppler constant is considerably greater than in a fast-spectrum core with oxide fuel and stainless steel cladding. This results from the considerably softer neutron spectrum caused by the carbon-based matrix material [7, 8].

An important remark has to be made about the axial core expansion reactivity effect. In fast reactors with traditional (rodded) fuel, the axial core expansion is determined either by fuel swelling and thermal expansion in the open-gap regime, or by fuel/clad expansion (closed gap). This is not the case for the GFR core due to the particular fuel design. The fuel deformation is accommodated by the free space within a cell (see Fig 4.26), and the axial expansion of the fuel plate is mainly determined by the thermal deformation of the SiC matrix. The original TRACE code was modified to provide the possibility for a choice between the two options. A matrix driven, core axial expansion was used for the present analysis.

As regards the radial expansion, this is assumed to be driven by the diagrid expansion, i.e. by coolant inlet temperature, and is thus the same for both models. For this reason, the corresponding reactivity component has not been explicitly presented in the plots while discussing the results.

5.3   TRANSIENTS AT THE BEGINNING OF CYCLE (BOC)

The presented results include the evolution of the following parameters: total reactor power, total reactivity, fuel temperature (Doppler) reactivity effect, axial core expansion reactivity effect, peak fuel temperature, and peak cladding temperature (temperature at the lateral-wall inner surface).

154

The various results for the transients are shown for different analysis options. In each case, the blue curve (referred to as "TRACE") represents the results obtained with the homogeneous 1D TRACE model. The green curve (referred to as "mech=OFF") shows the FRED 2D model results when only the thermal module is used and the mechanics is not calculated (no deformations); this is done in order to reveal the geometry homogenization effect on the temperature field. The red curve (referred to as "mech=ON") corresponds to the full usage of the 2D thermo-mechanical module, thus showing the net differences between the simplified and detailed models.

5.3.1   Steady-state analysis

Fig. 5.3 shows the steady-state temperature field at the hottest point in the core. Here, the dark green curve refers to the 1D TRACE model while the other curves are the results of the 2D FRED analysis. The red line is the temperature distribution along the cell axis, and the blue line that for the radial position corresponding to the fuel pellet boundary.
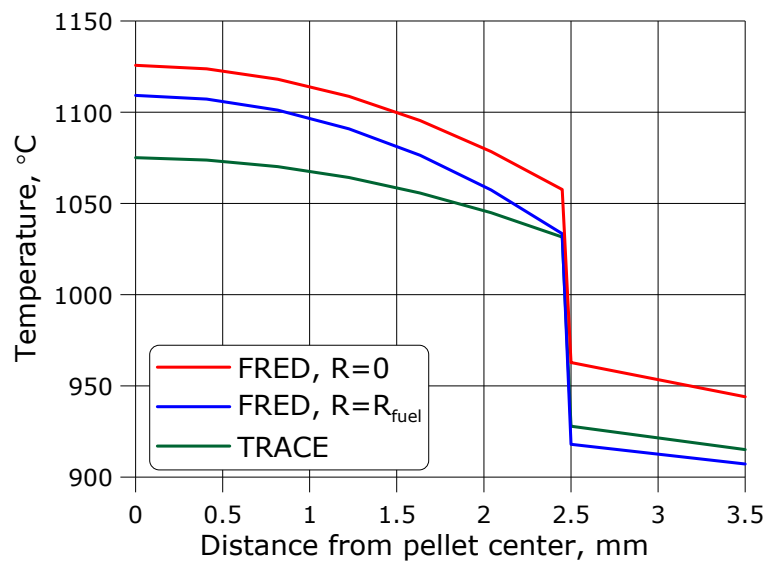

Fig. 5.3. Steady-state temperature profiles in the hottest cell

As can be seen, the temperature gradients in the fuel are lower for the TRACE model. This is a result of the cell homogenization and the corresponding decrease of the heat generation rate. The temperature drop across the gas gap is also lower due to the lower heat fluxes. This is a good illustration of the phenomena which were described in Section 4.3.3 (recommendations for 1D modeling).

5.3.2 UTOP

The results for this transient are shown in Fig. 5.4 to Fig. 5.6. The first figure presents the core power and the total reactivity, the second the fuel temperature feedback and the axial core expansion effect, while the third shows the peak fuel and cladding temperatures.
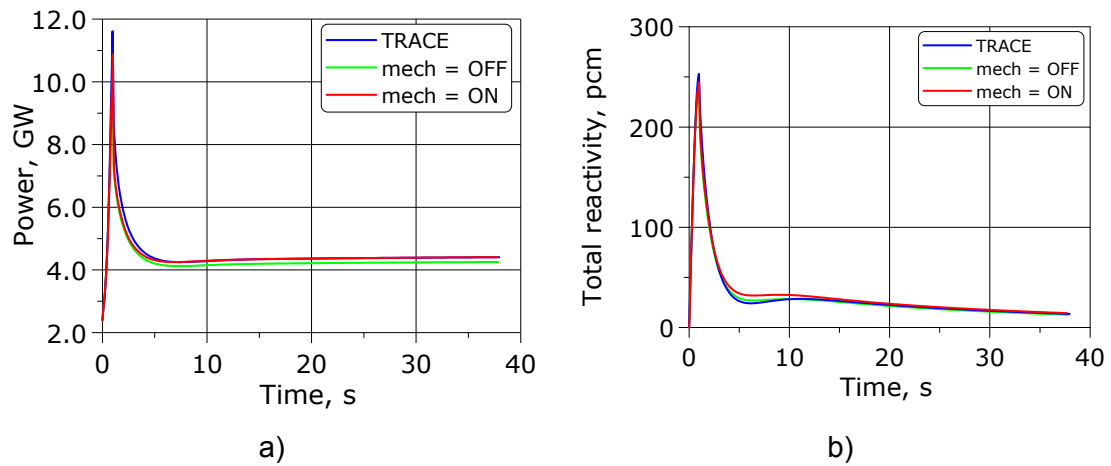

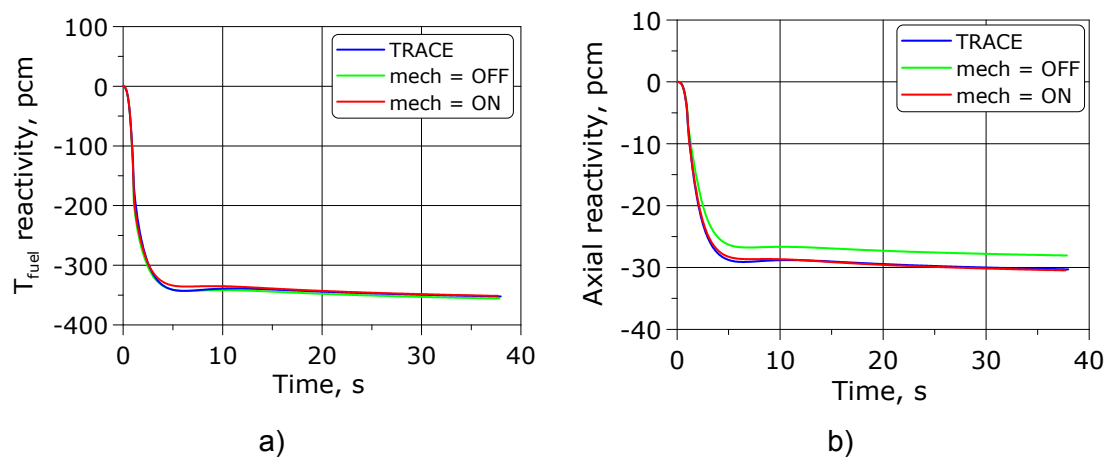**Fig. 5.4. a) Core power and b) total reactivity during the UTOP transient**

Fig. 5.5. a) Fuel temperature and b) axial core expansion reactivity effects during the UTOP transient
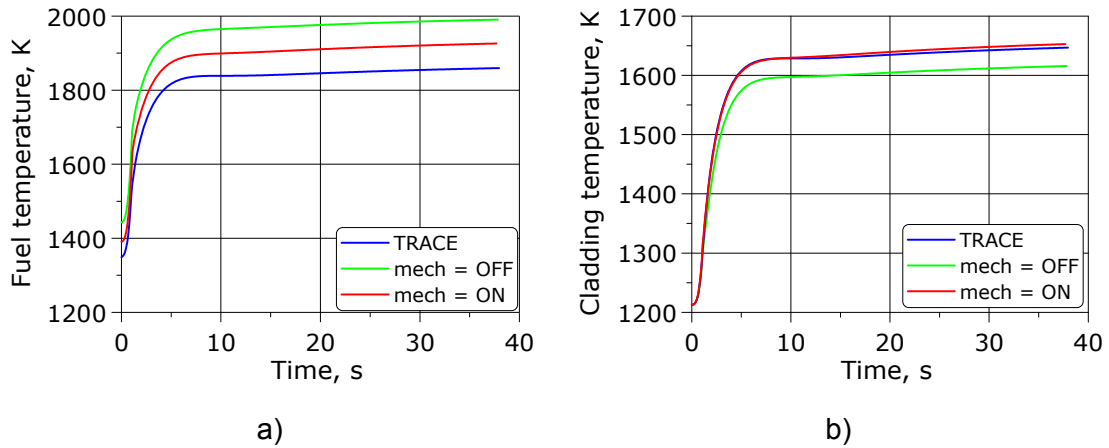
Fig. 5.6. Peak a) fuel and b) cladding temperatures during the UTOP

The power increases by 5 times during the first second of the transient and, after 10 seconds, stabilizes at approximately 175% of nominal power. The rapid decrease of power is caused by the rapid fuel heating (Fig. 5.6a) and the resulting strong Doppler feedback, which makes the major contribution (~ 90%) to the total reactivity change.

5.3.3 UOVC

The results for this transient are shown in Fig. 5.7 to Fig. 5.9. Again, the first figure presents the core power and the total reactivity, the second the fuel temperature feedback and the axial core expansion effect, while the third shows the peak fuel and cladding temperatures.
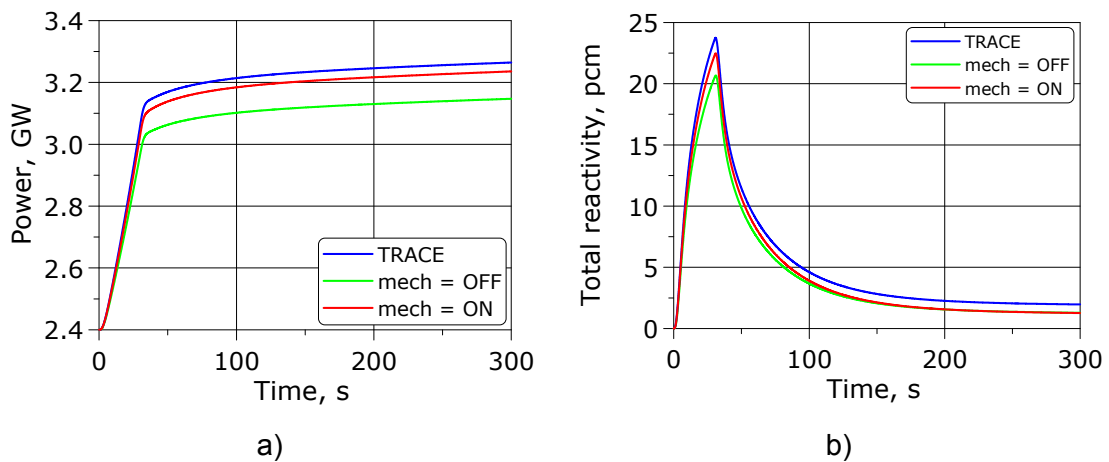

Fig. 5.7. a) Core power and b) total reactivity during the UOVC transient
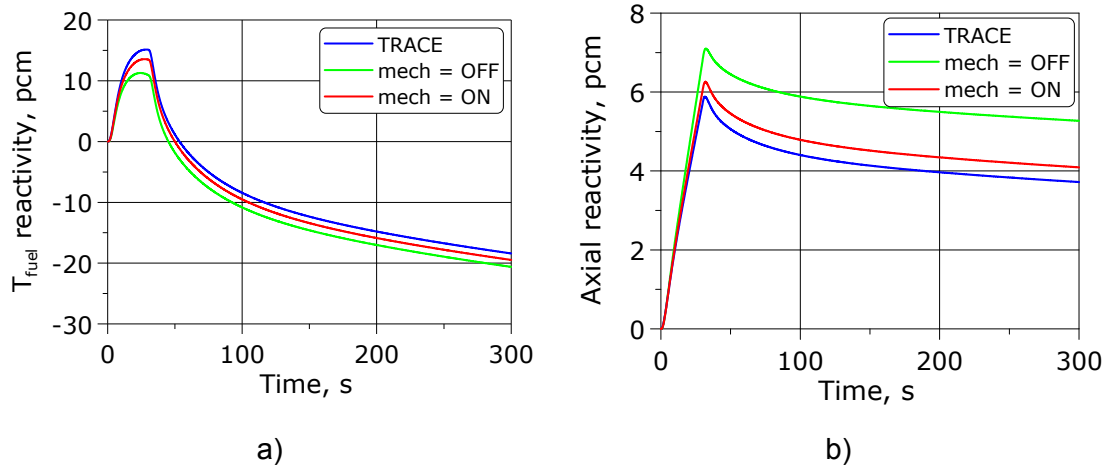
Fig. 5.8. a) Fuel temperature and b) axial core expansion reactivity effects during the UOVC transient
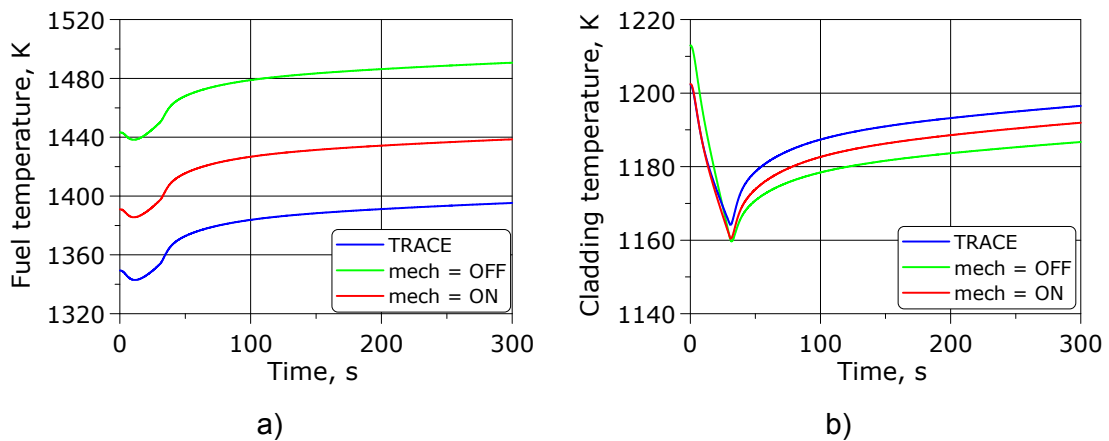

Fig. 5.9. Peak a) fuel and b) cladding temperatures during the UOVC transient

The decrease of the core inlet temperature is followed by the decrease of the fuel and cladding temperatures. Both effects lead to a positive reactivity insertion (see Fig. 5.8a, Fig. 5.8b). This positive reactivity, together with the stabilization of the inlet temperature (at 30s), leads to fuel and cladding temperatures increases and correspondingly to the decrease of the total reactivity and stabilization of the core power at about 130-140% of the nominal value. The differences between the models are more pronounced here than in the UTOP case. As previously, the 2D modeling of the fuel thermal expansion compensates somewhat for the geometry effect on the temperature field, so that the final TRACE and FRED (full thermo-mechanical model) results are quite close. The largest difference is obtained for the peak fuel temperature, the FRED predicted value being about 45K higher then that of TRACE throughout the transient.

5.3.4 ULOHS

The results for this transient are shown in Fig. 5.10 to Fig. 5.12. As before, the first figure presents the core power and the total reactivity, the second the fuel temperature feedback and the axial core expansion effect, while the third shows the peak fuel and cladding temperatures.

Fig. 5.10. a) Core power and b) total reactivity during the ULOHS transient

Fig. 5.11. a) Fuel temperature and b) axial core expansion reactivity effects during the ULOHS transient
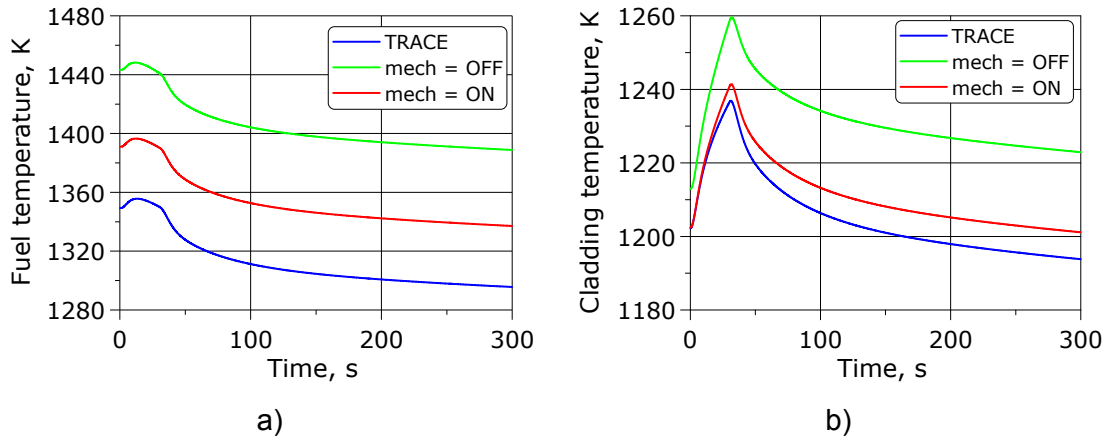
Fig. 5.12. Peak a) fuel and b) cladding temperatures during the ULOHS transient

In this case, the increase of the core inlet temperature is followed by the increase of the fuel and cladding temperatures. Both effects lead to the insertion of negative reactivity (see Fig. 5.11a, Fig. 5.11b). This, together with the stabilization of the inlet temperature (at 30s), leads to a decrease of the fuel and cladding temperatures, and correspondingly to an increase in total reactivity. The core power then stabilizes about 60-70% of the nominal value. The transient behavior is very similar to the UOVC case, the major difference being the sign of the inserted reactivity and the corresponding "inversion" of the various effects. As for the UOVC, the full thermo-mechanical model provides results which are very close to those of TRACE due to compensating effects. The largest difference is again obtained for the peak fuel temperature, the FRED predicted value being about 45K higher then that of TRACE.

5.3.5 ULOF

The results for this transient are shown in Fig. 5.13 to Fig. 5.15. Once again, the first figure presents the core power and the total reactivity, the second the fuel temperature feedback and the axial core expansion effect, while the third shows the peak fuel and cladding temperatures.
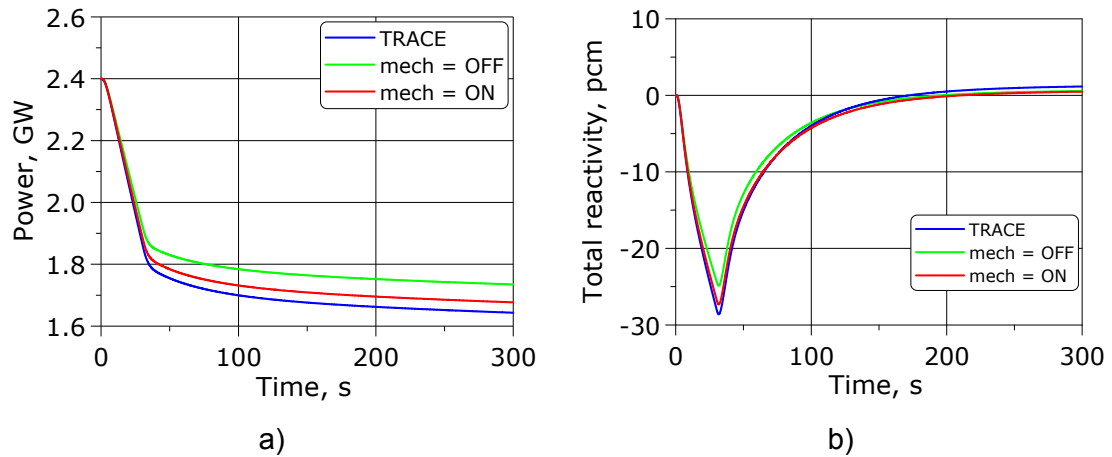
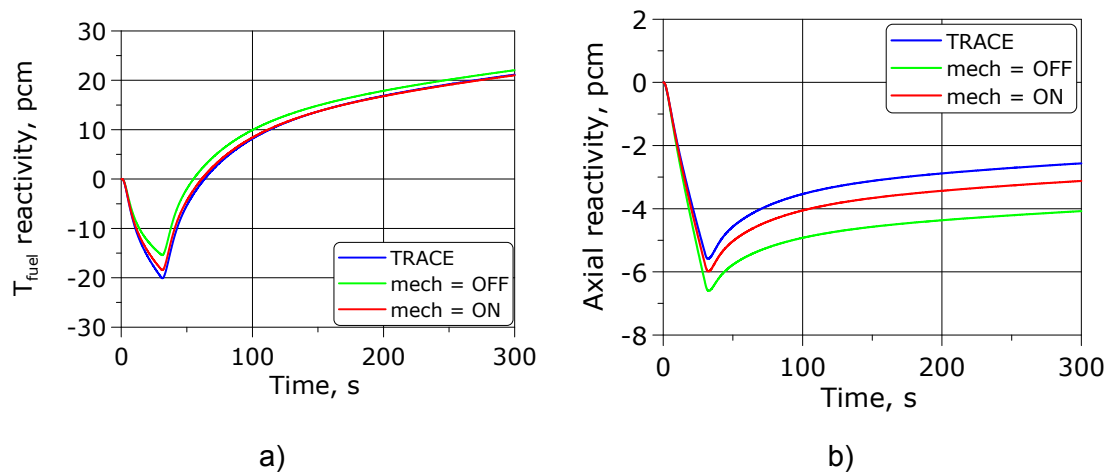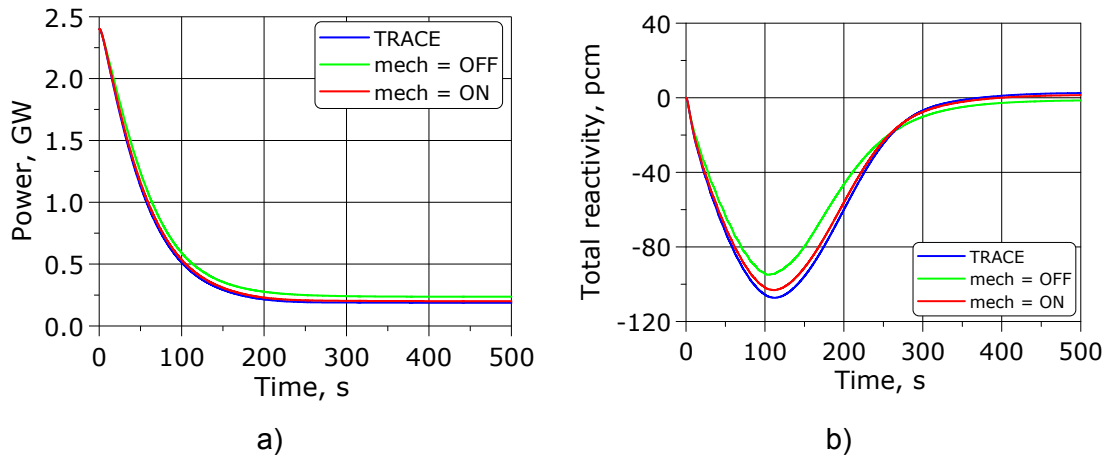Fig. 5.13. a) Core power and b) total reactivity during the ULOF transient
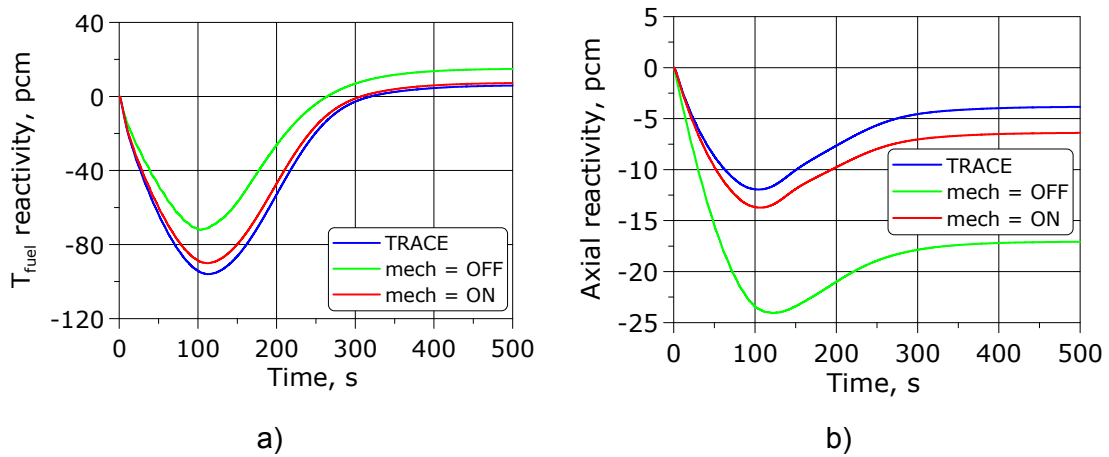

Fig. 5.14. a) Fuel temperature and b) axial core expansion reactivity effects during the ULOF transient
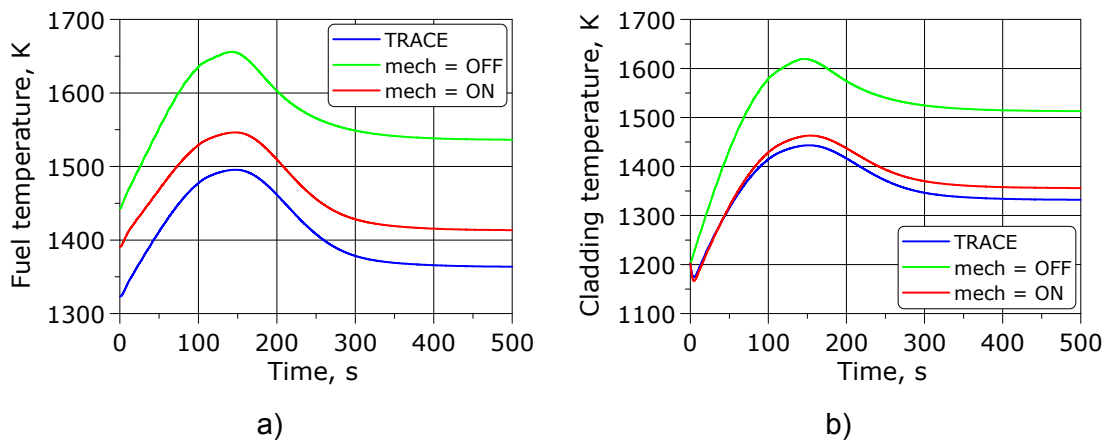

Fig. 5.15. Peak a) fuel and b) cladding temperatures during the ULOF transient

The loss of flow leads to a deterioration of the heat removal, thus causing increases of the fuel, cladding and coolant temperatures. The fuel heat-up leads to the insertion of negative reactivity and a reduction of the core power. The negative Doppler and axial core expansion reactivity effects reduce the core power to ~10% of the nominal value.

As in the transients described earlier, the geometry effect on the temperatures and reactivity is mitigated by that on the fuel thermal expansion, so that the power and total reactivity evolution appears similar between TRACE and the full 2D FRED treatment. The difference between the peak fuel temperatures is about 60K in this case, and again preserved throughout the transient.

5.3.6   Discussion of the results obtained for the BOC transients

As can be seen from the plots above, the 1D TRACE model in general underpredicts the temperatures for all the considered transients. The discrepancies between the temperature field predictions of the homogeneous and heterogeneous models occur due to multidimensional heat transfer in the cell which is taken into account by the latter. This effect was described and investigated in detail in the previous chapters. Thus, it was shown that, for certain conditions, when the radial gas gap and the fuel pellet radius-to-height (R/H) ratio are relatively small, the radial heat fluxes play a significant role in pellet cooling, yielding lower temperatures compared to the homogenized cell. When the R/H or the radial gas gap increases, the radial fuel boundary acts almost adiabatically, yielding higher temperatures. Fig. 4.16 – Fig. 4.19 show the effects in a qualitative manner.

As mentioned, the 1D model predictions were compared against the detailed model with the mechanical module switched either on or off. The largest 1D/2D discrepancies are obtained in the case of the purely thermal modeling. These are of the order of 100K. When the mechanics is switched on, the axial gas gaps become smaller due to fuel and matrix deformations which lead to enhancement of the heat transfer, and the temperatures go down, i.e. become closer to the 1D model results. This compensating effect results in the overall 1D/2D difference being quite moderate (typically 40-60K).

An important remark needs to be made with respect to the 1D model usage. The simplifications introduced in this context (mainly concerning the materials properties and heat transfer through the gas gap) affect the results significantly. The comparison of two different 1D fuel models (carried out using two different codes, TRACE and CATHARE) was reported in [8]. Differences of up to 200K were obtained for the fuel and cladding temperatures during some of the transients. This underlines the importance of the assumptions made in the 1D modeling.

162

It needs to be emphasized that the currently reported fuel and core behavior results, as also the 1D/2D differences, are only valid for the specific geometry used in the present analysis and for the material properties averaging procedure described in Section 3.3.1. Should one change the fuel and cell dimensions, the statements made here may no longer be correct.

The advantage of the 2D FRED model is that it can be expected to provide a reliable solution for any given design of the plate-type fuel, since the honeycomb structure geometry is explicitly taken into account. 1D-model predictions, on the other hand, would always need to be compared to a detailed solution to ensure that the honeycomb structure homogenization has been done in a reasonable manner.

It also needs to be mentioned that point kinetics has been used for the present transient analysis and hence, reactivity effects have been determined on the basis of the average temperature changes. Further, a given effect depends more on the *dT/dt* than on the exact temperature values. With there being no strong nonlinearities in the GFR materials properties (e.g. thermal conductivity), the rate of temperature change is almost the same for the 1D and 2D models.

As indicated, the major 1D/2D differences are obtained between the purely thermal (mech=OFF) models. The differences in cladding temperature result in significant differences in the core expansion effect. This is important for the transients where the axial core expansion and Doppler effects are of the same order of magnitude (UOVC and ULOHS). For the UTOP, the Doppler effect is much larger than the axial core expansion effect. Thus, in this case, the total reactivity is mostly determined by the fuel temperature evolution. The calculated fuel temperature change rate is then very similar for the 1D and 2D models, resulting in almost the same evolutions of the total reactivity and thus of the core power.

5.4   TRANSIENTS AT THE END OF CYCLE (EOC)

The crucial point for the end-of-cycle analysis is the axial gas gap closure due to fuel swelling, which significantly enhances the heat transfer. Realistic predictions of the core behavior are of secondary importance in the present research, since the main aim is to underline the impact of using the more accurate 2D thermo-mechanical model for the fuel. Accordingly, the analysis of the transients at EOC has been carried out largely from the viewpoint of assessing the effects of pellet-cladding contact; the kinetic parameters at EOC have been assumed to be the same as for the fresh fuel (see Table 5.1).

5.4.1   Steady-state analysis

The steady-state temperature profiles for the hottest cell at EOC are shown in Fig. 5.16. The temperature drop across the closed gap is caused by the roughnesses of the materials surfaces.
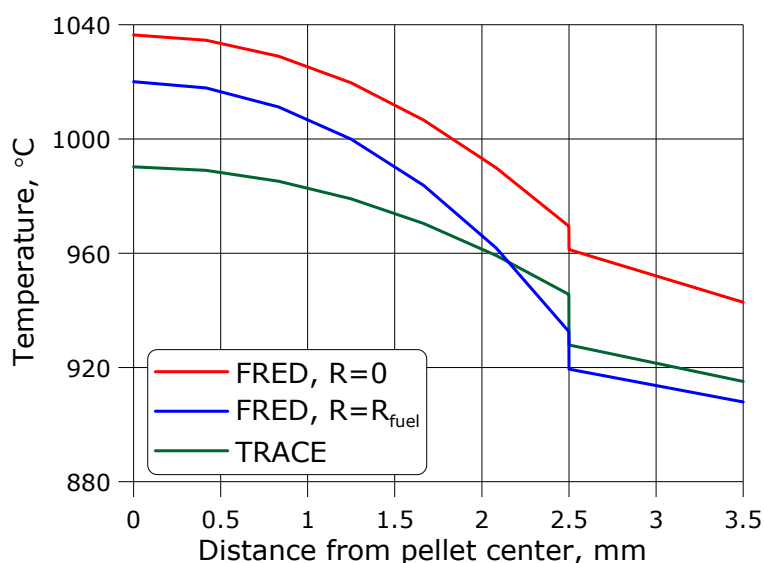
Fig. 5.16. Steady-state temperature profile in the hottest cell at EOC

The slightly higher temperature drop predicted by the 1D model can be explained by the peculiarities of the mathematical model implemented in TRACE. As previously, the peak fuel temperature is underpredicted by the homogeneous model.

164

5.4.2   UTOP

The results for this transient are shown in Fig. 5.17 to Fig. 5.19. As in the BOC cases, the first figure presents the core power and the total reactivity, the second the fuel temperature feedback and the axial core expansion effect, while the third shows the peak fuel and cladding temperatures.

a)   b)

Fig. 5.17. a) Core power and b) total reactivity during the UTOP transient at EOC

a)   b)

Fig. 5.18. a) Fuel temperature and b) axial core expansion reactivity effects during the UTOP transient at EOC
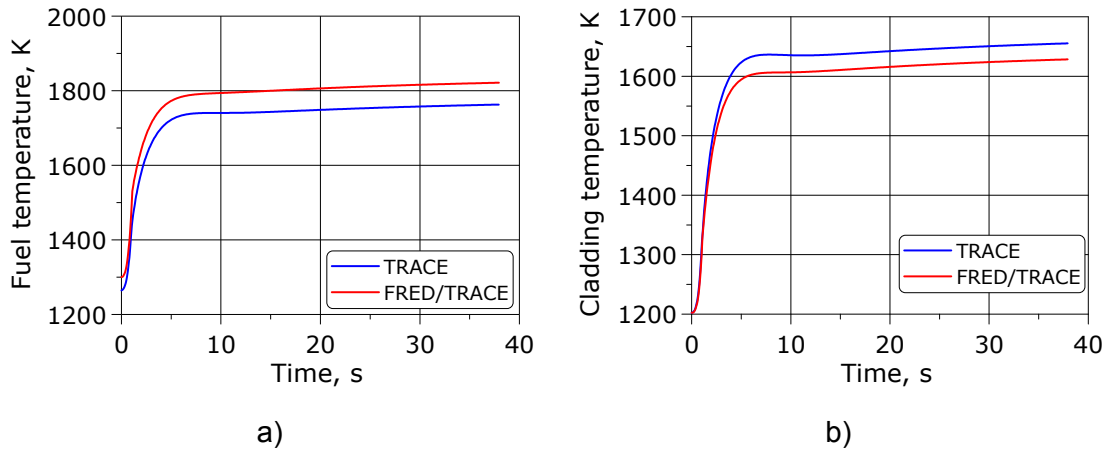
Fig. 5.19. Peak a) fuel and b) cladding temperatures during the UTOP transient at EOC

The GFR behavior during UTOP at EOC is very similar to that at BOC. As previously, the power increases by an order of magnitude during the first second of the transient and, after 10 seconds, stabilizes at approximately 175% of nominal power. The rapid decrease of power is caused by the rapid fuel heating (Fig. 5.6a), the corresponding Doppler effect accounting for ~ 90% of the total reactivity change.

5.4.3   UOVC

The results for this transient are shown in Fig. 5.20 to Fig. 5.22. Again, the first figure presents the core power and the total reactivity, the second the fuel temperature feedback and the axial core expansion effect, while the third shows the peak fuel and cladding temperatures.

Fig. 5.20. a) Core power and b) total reactivity during the UOVC transient at EOC

Fig. 5.21. a) Fuel temperature and b) axial core expansion reactivity during the UOVC transient at EOC

Fig. 5.22. Peak a) fuel and b) cladding temperatures during the UOVC transient at EOC

5.4.4   ULOHS

The results for this transient are shown in Fig. 5.23 to Fig. 5.25. As before, the first figure presents the core power and the total reactivity, the second the fuel temperature feedback and the axial core expansion effect, while the third shows the peak fuel and cladding temperatures.
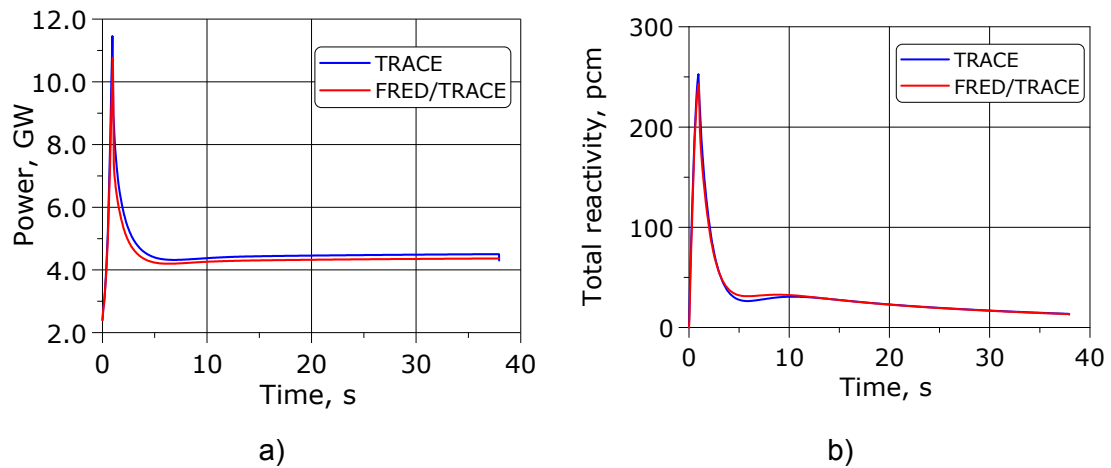
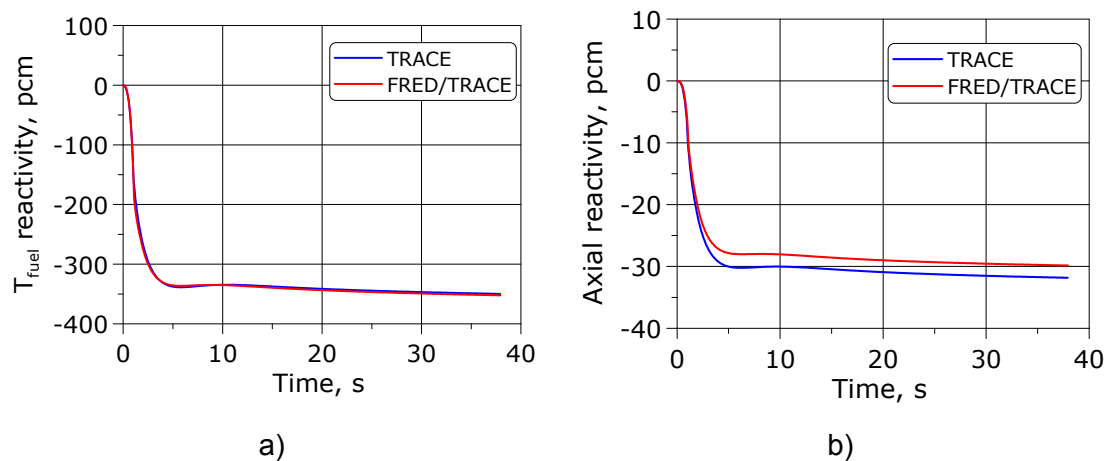**Fig. 5.23. a) Core power and b) total reactivity during the ULOHS transient at EOC**

**Fig. 5.24. a) Fuel temperature and b) axial core expansion reactivity effects during the ULOHS transient at EOC**
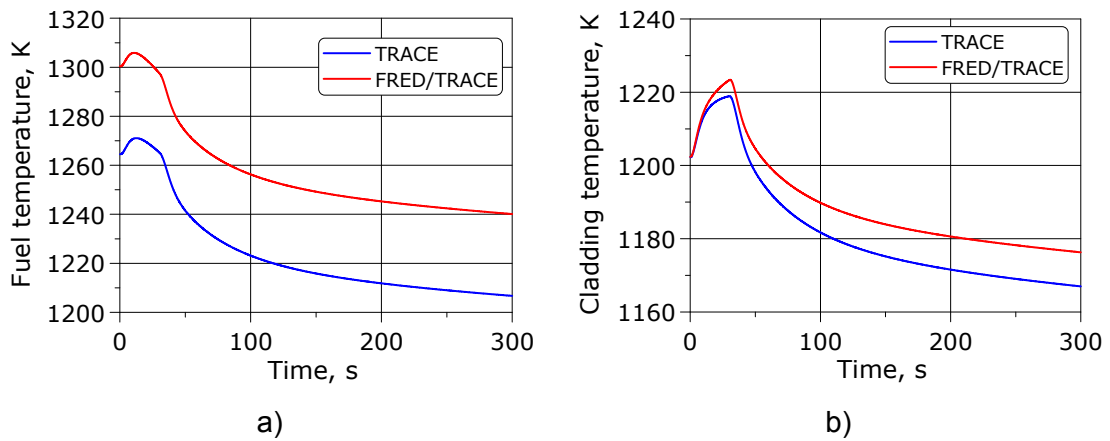
Fig. 5.25. Peak a) fuel and b) cladding temperatures during the ULOHS transient at EOC

5.4.5 ULOF

The results for this transient are shown in Fig. 5.20 to Fig. 5.22. Again, the first figure presents the core power and the total reactivity, the second the fuel temperature feedback and the axial core expansion effect, while the third shows the peak fuel and cladding temperatures.
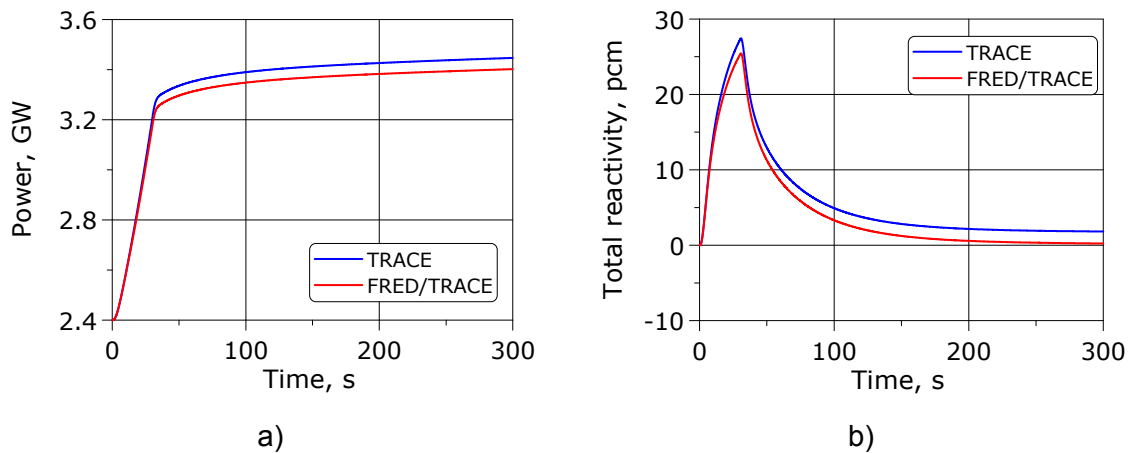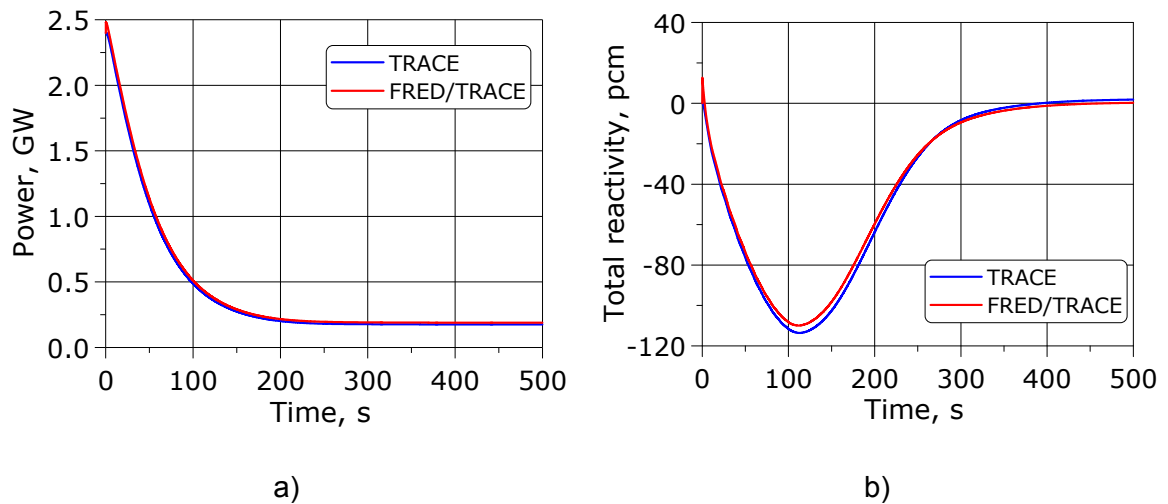

Fig. 5.26. a) Core power and b) total reactivity during the ULOF transient at EOC
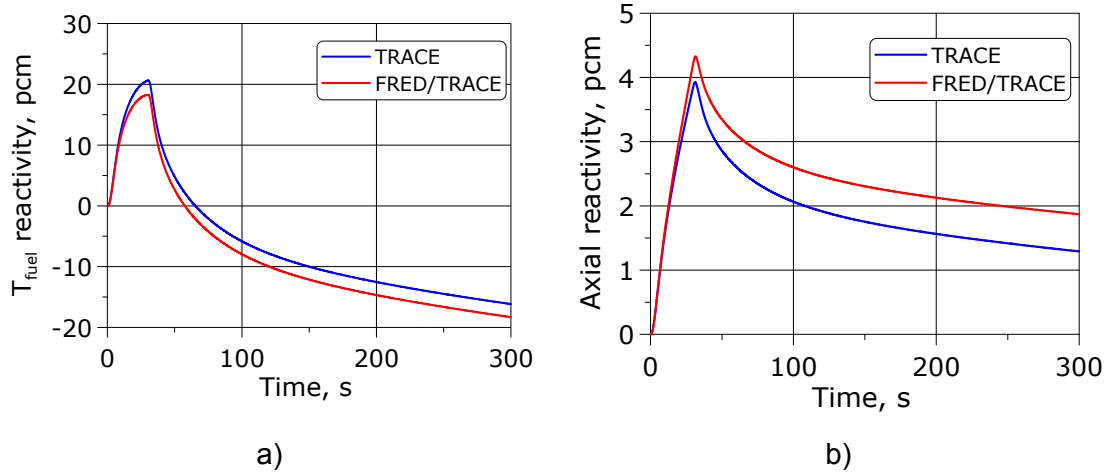

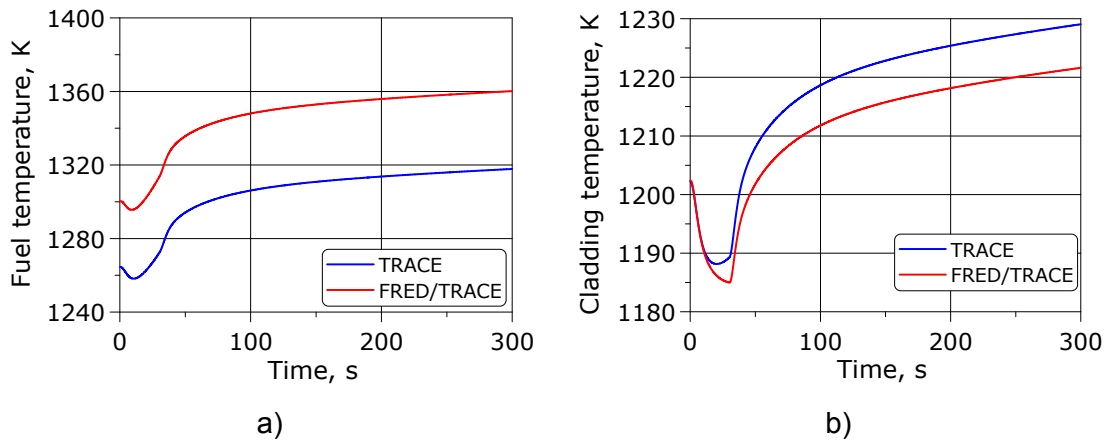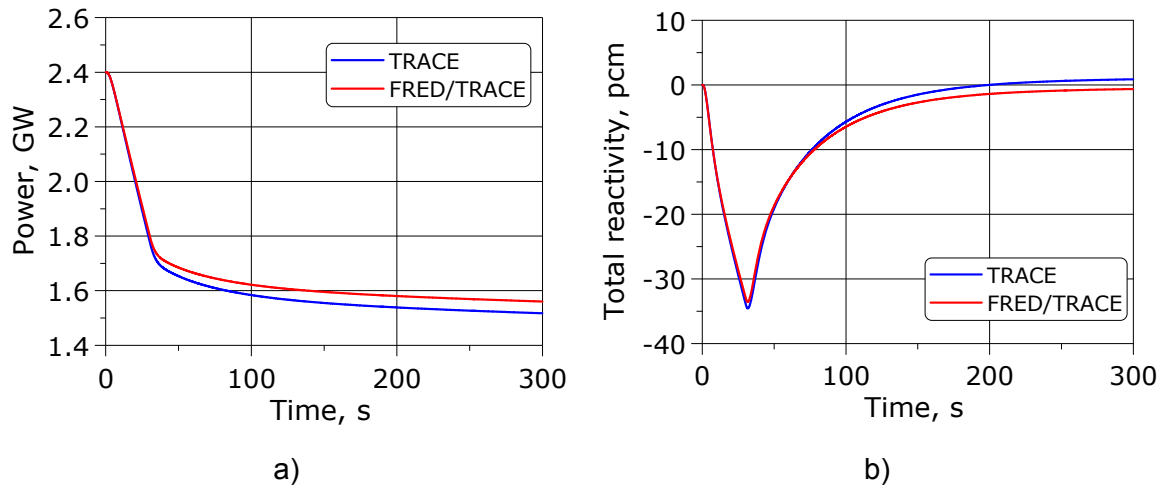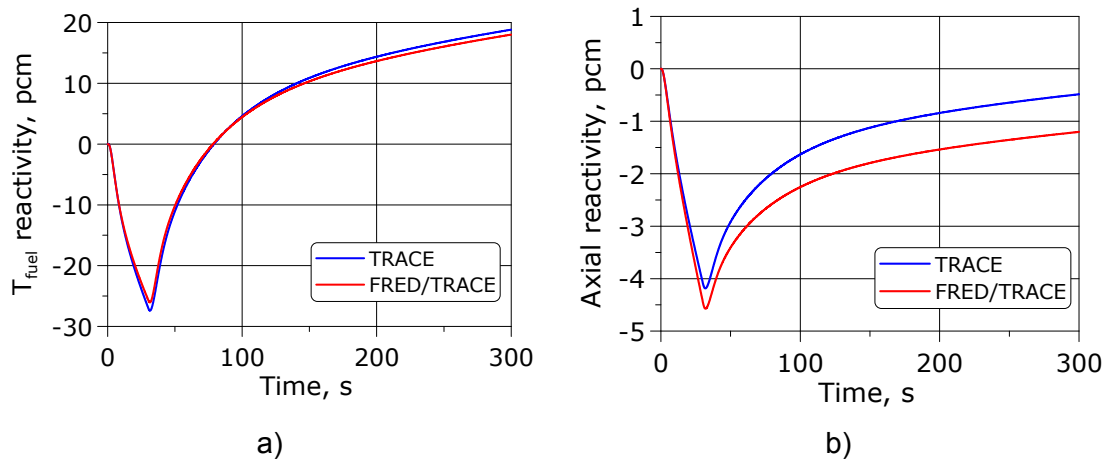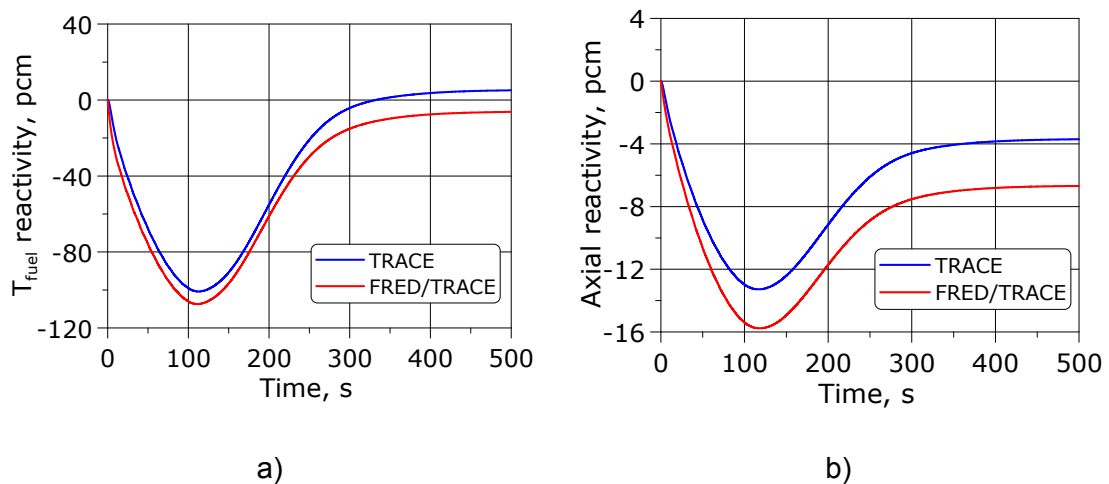**Fig. 5.27. a) Fuel temperature and b) axial core expansion reactivity effects during the ULOF transient at EOC**

a)   b)
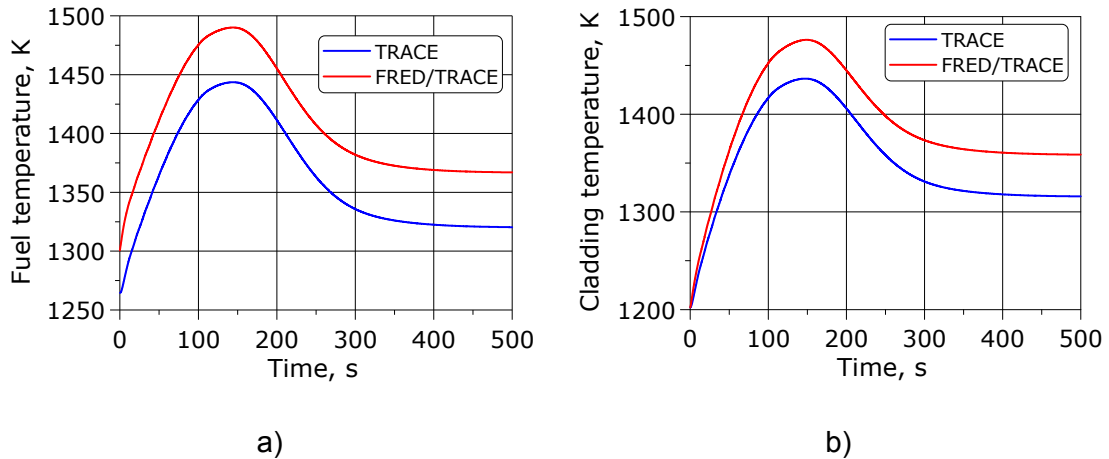
Fig. 5.28. Peak a) fuel and b) cladding temperatures during the ULOF transient at EOC

5.4.6   Discussion of the results obtained for the EOC transients

The core dynamics at EOC is very similar to that at BOC. The peak fuel temperatures are lower due to the gap closure, but the discrepancies between the different models are almost the same as for BOC. The common explanation lies, as discussed earlier, in the lower heat generation rate in the homogeneous model. The influence of the mechanical module was not analyzed separately, because the gap closure effect on the temperature field prevails over the impact of changes in the cell dimensions. Much of the conclusions to be drawn are thus similar to those made in Section 5.3.6.

5.5   SUMMARY

The present chapter was devoted to the application of the newly developed model for plate-type fuel to the analysis of a range of hypothetical GFR transients.

The aim has been to simulate the reactor behavior as close to reality as possible (so-called best estimate approach). Clearly, the reliability of a 1D treatment (homogenization of the inner structure) is disputable in this case. In the absence of appropriate experimental data to validate the codes, it is necessary to use either detailed mathematical models, which take the fuel peculiarities fully into account, or an appropriately simplified model which yields results in good agreement with the detailed solutions.

The developed 2D thermo-mechanical model was shown to provide results which are in good agreement with detailed 3D solutions. The principal difference between the homogenized (1D) and the newly developed (2D) models is the more realistic

temperature field predictions by the latter. The temperature field evolution drives the reactor feedbacks (which have been calculated in point-kinetics approximation in the present research). Major attention was paid to the Doppler effect (driven by the average fuel temperature) and to the axial core expansion feedback (driven by the cladding expansion).

A number of transients were calculated for both fresh fuel (BOC; pellet and cladding not in contact) and burnt fuel (EOC; pellet in hard contact with cladding), the differences between the two effectively reflecting the impact of gas gap closure and the corresponding heat transfer changes. Moreover, the BOC analysis was done with and without the accounting for fuel deformation effects. This enabled one to first see the pure geometry effect on the temperature field and then, separately, the influence of the pellet and cladding deformations.

The analysis has shown that, in all cases, the homogeneous model underpredicts the fuel temperatures. This is due to the heat generation being smeared over the entire cell crosscut and thus yielding correspondingly lower heat fluxes. The difference between the average temperatures remains almost constant during each transient.

The differences in the peak temperatures due to the geometry effect alone can be more than 100K. However, the deformation of the fuel and cladding decreases the gas gap and consequently decreases the temperature differences between the homogenized and newly developed models. This statement is valid for the given fuel design, with explicit consideration of the geometry resulting in higher temperatures for the detailed model. Should the temperatures predicted by the 2D model have been lower, the reduction of the gas gap would result in even lower temperatures and greater disagreement between the two models.

The present 1D/2D discrepancies in the relative power change during the UOVC and ULOHS transients, both at BOC and EOC, is up to about 5%. This is mainly determined by the differences in the cladding temperature, i.e. by the axial core expansion reactivity effect. The UTOP transient, on the other hand, is mainly influenced by the fuel temperature, i.e. the Doppler reactivity. While at BOC there is almost no difference in the power evolution between the homogeneous and new models, at EOC the relative power increase is about 7% lower with the 2D FRED treatment. For the ULOF transient, the differences in power evolution between the models are relatively small, viz. up to about 2%.

Thus, it is seen that the new model provides a more reliable estimation of the materials temperatures during a transient. These can be significantly different from the predictions of the homogeneous model, and moreover, the differences can be either positive or negative, depending on the geometry and boundary conditions. The discrepancies between the models are more moderate in the calculation of the reactivity feedbacks, since these depend more on dT/dt than on the absolute value of

temperature. For the considered transients, the differences in the relative power change were all less than 10%.

REFERENCES

1. K. Mikityuk, S. Pelloni, P. Coddington, E. Bubelis, R. Chawla, "FAST: An advanced code system for fast reactor transient analysis", Ann. Nucl. Energy, 32, 15, pp. 1613-1631, 2005.

2. F. Odar, C. Murray, R. Shumway, M. Bolander, D. Barber, J. Mahaffy, "TRACE V4.0 USER'S MANUAL", U.S. Nuclear Regulatory Commission, Office of Nuclear Regulatory Research, 2003.

3. K. Mikityuk, P. Fomitchenko, "FRED: Calculational Model of Fuel Rod Behavior Under Accident Conditions Coupled with RELAP5/MOD3", Proc. of 8th International Conference on Nuclear Engineering (ICONE-8), Baltimore, MD USA, 2000.

4. P. Petkevich, K. Mikityuk, P. Coddington, R. Chawla, "Development and benchmarking of a 2D transient thermal model for GFR plate-type fuel", Annals of Nuclear Energy 34, pp. 707-718, 2007.

5. G. Rimpault, "The ERANOS Data and Code System for Fast Reactor Neutronic Analyses", PHYSOR-2002, Seoul, Korea, Oct. 7-10, 2002.

6. G. Girardin, P. Coddington, K. Mikityuk, R. Chawla, "A 3D Full-Core Coupled Thermal-hydraulics/Kinetics TRACE/PARCS Model of the 2400 MWth Generation IV Gas-cooled Fast Reactor", PHYSOR-2008, Interlaken, Switzerland, Sept. 14-19, 2008.

7. S. Pelloni, E. Bubelis, K. Mikityuk, P. Coddington, "Calculations of Reactivity-initiated Transients in Gas-cooled Fast Reactors Using the Code System FAST", Ann. Nucl. Energy, 33, 6, pp. 499-509, 2006

8. H. Choi, G. Rimpault, J.C. Bosq, "A Physics Study of a 600-MW(thermal) Gas-Cooled Fast Reactor", Nucl. Sci. Eng., 152, pp. 204–218, 2006.

9. A. Epiney, P. Dumaz, P. Coddington, K. Mikityuk, R. Chawla, "Comparative transient analysis of the 2400MWth GFR with the TRACE and CATHARE codes", PHYSOR-2008, Interlaken, Switzerland, Sept. 14-19, 2008

6   SUMMARY AND CONCLUSIONS

The present research has been focused on the development and application of a 2D thermo-mechanical model for the innovative plate-type fuel foreseen for use in the Gen-IV Gas-cooled Fast Reactor (GFR). The need for the new model was driven by increased safety requirements, by recent trends to decrease the conservatism of the calculations and by the revolutionary fuel design. The work has also contributed to the understanding of the physical phenomena occurring in such fuel, thereby resulting in certain recommendations for improving the design as well as the usage of simplified calculation schemes. A summary of the work, the main achievements made and recommendations for future work are presented in the following sections.

6.1   SUMMARY

The introductory chapter gives the current state of nuclear energy production worldwide and a brief description of Generation-IV systems (reactor types which are foreseen to be built beyond 2030). In the latter context, emphasis is laid on the GFR, the corresponding research effort underway and the scope of the present thesis.

Chapter 2 serves to familiarize the reader with the state-of-the-art codes currently used for fast reactor safety analysis. Apart from a brief description of the codes and their application domain, the coupled (multi-physics) calculation methodology as employed in PSI's FAST code system is also presented. A large part of the chapter is devoted to the description of the thermo-mechanical model FRED as used for conventional fuels, since this has essentially served as basis for the present GFR fuel model.

The problem description and need for the new thermo-mechanical model are presented in the beginning of Chapter 3. The comparison of detailed (3D finite-elements) and simplified (1D) models underlines the inadequacy of the latter, the complex multi-dimensional heat transfer being shown to need more accurate treatment. Since use of the 3D model for transient calculations would be too costly in terms of CPU time (especially for structural analysis and modeling the contact between fuel and cladding), the present development work is shown to be necessary. The rest of the chapter is devoted to a detailed description of this work, i.e. the development of the 2D thermo-mechanical model for plate-type fuel, which combines an explicit treatment of the inner honeycomb structure with acceptable computational time.

The benchmarking of the developed model and certain detailed investigations of the GFR fuel behavior are presented in Chapter 4. The 3D finite-elements modeling of the fuel was used as basis in each case. Thus, in the second part of the chapter, novel insights are obtained into the fuel behavior. These contribute to better understanding of the basic phenomena and result in recommendations for fuel design improvement and for the mathematical modeling of such fuel using 1D models (which assume homogenization of the inner structure).

Chapter 5 is devoted to the application of the developed model for simulating a number of hypothetical GFR accident events, viz. reactivity insertion, core overcooling, loss of heat sink and loss of flow. The main aim has been to compare the transient behavior as calculated with and without the use of the new model, i.e. to reveal the effect of the improved temperature field on the reactor dynamics. The transients are calculated for both fresh (open axial gap) and burnt (closed gap) fuel.

6.2   MAIN ACHIEVEMENTS

6.2.1   Compilation of the material properties database

One of the specific features of the GFR is the choice of the fuel composition and the cladding material. The aim of achieving a high outlet coolant temperature resulted in the search for new highly conductive and refractory materials. Thus, bulk or fiber-reinforced SiC has been chosen as cladding, and the fuel composition is a mixture of uranium and plutonium carbides. The back-up options for the fuel are uranium-plutonium nitride and oxide mixtures. Nitrides are chosen since their performance is similar to that of carbides, while, in the case of oxides, there is a large amount of data and operating experience available.

Accordingly, the first part of the research was devoted to the compilation of an appropriate material properties database. The open literature was scanned for the thermal and mechanical properties of the mentioned materials, resulting in a large database assembled from a variety of sources (see Appendix A).

6.2.2   Development and validation of the new thermo-mechanical model

The development of the 2D FRED code was carried out in two parts. First, a purely thermal model was developed, the materials deformations and corresponding changes in the gas-gap thermal conductance not being taken into account. The aim was simply to find out how well the temperatures could be predicted by the 2D model. Particular attention was paid to the heat transfer through the radial gas gap as the complex shape (circular inside and hexagonal outside) cannot be explicitly

176

treated by the FRED R-Z model. It was found that the averaging of the radial gas gap for heat transfer calculations plays an important role and has a significant impact on the results. Two approaches to average the radial gas gap were analyzed:

- "traditional" averaging, i.e. averaging of the real gas gap value over angle,

- "advanced" averaging, i.e. averaging of the reciprocal gas gap value over angle.

The "advanced" averaging procedure provided results which are in very good agreement with those obtained from the 3D benchmarking calculations, and was accordingly adopted in the developed 2D model.

The benchmarking itself was not a trivial task as no calculating tools are readily available for this particular fuel design and no experimental data exist. Therefore, the multi-purpose finite-elements code ANSYS was chosen to build up a detailed 3D model for the plate-type fuel. The benchmarking was done on a unit-cell basis; the influence of adjoining cells on each other was not investigated. The finite-elements model was used to solve the coupled thermo-mechanical problem, including the situation for fuel-cladding contact. A special effort was made to simulate all the principal phenomena occurring in the fuel (see Appendix C for a more detailed description of the finite-elements modeling methodology).

As the temperature field is greatly affected by the deformation of the materials, the further development and benchmarking of the 2D model was done for the coupled thermo-mechanical problem. Both open and closed gap regimes were analyzed. Due to the high thermal conductivity of the GFR materials, the temperature field is mainly determined by the variations of the gas gaps rather then by the absolute dimensions of the pellet and cladding. It has been shown that the new model provides good results for deformations and temperature fields in both open and closed gap regimes. The stress distribution, however, cannot be accurately calculated due to the simplifications inherent to the developed model. Only integral values can be provided.

On the other hand, the main purpose of the currently developed model is to provide reliable data for the calculation of the principal neutronic feedbacks in the GFR core, viz. the fuel temperature for the Doppler effect and the fuel plate deformation for the axial core expansion effect. Both the concerned parameters have been shown to be adequately predicted with the new model. An accurate evaluation of the stresses is not necessary for the purpose of assessing the reactivity effects.

6.2.3   Other detailed investigations of the GFR fuel

Certain other detailed investigations using the 3D model were conducted in order to get an in-depth understanding of the GFR fuel behavior, i.e. to provide supplementary results which cannot be obtained with the 2D model due to its inherent simplifications. The investigations concerned both mechanical and thermal behavior, and resulted in recommendations for the fuel design as well as for improved usage of simplified 1D models.

Ways to optimize the fuel design

First of all, it has been found that the temperature field, typical for the GFR fuel, results in a strong radial dependence of the axial deformation. Thus, for the reference case of an initially flat pellet, the pellet edge gets raised relative to the rest of the pellet's axial surface. The gas gap closes axially, and with this occurring in a non-uniform manner, i.e. only at the pellet periphery, the local stresses within fuel and cladding increase significantly and may lead to fuel cracking or cladding failure. The investigations carried out have shown that there are several different ways to optimize the fuel design in order to mitigate such fuel-cladding interaction. One of the solutions is the shaping of the fuel pellet so that its axial surfaces become flatter after deformation, thus decreasing the stress concentration when contact occurs.

Another way is to change the dimensions of the fuel pellet so that no pellet-clad interaction occurs till end of life, or at least as long as possible. Two alternative geometries were analyzed in this context, with and without fuel volume preservation. It has been shown that the pellet-cladding interaction is decreased significantly. Moreover, the resulting higher fuel temperatures at beginning of life have been shown to have relatively little influence on the GFR fuel design goal of nearly zero fission gas release from the fuel matrix.

Usage of simplified 1D models

Since most readily available system codes for safety analysis use a 1D model for the fuel, it is useful to provide recommendations for such simplified treatment in the case of the GFR plate-type fuel. The detailed investigations of the heat transfer have shown that, for the reference fuel design, the temperature field can be well approximated by a 1D model with some slight modification of the calculating algorithm, viz. heat fluxes within the cell have to be calculated based on the fuel cross-sectional area while the heat flux for the wall temperature calculation has to be based on the total cell cross-sectional area. It needs to be borne in mind, however, that these considerations are only valid for fuel designs where the radial heat transfer in the fuel pellet can be neglected, which is the case for the reference design.

6.2.4 GFR transient behavior

The impact of the new model on GFR safety analysis has been achieved by comparing the results of predictions made, with and without its use, for a series of hypothetical accident events, viz.

- transient overpower (UTOP),

- core overcooling (UOVC),

- loss of heat sink (ULOHS),

- loss of flow (ULOF).

The scram was not actuated during the transients, in order to study the evolution of feedbacks (Doppler and axial expansion) to the maximum extent possible. Moreover, both fresh (open axial gap) and burnt (closed gap) fuel conditions were considered.

It has been shown that the pure geometry effects on the temperatures are quite significant. However, for the specific honeycomb structure considered, these are somewhat mitigated by the fuel and cladding expansions, and the corresponding decrease of the axial fuel-cladding gas gaps. Thus, the 2D model results are brought closer to those of the homogeneous model. However, this statement is only valid if the radial heat transfer in the fuel pellet can be neglected (as is the case for the reference fuel design).

The evolution of reactivity feedback and the reactor power have been evaluated, in the case of both 2D and 1D fuel modeling, using a point-kinetics approximation. The effects were thus driven by the average temperature change rate (dT/dt), rather than by the absolute temperature values. Correspondingly, the results from the two models are not drastically different. The more significant discrepancies have been obtained for the transients with the same magnitude of the Doppler and axial core expansion effects (UOVC, ULOHS). For the UTOP transient, which is mainly determined by the fuel temperature, very similar results are obtained for total reactivity and reactor power.

6.3 Recommendations for future work

Improvement of the mechanical model

Though it has been shown that the developed model is suitable for reliable predictions of the temperature field within plate-type GFR fuel, certain limitations were clearly brought during the benchmarking carried out against detailed 3D

solutions. Thus, for example, it was shown that stress distributions within the pellet and cladding are very non-uniform, and these cannot be precisely predicted by the 1.5D approach used for the mechanical part of the model (Section 3.6), which only allows average stress values to be obtained.

Creation of a fully 2D mechanical model for the GFR plate-type fuel is recommended to replace the existing 1.5D algorithm. This would allow a more precise handling of the boundary conditions and especially improved predictions of the fuel-cladding contact behavior. As a result, a much more detailed description of the stress-strain state of the pellet and cladding would be provided. Such a model could, moreover, allow much greater flexibility for specification of the fuel geometry, thus enabling studies for pellet shape optimization.

Extension of the materials database

It is clear that the final results obtained in thermo-mechanical modeling largely depend on the materials properties assumed. Accordingly, it is strongly recommended that all the currently used data for constituents of the GFR fuel are reviewed appropriately. For example, SiC as reference structural material could occur both as bulk (as considered in the present research) and/or as SiC-fiber reinforced material. The thermal and mechanical properties of the latter would depend on the fabrication procedure, fiber dimensions, etc.

Another important issue is the burnup dependence of the materials properties. Realistic predictions of the GFR behavior at the end of cycle require such specification for both fuel and cladding, but the corresponding data is relatively scarce currently.

Appendices

182

Appendix A: GFR materials properties database

This appendix provides an overview of available data on GFR materials properties.

A.1. List of used symbols and abbreviations

The following symbols and abbreviations are used throughout the present appendix.

Abbreviation	Description
ρ	Density, g/cm^3
ρ_T	Theoretical density, g/cm^3
c_p	Specific heat, $J/(kg \cdot K)$
λ	Thermal conductivity, $W/m\text{-}K$
α	Thermal expansion coefficient, $1/K$
σ_Y	Yield stress, Pa
T_{melt}	Melting temperature, K
E	Young's modulus, Pa
G	Shear modulus
ν	Poisson's ratio
CERCER	Fuel type with ceramic particles dispersed in a ceramic matrix
GCFR, GFR	Gas Cooled Fast Reactor, Gas Fast Reactor
ε	Deformation
σ	Stress, Pa
A_{Pu}	Atomic fraction of Pu, Pu/(Pu+U)
XO	local stoichiometry, O/M-ratio
P	porosity

A.2. Introduction

This appendix contains the material properties that are required for thermal and stress-strain calculations for the new fuel proposed for the next generation Gas-cooled Fast Reactor (GFR). It also provides a comparison of the data from different open sources. The fuel itself was described in Chapter 2. The reference materials are SiC_f/SiC and mixed uranium-plutonium carbide. Oxide and nitride fuels are also represented here as backup options.

A.3. Description of the needed data

This section presents the properties necessary both for thermal and stress-strain calculations. A brief description is given of the various parameters showing their importance and use in the calculations.

A.3.1. Generic data sources

The present database deals with a large number of materials and material properties. The generic data sources listed below provide the necessary information, in case a specific reference is not given.

Where a specific literature source for a material property is available, this is given immediately after the property description.

1. K. Lassmann, J. van de Laar, "TRANSURANUS HANDBOOK, Document Number Version 1 Modification 1 Year 1997 (V1M1J97)", Institute for Transuranium Elements, (1997), Karlsruhe (D).

2. MATPRO-Vers. 11, "A handbook of material properties for use in the analysis of lightwater reactor fuel rod behaviour", NUREC/CR 0497 TREE1280, EG&G Idaho, Inc. (1979), Idaho Falls, Idaho 83415.

3. D. Olander, "Fundamental aspects of nuclear reactor fuel elements". TID-26711-P1, Dep. of Nuclear Engineering, University of California (1976), Berkeley.

A.3.2. Essential properties for thermal calculations

This section presents the list of properties necessary for thermal calculations and gives a brief description of their use. Density, specific heat and thermal conductivity are not all the properties, but the most important. Later the database will be extended to include, for instance, emissivity, etc.

Density

The density is needed for time-dependent calculations. Together with specific heat (see below), it determines the stored energy of the material released during accidents and transients.

Specific heat

The specific heat is needed for time-dependent temperature calculations. Both the stored energy and temperature change rate depend on the specific heat. It is important in reactor transient analysis to have an accurate estimate of the material specific heat because the severity of the transient is greatly affected by the initial stored energy of the fuel and the rate of temperature increase.

Thermal conductivity

The thermal conductivity is needed to predict the temperature distribution within the fuel during reactor operation. This property, as well as closely associated models for fuel material porosity and sintering, are critical for accurate predictions of the fuel behavior in both steady-state and in off-normal transients because the fuel behavior is strongly dependent on the temperature.

Melting temperature

The melting temperature is important for accident considerations. It gives the permissible temperature margins to prevent fuel and cladding destruction.

A.3.3. Essential properties for stress-strain calculations

This section presents a list of properties necessary for stress-strain calculations and gives a brief description of their use. Thermal expansion, yield stress, melting temperature and elastic moduli are not all the properties, but the most important. Later the database will be extended to include, for instance, parameters of the stress-strain curve, radiative swelling and creep, etc.

Thermal expansion

The thermal expansion describes the dimensional changes in materials caused by changes in temperature. For instance, in the first GFR fuel option (coated-particles fuel), fuel dimensional changes together with the coating thermal expansion determines the porous carbon layer thickness, which due to the relatively low thermal conductivity determines the temperature level. For the dispersed fuel option (plate-type fuel), the fuel thermal expansion will influence both the gas gap size and the pressure of the helium in the free volume and therefore the heat transfer to the cladding and to the coolant. In the case of gas gap closure, the fuel/clad system thermal expansion strictly determines the stress-strain condition and the integrity of the fuel element. The fuel expansion influences also the core reactivity due to the change in the neutron leakage.

Yield stress

The yield point on a typical stress-strain curve separates regions of elastic and plastic deformations. If the stress reaches this point (the yield stress) and if the material has the possibility of plasticization, stresses can be relaxed by the flow of material, and deformation beyond this point is not recovered when the load is removed.

Young's and shear modulus

Elastic moduli are required to relate stress components to strain components in the elastic region by the generalized form of Hooke's law. In practice, materials are frequently assumed to be isotropic. In this case, only two independent elastic moduli (i.e. Young's modulus and the shear modulus) are needed to describe the relation between elastic stress and strain, below the yield point.

Hooke's law is given by:

$$\varepsilon_{ii} = \frac{1}{E} \cdot \left[\sigma_{ii} - v \cdot (\sigma_{jj} + \sigma_{kk}) \right]$$

$$\varepsilon_{ij} = \frac{\sigma_{ij}}{G}$$

$$G = \frac{E}{2 \cdot (1 + v)}$$

,

where:

v – Poisson's ratio (see below);

ε – deformation component;

186

σ – stress components;

G – shear modulus.

Poisson's ratio

The elastic constants are usually expressed in terms of Young's modulus, the shear modulus and Poisson's ratio. They are not independent, and Poisson's ratio can be related to Young's modulus and the shear modulus as follows:

$$v = \frac{E}{2 \cdot G} - 1 \text{ ,}$$

where:

v – Poisson's ratio;

E – Young's modulus;

G – shear modulus.

Poisson's ratio determines the dependence of the material deformations in different directions (e.g. the extension of the material in the X-direction causes constrictions along the Y and Z directions, etc.).

Creep

Creep is the term used to describe the tendency of a solid material to slowly move or deform permanently under the influence of stresses. It occurs as a result of long term exposure to levels of stress that are below the yield strength or ultimate strength of the material. Creep is more severe in materials that are subjected to heat for long periods, and near the melting point. It is often observed in glasses. Creep always increases with temperature. The general creep equation is written as follows:

$$\frac{d\varepsilon}{dt} = \frac{C \cdot \sigma^m}{d^b} \cdot e^{-\frac{Q}{kT}}$$

where

ε – creep strain;

C – a constant dependent on the material and the particular creep mechanism;

m and b – exponents dependent on the creep mechanism;

Q – activation energy of the creep mechanism;

σ – applied stress;

d – grain size of the material;

k – Boltzmann's constant;

T – absolute temperature.

Swelling under neutron irradiation

Neutron-induced swelling is the increase of volume and decrease of density of materials subjected to intense neutron radiation. Neutrons impacting the material's lattice rearrange its atoms, causing buildup of dislocations and voids. Together with the resulting strength reduction and embrittlement, it is a major concern for materials for nuclear reactors. Materials show significant differences in their swelling resistance.

A.4. Data necessary for thermal calculations

This section presents the material properties necessary for thermal calculations. Where more than one data source is used, they are presented as *option 1*, *option 2*, etc. Where the information is contained in the form of a correlation, the data is in most cases tabulated to provide a comparison of numerical values. As stated above, where specific original source references are available these are given after each subsection.

A.4.1. Density

Dioxide fuel

The correlation for uranium oxide and MOX fuel [1] is:

$$\rho_T = A_{Pu} \cdot 11.46 + (1 - A_{Pu}) \cdot 10.96$$

where, ρ_T – theoretical density, g/cm^3; A_{Pu} – atomic fraction of Pu, Pu/(Pu+U).

1. R.J. Guenther, J.O. Barner, R.K. Welty. "Fuel performance improvement program: description and characterization of HBWR Series H-2, H-3, and H-4 test rods", DOE/ET/34215-14, 1980 Mar 01.

Nitride fuel

Option 1 for uranium nitride [1]: the theoretical density of UN is ρ_T = 14.32 g/cm^3

Option 2 for uranium nitride [2]:

$$\rho = 14.42 - 2.779 \cdot 10^{-4} T_K - 4.897 \cdot 10^{-8} T_K^2$$

for temperature range $298 \leq T_K \leq 2523$

where

T_K – temperature, K.

1. R.B. Holden. "Ceramic fuel elements". Prepared under the direction of the American Society for Metals for The Division of Technical information United States Atomic Energy Commission, 1966.
2. S.L. Hayes, J.K. Thomas and K.L. Peddicord. "Material property correlation for uranium mononitride. I. Physical properties". J. Nucl. Mater. 171 (1990) 262 – 270.

Carbide fuel

According to [1], the theoretical density of UC is: ρ_T = 13.63 g/cm^3

1. R.B. Holden. "Ceramic fuel elements". Prepared under the direction of the American Society for Metals for The Division of Technical information United States Atomic Energy Commission, 1966.

Silicon carbide

ρ = 3.16 g/cm^3 [1]

1. D.L. Lide. CRC Handbook of chemistry and physics, 79th edition, 1998-1999, CRC, Boca Raton, FL.

A.4.2.   Specific heat

Dioxide fuel

<u>Option 1</u> for uranium oxide fuel [1]

c_p = 300 J/(kg·K).

<u>Option 2</u> for LWR uranium oxide fuel [2]

$$c_p = 12.54 + T_K \cdot (0.0170 + T_K \cdot (-0.117 \cdot 10^{-4} + T_K \cdot 0.307 \cdot 10^{-8})), \text{cal/(mol·K)}$$

where

T_K – temperature, K.

<u>Option 3</u> for uranium oxide and MOX fuel [3]

The specific heat capacity of oxide and MOX fuel is modeled empirically as a function of four parameters: temperature, composition, molten fraction, and oxygen-to-metal ratio. The correlation for fuel specific heat is valid for temperatures from 300 K to more than 4000 K.

$$c_p = \frac{K_1 \cdot \theta^2 \cdot e^{\frac{\theta}{T_K}}}{T_K^2 \cdot \left(e^{\frac{\theta}{T_K}} - 1 \right)^2} + K_2 \cdot T_K + \frac{Y \cdot K_3 \cdot E_D}{2 \cdot R \cdot T_K^2} e^{\frac{-E_D}{R T_K}} , \text{ J/kg·K}$$

where

190

T_K – temperature, K;

Y – local stoichiometry, oxygen to metal ratio;

R – universal gas constant, 8.3143 J/(mol·K);

θ – the Einstein temperature,

and the constants are given in Table 1.

Table 1. Constants used in UO$_2$ and PuO$_2$ specific heat correlations

Constant	UO$_2$	PuO$_2$	Units
K_1	296.7	347.4	J/kg·K
K_2	$2.43 \cdot 10^{-2}$	$3.95 \cdot 10^{-4}$	J/kg·K^2
K_3	$8.745 \cdot 10^{-7}$	$3.860 \cdot 10^{7}$	J/kg
θ	535.285	571.000	K
E_D	$1.577 \cdot 10^{-5}$	$1.967 \cdot 10^{-5}$	J/mol

The specific heat capacity of mixed (U, Pu)O$_2$ fuel is given by

$$c_{p,MOX} = X_{Pu} \cdot c_{p,Pu} + (1.0 - X_{Pu}) \cdot c_{p,U}, \quad \text{J/(kg·K)}.$$

where X_{Pu} – plutonium weight fraction.

The specific heat capacities of UO$_2$ and PuO$_2$ in the liquid state are given by

c_p = 503 J/kg·K.

1.   S. Glasstone, A. Sesonske. "Nuclear reactor engineering". 3rd edition. Prepared under the auspices of The Technical Information Centre, U.S. Department of Energy

2.   Schuster, Zimmerer, KfK-Ext. 8/77-1 (1977)

3.   MATPRO-Vers. 11. "A handbook of material properties for use in the analysis of light water reactor fuel rod behaviour". NUREC/CR 0497 TREE1280, EG&G Idaho, Inc. (1979), Idaho Falls, Idaho 83415.

Nitride fuel

Option 1 for uranium nitride [1]

c_p = 0.1502 + 1.505·10^{-4}·T_K - 5.948·10^{-8}·$T_K{}^2$, J/(g·K)

Option 2 for uranium nitride [2]

c_p = 12.0 + 2.3·10^{-3}·T_K, cal/(mol·K)

Option 3 for uranium nitride [3]

Tabulated data are presented in Table 2.

Option 4 for uranium nitride [4]

$$c_p = 51.14 \cdot \frac{\theta}{T_K} \cdot \frac{e^{\frac{\theta}{T_K}}}{\left[e^{\frac{\theta}{T_K}} - 1 \right]^2} + 9.491 \cdot 10^{-3} \cdot T_K + \frac{2.642 \cdot 10^{11}}{T_K^2} \cdot e^{-\frac{18081}{T_K}}, \quad J/(\text{mol·K})$$

for the temperature range 298 ≤ T_K ≤ 2628

where

θ – the emperically determined Einstein temperature of UN, 365.7 K;

T_K – temperature, K.

Table 2. Comparison of the specific heat of uranium nitride, J/(kg·K)

T, K	Option 1	Option 2	Option 3
273	186.85	209.80	180.03
422	203.12	215.50	210.18
589	218.21	221.88	223.16
755	229.92	228.22	230.27
922	238.40	234.60	235.30
1089	243.56	240.99	239.90
1255	245.40	247.33	243.67
1422	243.94	253.71	247.86

1.   E.O. Speidel, D.L. Keller. "Fabrication and properties of hot-pressed uranium mono-nitride", BMI-1633, EURAEC-706 pp.1 (1963).

2.   Report KfK 111, Chapter VI, Figs. 4 and 8.

3.   Y.S. Touloukian et al. Thermophysical properties of matter (Volumes 2, 5, 13). IFI/PLENUM - New York-Washington, 1977.

4.   S.L. Hayes, J.K. Thomas and K.L. Peddicord. "Material property correlation for uranium mononitride. IV. Thermodynamic properties". J. Nucl. Mater. 171 (1990) 300 – 318.

Carbide fuel

Option 1 for uranium carbide

c_p = 0.20088 + 3.852·10^{-5}·T_K, J/g·K.

Option 2 for uranium carbide [1]

c_p = 13.0 + 2.3·10^{-3}·T_K, cal/(mol·K).

Option 3 [2]

Tabulated data for uranium and plutonium carbide are presented in Table 3.

Table 3. Comparison of the specific heat of uranium carbide and plutonium carbide, J/(kg·K)

T, K	Option UC	Option 2 UC	Option 3 UC	Option 3 PuC
300	212.44	229.27	169.47	-----
400	216.29	233.12	205.57	189.87
500	220.14	236.97	223.74	203.73
600	223.99	240.82	234.86	213.32
700	227.84	244.68	242.57	217.92
800	231.67	248.53	248.51	222.36
900	235.55	252.38	253.40	226.00
1000	239.4	256.23	257.64	229.10
1100	243.25	260.08	261.48	231.91
1200	247.10	263.94	265.03	234.54
1300	250.96	267.79	268.36	237.01
1400	254.81	271.64	271.56	239.19

1500	258.66	275.49	274.63	241.66
1600	262.51	279.34	277.67	243.63
1700	266.36	283.20	280.6	245.93
1800	270.22	287.05	288.14	247.90
1900	-----	-----	-----	249.91

1. Report KfK 111, Chapter VI, Figs. 4 and 8

2. Y.S. Touloukian et al. Thermophysical properties of matter (Volumes 2, 5, 13). IFI/PLENUM - New York-Washington, 1977.

Silicon carbide

Tabulated data are presented in Table 4 [1].

Table 4. Specific heat of silicon carbide

T, K	c_p, J/kg·K
266	336.52
276	350.37
286	365.18
300	383.81
400	501.31
500	561.74
600	599.95
700	627.42
800	649.39
900	668.02
1000	684.50
1100	699.79
1200	714.12
1300	727.73
1400	740.86
1500	753.76
1600	766.42
1700	778.84
1800	791.02

1.   Y.S. Touloukian et al. Thermophysical properties of matter (Volumes 2, 5, 13). IFI/PLENUM - New York-Washington, 1977.

A.4.3.   Thermal conductivity

Oxide fuel

<u>Option 1</u> for uranium oxide and MOX $(U_{0.8}Pu_{0.2})O_2$ fuel [1].

This option is only validated for a Pu content of maximum 20%, i.e. $X_{Pu} \le 0.20$.

$$\lambda = C_1 + (C_2 - C_1)\frac{X_{Pu}}{0.2}\lambda_{RF}, \text{ W/(m·K)}$$

where

$$C_1 = \left(\frac{1}{3.11 + 0.0272 \cdot T_C} + 5.39 \cdot 10^{-13} \cdot T_C^3\right) \cdot 1.11 \cdot 10^2$$

$$C_2 = \left(\frac{1}{0.042 + 2.71 \cdot 10^{-4} \cdot T_K} + 69.0 \cdot 10^{-12} \cdot T_K^3\right) \cdot 1.11$$

The conductivity reduction factor λ_{RF} due to fission product depletion, i.e. the burnup dependent degradation of the fuel thermal conductivity, is calculated separately as follows:

$$\lambda_{RF} = \frac{1.}{1.0 + \dfrac{a \cdot F \cdot \lambda}{T_C}}, \text{ W/(m·K)}$$

where

B – burnup, atom %

T_C – temperatire, C

$$F = \frac{FD}{1.0 \cdot 10^{20}}$$

$$FD = B \cdot 2.03 \cdot 10^{20}$$

for $T_C < 500°C$

$$FD < 1.0 \cdot 10^{15} \Rightarrow a = 0$$

$$FD < 1.0 \cdot 10^{16} \Rightarrow a = 20.0 \cdot 1500.0$$

$$FD < 1.0 \cdot 10^{17} \Rightarrow a = 200.0 \cdot 1500.0$$

$$FD < 1.0 \cdot 10^{18} \Rightarrow a = 75.0 \cdot 1500.0$$

$$FD < 1.0 \cdot 10^{19} \Rightarrow a = 20.0 \cdot 1500.0$$

$$FD \geq 1.0 \cdot 10^{19} \Rightarrow a = \frac{200.0 \cdot 1500.0}{10.0 \cdot F}$$

for $T_C < 1600°C$

$$FD < 1.0 \cdot 10^{19} \Rightarrow a = 0$$

$$FD < 1.0 \cdot 10^{20} \Rightarrow a = 45.0$$

$$FD < 1.0 \cdot 10^{22} \Rightarrow a = 450.0$$

$$FD \geq 1.0 \cdot 10^{22} \Rightarrow a = \frac{450.0 \cdot 10^2}{F}$$

for $T_C \geq 1600°C$

$$FD < 1.0 \cdot 10^{20} \Rightarrow a = 0$$

$$FD < 1.0 \cdot 10^{22} \Rightarrow a = 450.0$$

$$FD \geq 1.0 \cdot 10^{22} \Rightarrow a = \frac{450.0 \cdot 10^2}{F}$$

Option 2 for oxide fuel [2].

$$\lambda = \frac{1}{0.0375 + 2.165 \cdot 10^{-4} \cdot T_K + 0.0142 \cdot B} + \frac{4.715 \cdot 10^9}{T_K^2} \cdot e^{\frac{-16361.}{T_K}} \text{ , W/(m·K)}$$

where B – burnup at, % of the heavy metal;

T_K – temperature, K;

Option 3 for LMFBR MOX fuel [3].

$$\lambda = \left(\frac{1}{AC + 2.885 \cdot 10^{-4} T_K} + 76.38 \cdot 10^{-12} T_K^3 \right) \frac{1 - P}{0.864(1 + 2 \cdot P)} \text{ , W/(m·K)}$$

196

where T_K is temperature in K (for T_K <500 T_K =500), P – fuel porosity.

$$AC = 1.528 \cdot \sqrt{ZO + 0.00931} - 0.1055 + 0.44 \cdot \frac{B}{100};$$

$ZO = 2.0 - XO$, where XO – local stoichiometry, O/M-ratio (for Z0<0 Z0=0), B – burnup, at. % of the heavy metal.

Option 4 for oxide fuel [4].

$$\lambda = \frac{1}{0.118 + 2.38 \cdot 10^{-4} \cdot T_C + 0.0142 \cdot B} + 8.775 \cdot 10^{-11} \cdot T_C^3, \text{ W/(m·K)}$$

Where

B – burnup, at. %;

T_C – temperature, °C.

1.   D. Olander. "Fundamental aspects of nuclear reactor fuel elements".TID-26711-P1, Dep. of Nuclear Engineering, University of California (1976), Berkeley, 127 (for UO$_2$)
      and
      A.B.G. Washington. TRG Report 2236 (1973) (for MOX)
      and
      R.C. Daniel, I. Cohen. WAPD-246 (1964) (for degradation of thermal conductivity as a function of burnup)
2.   J.H. Harding, D.G. Martin. "A recommendation for the thermal conductivity of UO$_2$". J. Nucl. Mat, 166 (1989) 223-226.
3.   Y. Philipponneau. J. Nucl. Mater., 188 (1992) 194-197.
4.   K. Lassmann, A. Moreno. ATKE, 30 (1977) 207-215
      and
      P.G. Lucuta et al. "Thermal conductivity of hyperstoichiometric SIMFUEL". J. Nucl. Materials, 223 (1995) 51-60 (for degradation of thermal conductivity as a function of burnup)

Nitride fuel

Option 1 for UN and (U$_{0.85}$Pu$_{0.15}$)N fuel [1].

$$\lambda = C_1 + (C_2 - C_1) \cdot \frac{A_{Pu}}{0.15}, \text{ W/(m·K)}$$

where

for $T_C < 1800°C$, $C_1 = (10.55 + 0.02 \cdot T_C - 5.96 \cdot 10^{-6} \cdot T_C^2)$;

for $T_C \geq 1800°C$, $C_1 = 0.2724 \cdot 10^2$;

for $T_C < 1900°C$, $C_2 = (0.01234 + 7.744 \cdot 10^{-6} \cdot T_C - 1.279 \cdot 10^{-10} \cdot T_C^2) * 10^3$;

for $T_C \geq 1900°C$, $C_2 = 0.228 \cdot 10^2$.

Option 2 for UN fuel [2].

$\lambda = 1.28 \cdot 10^{-4} T_C + 0.123$, W/(cm·K)

Option 3 for uranium nitride [3]

Tabulated data are presented in Table 5.

Option 4 for UN fuel [4].

$\lambda = 1.864 \cdot e^{-2.14 \cdot P} \cdot T_K^{0.361}$, W/(cm·K)

for temperature range $298 \leq T_K \leq 1923$,

where

T_K – temperature in degrees Kelvin;

P – porosity, as a volume fraction.

Table 5. Thermal conductivity of uranium nitride

T, K	Option 1		Option 2	Option 3
	λ_{UC}, W/mK	λ $(U_{0.85}Pu_{0.15})C$, W/mK	λ_{UC}, W/mK	λ_{UC}, W/mK
273	10.55	12.34	12.30	13.1
348	12.02	12.92	13.26	13.6
373	12.49	13.11	13.58	13.8
473	14.31	13.88	14.86	14.4
573	16.01	14.65	16.14	15.1
673	17.60	15.42	17.42	15.9
773	19.06	16.18	18.70	16.6
873	20.40	16.94	19.98	17.4
973	21.63	17.70	21.26	18.2
1073	22.74	18.45	22.54	19.0
1173	23.72	19.21	23.82	19.6
1273	24.59	19.96	25.10	20.3

1. Hj. Matzke. North Holland Publ. (1986) (for UN) and C.A. Alexander et al, BMI-X-659 (1975) for mixed nitride.

2. R.B. Holden. "Ceramic fuel elements". Prepared under the direction of the American Society for Metals for The Division of Technical information, United States Atomic Energy Commission. 1966

3. Y.S. Touloukian et al. Thermophysical properties of matter (Volumes 2, 5, 13). IFI/PLENUM - New York-Washington, 1977.

4. S.L. Hayes, J.K. Thomas and K.L. Peddicord. "Material property correlation for uranium mononitride. III. Transport properties". J. Nucl. Mater. 171 (1990) 289 - 299.

Carbide fuel

Option 1 for UC and $(U_{0.825}Pu_{0.175})C$ fuel [1].

$$\lambda = C_1 + (C_2 - C_1) \cdot \frac{A_{Pu}}{0.175}, \text{ W/(m·K)}$$

for $T_C < 700°C$, $C_1 = (21.7 - 3.04 \cdot 10^{-3} \cdot T_C + 3.61 \cdot 10^{-6} \cdot T_C^2)$;

for $T_C \geq 700°C$, $C_1 = (20.2 - 1.48 \cdot 10^{-3} \cdot T_C)$;

for $T_C < 500°C$, $C_2 = (0.175 - 5.65 \cdot 10^{-5} \cdot T_C + 8.14 \cdot 10^{-8} \cdot T_C^2)*100$;

for $T_C \geq 500°C$, $C_2 = (0.1276 + 8.71 \cdot 10^{-5} \cdot T_C - 1.88 \cdot 10^{-8} \cdot T_C^2)*100$;

where

T_C – fuel temperature, °C;

A_{Pu} – atomic fraction of Pu, Pu/(Pu+U).

The source [2] gives a constant value of 23 W/mK for the thermal conductivity over the range 100 to 1800 °C for carbides in the general vicinity of the monocarbide composition. But also mentioned is that this value is subject to revision, and it may well be that the conductivity does in fact increase with temperature above 500 °C.

Option 2 for uranium carbide [3]

Tabulated data are presented in Table 6.

Table 6. Thermal conductivity of uranium carbide

Option 1			Option 2	
T, K	λ_{UC}, W/mK	λ ($U_{0.825}Pu_{0.175}$)C, W/mK	T, K	λ_{UC}, W/mK
373	21.43	17.02	379.2	20.00
473	21.24	16.70	384.2	18.70
573	21.11	16.54	435.2	20.30
673	21.06	16.54	440.2	18.60
773	21.08	16.65	448.2	18.40
873	21.18	17.31	457.2	18.10
973	21.24	17.94	590.2	18.30
1073	21.38	18.52	602.2	18.30
1173	21.53	19.08	694.2	18.80
1273	21.68	19.59	708.2	17.60
1373	21.83	20.07	868.2	20.00
1473	21.98	20.50	890.2	20.80
1573	22.12	20.91	987.2	21.40
1673	22.27	21.27	1012.2	23.30
1773	22.42	21.60	1099.2	24.10

1873	22.57	21.88	1127.2	24.50
1973	22.72	22.13	1233.2	26.70
2073	22.86	22.35	1259.2	27.60
2173	23.01	22.52		
2273	23.16	22.66		

1. H.D. Lewis, J.F. Kerrisk. LA-6096-MS (1976) (*for carbide and mixed carbide*).

2. R.B. Holden. "Ceramic fuel elements". Prepared under the direction of the American Society for Metals for The Division of Technical information, United States Atomic Energy Commission. 1966

3. Y.S. Touloukian et al. Thermophysical properties of matter (Volumes 2, 5, 13). IFI/PLENUM - New York-Washington, 1977.

Silicon carbide

Tabulated data are presented in Table 7 [1].

Table 7. Thermal conductivity of silicon carbide

T, K	λ, W/(m·K)
888	104.00
889	103.00
1130	67.00
1133	66.60
1388	39.50
1389	39.50
1414	36.00
1528	24.90
1528	25.10
1800	13.20
1800	13.20
1801	13.50

Studies of the silicon carbide mechanical properties and thermal conductivity after cyclic thermal shock can be found in [2]. SiC matrix, with dispersed CeO_2 as a surrogate material for PuO_2, is discussed.

1.   Y.S. Touloukian et al. Thermophysical properties of matter (Volumes 2, 5, 13). IFI/PLENUM - New York-Washington, 1977.

2.   Y.W. Lee, S.C. Lee, C. Degueldre et al. "Study on the mechanical properties and thermal conductivity of silicon carbide-, zirconia- and magnesia aluminate-based simulated inert matrix nuclear fuel materials after cyclic thermal shock". J. Nucl. Mater. 319 (2003) 15-23

A.4.4. Melting temperature

Dioxide fuel

For compositions with plutonium content greater than zero, the MOX fuel solidus and liquidus points are given by [1]:

T_{sol} = 3113.15 – 5.41395·C + 7.468390·10^{-3}·C^2 – 3.2·10^{-3}·Bu;

T_{liq} = 3113.15 – 3.21660·C – 1.448518·10^{-2}·C^2 – 3.2·10^{-3}·Bu;

for plutonium content equals zero [1]:

T_{sol} = 3113.15 - 3.2·10^{-3}·Fbu;

T_{liq} = T_{sol},

where

T_{sol} – solidus temperature, K

T_{liq} – liquidus temperature, K

C – PuO_2 content. wt%

Bu – burnup, MW·d / tU

1. MATPRO-Version 11. "A handbook of material properties for use in the analysis of lightwater reactor fuel rod behaviour". NUREC/CR 0497 TREE1280, EG&G Idaho, Inc. (1979), Idaho Falls, Idaho 83415.

Nitride fuel

For uranium nitride fuel [1]:

T_{melt} = 2862, °C.

1. E.H.E. Pietsch et al. "Gmelin Handbook of inorganic and organometallic chemistry". 8th ed. / begun under the auspices of the Deutsche Chemische Gesellschaft by R. J. Meyer ; continued by E. H. E. Pietsch et al.

2.   S.L. Hayes, J.K. Thomas and K.L. Peddicord. "Material property correlation for uranium mononitride. IV. Thermodynamic properties". J. Nucl. Mater. 171 (1990) 300 – 318.

Uranium carbide

Option 1 for UC fuel [1]:

T_{melt} = 2500 °C.

Option 2 for UC fuel [2]:

$$T_{melt} = 3035.0 \cdot P_{N_2}^{0.02832} \ K$$

for nitrogen pressure range $10^{-13} \leq P_{N_2} \leq 7.5$,

where

P_{N_2} – nitrogen pressure, atm.

1.   G.M. Nickerson, W.E. Kastenberg, Nucl. Eng. Des., Vol. 36, 1976
2.   T. Preusser, Dissertation, KfK-Bericht 3426 (1982)

Silicon carbide

T_{melt} = 2830 °C [1].

1.   D.L. Lide. CRC Handbook of chemistry and physics, 79th edition, 1998-1999, CRC, Boca Raton, FL.

A.4.5.   Emissivity

Silicon carbide

Tabulated data are presented in Table 8 [1]. The reported uncertainty is ±20%.

Table 8. Emissivity of silicon carbide

T, K	ε
644	0.67
811	0.69
1089	0.75
1367	0.79
1644	0.83

1. Y.S. Touloukian et al. Thermophysical properties of matter (Volumes 8). IFI/PLENUM - New York-Washington, 1972.

A.5. Data necessary for strain-stress calculations

A.5.1. Thermal expansion

Dioxide fuel

Option 1 for oxide and MOX fuel [1].

$$\beta = 1.0 - 5.1 \cdot (XO - 2.00)$$
$$\alpha_{UO_2} = 7.107 \cdot 10^{-6} + 5.162 \cdot 10^{-9} \cdot T_C + 3.42 \cdot 10^{-13} \cdot T_C^2$$
$$\alpha_{PuO_2} = 8.496 \cdot 10^{-6} + 4.302 \cdot 10^{-9} \cdot T_C + 11.14 \cdot 10^{-16} \cdot T_C^2$$
$$\alpha_{(U,Pu)O_2} = \left(X_{Pu} \cdot \alpha_{PuO_2} + (1 - X_{Pu}) \cdot \alpha_{UO_2} \right) \cdot \beta$$

where $\alpha_{(U,Pu)O_2}$ – mixed fuel thermal expansion coefficient;

α_{UO_2}, α_{PuO_2} – thermal expansion coefficient for UO_2 and PuO_2, respectively;

X_{Pu} – weight fraction of PuO_2, i.e. $PuO_2/(U,Pu)O_2$;

T_C – fuel temperature, °C;

XO – local stoichiometry, O/M-ratio.

Option 2 for uranium dioxide [2]

Tabulated data are presented in Table 9.

Table 9. Thermal linear expansion of uranium oxide

T, K	Option 1		Option 2
	α_{UO2}, 1e-6/K	α_{PuO2}, 1e-6/K	α_{UO2}, 1e-6/K
293	7.2	8.6	9.4
400	7.8	9.0	9.6
600	8.8	9.9	9.9
800	9.9	10.8	10.3
1000	11.0	11.6	10.9
1200	12.2	12.5	11.6
1400	13.4	13.3	12.5
1600	14.6	14.2	13.4
1800	15.8	15.1	14.6
2000	17.0	15.9	15.8
2200	18.3	16.8	17.2
2400	19.6	17.7	18.7
2600	21.0	18.5	20.4

1.   T. Hiyama, PNC technical information, Power Reactor and Nuclear Fuel Development Corporation.
2.   Y.S. Touloukian et al. Thermophysical properties of matter (Volumes 2, 5, 13). IFI/PLENUM - New York-Washington, 1977.

Nitride fuel

Option 1 for uranium nitride [1]:

$$\alpha = \left(7.1 + 3.2 \cdot 10^{-3} T_c - 0.86 \cdot 10^{-6} T_C^2\right) \cdot 10^{-6},$$

where T_C is the temperature in degrees Celsius.

Option 2 for uranium nitride [2]

Tabulated data are presented in Table 10.

Option 3 for uranium nitride [3]

$$\alpha = 7.096 \cdot 10^{-6} + 1.409 \cdot 10^{-9} T_K$$

For the temperature range $298 \leq T_K \leq 2523$, where T_K is the temperature in K.

Table 10. Thermal linear expansion of uranium nitride

T, K	Option 1 α_{UN}, 1e-6/K	Option 2 α_{UN}, 1e-6/K	Option 3 α_{UN}, 1e-6/K
293	7.16	5.7	7.51
300	7.19	5.8	7.52
400	7.49	6.5	7.66
500	7.78	7.1	7.80
600	8.05	7.3	7.94
700	8.31	7.6	8.08
800	8.55	7.8	8.22
900	8.77	8.0	8.36
1000	8.97	8.2	8.51
1200	9.33	8.7	8.79
1400	9.61	9.1	9.07
1600	9.83	9.5	9.35
1800	9.98	9.9	9.63
2000	10.06	10.2	9.91
2200	10.07	10.5	10.20
2400	10.02	10.9	10.48
2500	9.96	11.0	10.62

1. R.B. Holden. "Ceramic fuel elements". Prepared under the direction of the American Society for Metals for The Division of Technical information United States Atomic Energy Commission, 1966.

2. Y.S. Touloukian et al. Thermophysical properties of matter (Volumes 2, 5, 13). IFI/PLENUM - New York-Washington, 1977.

3.   S.L. Hayes, J.K. Thomas and K.L. Peddicord. "Material property correlation for uranium mononitride. I. Physical properties". J. Nucl. Mater. 171 (1990) 262 – 270.

Carbide fuel

Tabulated data for uranium and plutonium carbide are presented in Table 11 [1].

Table 11. Thermal linear expansion of uranium carbide and plutonium carbide

T, K	α_{UC}, 1e-6/K	α_{PuC}, 1e-6/K
293	9.8	8.20
300	9.8	8.30
400	10.1	8.90
500	10.3	9.40
600	10.6	9.90
700	10.8	10.30
800	11.0	10.7
900	11.3	11.1
1000	11.4	11.4
1100	-----	11.7
1200	11.8	12.0
1300	-----	12.2
1400	12.1	
1600	12.3	
1800	12.5	
2000	12.6	

1.   Y.S. Touloukian et al. Thermophysical properties of matter (Volumes 2, 5, 13). IFI/PLENUM - New York-Washington, 1977.

Silicon carbide

Tabulated data for silicon carbide are presented in Table 12 [1].

Table 12. Thermal linear expansion of silicon carbide

T, K	α, 1e-6/K
293	3.3
300	3.4
400	4.0
500	4.2
600	4.5
700	4.7
800	4.9
900	5.1
1000	5.3
1200	5.6
1400	6.0
1600	6.2
1800	6.5
2000	6.7
2200	6.9
2400	7.0
2600	7.1
2800	7.1

1. Y.S. Touloukian et al. Thermophysical properties of matter (Volumes 2, 5, 13). IFI/PLENUM - New York-Washington, 1977.

A.5.2. Yield stress

Dioxide fuel

Option 1, standard for oxide fuel and MOX fuel

$$for\ T_C \leq 1800.0 \Rightarrow \sigma_Y = 1176.1 - 1.688 \cdot T_C + 8.179 \cdot 10^{-4} \cdot T_C^2 - 1.293 \cdot 10^{-7} \cdot T_C^3$$
$$for\ T_C > 1800.0 \Rightarrow \sigma_Y = 33.62$$

where σ_Y – yield stress, MPa; T_C – temperature, °C.

Option 2 for LWR oxide fuel [1]:

$$for\ T_C \leq 1733.8 \Rightarrow \sigma_Y = \left(13.6 + \frac{1}{4500} \cdot T_C\right) \cdot 9.81$$

$$for\ T_C > 1733.8 \Rightarrow \sigma_Y = (66 - 0.03 \cdot T_C) \cdot 9.81$$

$$for\ \sigma_Y < 10 \Rightarrow \sigma_Y = 10.0$$

where σ_Y – yield stress, MPa; T_C – temperature, °C.

Table 13. Yield stress of UO$_2$, MPa

T, °C	Option 1	Option 2
100	1015.3	133.634
200	870.2	133.852
300	739.8	134.07
400	623.5	134.288
500	520.4	134.506
600	429.8	134.724
700	350.9	134.942
800	283.0	135.16
900	225.1	135.378
1000	176.7	135.596
1100	136.9	135.814
1200	104.8	136.032
1300	79.9	136.25
1400	61.2	136.468
1500	48.0	136.686
1600	39.5	136.904
1700	35.0	137.122
1800	33.6	117.72
1900	33.6	88.29
2000	33.6	58.86

1.   R.F. Canonet et al. "Deformation of UO$_2$ at high temperatures". J. American Ceramic Society, 54 (1971).

Nitride fuel

Option 1, for uranium nitride fuel:

$$for\ T_K \leq 1423.0 \Rightarrow \sigma_Y = 650.0$$
$$for\ 1423.0 < T_K \leq 2058.0 \Rightarrow \sigma_Y = 2073.0 - T_K$$
$$for\ T_K > 2058.0 \Rightarrow \sigma_Y = 15.0$$

Option 2, TRANSURANUS standard for uranium nitride fuel:

$$\sigma_Y = Max(10.0;\ (13 - 3 \cdot 10^{-3} \cdot T_C) \cdot 9.81)$$

where σ_Y – yield stress, MPa; T_C – temperature, °C; T_K – temperature, K.

Table 14. Yield stress of uranium nitride, MPa

T, K	Option 1	Option 2
300	650.0	126.7
400	650.0	123.8
500	650.0	120.8
600	650.0	117.9
700	650.0	115.0
800	650.0	112.0
900	650.0	109.1
1000	650.0	106.1
1100	650.0	103.2
1200	650.0	100.2
1300	650.0	97.3
1400	650.0	94.4
1500	573.0	91.4
1600	473.0	88.5
1700	373.0	85.5
1800	273.0	82.6
1900	173.0	79.6
2000	73.0	76.7
2100	15.0	73.8
2200	15.0	70.8
2300	15.0	67.9

Carbide fuel

Option 1 for uranium carbide fuel [1]:

$$\sigma_1 = 626.0 - 0.54 \cdot T_K + 3.741 \cdot 10^{-4} \cdot T_K^2$$
$$\sigma_2 = 2263.0 - 1.17 \cdot T_K$$
$$\sigma_3 = Min(\sigma_1; \sigma_2)$$
$$\sigma_4 = \frac{20 \cdot (2753 - T_K)}{836}$$
$$\sigma_Y = Max(\sigma_3; \sigma_4)$$

Option 2 for uranium carbide fuel [2]:

$$\sigma_Y = Max(10.0; (13 - 3 \cdot 10^{-3} \cdot T_C) \cdot 9.81)$$

where σ_Y – yield stress, MPa; T_C – temperature, °C; T_K – temperature, K.

Table 15. Yield stress of UC, MPa

T, K	Option 1	Option 2
300	497.7	126.7
400	469.9	123.8
500	449.5	120.8
600	436.7	117.9
700	431.3	115.0
800	433.4	112.0
900	443.0	109.1
1000	460.1	106.1
1100	484.7	103.2
1200	516.7	100.2
1300	556.2	97.3
1400	603.2	94.4
1500	508.0	91.4
1600	391.0	88.5
1700	274.0	85.5
1800	157.0	82.6
1900	40.0	79.6
2000	18.0	76.7
2100	15.6	73.8
2200	13.2	70.8
2300	10.8	67.9

1. P. Werner, H. Blank. "Mechanical properties of advanced fuels under compressive deformation". Nucl. Technol., 52 (1981), 73-85.

2. T. Preusser. "Modelling of carbide fuel rods". Nucl. Technology, 57 (1982), 343-371 and T. Preusser. Dissertation, KfK-Bericht 3426 (1982).

Silicon carbide

σ_Y = 21 GPa (single crystal) [1].

1. Proceedings of IEEE,Vol 70,No.5,May 1982, p.421.

A.5.3. Young's modulus

Dioxide fuel

Option 1 for uranium oxide and MOX fuel [1].

$$E = 2.23 \cdot 10^5 \cdot (1 - 1.92 \cdot P)$$

Option 2 for LWR uranium oxide fuel [2].

$$E = (1 - 2.6 \cdot P) \cdot \left[22.43 \cdot 10^{-4} - 31.19 \cdot T_C \right]$$
$$for\ P > 0.3 \Rightarrow P = 0.3$$
$$for\ E < 1000 \Rightarrow E = 1000$$

Option 3 for uranium oxide and MOX fuel [3].

$$E = 2.334 \cdot 10^5 \cdot (1 - 2.752 \cdot P) \cdot \left[1 - 1.0915 \cdot 10^{-4} \cdot T_K \right] \cdot e^{\frac{-OMEXP}{|2-XO|}}$$
$$for\ E < 1000 \Rightarrow E = 1000$$
$$for\ XO > 2 \Rightarrow OMEXP = 1.34, \text{ else } OMEXP = 1.75$$

where

E – Young's modulus, MPa;

P – porosity of the fuel material;

T_C – temperature, °C;

T_K – temperature, K;

XO – local stochiometry, O/M ratio.

1.   D. Olander. "Fundamental aspects of nuclear reactor fuel elements". TID-26711-P1, Dep. of Nuclear Engineering, University of California (1976), Berkeley, 335
2.   K. Lassmann, A. Moreno. ATKE, 30 (1977) 207-215
3.   MATPRO - Version 11. "A handbook of material properties for use in the analysis of lightwater reactor fuel rod behaviour". NUREC/CR 0497 TREE1280, EG&G Idaho, Inc. (1979), Idaho Falls, Idaho 83415.

Nitride fuel

<u>Option 1</u> for uranium nitride fuel [1]:

$$E = 2.83 \cdot 10^5 \cdot (1 - 2.72 \cdot P) \cdot \left(1 - \frac{0.285 \cdot (T_C - 24.85)}{2775.0} \right)$$

<u>Option 2</u> TU option for uranium nitride fuel:

$$E = 2.668 \cdot 10^5 \cdot (1 - 2.72 \cdot P) \cdot \left[1 - 0.92 \cdot 10^{-4} \cdot (T_K - 293) \right]$$
$$for\ P > 0.3 \Rightarrow P = 0.3$$
$$for\ E < 1000 \Rightarrow E = 1000$$

<u>Option 3</u> for uranium nitride fuel [2]:

$$E = 0.258 \cdot D^{3.002} \cdot \left[1 - 2.375 \cdot 10^{-5} \cdot T_K \right]$$

for temperature range $298 \leq T_K \leq 2523$,

where

D – density, % of theoretical density;

E – Young's modulus, MPa;

P – porosity of the fuel material;

T_C – temperature, °C;

T_K – temperature, K.

1.   A.R. Hall. "Elastic Moduli and Internal Friction of Some Uranium Ceramics", J. Nucl. Mater. 37 (1970), 314-323.

2.   S.L. Hayes, J.K. Thomas and K.L. Peddicord. "Material property correlation for uranium mononitride. II. Mechanical properties". J. Nucl. Mater. 171 (1990) 271 – 288.

Carbide fuel

Option 1 for uranium carbide fuel [1]:

$$E = 2.25 \cdot 10^5 \cdot (1 - 2.31 \cdot P) \cdot (1 - 1 \cdot 10^{-4} \cdot T_C)$$

Option 2 for uranium carbide fuel [2, 3]:

$$E = 2.15 \cdot 10^5 \cdot (1 - 2.3 \cdot P) \cdot \left[1 - 0.92 \cdot 10^{-4} \cdot (T_C - 25)\right]$$
$$for\ P > 0.3 \Rightarrow P = 0.3$$
$$for\ E < 1000 \Rightarrow E = 1000$$

where:

E – Young's modulus, MPa;

P – porosity of the fuel material;

T_C – temperature, °C.

1.   T.L. George, K. Peddicord. "SPECKLE-III. A computer code for calculating the thermal-mechanical behaviour of sphere-pac fuel pins". OSU-EIR-64, Oregon State University – Eidg. Inst. für Reactorforschung, (1982)

2.   AERE-M2643 (1974)

3.   T. Preusser, KFK 3426 (1982), 65

Silicon carbide

Option 1 [1]

E (T = 20°C) = 466 GPa;

E (T = 1300°C) = 430 GPa.

Option 2

Tabulated data for silicon carbide are presented in Table 16 [2, 3].

Table 16. Young's modulus for silicon carbide

Specimen	Value, GPa	Ref
Single crystal	700	[2]
Ceramic, ρ = 3128 kg/m^3, at room temperature	401.4	[3]
Ceramic, ρ = 3120 kg/m^3, at room temperature	410.5	[3]
Ceramic, pressureless sintered, at room temperature	302.8	[3]
Ceramic, hot pressed, at room temperature	440	[3]
Ceramic, self bonded, at room temperature	410.4	[3]
Ceramic, hot pressed, at T = 20 °C	430.4 – 450.4	[3]
Ceramic, sintered, at T = 20 °C	375 – 420	[3]
Ceramic, reaction sintered, at T = 20 °C	350 – 375	[3]
Ceramic, reaction sintered, at T = 400 °C	379.3	[3]
Ceramic, reaction sintered, at T = 800 °C	365.5	[3]
Ceramic, reaction sintered, at T = 1200 °C	351.7	[3]
Ceramic, reaction sintered, at T = 1400 °C	200 – 320	[3]
Ceramic, sintered, at T = 1400 °C	300 – 400	[3]
Ceramic, hot pressed , at T = 1400 °C	380	[3]

1. D.L. Lide. CRC Handbook of chemistry and physics, 79th edition, 1998-1999, CRC, Boca Raton, FL.

2. Proceedings of IEEE,Vol 70,No.5,May 1982, p.421.

3.   CRC Materials Science and Engineering Handbook, p.507-508

A.5.4.   Poisson's ratio

Dioxide fuel

<u>Option 1</u> for uranium oxide and MOX fuel [1].

$$\nu = 1.32 \cdot (1 - 0.26 \cdot P) - 1$$

<u>Option 2</u> for LWR uranium oxide fuel [2].

$$\nu = 0.32$$

<u>Option 3</u> for uranium oxide and MOX fuel [3].

$$for\ X_{Pu} = 0 \Rightarrow \nu = 0.316$$
$$for\ X_{Pu} > 0 \Rightarrow \nu = 0.276$$

where

P – porosity of the fuel material;

X_{Pu} – weight fraction of PuO_2, i.e. $PuO_2/(U,Pu)O_2$.

1.   D. Olander. "Fundamental aspects of nuclear reactor fuel elements". TID-26711-P1, Dep. of Nuclear Engineering, University of California (1976), Berkeley, 127 (for UO_2).

2.   K. Lassmann, A. Moreno. ATKE, 30 (1977) 207-215.

3.   MATPRO - Version 11. "A handbook of material properties for use in the analysis of lightwater reactor fuel rod behaviour". NUREC/CR 0497 TREE1280, EG&G Idaho, Inc. (1979), Idaho Falls, Idaho 83415.

Nitride fuel

<u>Option 1</u> for uranium nitride fuel [1]:

$$v = 0.284 \cdot (1 - 1.31 \cdot P) \cdot \left(1.0 - \frac{0.124 \cdot (T_C - 24.85)}{2775.0} \right)$$

Option 2 TU standard for uranium nitride fuel:

$$for P > 0.3 \Rightarrow P = 0.3$$
$$v = 0.284 - 0.373 \cdot P$$

Option 3 for uranium nitride fuel [2]:

$$v = 1.26 \cdot 10^{-3} \cdot D^{1.174}$$

for temperature range $298 \leq T_K \leq 2523$,

where

D – density, % of theoretical density;

P – porosity of the fuel material;

T_C – temperature, °C.

T_K – temperature, K.

1. C.A. Alexander, J.S. Odgen. BMI-X-659, 1975.
2. S.L. Hayes, J.K. Thomas and K.L. Peddicord. "Material property correlation for uranium mononitride. II. Mechanical properties". J. Nucl. Mater. 171 (1990) 271 – 288.

Carbide fuel

Option 1 for uranium carbide fuel [1]:

$$v = 0.29 \cdot (1 - 0.99 \cdot P) \cdot (1 - 0.29 \cdot 10^{-4} \cdot T_C)$$

Option 2 for uranium carbide fuel [2]:

$$for P > 0.3 \Rightarrow P = 0.3$$
$$v = 0.288 - 0.286 \cdot P$$

where P – porosity of the fuel material; T_C – temperature, °C.

1.   T.L. George, K. Peddicord. "SPECKLE-III. A computer code for calculating the thermal-mechanical behaviour of sphere-pac fuel pins". OSU-EIR-64, Oregon State University – Eidg. Inst. für Reactorforschung, (1982)

2.   A. Padel, Ch. de Novion. "Constantes elastiques des carbures, nitrures et oxides d'uranium et de plutonium". J. Nucl. Mater., 33 (1969), 40-51

Silicon carbide

<u>Option 1</u> for silicon carbide [1]

ν = 0.21

<u>Option 2</u> for silicon carbide [2]

ν = 0.183 – 0.192 (ceramic, at room temperature, ρ = 3128 kg/m^3)

1.   D.L. Lide. CRC Handbook of chemistry and physics, 79th edition, 1998-1999, CRC, Boca Raton, FL.

2.   CRC Materials Science and Engineering Handbook, p.537

A.5.5.   Creep

Carbide and nitride fuel

The creep curves can be represented by the following equation [1]:

$$\frac{d\varepsilon}{dt} = A\sigma^n e^{-\frac{\Delta H}{RT}}$$

with values of the parameters A, n and ΔH as given in Table 17.

Table 17. Parameters of the creep equation

Fuel	A, h^{-1}	n	ΔH, J/mol	Reference
UN	7.39	4.5	326.8·10³	Hayes et al. (1990b)
(U$_{0.85}$Pu$_{0.15}$)C$_{1+x}$	1.57·10¹¹	2.4	506·10³	Hall (1973)
UC$_{1-x}$	4.06·10³	1.04	188·10³	Killey (1971)

Out-of-pile creep data covered by this table have been determined in high density samples. When applying them to problems in fuel modeling they can be used in form of the creep equation only if relevant local, that is, microscopic, phenomena are described. Otherwise, data have to be transformed into relations which take account of porosity.

1.   R.W. Cahn, P. Haasen, E.J. Kramer. "Material Science and Technology. A Comprehensive Treatment". Volume 10a/10b, Nuclear Materials, Part I.

Nitride fuel

$$\varepsilon' = 2.054\cdot10^{-3}\cdot\sigma^{4.5}\cdot e^{-\frac{39369.5}{T_K}}$$

for temperature range $298 \leq T_K \leq 2523$,

and $20 \leq \sigma \leq 34$

where

T_K – temperature, K.

1.   S.L. Hayes, J.K. Thomas and K.L. Peddicord. "Material property correlation for uranium mononitride. II. Mechanical properties". J. Nucl. Mater. 171 (1990) 271 – 288

A.5.6.   Irradiation creep and stress relaxation

Carbide and nitride fuel

The rate of deformation is proportional to stress and fission rate [1]:

$$\frac{d\varepsilon}{dt} = A_c \sigma \frac{dF}{dt}$$

where

σ – stress, MPa

dF/dt – fission rate, $1/(cm^3 \cdot s)$.

For the relaxation of thermoelastic stress fields by irradiation creep, a relaxation time τ_{rel} can be estimated by equating the irradiation induced creep strain with the elastic strain from Hook's law. For nonaxial stress fields, the equivalent strain has to be used. This gives

$$\tau_{rel} = \frac{f_{rel}}{E \cdot A_c \cdot \frac{dF}{dt}}$$

Here f_{rel} is a numerical factor of the order 1, E is Young's modulus, and A_c can be taken from Table 18.

Table 18. Parameters of the creep and relaxation equations

Fuel	A_c, $10^{-21} \frac{cm^3 \cdot s}{h \cdot MPa \cdot f}$	T-range, K	Burnup, at.%	dF/dT, $1/(cm^3 \cdot s)$	Porosity, %	σ-range, MPa	Sress type
UN	~0.2	970-1170		$3.6 \cdot 10^{13}$	4	20	compression
UC	0.42	720-1070		$7 \cdot 10^{12}$		34	bending
MC	3.0	770-1020	0-10		15	10-40	compression
MC	1.37	770-990	0-9	$1-1.5 \cdot 10^{12}$	5	2-50	compression
MC	~0.2				0		compression

A.5.7.   Swelling under irradiation

Carbide fuel

The data is taken from [1]

For the model, the case of "hard" contact between the cladding and the fuel with low density fuel is taken as a minimum. Freund et al. [2] specify a value for both UC and (U,Pu)C:

$$\frac{\Delta V}{V} = 0.4667 \left(\frac{\text{vol\%}}{10\text{MWd/kg}} \right)$$

This value includes the "hot pressing" effect in contact, so that an additional treatment of hot pressing is unnecessary.

The maximum values are set for the case of swelling with high density fuel, without contact, and with a temperature below that at which strong gas bubble swelling occurs. The following values are used:

For UC:

$$\frac{\Delta V}{V} = 2.1780 \left(\frac{\text{vol\%}}{10\text{MWd/kg}} \right)$$

and

for (U,Pu)C:

$$\frac{\Delta V}{V} = 1.3838 \left(\frac{\text{vol\%}}{10\text{MWd/kg}} \right)$$

Apart from the unhindered swelling due to solid fission products, these values take into consideration the temperature-independent reaction of gas swelling, which also contributes to the change in local porosity.

Above 900°C for mixed carbide and 700°C for uranium carbide, the existence of gas bubbles is accepted. It is described with an increasing parabolic function that is limited to 4.56% volume swelling for UC and 3.4% for (U,Pu)C. These limits are based on measurements made at high temperatures. The gas bubble swelling is considered to be proportional to burnup. In consideration of the influence of porosity, the hindering of swelling due to constant with the cladding tube, and the dependence of breakaway swelling on burnup, the retained functions are corrected with corresponding model parameters. The following equations for swelling due to solid particles and gas bubbles result:

For UC:

up to 700°C

$$\frac{\Delta V}{V} = 0.4667 + 1.711 \cdot f(P, pc)$$

above 700°C

$$\frac{\Delta V}{V} = 0.4667 + 1.711 \cdot f(P, pc) + \left[\left(6.412 - 0.0198 \cdot T_C + 0.152 \cdot 10^{-4} \cdot T_C^2 \right) \cdot f(BU) \cdot f(P, pc) \right]$$

upper limit:

$$\frac{\Delta V}{V} = 4.558$$

and for (U,Pu)C:

up to 900°C

$$\frac{\Delta V}{V} = 0.4667 + 0.9171 \cdot f(P, pc)$$

above 900°C

$$\frac{\Delta V}{V} = 0.4667 + 0.9171 \cdot f(P, pc) + \left[\left(11.8062 - 0.0257 \cdot T_C + 0.1398 \cdot 10^{-4} \cdot T_C^2 \right) \cdot f(BU) \cdot f(P, pc) \right]$$

upper limit:

$$\frac{\Delta V}{V} = 3.406$$

correction:

$$f(BU) = \left(\frac{BU}{BU_0} - a \right), \; f(BU) \geq 0$$

correction:

$$f(P, pc) = e^{-(P-0.04)} \cdot e^{-\left(\frac{pc}{pc_0} \cdot b \right)}$$
$$(P - 0.04) \geq 0$$

where

$\dfrac{\Delta V}{V}$ – volume swelling, $\dfrac{\text{vol}\%}{10\,\text{MWd}/\text{kg}}$

T_C – temperature, °C

BU – burnup, MWd/kg

P – porosity

pc – contact pressure, Mpa

a, b – model parameters

BU_0 = 10 – constant, MWd/kg

pc_0 = 1 – constant, Mpa.

Through variation of the model parameter a between 0 and 5, the onset of gas bubble swelling can be varied from 0 to 5% burnup. However, adjustments should only be made when taking into account the retarding of fission gas release (FGR) with burnup, as described in Section A.5.8. With the choice of the parameter b between 0 and 1, the influence of contact pressure can be suppressed or emphasized. Up to now, good results have been obtained with a = 2 and b = 0.1.

1.   T. Preusser, Modelling of Carbide Fuel Rods, Nucl. Technol. 57 (1982) 343.
2.   D. Freund, H. Elbel and H. Steiner, "Auslegung, Bestrahlung und Nachuntersuchung der UC- und (U,Pu)C-Brennstabe der Versuchsgruppen Mol-11/K1 and Mol-11/K2",KfK-Bericht 2268, Kernforschungszentrum Karlsruhe, June 1976.

A.5.8.   Fission gas release

Carbide fuel

The fission gas release rate can be calculated as follows [1]

$$f_{res}^{gas} = f^{gas}(T_z) \cdot \left(1 - e^{-1.5 \cdot \left(BU - BU^{free}\right)}\right),$$

where

f_{res}^{gas} – resulting fission gas release rate

f^{gas} – temperature dependence of the fission gas release rate

BU – percent of burnup

BU^{free} – percent of burnup at which fission gas release begins

T_z – temperature, °C.

Empirical correlations are used for BU^{free}:

for T_z < 1455 °C,   *BU^{free}* = 2

for 1455 < T_z < 2325 °C,   *BU^{free}* = -0.0023 · T_z + 5.3504

for T_z > 2325 °C,   *BU^{free}* = 0

For the temperature dependence of the fission gas release rate, the following correlations can be used:

for T_z < 1000 °C, $f^{gas} = 0$

for 1000 < T_z < 2070 °C, $f^{gas} = 0.000467 \cdot T_z - 0.467$

for T_z > 2325 °C, $f^{gas} = 0.741918 \cdot \ln\left(0.7675 \cdot T_z\right) - 4.968477$

1.   T. Preusser, Modelling of Carbide Fuel Rods, Nucl. Technol. 57 (1982) 343.

Appendix B: FRED input deck description

The FRED input deck consists of cards. Free format is used. Any card starting with * is a comment card. Each card input is organized as follows:

xxxxxx   value 1   value 2   …   value N

xxxxxx: 6-digit card number

value 1 … value N: values of the corresponding variables

The FRED code is used for both traditional fuel rods and for GFR plate-type fuel analysis. Therefore the "fuel rod" in the following descriptions should be understood as a hexagonal cell when the GFR fuel is considered.

Time integration card (crdno=000000)

000000   meth   rtol   atol

meth: time integration method indicator:

GEAR0 – backward differentiation formula with automatically generated Jacobi matrix;

rtol: relative tolerance parameter;

atol: absolute tolerance parameter.

Transient card (crdno=000001)

000001   itran   nout

itran: transient indicator:

0 – steady-state calculation

1 – transient calculation

nout: frequency (FRED output is written for every set of **nout** time steps).

Options card (crdno=000002)

000002   imech   icreep   iaxial   jaxial   jrad   jfuro

imech: option for cladding mechanical calculation:

0 – no mechanical calculation

2 – mechanical calculation

icreep: option for cladding creep calculation

0 – no clad creep calculation

1, 2, 3, 4 – not used for the GFR fuel.

iaxial: option for axial heat conductance:

0 – no axial heat conductance is calculated (not valid for GFR fuel)

1 – axial heat conductance is calculated

For GFR analysis, the axial heat transfer is always calculated, no matter which value is input.

jaxial: data for this axial slice is output on the screen

jrad: data for this cladding radial node is output on the screen and in the output files

jfuro: data for this fuel rod is output on the screen.

Fuel rod axial division card (crdno=000003)

000003   dz0   nz   Nfr   ngeom

dz0:   axial slice height (m)

nz: number of axial slices

nfr: number of fuel rods with such parameters

ngeom: fuel geometry identifier.

1 – cylindrical fuel rods

3 – GFR plate-type fuel.

Remark 1:   For the GFR analysis, **nz** is the number of axial nodes in the fuel pellet.

Remark 2:   For the GFR analysis, **nz** has to be odd. The axial slice height has to be calculated as: **dz0 = hfuel/(nz-1)**. This is because the first and the last nodes are put on the fuel pellet flat ends, and the corresponding axial levels are half-height of the axial levels within the pellet.

Tangential division card (crdno=000004)

000004   ntet

ntet: number of calculational tangential sectors (the value is equalized to 1 for the GFR analysis)

Restart card (crdno=000005)

```
000005          r1          s1
```

r1:   option for reading fuel rod temperatures from REST_HEX.dat file:

0: do not read temperatures from restart file.

1: read temperatures from restart file.

s1:   option for writing fuel rod temperatures to REST_HEX.dat file:

0: do not save temperatures in restart file.

1: save temperatures in restart file.

Initial temperature card (crdno=000006)

```
000006          tem0
```

tem0:   initial temperature (K).

Remark: One and the same temperature is written in all FRED structures at the beginning of a new calculation.

Fuel pellet card (crdno=100001)

```
100001     fmat     fden     pucont     rfi     rfo     ruff     nf     nfr
```

fmat: fuel type:

uo2: uranium or mixed uranium-plutonium dioxide

230

un: uranium nitride

uc: uranium carbide or mixed uranium-plutonium carbide

fden: initial fuel density at room temperature (with accounting of porosity), kg/m^3

pucont: plutonium content, relative units;

rfi: radius of fuel pellet inner hole, m

rfo: outer radius of fuel pellet, m

ruff: roughness of outer surface of fuel pellet, m

nf: number of radial nodes in fuel pellet

nfr: number of fuel rods with such parameters.

Fuel-clad gap card (crdno=100002)

100002   gmat   dgap   pin   vpl   nvplen   i   j   k   nfr

gmat: material in fuel-clad gap:

he: helium

dgap: initial fuel-clad gap width, m

pin: initial gas pressure inside fuel rod, Pa

vpl: initial gas plenum volume, m^3

nvplen, i, j, k: number of TRACE hydraulic component cell adjacent to the gas plenum

nfr: number of fuel rods with such parameters.

Remark 1: All data are for cold conditions.

Remark 2: No common gas plenum exists in the GFR case; therefore **nvplen, i, j, k** are input but never used in the code

Remark 3:   For GFR fuel analysis, dgap is the geometrically averaged radial gas gap, which can be calculated as follows:

$$dgap = \left(r_{fuel} + \delta_{rad}^{\min}\right) \cdot \sqrt{\frac{2\sqrt{3}}{\pi}} - r_{fuel} ,$$

where

r_{fuel}:   fuel radius

$\delta_{rad}^{\min}$:   minimal radial gap, i.e. distance between the fuel pellet and the inner cell wall in case of their concentric arrangement.

The formula is derived for the reduced cell geometry: the hexagonal cell wall is approximated by a cylindrical one.

Fuel rod cladding card (crdno=100003)

100003	cmat	rco	cden	rufc	nc	nfr

fmat: cladding material:

zrn: Zr+1%Nb

zry: zyrcalloy-4

ss823: stainless steel EP-823 (12%Cr-Si)

sic: silicon carbide

rco: outer radius of the cylindrical cell equivalent to the original hexagonal one, m

cden: cladding initial density at room temperature (with accounting of porosity), kg/m^3

rufc: roughness of cladding inner surface, m

nc: number of radial nodes in cladding

nfr: number of fuel rods with such parameters

232

TRACE cooling interface card (crdno=100005)

100005   nfrus   i2   r2

nfrus: identifier of TRACE heat structure corresponding to FRED structure

i2:   number of axial levels within the heat structure (equals to number of cells simulated for a given heat structure)

r2:   initial height of the given heat structure's axial level

Remark 1:   The number of these cards equals the number of simulated structures.

Remark 2:   If ngeom = 1 (fuel rods analysis), then i2 and r2 should not be input.

Burnup conversion factor card (crdno=100006)

100006   bcnvr

bcnvr: MW·d/kg-to-% burnup conversion factor

Remark: If the card is not input, the value 0.123 is used (corresponds to ^{235}U fission by thermal neutrons)

Radiative damage rate card (crdno=100007)

100007   ddpa

ddpa: radiative damage rate (dpa/s).

Lateral walls of the fuel plate card (GFR analysis only) (crdno=100008)

100008   clad_bot   clad_top   gap_bot   gap_top   nfr

clad_bot: 1st lateral wall's thickness

clad_top: 2nd lateral wall's thickness

gap_bot: 1st axial gas gap width

gap_top: 2nd axial gas gap width

nfr: number of fuel rods with such parameters

Table 'fission gas release (FGR) from fuel vs. temperature' (crdno=400003)

400003   temp   fgr

temp: fuel temperature, K

fgr: fission gas release from fuel

Remark 1:   Input as many cards as many data pairs ara available

Remark 2:   If the card is not input, built-in correlations are used.

Remark 3:   This card is used, as a rule, for simulation of FGR under steady-state operational conditions (e.g. base irradiation).

Table 'fuel swelling vs temperature' (crdno=400004)

400003   bup   fswel

bup: fuel burnup, at%

fswel: volumetric fuel swelling, %

Remark 1: Input as many cards as many data pairs ara available

Remark 2: If the card is not input, built in correlations are used.

Remark 3: This card is used, as a rule, for simulation of fuel swelling under steady-state operational conditions (e.g. base irradiation).

Base irradiation calculation card (crdno=600000)

600000 baseir tss dtirrad steps

basir: base irradiation calculation flag

0: no base irradiation analysis

1: perform base irradiation analysis

tss: time at which stand-alone base irradiation calculation starts, s

dtirrad: time-step for base irradiation analysis, s

nsteps: number of time-steps

Remark: This card is input to perform a FRED stand-alone base-irradiation calculation. The thermal-hydraulic code is by-passed. The reason to avoid the TRACE code is the impossibility of the latter to generate time-steps large enough (~ 1 day) for burnup analysis.

Appendix C: Description of the 3D finite-elements model used for benchmarking

As mentioned at the outset, no tools have been readily available for the analysis of the novel GFR plate-type fuel. Moreover, no experimental data exist for such a fuel. In spite of these difficulties, a benchmarking procedure has had to be established for verification of the developed model. It was decided to limit the benchmarking to the consideration of a single cell. Zero heat flux is assumed between neighboring cells, and the boundaries of a cell (apart from the cooled surface) are assumed to be adiabatic.

A 3D model was built using the finite-elements ANSYS code and its results were adopted as a reference solution. The present appendix is devoted to the description of the 3D model and the algorithms to benchmark the simplified solution. The geometry of the cell is shown in Fig. 1.
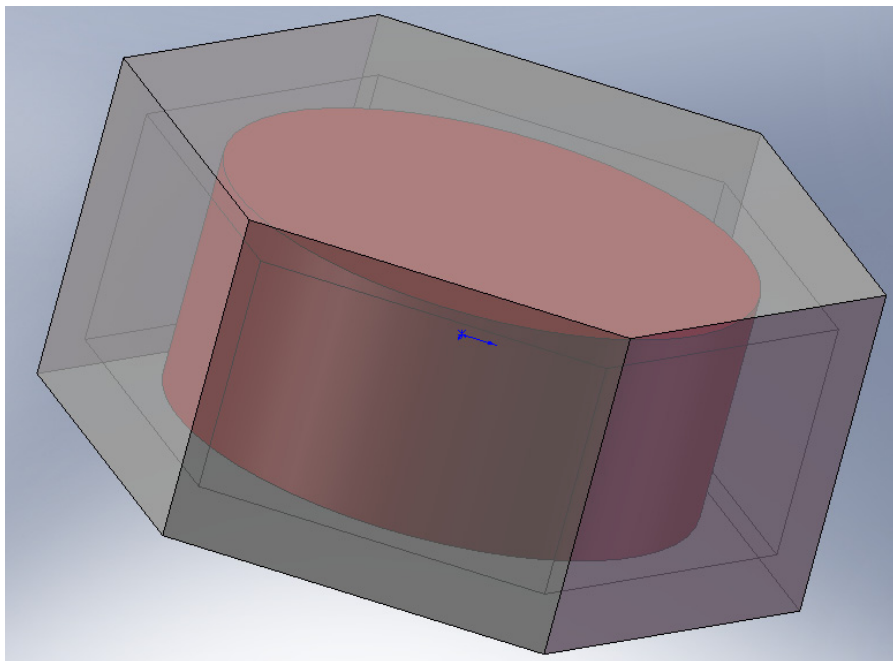
Fig.1. Original geometry of the GFR cell

However as the cell is hexagonal and the fuel pellet is supposed to be concentric with the cladding, there is no need to model the whole cell. The model can be limited to a 30° sector and half height of a cell as shown in Fig. 2.
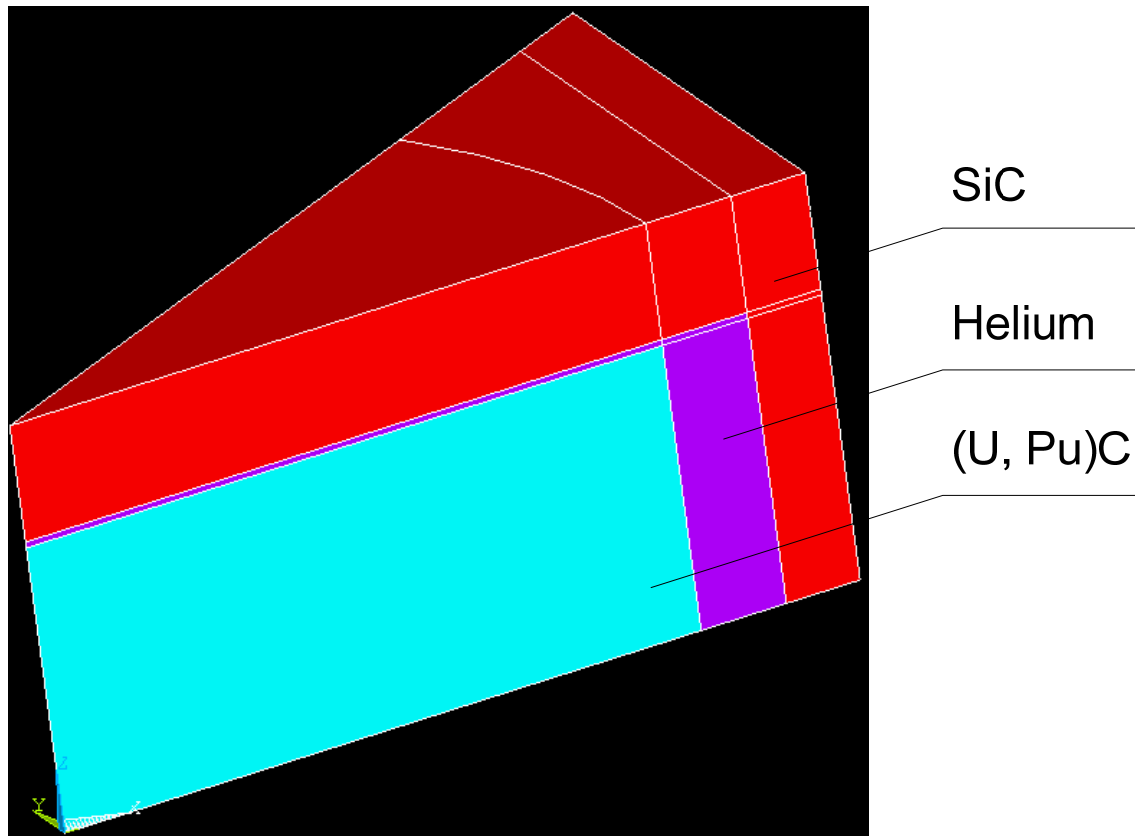
Fig. 2. Geometry of a solid model used for benchmarking

This model was used to benchmark both thermal and thermo-mechanical models, the main differences being in the meshing of the volumes corresponding to the gas gap and in the element types used for different analysis types.

Benchmarking of the thermal model

The element type used for the ANSYS thermal analysis is SOLID90. The SOLID90 element is a 20-node brick element with a single degree of freedom, temperature, at each node. Quadratic interpolation for the temperature field is used within the element. It provides a solution of higher precision than the analogous SOLID70 element which has 8 nodes and uses linear interpolation. The SOLID90 element is applicable to a 3-D, steady-state or transient thermal analysis. The geometry of the element and the location of the nodes are shown in Fig. 3. The nodes are marked by letters, and the faces by numbers. Apart from the original geometry, reduced versions are shown on the right side. They are supposed to be used when the volume geometry is complicated and cannot be meshed by hexahedral elements.
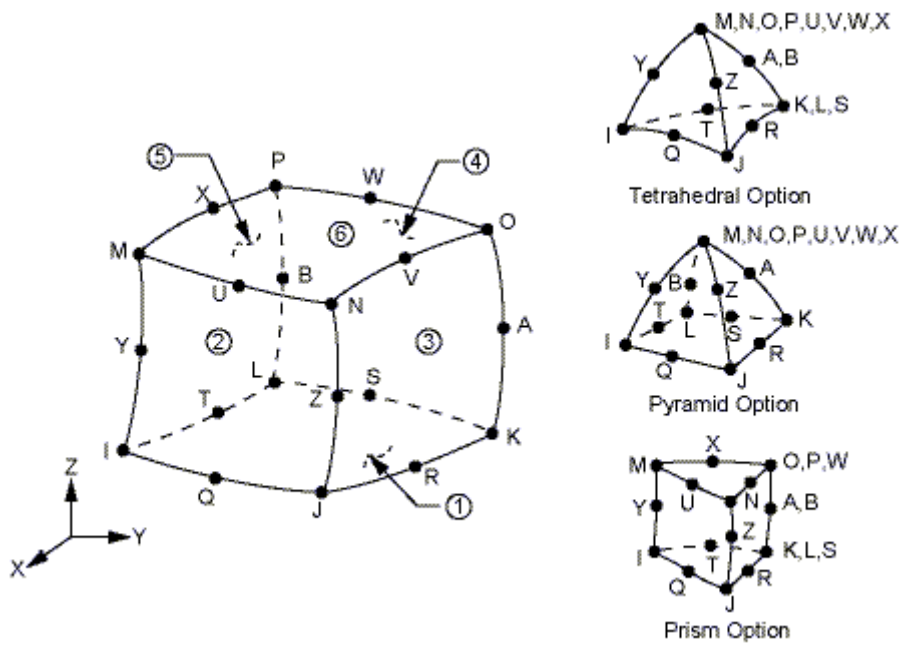
Fig. 3. 20-node brick element geometry

A regular mesh containing only hexahedral elements was created for the geometry shown in Fig. 2. The boundary conditions for the thermal model were given by the bulk coolant temperature (T_{bulk}), heat exchange coefficient (α) and the heat generation rate (q_V). The meshed model and the application of boundary conditions are shown in Fig. 4.
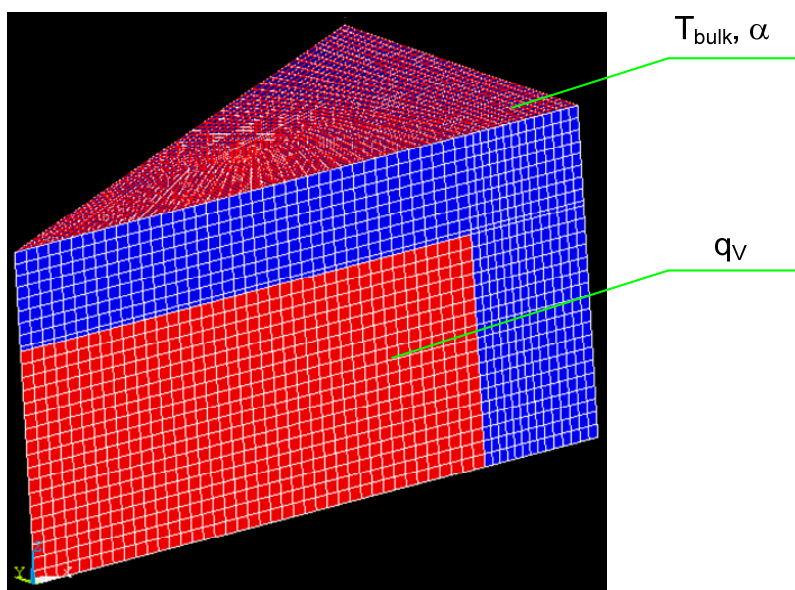
Fig. 4. FE mesh of the thermal model and the boundary conditions

All the surfaces, apart from the cooled one, are adiabatic due to the assumed symmetry. Heat generation only exists in the fuel, and the corresponding elements are assigned the red color in the figure.

Dedicated macros in ANSYS Parametric Design Language (APDL) were written to automatize the geometry creation and the mesh generation. The geometry is fully parameterized, and the boundary conditions can be either user input or taken from external files if a transient with time-dependent boundary conditions is to be calculated.

Benchmarking of the thermo-mechanical model

The element type used for the ANSYS structural analysis is SOLID186. SOLID186 is a second-order 3-D 20-node solid element that exhibits quadratic displacement behavior. The element is defined by 20 nodes (the same as SOLID90) having three degrees of freedom per node: translations in the nodal x, y, and z directions. The element supports plasticity, hyperelasticity, creep, stress stiffening, large deflection, and large strain capabilities.

The identical mesh was used for the thermal and mechanical problems. The identity of the two meshes allowed a simple node-by-node transfer of the temperature field as a body load for the mechanical analysis.

Particular attention was paid to the gas gap modeling. The same element type cannot be used to model the gas gap, as pellet-cladding contact is foreseen and the finite-elements of the gap cannot be squeezed to zero volume or zero thickness. On the other hand, the heat transfer through the gas gap is an important phenomena and the variation of the gap greatly influences the thermal solution. Therefore, it was decided not to use brick elements to model the heat transfer through the gap at the places where the contact is most likely to appear.

For the reference GFR fuel design, axial contact is expected and the radial is unlikely to occur. Accordingly, the radial gas gap was meshed by SOLID186 elements and the heat transfer between the contacting surfaces (axial gap) was modeled by use of the LINK34 element. LINK34 is a uniaxial element with the ability to convect heat between its nodes. The element has a single degree of freedom, temperature, at each node point. The convection element is applicable to a 2-D (plane or axisymmetric) or 3-D, steady-state or transient thermal analysis. The peculiarity of this element is that its nodes may or may not be coincident, which is important for simulating the contact heat transfer.

It must be mentioned that, for alternative fuel geometries, radial contact could be possible. To model such configurations, link elements would also have to be used for the radial heat transfer.
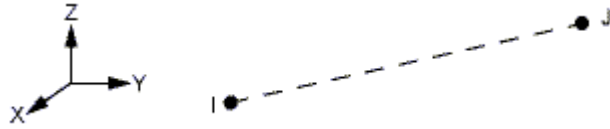
240

Fig. 5. LINK34 geometry

The geometry and node locations for a LINK34 element are shown in Fig. 5. The element is defined by two nodes, a convection surface area, two empirical terms, and a film coefficient. In an axisymmetric analysis, the convection area must be expressed on a full 360° basis. The form of the convection equation of the LINK34 element is defined by the KEYOPT(3). For the present analysis, this was set to 2, which means that the heat transfer is determined by the crossectional area of the element and the film coefficient. The convection function in this case is defined as follows:

$$q = h_f \cdot A \cdot (T_I - T_J)$$

where:

q: heat flow rate (Heat/Time)

h_f: film coefficient (Heat/Length^2*Time*Deg)

A: area (Length^2)

T: temperature (this substep) (Deg)

The area was in the input data and was not changed during the solution. The film coefficient was recalculated after each iteration/time-step as explained below.

The contacting surfaces were meshed by the CONTA174 and TARGE170 elements. These are elements which are used to represent the contact and sliding between two surfaces. They are located on the surfaces of the solid elements and have the same geometrical characteristics as the solid elements faces with which they are connected.

Resulting meshes for the thermal and structural parts of the coupled analysis are shown in the following figures:

Fig. 6: thermal mesh for the fuel configuration with only axial contact possible,

Fig. 7: thermal mesh for the fuel configuration with both axial and radial contacts possible,

Fig. 8: structural mesh for the fuel configuration with only axial contact possible,

Fig. 9: structural mesh for the fuel configuration with both axial and radial contacts possible.
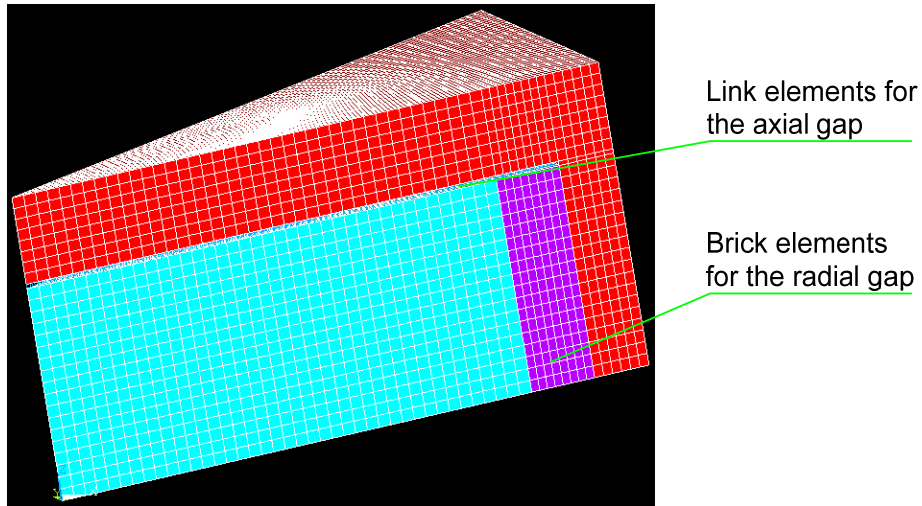
Link elements for the axial gap

Brick elements for the radial gap

Fig. 6. Mesh for the thermal part of the coupled analysis if radial contact cannot occur

Link elements for the axial gap

Link elements for the radial gap
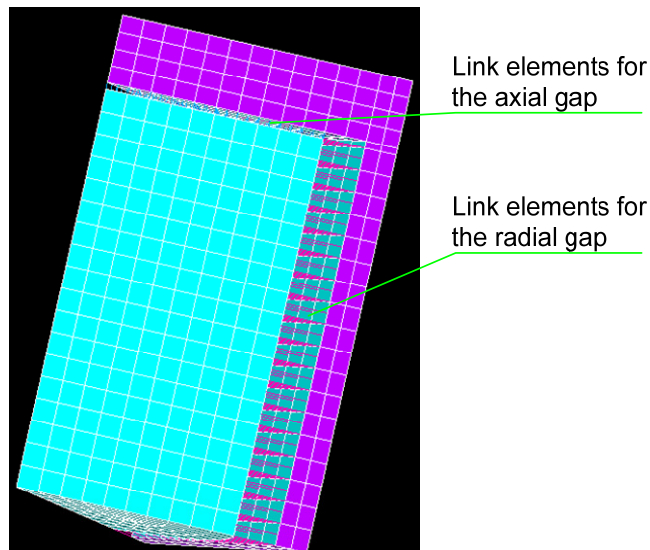
Fig. 7. Mesh for the thermal part of the coupled analysis if radial contact can occur
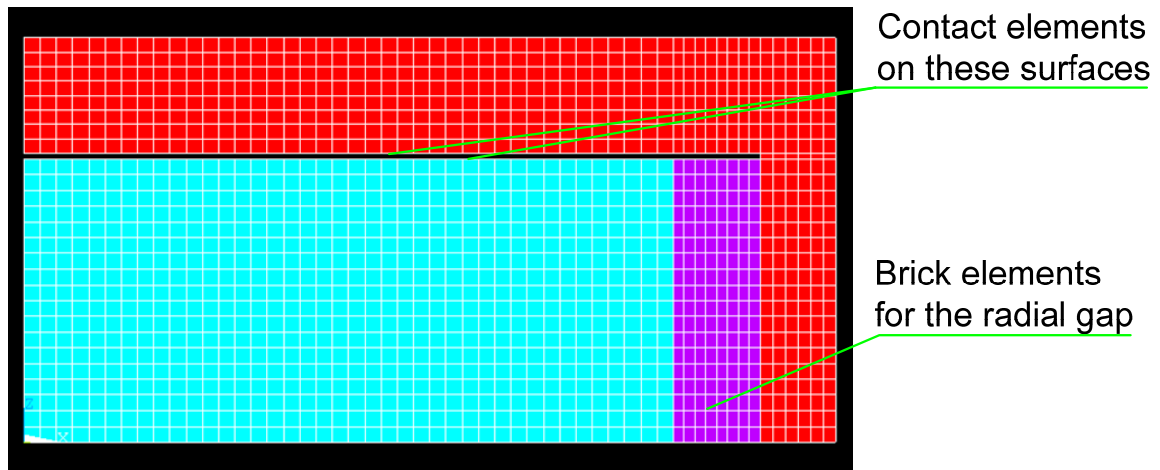
Fig. 8. Mesh for the structural part of the coupled analysis if radial contact cannot occur
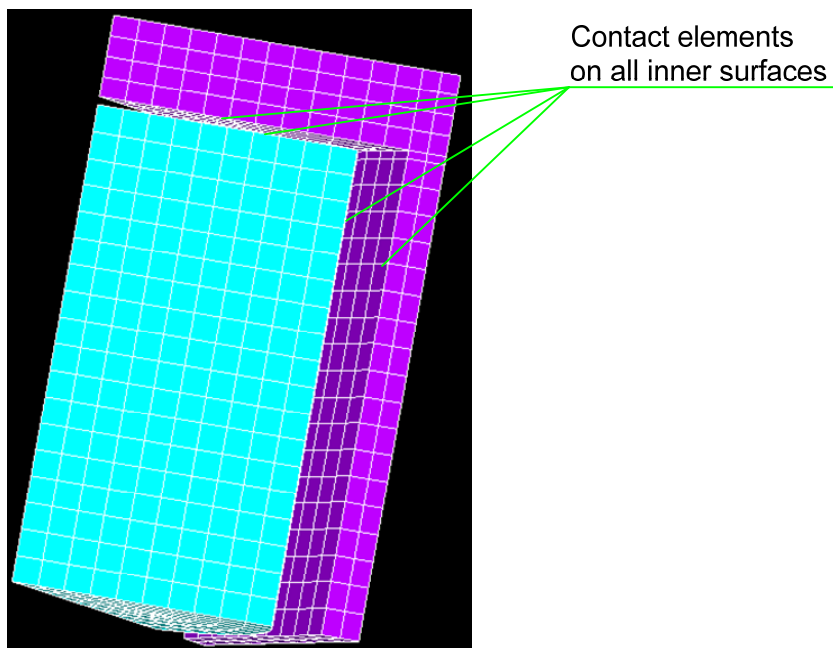
Fig. 9. Mesh for the structural part of the coupled analysis if radial contact can occur

In case of the meshed gas volume (Fig. 8), attention has to be paid to the gas properties assignment. The gas must have no influence on the structure and the fuel (deformations due to the gas pressure are negligible); therefore, its Young's modulus was artificially specified to be several orders of magnitude lower then that of the fuel and cladding. The thermal expansion coefficient was set to zero. This helps to trace the changes of the gas gap size without affecting the fuel and cladding deformations.

An important remark has to be made about the boundary conditions for the outer radial surface of a cell. It represents a boundary with the neighboring cell (see Fig. 10) and therefore has to fulfill the following requirements:

- it has to remain flat during deformation,

- symmetry boundary conditions are not applicable as the wall can be displaced during deformation (expansion or shrinkage of the honeycomb structure)

The following steps were taken to realistically model the wall:

- The active coordinate system (CS) is rotated so that the X-axis is perpendicular to the surface of interest and the Z-axis is parallel to the cell axis, as shown in Fig. 10,

- The local coordinate systems of all the nodes on a given surface are aligned with the active CS (this can be achieved via either the NROTAT command or through the graphical user interface),

- The displacement along the X-axis (UX degree of freedom) is coupled for all the nodes on this surface (this can be achieved via either the CP command or through the graphical user interface).
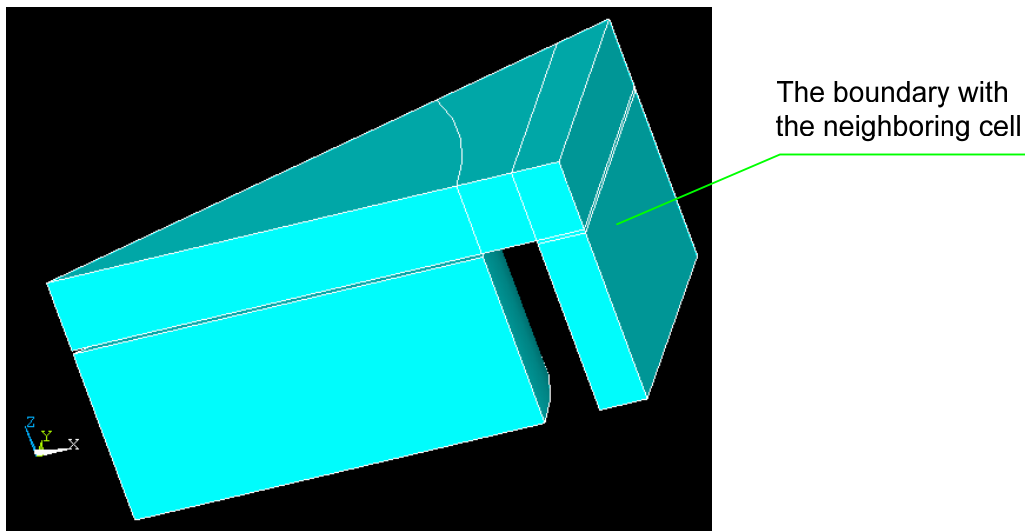
Fig. 10 The surface between neighboring cells and the coordinate system orientation for the structural analysis

The coupled thermo-mechanical modeling was divided into two steps. Firstly, the thermal problem was solved. The obtained temperatures were used as a body load for the mechanical analysis. After that, the thermal solutions were redone with accounting of the changes of the fuel, matrix and gas gap dimensions. The iterative procedure was continued until convergence was obtained for the given parameter (peak fuel temperature in the present work). This scheme was applied to get the steady-state solution.

For the transient analysis, the time-steps, and the evolution of the heat generation rate, bulk coolant temperature and the heat exchange coefficient were specified in external files and then read into tables by ANSYS. These data were provided by the TRACE calculations. In this case, the transient thermal analysis is divided into a number of specified time-steps. After each of them, a mechanical analysis is performed to update the geometry. Schematically, this is shown in Fig. 11.
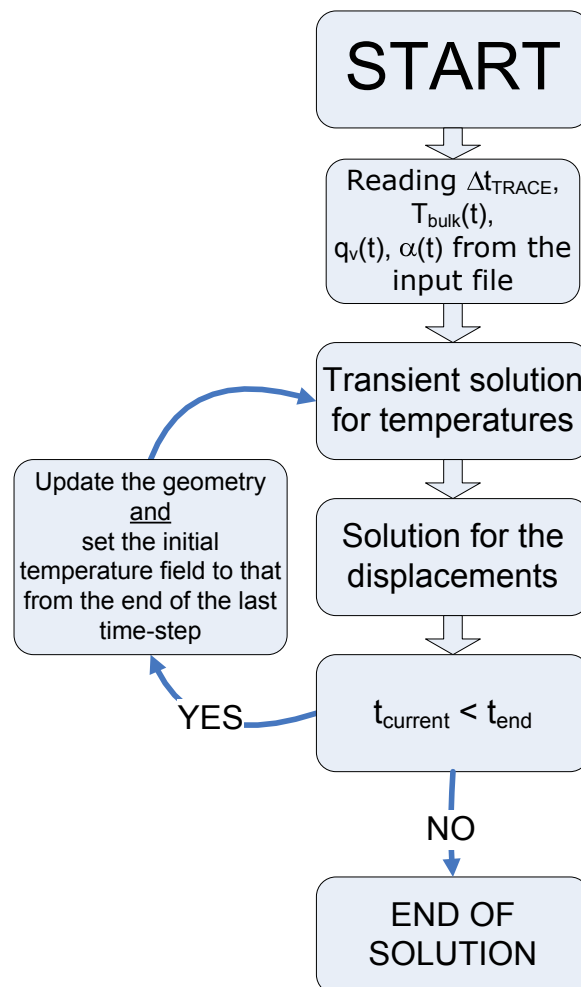
Fig. 11. Flow-chart of the transient thermo-mechanical analysis

245

The coupled thermo-mechanical problem was solved by specifying different environments for the thermal and mechanical parts in ANSYS. The environment assumes specification of the element types, real constants, key options, boundary conditions and material properties for each part. There are other techniques in ANSYS to solve coupled problems, but these could not be applied easily to the given type of analysis.

ACKNOWLEDGEMENTS

CURRICULUM VITAE

Petkevich Petr

PERSONAL INFORMATION

Date of birth: June 23, 1981

Place of birth: Moscow, Russia

Nationality: Russian

EDUCATION

2004-2008   **Paul Scherrer Institute / École Polytechnique Fédérale de Lausanne**   Switzerland
LABORATORY FOR REACTOR PHYSICS AND SYSTEMS BEHAVIOUR (LRS)

Position: Doctoral student
Thesis topic: *"Development and Application of an Advanced Fuel Model for the Safety Analysis of the Generation IV Gas Cooled Fast Reactor"*
Thesis director: Prof. Rakesh Chawla

1998-2004   **Moscow State Engineering Physics Institute (Technical University)**   Moscow, Russia
DEPARTMENT OF THEORETICAL AND EXPERIMENTAL NUCLEAR REACTOR PHYSICS

Diploma thesis: "*Calculational Studies of Neutronic Parameters of Molten Salt Reactor – Burner of Minor Actinides*". Accomplished at the Russian Research Centre "Kurchatov Institute" (RRC "KI").
Thesis director: Dr. P.N. Alekseev
Qualification: Engineer, with "Nuclear Reactors and Power Facilities" as speciality

PROFESSIONAL EXPERIENCE

2004-2008   **Paul Scherrer Institute / École Polytechnique Fédérale de Lausanne**   Switzerland
LABORATORY FOR REACTOR PHYSICS AND SYSTEMS BEHAVIOUR (LRS)

Main task: Research related to the Generation-IV Gas-cooled Fast Reactor.

2003-2004	**Russian Research Centre "Kurchatov Institute" (RRC "KI")**	Moscow, Russia

DEPARTMENT OF PHYSICAL & TECHNICAL RESEARCH ON ADVANCED REACTORS

Main task: Neutronic studies and safety assessment of the Molten Salt Reactor – Burner of Minor Actinides.

2003-2004	**Électricité de France R&D**	Clamart Cedex, France

DEPARTMENT SINETICS

Main task: Neutronic investigations of the fast molten salt reactor with on-line fuel reprocessing and natural uranium feed

PUBLICATIONS AND CONFERENCE PAPERS

P. Petkevich, K. Mikityuk, P. Coddington, R. Chawla. "Development and benchmarking of a 2D transient thermal model for GFR plate-type fuel", Annals of Nuclear Energy 34, pp. 707-718, 2007.

P. Petkevich, K. Mikityuk, P. Coddington, S. Pelloni, R. Chawla. "Comparative Transient Analysis of a Gas-cooled Fast Reactor for Different Fuel Types", Proceedings of ICAPP '06, Paper 6312, Reno, NV USA, June 4-8, 2006

P. Petkevich, K. Mikityuk, P. Coddington, R. Chawla. "A 2D Transient Model for Gas-Cooled Fast Reactor Plate-Type Fuel", Proceedings of ICAPP '07, Paper 7330, Nice-Acropolis, France, May 13-18, 2007

P. Petkevich, K. Mikityuk, P. Coddington, R. Chawla. " Thermal-Mechanical Modelling of Gas-Cooled Fast Reactor Plate-Type Fuel", Proceedings of IYCE-2007, Paper 290, Budapest, Hungary, May 30 - June 2, 2007

P. Petkevich, K. Mikityuk, P. Coddington, R. Chawla, "GFR transient analysis employing a 2D thermomechanical model for the plate-type fuel", PHYSOR-2008, Interlaken, Switzerland, Sept. 14-19, 2008.